Technische Universität München
Fakultät für Elektrotechnik und Informationstechnik
Lehrstuhl für Hochfrequenztechnik

Propagating Plane-Wave Expansions for Microwave Near-Field Imaging and Radar Cross Section Determination

Ole Neitz

Vollständiger Abdruck der von der Fakultät für Elektrotechnik und Informationstechnik der Technischen Universität München zur Erlangung des akademischen Grades eines

– Doktor-Ingenieurs –

genehmigten Dissertation.

Vorsitzender:	Prof. Dr.-Ing. Ulrich Wagner
Prüfer der Dissertation:	1. Prof. Dr.-Ing. Thomas F. Eibert
	2. Prof. Dr. Romanus Dyczij-Edlinger

Die Dissertation wurde am 18.11.2019 bei der Technischen Universität München eingereicht und durch die Fakultät für Elektrotechnik und Informationstechnik am 02.03.2020 angenommen.

Danksagung

Dass ich die vorliegende Arbeit anfertigen konnte, verdanke ich vor allem Herrn Prof. Dr.-Ing. Thomas Eibert, der mich unbekannterweise an seinem Lehrstuhl aufnahm, mir von Beginn an viel Vertrauen schenkte und mich bis zum Schluss in allen fachlichen Belangen großartig unterstützte. Ein besonderer Dank gilt zudem Raimund, der mir während vieler Stunden in der Messkammer (und am Schreibtisch) so tatkräftig zur Seite stand. Bedanken möchte ich mich auch bei allen anderen Kollegen und Kolleginnen am Lehrstuhl für Hochfrequenztechnik, die ich im Laufe der Jahre kennenlernen durfte. Sie haben nicht nur dafür gesorgt, dass es eine sehr lehrreiche, sondern auch kulturell und sportlich sehr abwechslungsreiche Zeit war, und dass mir das Ankommen in München so leicht fiel. Mein größter Dank aber geht an Anika, die mit mir zusammen den gesamten Weg gegangen ist.

München, Sommer 2020

Kurzfassung

Der Radar-Streuquerschnitt (RCS, engl. “radar cross section”) ist ein Maß für das Streuverhalten eines Objektes in Bezug auf einfallende und gestreute elektromagnetische Wellen und spielt eine wichtige Rolle zur Charakterisierung der Detektierbarkeit eines Objektes mithilfe von Radar-Sensoren. Darüber hinaus entspricht der RCS dem Raumfrequenzspektrum einer Verteilung von lokalisierten Streuzentren oder äquivalenten Quellen, was folglich auch die Berechnung eines räumlichen Bildes des Objektes ermöglicht. Ein wesentliches Problem beim Messen des RCS oder beim Aufnehmen eines Radar-Bildes besteht darin, eine Größe zu bestimmen, die bezüglich einfallender und gestreuter, *ebener* Wellen definiert ist. Nur für ausreichend große Abstände zwischen Sende- und Empfangsantenne sowie dem Testobjekt ist die Annahme von ebenen Wellen gerechtfertigt und es ist möglich, den RCS direkt zu messen ohne systematische Fehler einzuführen. Zu diesem Zweck werden in der Regel große Freifeldmessplätze genutzt oder geschlossene Messhallen, in denen große Parabolspiegel auf relativ kleinem Raum das Feld einer ebenen Welle erzeugen. Somit ist es zwar möglich, in einer kontrollierten Messumgebung zu arbeiten, gleichzeitig ist die Errichtung dieser Anlagen allerdings teuer und aufwändig. Aus diesem Grund besteht ein anhaltendes Interesse an der Erforschung von Verfahren zur rechnerischen Bestimmung des RCS aus Messdaten, die in kurzer Distanz zum Testobjekt (im Nahfeld) aufgenommen werden.

In dieser Arbeit werden leistungsfähige Algorithmen zur Bestimmung des RCS aus Nahfeld-Streumessdaten hergeleitet, mit denen es möglich ist, große Datenmengen zu verarbeiten und Gleichungssysteme mit einer hohen Anzahl von unbekannten Koeffizienten zu lösen. Die Algorithmen basieren auf einer Entwicklung des elektrischen Feldes in Spektren ebener Wellen, was die Anwendung von hierarchischen Verfahren ermöglicht, mit denen folglich auch elektrisch große Probleme effizient behandelt werden können. Im Gegensatz zu üblichen existierenden Verfahren können die Messpunkte entlang unregelmäßiger Konturen um das Testobjekt herum aufgenommen werden, ohne Einbußen hinsichtlich der Effizienz des Algorithmus in Kauf zu nehmen. Dies eröffnet neue vielseitige Möglichkeiten für die Realisierung von Systemen zur RCS-Messung und Nahfeld-Radarbildgebung.

Von dem eng verwandten Fall der Antennenmesstechnik ausgehend, wird eine auf ebenen Wellen basierende Nahfeld-Übertragungsgleichung zur Bestimmung des Antennengewinns hergeleitet und ein Algorithmus zur Lösung des hieraus folgenden linearen Gleichungssystems diskutiert. Mithilfe simulierter und gemessener Testdaten wird die Genauigkeit und Leistungsfähigkeit des Algorithmus überprüft. Anschließend wird gezeigt, wie diese Formulierung durch das Treffen einiger vereinfachender Annahmen auch für monostatische Streuprobleme genutzt werden kann. Zu diesem Zweck wird eine Nahfeld-Radar-Gleichung hergeleitet und der Zusammenhang zwischen RCS und räumlicher Streuzentrenverteilung (dem Radar-Bild) sowie dessen effiziente Berechnung untersucht. Aufgrund der zur Herleitung getroffenen, vereinfachenden Annahmen ist dieses Verfahren jedoch in seiner Genauigkeit zwangsläufig begrenzt. Um diese Limitierung zu überwinden, wird ein weiterer Algorithmus hergeleitet. Dieser basiert auf der Lösung eines Feldsynthese-Problems, welches durch die Aufnahme von

einer Reihe von bistatischen Streudaten gelöst werden kann. Wiederum werden simulierte und gemessene Testdaten verwendet, um die beiden Ansätze zu überprüfen und zu vergleichen. Zwar benötigt das zuerst genannte Verfahren nur monostatisch gemessenen Streudaten, jedoch zeigt sich die begrenzte Genauigkeit im Fall von kompliziert geformten Streuobjekten. Für das Feldsynthese-Verfahren genügen vergleichsweise wenig Messpunkte, jeweils um alle Positionen der Sendeantenne herum aufgenommen, um den monostatischen RCS mit hoher und kontrollierbarer Genauigkeit zu bestimmen.

Abstract

As a measure for the scattering behavior of an object with respect to incident and scattered electromagnetic waves, the radar cross section (RCS) plays an important role for characterizing the detectability of an object by a radar sensor. Moreover, determining the RCS allows for computing a spatial image of the object, as the RCS corresponds to the spatial frequency spectrum of a distribution of scattering centers or equivalent sources. However, when measuring the RCS or acquiring a radar image, the problem is to determine a quantity that is defined with respect to incident and scattered *plane* waves. Only if the separation between the transmitting and receiving antennas and the object under test is sufficiently large, the assumption of plane waves is valid and it becomes possible to directly determine the RCS without introducing a systematic error. Commonly, outdoor test ranges or compact indoor ranges, where large parabolic reflectors synthesize the field of a plane wave, are employed. While the latter offer a controlled measurement environment, such facilities are also costly to build and consequently there is an ongoing interest in acquiring scattering measurement data in close distance to the object (in the near-field region) and perform numerical computations to determine the far-field RCS.

In this thesis, highly efficient algorithms are presented to determine the RCS from near-field measurements. The algorithms are based on a propagating plane-wave expansion of the electric field, which allows the integration into a hierarchical multi-level scheme and, thus, ensures the ability to efficiently handle even electrically large problems. In contrast to most existing methods, the measurement samples can be acquired on completely irregular scan surfaces around the object under test without compromising computational efficiency. In this way, a variety of new possibilities emerge for realizing RCS measurement and radar imaging systems.

Starting from the closely related antenna measurement case, a propagating plane-wave based near-field transmission equation for determining the antenna gain is derived and an algorithm for solving the resulting linear system of equation is discussed. Simulated and measured test data is employed to validate the accuracy and performance of the formulation. It is then shown how this algorithm can also be used for monostatic scattering problems under some simplifying assumptions. To this end, a near-field radar transmission equation is derived and the relation of the RCS to a spatial scattering center distribution is discussed, including the efficient computation of the corresponding radar image. In order to overcome the accuracy limitations of the monostatic approach, which are imposed by the underlying linearizing assumptions, a second algorithm is derived. This approach is based on solving a field synthesis problem by acquiring multiple sets of bistatic scattering data. Again using simulated and measured test data, the two algorithms are validated and compared. While the first approach requires only monostatic scattering data, its accuracy limitations become apparent in the case of objects with complicated shape. With the second approach, relatively few measurement samples around each position of the transmitting antenna are sufficient to determine the monostatic RCS with high and controllable accuracy.

Contents

Abbreviations

1D	one-dimensional
2D	two-dimensional
3D	three-dimensional
AUT	antenna under test
CCR	compensated compact range
CS	compressive sensing
CW	continuous wave
DFT	discrete Fourier transform
DUT	device under test
FEKO	Feldberechnung für Körper mit beliebiger Oberfläche (engl. “field calculations involving bodies of arbitrary shape”, computational electromagnetics software)
FF	far field
FFT	fast Fourier transform
FFTW	fastest Fourier transform in the west
FIAFTA	fast irregular antenna field transformation algorithm
FMM	fast multipole method
GMRES	generalized minimal residual
IFFT	inverse fast Fourier transform
ISAR	inverse synthetic aperture radar
MLFMM	multi-level fast multipole method
MoM	method of moments
NE	normal error
NF	near field
NFFFT	near-field to far-field transformation
NR	normal residual
NSI	Nearfield Systems Inc. (now NSI-MI Technologies))
OEWG	open ended waveguide
PAMS	portable antenna measurement system
PEC	perfectly electrically conducting
PSF	point spread function
PWS	plane-wave spectrum

RCS	radar cross section
RF	radio frequency
RWG	Rao-Wilton-Glisson (low order basis functions on triangles)
Rx	receiving
SAR	synthetic aperture radar
SNR	signal-to-noise ratio
SVD	singular value decomposition
SWE	spherical-wave expansion
TEM	transverse electromagnetic
TUM	Technical University of Munich
Tx	transmitting
UAV	unmanned aerial vehicle

Notation

Symbol	Description	Unit
$*$	convolution	
$\mathcal{F}$	Fourier transform	
$\mathcal{F}^{-1}$	inverse Fourier transform	
$\lceil \cdot \rceil$	ceil value to next integer	
$\lfloor \cdot \rfloor$	floor value to next integer	
$\bar{\mathbf{x}}$	dyadic variable	
$[\cdot]^{\mathrm{H}}$	conjugate transpose (hermitian) of a matrix or vector	
$\|\cdot\|_2$	ℓ^2-norm of a matrix or vector	
$\nabla\cdot$	divergence of a vector field	
$\nabla\times$	curl of a vector field	
$\hat{x}$	unit vector in the direction of $\boldsymbol{x}$	
β	bistatic angle	
$\boldsymbol{\beta}(\boldsymbol{r})$	RWG basis function	
$\varepsilon(\boldsymbol{r})$	permittivity	As/(Vm)
ε_0	permittivity of vacuum	As/(Vm)
$\varepsilon_r(\boldsymbol{r})$	relative permittivity	
λ	wavelength	m
λ_0	free-space wavelength	m
$\kappa(\boldsymbol{r})$	conductivity	A/(Vm)
$\mu(\boldsymbol{r})$	permeability	Vs/(Am)
μ_0	permeability of vacuum	Vs/(Am)
$\mu_r(\boldsymbol{r})$	relative permeability	
$\rho_e(\boldsymbol{r})$	electric charge density	$\mathrm{As/m^3}$
$\rho_m(\boldsymbol{r})$	magnetic charge density	$\mathrm{Vs/m^3}$
σ	radar cross section	$\mathrm{m^2}$
ω	angular frequency	1/s
$\boldsymbol{B}(\boldsymbol{r})$	magnetic flux density	$\mathrm{Vs/m^2}$
$\boldsymbol{D}(\boldsymbol{r})$	electric flux density	$\mathrm{As/m^2}$
$\boldsymbol{E}(\boldsymbol{r})$	electric field	V/m
$\boldsymbol{F}_{smn}(\boldsymbol{r})$	spherical wave function for outgoing fields	

Symbol	Description	Unit
$G(\boldsymbol{r},\boldsymbol{r'})$	free-space scalar Green's function	$1/\mathrm{m}$
$\overline{\mathbf{G}}_J^E(\boldsymbol{r},\boldsymbol{r'})$	free-space dyadic Green's function for the electric field due to electric currents	$\mathrm{V}/(\mathrm{Am}^2)$
$\overline{\mathbf{G}}_M^E(\boldsymbol{r},\boldsymbol{r'})$	free-space dyadic Green's function for the electric field due to magnetic currents	$1/\mathrm{m}^2$
$\boldsymbol{H}(\boldsymbol{r})$	magnetic field	A/m
$\boldsymbol{J}(\boldsymbol{r})$	electric current density	A/m^2
$\boldsymbol{J}_A(\boldsymbol{r})$	electric surface current density	A/m
$\tilde{\boldsymbol{J}}(\boldsymbol{k})$	plane-wave spectrum of electric current density	V
$\boldsymbol{K}_{smn}(\vartheta,\varphi)$	spherical wave function of outgoing fields under far-field conditions	
$\boldsymbol{M}(\boldsymbol{r})$	magnetic current density	V/m^2
$\boldsymbol{M}_A(\boldsymbol{r})$	magnetic surface current density	V/m
$\tilde{\boldsymbol{M}}(\boldsymbol{k})$	plane-wave spectrum of magnetic current density	V
$\mathrm{P}_l(x)$	Legendre polynomial of degree l	
$\mathrm{P}_l^m(x)$	associated Legendre polynomial of degree l and order m	
$\bar{\mathrm{P}}_l^m(x)$	normalized associated Legendre polynomial of degree l and order m	
$\tilde{\boldsymbol{Q}}(\boldsymbol{k})$	scattered plane-wave spectrum	V
$\bar{\mathbf{S}}(\boldsymbol{k})$	scattering matrix	
$T_L(x)$	FMM translation operator of order L	$1/\mathrm{m}$
$\tilde{\boldsymbol{V}}(\boldsymbol{k})$	plane-wave spectrum	V
$\boldsymbol{W}(\boldsymbol{k})$	gain normalized probe pattern	
Z_F	wave impedance	V/A
c_0	speed of light in vacuum	m/s
$\mathrm{h}_l^{(2)}(x)$	spherical Hankel function of the second kind of order l	
j	imaginary unit $\sqrt{-1}$	
$\mathrm{j}_l(x)$	spherical Bessel function of the first kind of order l	
k	wave number	$1/\mathrm{m}$
$\boldsymbol{k}$	wave vector	$1/\mathrm{m}$
$\hat{k}$	unit vector in direction of $\boldsymbol{k}$	
$\bar{\mathbf{s}}(\boldsymbol{r})$	spatial scattering center distribution	$1/\mathrm{m}^2$

1 Introduction

The radar cross section (RCS) of an object is a measure of its scattering behavior with respect to incident and scattered electromagnetic plane waves. Its value corresponds to the size of a fictitious area that scatters the power of the incident electromagnetic field isotropically in all directions. Historically, its significance resulted from the question if an object, such as a ship or an aircraft, is detectable by a radar sensor, dependent on the direction of illumination and reception [Ruck et al. 1970, p. 7]. While in the early days of radar, the main purpose of radar systems was to detect and localize an object, the increased sensitivity of these systems later allowed to additionally distinguish different objects based on their specific RCS profile [Jenn 2005]. In recent years, the question arose if it is equally possible to detect unmanned aerial vehicles (UAVs), as their popularity and wide spread is considered an increasing security risk, in particular for the air traffic [Guay et al. 2017; Pieraccini et al. 2017]. Beside these classical applications, more fields of use emerged from the wide availability and low costs of radar sensors. In the context of assisted and autonomous driving, accurate RCS characterization is considered an important factor to ensure the proper functionality of automotive radar sensor systems [Marchetti et al. 2019] as well as for the modeling of propagation channels in car-to-car communications [Myint et al. 2019]. Both applications are expected to contribute significantly to the reliable and safe operation of future autonomous vehicles.

The RCS, as will be shown in this thesis, corresponds to the spatial frequency spectrum (also known as the angular spectrum) of a localized distribution of scattering centers. Thus, by an inverse Fourier transform it is possible to obtain an equivalent image of an object under test from knowledge of the RCS over a sufficiently large angular range. In the context of RCS measurements, this imaging principle has been used originally to identify those parts of a scattering object that contribute most to the power scattered into a certain direction [Mensa 1990]. However, a variety of different applications for radar imaging were developed over the past decades. Probably the most prominent ones are remote sensing of the earth [Mott 2007], observation of space targets [Mehrholz et al. 2002], ground penetrating radar for subsurface imaging [Peters et al. 1994] and body scanners for security applications [Ahmed et al. 2012]. Moreover, there is an ongoing interest in using microwave frequencies for medical imaging purposes, potentially offering a non-ionizing and low-cost alternative to conventional X-ray-based tomography [Chandra et al. 2015].

In both RCS measurements and radar imaging one faces the problem of determining a quantity that is defined with respect to incident and scattered plane waves. It is only for a sufficiently large separation between the antennas of the radar sensor and the object under test that the assumption of locally plane waves can be made without introducing a systematic error to the result [Ruck et al. 1970, p. 910]. In this case, when the antennas are said to be in the far field (FF) of the object (and vice versa) the RCS can be measured directly by evaluating the well known radar range equation [Fink 1945]. As the required separation grows with the size of the object under test as well as with the employed frequency of the electromagnetic field, large (typically outdoor) test ranges are needed for such direct measurements [IEEE 2007, p. 5].

Alternatively, compact (indoor) range facilities are commonly employed to synthesize the field of a plane wave in a shorter distance to the test object by the help of large parabolic reflectors or dielectric lenses [Knott 2006, p. 299]. As such facilities are very costly to build, other methods that allow the acquisition of measurement samples closer to the object, in the near field (NF), and inside a controlled environment are a topic of ongoing research. These methods usually employ a numerical correction/computation technique to determine the RCS from the acquired measurement data in a post-processing step. Similarly, for some electromagnetic imaging applications, such as the aforementioned body scanners or medical imaging scenarios, the measurement setup will never allow the assumption of incident and scattered plane waves due to the short distance between the radar sensor and the object under test. Thus, also in these cases some NF method is needed to compute an undistorted image.

The development and implementation of efficient algorithms for determining the far-field RCS from NF measurement data is the main task that is covered by this thesis. Having determined the RCS, a spatial image of the scattering center distribution can be computed as well. Two different strategies to obtain a three-dimensional (3D) image of an object under test have been implemented and will be evaluated. At this point it may already be noted that the problem of RCS measurements bears resemblance with the one of determining the FF radiation pattern of an antenna [Parini et al. 2014]. As will be shown in this thesis, under some simplifying assumptions also the problem of determining the RCS of an object under test can be understood as an inverse source problem [P. C. Hansen 2010], similar to the antenna measurement case. Consequently, algorithms that were originally developed for transforming the measured NF data of antennas into the FF, a process which is commonly called near-field to far-field transformation (NFFFT), can be modified for the purpose of RCS measurements. In both cases one of the main challenges is to implement an efficient and versatile solution method. This is crucial, as the number of unknown solution coefficients and measurement samples can easily be on the order of several millions or more. The algorithms presented in this thesis are based on a propagating plane-wave expansion of the electric field, which allows the integration into a hierarchical multi-level fast multipole method (MLFMM) scheme [Chew et al. 2001]. Consequently, and in contrast to most other existing methods, also large problems with almost arbitrarily distributed measurement samples can be handled efficiently. In this way, a variety of new possibilities emerge for realizing RCS measurement and radar imaging systems as will be discussed in the final outlook section of this thesis.

A brief overview on the development of existing methods for NF antenna and RCS measurements as well as for electromagnetic imaging is given in the next section. In all cases it is assumed that the measurements are performed in a non-reflective environment. Usually, this is sufficiently well fulfilled in an absorber lined anechoic chamber as long as the measurement frequencies are not too low and the chamber is of reasonable size [IEEE 2012].

1.1 Overview of Existing Algorithms

As will be shown in this thesis, the problem of determining the FF radiation pattern of an antenna as well as the one of determining the RCS can be cast into a form where one is interested in determining some (equivalent) sources from observations of the fields they create. Consequently, they both belong to the field of inverse source problems [Devaney 2012]. In the

scattering (RCS) case, the equivalent sources will generally be excitation dependent but it is equally possible to define the problem in terms of, for example, a scattering potential that only depends on the material properties of the object under test. If one seeks to determine these material properties in the spatial domain from measurements of the scattered field, one faces an inverse scattering problem [Colton and Kress 2013].

1.1.1 Near-Field Antenna Measurements

While the theory of inverse problems is nowadays well established, many algorithms for NF antenna measurements still rely on the classical modal expansion techniques that avoid the computationally more demanding explicit evaluation of the involved integral representations [Yaghjian 1986]. They employ the orthogonality of the used basis functions over their corresponding measurement surface, that is planes, cylinders or spheres, in order to efficiently evaluate the resulting equations by means of fast Fourier transforms (FFTs). An obvious drawback is the limitation to the aforementioned canonical scan surfaces, which prevents the use of, e.g., crane-based solutions as presented by Geise et al. [2019] where the path described by the measurement probe is almost inevitably irregular. Moreover, the modal expansion approaches lose much of their efficiency when higher order probes (that potentially offer a larger frequency bandwidth) have to be taken into account [T. B. Hansen 2011].

One of the first examples employing equivalent surface currents for an NFFFT was given by Petre and Sarkar [1992], though both the reconstruction surface (on which the equivalent currents reside) as well as the scan surface were still limited to planes. It is only in more recent years that the possibility of reconstructing surface currents on arbitrarily shaped surfaces gained more attention [Alvarez et al. 2007] and that it was successfully employed for NF measurements and antenna diagnostics [Eibert and Schmidt 2009]. The algorithm in the latter examples already uses propagating plane-wave based expansions of the radiated fields and a hierarchical MLFMM scheme as introduced to the field of NFFFTs by Schmidt and Eibert [2009].

1.1.2 Microwave Imaging Algorithms

Determining an equivalent surface current distribution can already be thought of being a kind of electromagnetic imaging algorithm, allowing, e.g., the detection of defective array elements. However, a suitable shape for the reconstruction has to be known (or assumed) a priori, which is obviously undesired in most imaging scenarios where the primary task is to determine the shape of an object in the first place. In general, electromagnetic imaging algorithms can be said to belong to the broad class of inverse scattering problems. If the goal is to determine the material parameters of an object under test, one usually faces the challenge to solve a non-linear problem that typically has to be solved iteratively by some optimization strategy [Colton and Kress 2013, p. 249]. In most cases, it is also assumed that far-field observations of the scattered field are available in order to establish a simpler integral relation between the incident and scattered fields. If this is not the case, one may try a two step procedure by first solving an “exterior” NFFFT as, for example, described by Kılıç and Eibert [2015]. However, the enormous computational costs for solving the non-linear problem still limit many inverse scattering algorithms to the solution of rather small objects. Alternatively, one may

solve a linearized problem by employing, e.g., the linear sampling method (LSM), which only determines the shape of an object by solving for inhomogeneities in the background medium [Cakoni et al. 2011]. A considerable simplification that leads to a linear problem results from a weak scattering assumption, most prominently the Born approximation [Devaney 2012, p. 256]. Almost all classical radar imaging techniques rely (at least implicitly) on this assumption together with the concept of synthetic aperture radar (SAR) imaging [Mensa 1990]. SAR is based on moving the transmitting and receiving antenna around (or in front of) the object in order to create a virtual antenna array. Of course the same effect can be obtained by rotating the object, in which case a spherical scan surface is realized. This procedure is then called inverse synthetic aperture radar (ISAR) [Özdemir 2012]. Under far-field conditions an ISAR image can be simply obtained by inverting the Fourier integral that relates the scattered field (the RCS) with the spatial scattering center distribution (the image). This process is also known as "backpropagation" or "backprojection" and was shown to be essentially identical to tomographic projection algorithms used in medical X-ray computed tomography (CT) imaging [Munson et al. 1983]. Taking into account that at microwave frequencies diffraction effects can generally not be neglected, the theory of diffraction tomography was established [Devaney 2012, p. 360]. A straight-forward way to accelerate the inverse Fourier transform in order to obtain the image is to perform an interpolation from the spherical far-field data grid to a Cartesian one (known as polar reformatting), followed by an FFT. More sophisticated algorithms perform a deconvolution [Desai and Jenkins 1992], multilevel domain decomposition [Boag 2001] or a hierarchical disaggregation in the spatial frequency domain [Schnattinger et al. 2011].

The problem, however, of all mentioned approaches is that they assume incident and scattered plane waves (they work on the angular spectrum of plane waves). Obviously, in any NF scenario this assumption will not be fulfilled and the direct application of FF algorithms will lead to distorted images. Assuming sets of independent scattering centers NF imaging algorithms exist that employ focusing operators, where in the case of spherical measurement setups fast cyclic convolutions can be used to accelerate the evaluation of the involved integrals [Broquetas et al. 1998]. Alternatively, for monostatic setups, where transmitter and receiver coincide, one may assume the scattering centers itself to be the source of radiation [Cafforio et al. 1991]. This "radiating reflectors" originates from the field of geophysics where it was used for acoustic imaging [Claerbout 1985]. ISAR NF imaging algorithms based on the radiating reflectors model and using modal expansions on canonical scan surfaces were investigated by Fortuny-Guasch and Lopez-Sanchez [2001]. An inverse source interpretation already employing propagating plane-wave spectra was given by Schnattinger [2014].

1.1.3 Near-Field Radar Cross Section Measurements

As noted by, for example, Vaupel and Eibert [2006], the spatial scattering center representation of an object can also be used to compute the RCS from monostatic NF measurements. Although the underlying linearizing assumptions are usually not fulfilled, in many cases relatively accurate results can still be obtained with these "image-based" methods as demonstrated by, e.g., LaHaie [2003] and Schnattinger et al. [2014]. The latter method already employed an MLFMM scheme with plane-wave expansions, though it was never validated by actual scattering measurements. Other methods used low-pass filtering [Melin 1987], extrapolation [Falconer 1988] or an approximate deconvolution [Cown and Ryan 1989], where the latter example already described

the reconstruction of all polarimetric components of the scattering matrix. Nonetheless, it is well known that without the linearizing assumptions and for a correct determination of the full bistatic scattering matrix also a full set of bistatic NF measurements is required [Dinallo 1984]. Obviously, this is unfeasible to realize in most practical cases. Methods using a limited set of bistatic measurement samples have been reported, however, again limited to planar [Farr et al. 1989] or cylindrical [Bucci and Migliore 2006] scan surfaces in order to employ an FFT-based acceleration. Due to the large amount of measurement data that has to be processed, the efficiency and speed of any RCS transformation algorithm is considered to be of even more importance than in the antenna measurement case.

1.2 Scope and Outline of the Thesis

The main objective of this thesis is to derive and investigate efficient and versatile algorithms for the accurate determination of the (far-field) RCS from near-field measurements. As discussed in the previous section, the task of determining the radiation pattern in NF antenna measurements is closely related to this and will serve as a starting point for the derivations. Having determined the RCS also an NF radar image can be computed. The corresponding relations as well as the efficient computation are, thus, considered too. To this end the thesis is organized as follows. Chapter 2 presents the theoretical background for setting up the inverse source problems that are encountered later on in both, antenna and RCS measurements. Starting from some basic electromagnetics an integral representation of the electric field is derived. Here it is employed that equivalent currents defined over a closed surface enclosing the original sources can be used to represent the electric field of an antenna or a scattering object anywhere outside the source region. By means of the reciprocity theorem the interaction between the equivalent currents of a transmitting and a receiving antenna can be described. This forms the basis for the transmission equation in NF antenna measurements. Expanding the Green's functions in the integral representation of the electric fields in spectra of propagating plane waves leads to the representation that builds the core of the transformation algorithms. At the end of the chapter the ill-posedness of the inverse problem is discussed and a regularizing solution strategy is presented.

In Chapter 3 the theoretical foundations introduced before are combined to first derive a gain-normalized transmission equation for antenna NF measurements and then describe the implementation of an efficient algorithm do determine the FF radiation pattern as well as the gain of an antenna under test (AUT). This is in contrast to previously introduced formulations that did not establish a direct relation to the actually measurable network parameters (the transmission factor) and were, thus, only able to determine the radiation pattern. It is then shown how in the limiting far-field case, i.e., for a very large separation between the transmitting and receiving antennas, this new propagating plane-wave based transmission equation simplifies to the well known Friis equation, thus constituting a generalization of the latter. To set up a linear system of equations the necessary discretization of the plane-wave spectra is discussed as well as the choice of basis functions and different numerical integration strategies. These have to be chosen such that they can be integrated into a hierarchical MLFMM scheme that requires repeated two-dimensional (2D) interpolations of the plane-wave spectra. At the end of the chapter a set of test and application examples is given to demonstrate the accuracy and

versatility of the implementation. In particular the algorithm is able to handle the case of irregularly distributed measurement data on scan surfaces that do not completely enclose the AUT. In fact, a relatively small scan area around the boresight direction of the AUT is often sufficient to accurately determine the maximum antenna gain.

Chapter 4 starts with a brief review of the classical scattering matrix description of an object under test as it is typically encountered in FF radar applications. Employing an integral representation of the scattered electric field the concept of *scattered* plane-wave spectra is introduced. It is shown how under some linearizing assumptions the scattered plane-wave spectrum can be understood as the generalization of the scattering matrix, quite similar to the antenna case encountered before. Indeed, also in this case a transmission equation between the antenna creating the incident field and an antenna receiving the scattered field can be set up that simplifies to the classical radar range equation under FF conditions. This is achieved by, again, correctly taking into account the measured network parameters as well as the gain-normalized radiation patterns of the transmitting and receiving antenna.

The Fourier integral relation between the scattered plane-wave spectra and the spatial scattering center distribution (that is the spatial representation of the scatterer) establishes the basis for most radar imaging algorithms. Two algorithms for the efficient evaluation are presented in the following. By assuming these scattering centers to be the actual sources of the scattered field, it is possible to determine the RCS by measuring the scattered near field only in the direction of the transmitting antenna (monostatic measurements). This is done by solving again a linear inverse source problem with the hierarchical algorithm introduced before. In order to overcome the accuracy limitations of this linearized approach, a second algorithm is derived. It employs a limited set of bistatic scattering data (i.e., the scattered field is measured at multiple locations for each transmitter position) to solve for the RCS by means of a plane-wave field synthesis approach. It is shown how the angular range that is spanned by the bistatic configuration determines the accuracy of the field synthesis and, thus, also of the RCS result. This is in contrast to the previous method, where the actually achievable accuracy is more or less unpredictable. The different algorithms for determining the RCS and to compute a spatial image are evaluated in Chapter 5 by employing test data from both simulations and scattering measurements.

Finally, Chapter 6 concludes this work by summarizing the main results and by giving an outlook on possible future work.

2 Theoretical Background

In order to derive the transmission equations employed in later chapters for measuring antenna patterns or the RCS, some necessary electromagnetic principles will be given in the following. Starting from Maxwell's equations and the constitutive material relations, the curl-curl equations of the electric and magnetic field are derived to formally separate both quantities from each other. In the case of a homogeneous background medium, it may be shown that these equations can be solved in the form of integral representations by using the dyadic Green's functions of the background medium. In order to describe the radiation (or similarly the scattering) of a device under test (DUT) in this form, that is by radiating sources in free space, the equivalence principle can be invoked. It allows one to uniquely describe the radiation of the true (but usually unknown) physical currents by means of a set of equivalent sources in free space. This is shown by means of equivalent volume and surface current densities. Next the reciprocity theorem will be introduced as it forms the basis for describing the interaction between the transmitting and receiving antenna and is, thus, also the basis for the later derivation of the transmission equations.

Expanding the scalar Green's function into propagating plane waves forms the core of the efficient description of the electromagnetic interactions that are employed throughout this thesis. The basic relation of this expansion will be derived and some important properties will be investigated. Using the expansion to describe the radiated electric field of some current densities leads to the definition of the angular spectrum of propagating plane waves. It directly corresponds to the far-field radiation pattern of the sources and will play a central role throughout this thesis. An alternative representation of this plane-wave spectrum can be obtained in terms of spherical wave functions that are based on a spherical multipole expansion of the electric field. As a direct sampling of the plane-wave spectrum may (depending on the chosen sampling grid) carry a lot of redundant information, using the spherical multipole representation can be beneficial in order to reduce the number of unknowns in a numerical implementation and possibly improve the conditioning of the system matrix. The latter aspect is considered in the last part of this chapter, introducing the inverse source problem from a mathematical perspective and discussing some properties and basic solution strategies.

2.1 Maxwell's Equations

In the following a harmonic time dependency $\mathrm{e}^{\mathrm{j}\omega t}$ is assumed, where j is the imaginary unit, ω is the angular frequency and t the time. Maxwell's equations in their differential form may then be written as [Chew 1995, p. 5]

$$\nabla \times \boldsymbol{H}(\boldsymbol{r}) = \mathrm{j}\omega \boldsymbol{D}(\boldsymbol{r}) + \boldsymbol{J}(\boldsymbol{r}) \tag{2.1}$$

$$\nabla \times \boldsymbol{E}(\boldsymbol{r}) = -\mathrm{j}\omega \boldsymbol{B}(\boldsymbol{r}) - \boldsymbol{M}(\boldsymbol{r}) \tag{2.2}$$

$$\nabla \cdot \boldsymbol{D}(\boldsymbol{r}) = \rho_e(\boldsymbol{r}) \tag{2.3}$$

$$\nabla \cdot \boldsymbol{B}(\boldsymbol{r}) = \rho_m \tag{2.4}$$

where $\boldsymbol{E}(\boldsymbol{r})$, $\boldsymbol{H}(\boldsymbol{r})$, $\boldsymbol{D}(\boldsymbol{r})$, $\boldsymbol{B}(\boldsymbol{r})$ are the electric field, the magnetic field, the electric flux density and the magnetic flux density, respectively. $\boldsymbol{J}(\boldsymbol{r})$ and $\rho_e(\boldsymbol{r})$ are free electric current and charge densities. The fictitious magnetic current density $\boldsymbol{M}(\boldsymbol{r})$ and magnetic charge density $\rho_m(\boldsymbol{r})$ are introduced to obtain full symmetry in the four equations. The vector $\boldsymbol{r}$ denotes the position in $\mathbb{R}^3$.

The (electric and magnetic) currents and charges are generally not independent from each other as can be seen by, e.g., taking the divergence of (2.1) and using (2.3), which leads to the continuity equation for the electric charges

$$\nabla \cdot \boldsymbol{J}(\boldsymbol{r}) = -\mathrm{j}\omega\rho_e(\boldsymbol{r}). \tag{2.5}$$

Similarly, one obtains for the magnetic sources

$$\nabla \cdot \boldsymbol{M}(\boldsymbol{r}) = -\mathrm{j}\omega\rho_m(\boldsymbol{r}). \tag{2.6}$$

2.1.1 Constitutive Relations

The constitutive relations relate the electric and magnetic flux densities $\boldsymbol{D}(\boldsymbol{r})$ and $\boldsymbol{B}(\boldsymbol{r})$ to the electric and magnetic fields $\boldsymbol{E}(\boldsymbol{r})$ and $\boldsymbol{H}(\boldsymbol{r})$ via the material properties of the surrounding media. In general, the relations

$$\boldsymbol{D} = \boldsymbol{D}(\boldsymbol{E}, \boldsymbol{H}) \tag{2.7}$$
$$\boldsymbol{B} = \boldsymbol{B}(\boldsymbol{E}, \boldsymbol{H}) \tag{2.8}$$

may be non-linear, inhomogeneous, bianisotropic and frequency dependent [Kong 1986, p. 3–8]. However, for the following derivations it will be sufficient to assume isotropic, linear media. In this case, the constitutive relations can be written as

$$\boldsymbol{D}(\boldsymbol{r}) = \varepsilon(\boldsymbol{r})\boldsymbol{E}(\boldsymbol{r}) = \varepsilon_0\varepsilon_r(\boldsymbol{r})\boldsymbol{E}(\boldsymbol{r}) \tag{2.9}$$
$$\boldsymbol{B}(\boldsymbol{r}) = \mu(\boldsymbol{r})\boldsymbol{H}(\boldsymbol{r}) = \mu_0\mu_r(\boldsymbol{r})\boldsymbol{H}(\boldsymbol{r}) \tag{2.10}$$

where $\varepsilon(\boldsymbol{r})$ and $\mu(\boldsymbol{r})$ are the permittivity and permeability of the corresponding medium, respectively, which can also be expressed in terms of the free-space (vacuum) quantities ε_0 or μ_0 and the relative permittivity $\varepsilon_r(\boldsymbol{r})$ or relative permeability $\mu_r(\boldsymbol{r})$.

2.1.2 Cur-Curl Equation of the Electric Field

The electric and magnetic field are coupled by the first two of Maxwell's equations. Thus, it is generally sufficient to solve for one of the two fields to determine both. To obtain expressions where the electric and magnetic field are formally separated, the curl operator is applied on (2.2) after using (2.10). With (2.9) and (2.1) one obtains

$$\nabla \times \frac{1}{\mu(\boldsymbol{r})}\nabla \times \boldsymbol{E}(\boldsymbol{r}) - k_0^2\varepsilon(\boldsymbol{r})\boldsymbol{E}(\boldsymbol{r}) = -\mathrm{j}\omega\boldsymbol{J}(\boldsymbol{r}) - \nabla \times \left(\frac{1}{\mu(\boldsymbol{r})}\boldsymbol{M}(\boldsymbol{r})\right) \tag{2.11}$$

where $k_0 = \omega\sqrt{\mu_0\varepsilon_0} = 2\pi/\lambda_0$ is the free-space wave number and λ_0 denotes the free-space wavelength. Similarly, for the magnetic field it holds that

$$\nabla \times \frac{1}{\varepsilon(\boldsymbol{r})}\nabla \times \boldsymbol{H}(\boldsymbol{r}) - k_0^2\mu(\boldsymbol{r})\boldsymbol{H}(\boldsymbol{r}) = -\mathrm{j}\omega\boldsymbol{M}(\boldsymbol{r}) + \nabla \times \frac{1}{\varepsilon(\boldsymbol{r})}\boldsymbol{J}(\boldsymbol{r}). \tag{2.12}$$

Obviously, the relations simplify considerably if the medium is unbounded and homogeneous, i.e., ε and μ are no longer functions of $\boldsymbol{r}$. In that case (2.11) becomes, after multiplying with μ,

$$\nabla \times \nabla \times \boldsymbol{E}(\boldsymbol{r}) - k^2\boldsymbol{E}(\boldsymbol{r}) = -\mathrm{j}\omega\mu\boldsymbol{J}(\boldsymbol{r}) - \nabla \times \boldsymbol{M}(\boldsymbol{r}), \tag{2.13}$$

which is commonly referred to as the inhomogeneous curl-curl equation of the electric field [Tai 1994, p. 48]. Here $k = \omega\sqrt{\mu\varepsilon}$ is the wave number of the homogeneous background medium. As will be shown, the solution to this differential equation can be obtained by employing the corresponding dyadic Green's function.

In a source-free medium with $\boldsymbol{J} = \boldsymbol{M} = 0$, (2.13) reduces to the homogeneous differential equation

$$\nabla \times \nabla \times \boldsymbol{E}(\boldsymbol{r}) - k^2\boldsymbol{E}(\boldsymbol{r}) = 0. \tag{2.14}$$

A simple solution to this equation is the field of a plane wave traveling in the direction of $\pm\boldsymbol{k}$, that is

$$\boldsymbol{E}(\boldsymbol{r}) = \boldsymbol{E}_0 \mathrm{e}^{\pm\mathrm{j}\boldsymbol{k}\cdot\boldsymbol{r}} \tag{2.15}$$

where $\boldsymbol{k} = k_x\hat{x} + k_y\hat{y} + k_z\hat{z}$ and $\boldsymbol{E}_0$ denotes the magnitude and polarization of the wave.

2.1.3 Free-Space Solution in Terms of the Dyadic Green's Function

To solve (2.13) in the presence of $\boldsymbol{J}$ and $\boldsymbol{M}$ one may introduce the electric and magnetic dyadic Green's functions of free space[1] $\overline{\mathbf{G}}_e(\boldsymbol{r},\boldsymbol{r}')$ and $\overline{\mathbf{G}}_m(\boldsymbol{r},\boldsymbol{r}')$, respectively. They are defined to be the functions that satisfy

$$\nabla \times \nabla \times \overline{\mathbf{G}}_e(\boldsymbol{r},\boldsymbol{r}') - k^2\overline{\mathbf{G}}_e(\boldsymbol{r},\boldsymbol{r}') = \bar{\mathbf{I}}\,\delta(\boldsymbol{r}-\boldsymbol{r}') \tag{2.16}$$

and

$$\nabla \times \nabla \times \overline{\mathbf{G}}_m(\boldsymbol{r},\boldsymbol{r}') - k^2\overline{\mathbf{G}}_m(\boldsymbol{r},\boldsymbol{r}') = \nabla \times \bar{\mathbf{I}}\,\delta(\boldsymbol{r}-\boldsymbol{r}') \tag{2.17}$$

where $\bar{\mathbf{I}}$ is the unit dyad and $\delta(\boldsymbol{r})$ the Dirac delta function [Tai 1994, p. 59]. The Green's functions can be found by, e.g., employing the method of potentials [Jin 2015, p. 61–67], which results in

$$\overline{\mathbf{G}}_e(\boldsymbol{r},\boldsymbol{r}') = \left(\bar{\mathbf{I}} + \frac{1}{k^2}\nabla\nabla\right) G(\boldsymbol{r},\boldsymbol{r}') \tag{2.18}$$

$$\overline{\mathbf{G}}_m(\boldsymbol{r},\boldsymbol{r}') = -\nabla \times G(\boldsymbol{r},\boldsymbol{r}'), \tag{2.19}$$

[1] In most cases, the isotropic, homogeneous medium will simply be air (or vacuum) and it is common to refer to it as free space. Nonetheless, all solutions given here are equally valid for any isotropic, homogeneous medium.

where

$$G(\boldsymbol{r},\boldsymbol{r}') = \frac{\mathrm{e}^{-\mathrm{j}k|\boldsymbol{r}-\boldsymbol{r}'|}}{4\pi\,|\boldsymbol{r}-\boldsymbol{r}'|} \tag{2.20}$$

is the free-space scalar Green's function that fulfills the Sommerfeld radiation condition of outward propagating waves with vanishing magnitude at infinity [Chew 1995, p. 35].

The electric field in (2.13) due to the current densities $\boldsymbol{J}(\boldsymbol{r})$ and $\boldsymbol{M}(\boldsymbol{r})$ can now be found by solving

$$\boldsymbol{E}(\boldsymbol{r}) = \iiint\limits_V \left[\overline{\mathbf{G}}_J^E(\boldsymbol{r},\boldsymbol{r}')\cdot\boldsymbol{J}(\boldsymbol{r}') + \overline{\mathbf{G}}_M^E(\boldsymbol{r},\boldsymbol{r}')\cdot\boldsymbol{M}(\boldsymbol{r}')\right]\,\mathrm{d}v' \tag{2.21}$$

where the integration volume V includes all source contributions. The free-space dyadic Green's functions to determine the electric field due to electric and magnetic current densities are

$$\overline{\mathbf{G}}_J^E(\boldsymbol{r},\boldsymbol{r}') = -\mathrm{j}kZ_\mathrm{F}\,\overline{\mathbf{G}}_e(\boldsymbol{r},\boldsymbol{r}') = -\mathrm{j}kZ_\mathrm{F}\left(\bar{\mathbf{I}} + \frac{1}{k^2}\nabla\nabla\right)G(\boldsymbol{r},\boldsymbol{r}') \tag{2.22}$$

and

$$\overline{\mathbf{G}}_M^E(\boldsymbol{r},\boldsymbol{r}') = \overline{\mathbf{G}}_m(\boldsymbol{r},\boldsymbol{r}') = -\nabla\times\bar{\mathbf{I}}\,G(\boldsymbol{r},\boldsymbol{r}'), \tag{2.23}$$

respectively, with $Z_\mathrm{F} = \sqrt{\mu/\varepsilon}$ being the free-space wave impedance.

2.1.4 Far-field Approximation

For observation points $\boldsymbol{r}$ sufficiently far away from the source, it can be observed that the normalized radiated electric and magnetic fields (the radiation characteristic) are essentially no longer dependent on the actual distance $|\boldsymbol{r}-\boldsymbol{r}'|$ between source and observation point. The observation point is then said to be located in the far-field region of the source [Balanis 2012, p. 283]. Observation points closer to the sources are in the near field (NF). In the far-field case, the scalar Green's function is usually approximated by

$$G_\mathrm{FF} \approx G(\boldsymbol{r},\boldsymbol{r}') = \frac{1}{4\pi r}\mathrm{e}^{-\mathrm{j}k\frac{\boldsymbol{r}\cdot\boldsymbol{r}'}{r}} \tag{2.24}$$

where $r = |\boldsymbol{r}|$ and when computing the electric and magnetic field, terms decaying faster than r^{-1} are neglected. This results in a spherical transverse electromagnetic (TEM) wave propagating radially away from the sources and the dyadic Green's functions for electric and magnetic current densities are written as

$$\overline{\mathbf{G}}_{J,\mathrm{FF}}^E(\boldsymbol{r},\boldsymbol{r}') \approx -\mathrm{j}kZ_\mathrm{F}\left(\bar{\mathbf{I}} - \hat{k}\hat{k}\right)G_\mathrm{FF}(\boldsymbol{r},\boldsymbol{r}') \tag{2.25}$$

and

$$\overline{\mathbf{G}}_{M,\mathrm{FF}}^E(\boldsymbol{r},\boldsymbol{r}') \approx -\boldsymbol{k}\times\bar{\mathbf{I}}G_\mathrm{FF}(\boldsymbol{r},\boldsymbol{r}'), \tag{2.26}$$

respectively. Computing the electric field thus reduces to

$$\boldsymbol{E}_\mathrm{FF}(\boldsymbol{r}) = -\mathrm{j}\frac{kZ_\mathrm{F}}{4\pi r}\left(\bar{\mathbf{I}} - \hat{k}\hat{k}\right)\cdot\iiint\limits_V \boldsymbol{J}(\boldsymbol{r}')\,\mathrm{e}^{-\mathrm{j}k\frac{\boldsymbol{r}\cdot\boldsymbol{r}'}{r}}\,\mathrm{d}v' + \mathrm{j}\frac{\boldsymbol{k}}{4\pi r}\times\iiint\limits_V \boldsymbol{M}(\boldsymbol{r}')\,\mathrm{e}^{-\mathrm{j}k\frac{\boldsymbol{r}\cdot\boldsymbol{r}'}{r}}\,\mathrm{d}v', \tag{2.27}$$

which is obviously much easier to evaluate than the general form in (2.21). With respect to the observation distance from a radiator with reasonable size (i.e., large compared to the wavelength), an often stated criterion for applying the far-field approximation is $r \geq 2D^2/\lambda$ (called the Fraunhofer distance), where D is the maximum extent of the radiator in any dimension. This corresponds to a maximum error in the phase term of 22.5° [Parini et al. 2014].

2.2 Equivalence Principles

As was shown in the previous section, in the case of sources radiating into an unbounded homogeneous region ("free space") a solution to Maxwell's equations may be found in terms of a spatial convolution of the electric and magnetic current densities with the corresponding dyadic Green's function of free space. This leads to the integral representation (2.21). In any realistic scenario, there are no current sources radiating into free space but sources in the presence of some kind of mechanical structure (e.g., the antenna) or a scattering object. In order to describe the radiation in the form of (2.21) one usually invokes some kind of equivalence principle. Most commonly, this is the surface equivalence principle, which is a consequence of the uniqueness theorem and allows the description of the field inside a source free region by the equivalent current sources on the boundary surface of that region [Jin 2015, p. 107]. In the context of scattering problems also the volume equivalence principle is widely used [Volakis and Sertel 2012, p. 15]. Both principles will be briefly introduced in the following.

2.2.1 Surface Equivalence Principle

The surface equivalence principle goes back to Huygens 1690, Love 1901 and Schelkunoff 1936. In the form commonly adopted for electromagnetic problems, it provides a mathematical description of Huygens' principle, that is the fields inside a source free region are uniquely determined by the tangential fields along an enclosing boundary [Balanis 2012, p. 328]. This is illustrated in Figure 2.1, where some electromagnetic sources, represented here by the electric and magnetic current densities $\boldsymbol{J}$ and $\boldsymbol{M}$, radiate in the presence of an arbitrary medium with material properties μ and ε. All sources and material inhomogeneities can be enclosed by a virtual surface A (the Huygens surface) that must be sufficiently smooth and has the unit normal $\hat{n}$. The outside region can be thought of being closed by a spherical boundary A_∞, whose radius tends to infinity and which consequently does not contribute to the overall radiation [Harrington 2001, p. 102]. By introducing equivalent electric and magnetic surface current densities

$$\boldsymbol{J}_A = \hat{n} \times (\boldsymbol{H} - \boldsymbol{H}') \qquad \text{and} \qquad \boldsymbol{M}_A = -\hat{n} \times (\boldsymbol{E} - \boldsymbol{E}'), \tag{2.28}$$

respectively, on the surface A, the sources inside A (as well as the material) may be removed without changing the radiated field outside of A [Quijano and Vecchi 2010]. As shown in Figure 2.1 b), the equivalent currents now radiate in an unbounded homogeneous region, consequently the electric field can be computed in terms of the free-space dyadic Green's

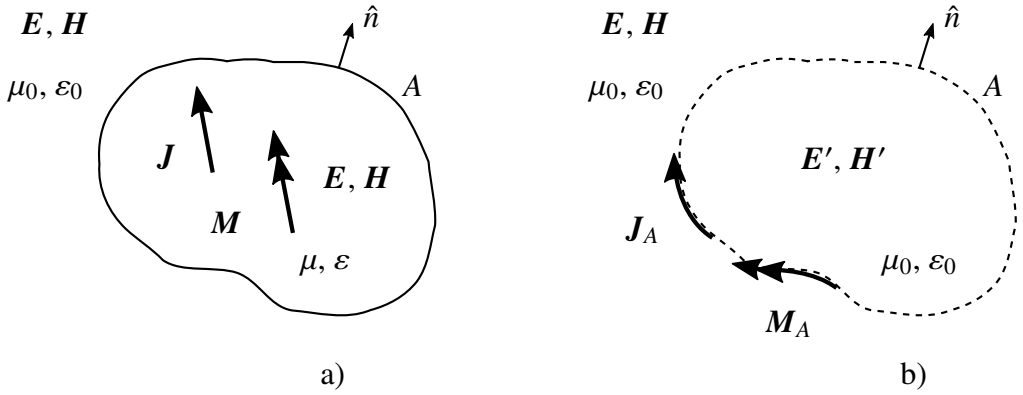

Figure 2.1: Illustration of the surface equivalence principle: a) Original problem, b) Equivalent problem with surface current densities radiating into free space.

function as introduced before, that is

$$\boldsymbol{E}(\boldsymbol{r}) = \oiint_A \left[\overline{\mathbf{G}}_J^E(\boldsymbol{r},\boldsymbol{r}') \cdot \boldsymbol{J}_A(\boldsymbol{r}') + \overline{\mathbf{G}}_M^E(\boldsymbol{r},\boldsymbol{r}') \cdot \boldsymbol{M}_A(\boldsymbol{r}') \right] \mathrm{d}a'. \tag{2.29}$$

The fields $\boldsymbol{E}'$ and $\boldsymbol{H}'$ inside A are somewhat arbitrary, except that they have to fulfill the given boundary conditions for the equivalent currents radiating into free space and that, of course, they are a valid solution to Maxwell's equations. In general, $\boldsymbol{E}'$ and $\boldsymbol{H}'$ are not known and, thus, also $\boldsymbol{J}_A$ and $\boldsymbol{M}_A$ will be unknown. Enforcing a zero interior field $\boldsymbol{E}' = \boldsymbol{H}' = 0$, which is known as the Love's equivalence principle [Volakis and Sertel 2012, p. 18], establishes a direct relation between the equivalent currents and the tangential fields outside of A. In this case, knowledge of the tangential fields of $\boldsymbol{E}$ and $\boldsymbol{H}$ on A is sufficient to describe $\boldsymbol{J}_A$ and $\boldsymbol{M}_A$ as can be seen from (2.28). The general case with non-zero $\boldsymbol{E}'$ and $\boldsymbol{H}'$ inside A is particularly interesting for the inverse problem, that is determining the equivalent surface current densities from the measurement of $\boldsymbol{E}$ outside of A. The corresponding integral equation (2.29) can then be solved for $\boldsymbol{J}_A$ and $\boldsymbol{M}_A$ without enforcing a specific interior field. It must be noted that, except for the zero interior field case, the equivalent surface currents are not unique as infinitely many solutions are possible. Moreover, as long as one is only interested in determining the exterior fields in an unbounded medium, it would be generally sufficient to work with electric or magnetic surface currents only [Harrington 2001, p. 107-108].

With respect to scattering problems, where the primary sources (the sources that generate the incident field) usually lie somewhere outside the region of interest that contains the scattering object, the surface equivalence principle holds similarly. The total field outside of A is then said to be due to an incident and scattered part, that is

$$\boldsymbol{E}(\boldsymbol{r}) = \boldsymbol{E}_{\mathrm{inc}}(\boldsymbol{r}) + \boldsymbol{E}_{\mathrm{sca}}(\boldsymbol{r}). \tag{2.30}$$

The incident field $\boldsymbol{E}_{\mathrm{inc}}$ is due to the primary sources and the scattered field $\boldsymbol{E}_{\mathrm{sca}}$ due to equivalent surface currents on A that, according to (2.28), obviously depend on the total field itself.

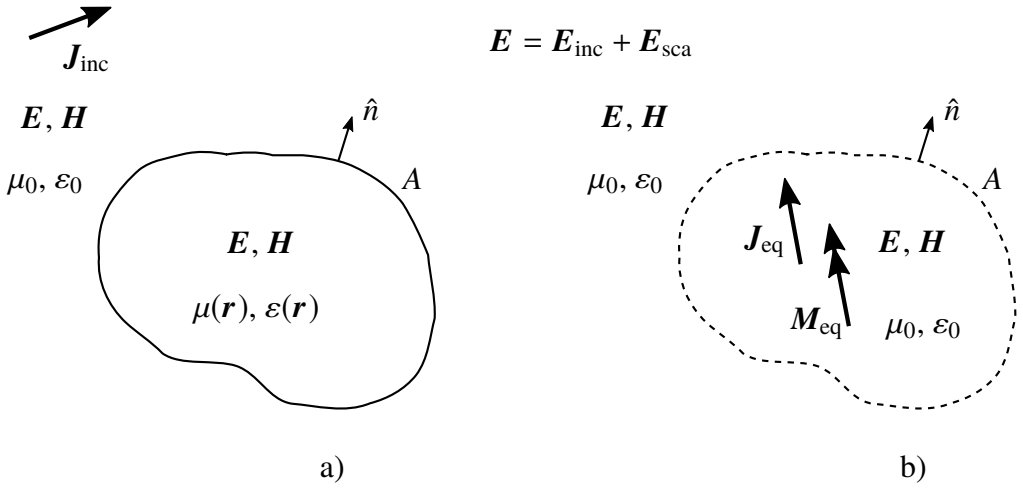

Figure 2.2: Illustration of the volume equivalence principle: a) Original problem, b) Equivalent problem with equivalent current densities radiating into free space.

2.2.2 Volume Equivalence Principle

Consider the scattering scenario depicted in Figure 2.2. The primary current sources $\boldsymbol{J}_{\text{inc}}$ radiate in the presence of an inhomogeneous scatterer with material properties $\mu(\boldsymbol{r})$ and $\varepsilon(\boldsymbol{r})$, which results in the total fields $\boldsymbol{E}$ and $\boldsymbol{H}$. The undisturbed electric field that would be created by $\boldsymbol{J}_{\text{inc}}$ in free space is called the incident field $\boldsymbol{E}_{\text{inc}}$. As introduced before, the total field is the sum of the incident and scattered field, i.e., $\boldsymbol{E} = \boldsymbol{E}_{\text{inc}} + \boldsymbol{E}_{\text{sca}}$ and similarly for the magnetic field. To compute the total field in the presence of the scattering object one may introduce the equivalent (volume) current densities radiating into free space [Volakis and Sertel 2012, p. 16]

$$\boldsymbol{J}_{\text{eq}}(\boldsymbol{r}) = \mathrm{j}\omega(\varepsilon(\boldsymbol{r}) - \varepsilon_0)\boldsymbol{E}(\boldsymbol{r}) \tag{2.31}$$

and

$$\boldsymbol{M}_{\text{eq}}(\boldsymbol{r}) = \mathrm{j}\omega(\mu(\boldsymbol{r}) - \mu_0)\boldsymbol{H}(\boldsymbol{r}) \tag{2.32}$$

that depend on the total field and create the scattered field $\boldsymbol{E}_{\text{sca}}$. In terms of these equivalent current densities the total field can now be computed as

$$\boldsymbol{E}(\boldsymbol{r}) = \iiint_V \left[\overline{\mathbf{G}}_J^E(\boldsymbol{r},\boldsymbol{r}') \cdot \boldsymbol{J}_{\text{inc}}(\boldsymbol{r}') + \overline{\mathbf{G}}_J^E(\boldsymbol{r},\boldsymbol{r}') \cdot \boldsymbol{J}_{\text{eq}}(\boldsymbol{r}') + \overline{\mathbf{G}}_M^E(\boldsymbol{r},\boldsymbol{r}') \cdot \boldsymbol{M}_{\text{eq}}(\boldsymbol{r}')\right] \mathrm{d}v' \tag{2.33}$$

$$= \boldsymbol{E}_{\text{inc}}(\boldsymbol{r}) + \iiint_V \left[\overline{\mathbf{G}}_J^E(\boldsymbol{r},\boldsymbol{r}') \cdot \boldsymbol{J}_{\text{eq}}(\boldsymbol{r}') + \overline{\mathbf{G}}_M^E(\boldsymbol{r},\boldsymbol{r}') \cdot \boldsymbol{M}_{\text{eq}}(\boldsymbol{r}')\right] \mathrm{d}v', \tag{2.34}$$

where the integration volume V contains all sources.

2.3 The Reciprocity Theorem

In order to derive a transmission equation between a transmitting and a receiving antenna, the reciprocity theorem is a valuable tool as it establishes a relation between two independent sets

of electromagnetic fields and sources. Consider the fields $\boldsymbol{E}_1$, $\boldsymbol{H}_1$, generated by electric and magnetic current densities $\boldsymbol{J}_1$ and $\boldsymbol{M}_1$, respectively, as well as the fields $\boldsymbol{E}_2$, $\boldsymbol{H}_2$, generated by electric current densities $\boldsymbol{J}_2$ and and magnetic current densities $\boldsymbol{M}_2$. Provided that both sets obey Maxwell's equations independently from each other and all surrounding media are isotropic (or anisotropic but symmetric), the following Lorentz reciprocity theorem in integral form can be established [Jin 2015, p. 102],

$$\oiint_A (\boldsymbol{H}_2 \times \boldsymbol{E}_1 - \boldsymbol{H}_1 \times \boldsymbol{E}_2) \cdot \mathrm{d}\boldsymbol{a} = \iiint_V (\boldsymbol{E}_1 \cdot \boldsymbol{J}_2 + \boldsymbol{H}_2 \cdot \boldsymbol{M}_1 - \boldsymbol{E}_2 \cdot \boldsymbol{J}_1 - \boldsymbol{H}_1 \cdot \boldsymbol{M}_2)\, \mathrm{d}v \quad (2.35)$$

where V is a finite volume with enclosing surface A. Assuming all existing sources are enclosed by A, the left-hand side of (2.35) vanishes, as can be shown by considering a spherical volume whose radius tends to infinity [Volakis and Sertel 2012, p. 20]. The resulting volume integral over all sources may then be written as

$$\iiint_V (\boldsymbol{E}_1 \cdot \boldsymbol{J}_2 - \boldsymbol{H}_1 \cdot \boldsymbol{M}_2)\, \mathrm{d}v = \iiint_V (\boldsymbol{E}_2 \cdot \boldsymbol{J}_1 - \boldsymbol{H}_2 \cdot \boldsymbol{M}_1)\, \mathrm{d}v, \quad (2.36)$$

which is sometimes called the Rayleigh-Carson reciprocity theorem [Carson 1929]. In general, (2.36) states that the sources and fields can be interchanged without modifying the result of the integral.

Consider now two antennas with discrete terminal regions T_1, T_2 where the current densities $\boldsymbol{J}_1$ and $\boldsymbol{J}_2$ are impressed ($\boldsymbol{M} = 0$). $\boldsymbol{E}_1$ is the electric field when only antenna 1 is radiating ($\boldsymbol{J}_2 = 0$) and vice versa. Evaluating the volume integrals in (2.36) reduces to the terminal region and one obtains [Kong 1986, p. 400]

$$\iiint_{T_1} \boldsymbol{E}_2 \cdot \boldsymbol{J}_1 \,\mathrm{d}v = \iiint_{T_2} \boldsymbol{E}_1 \cdot \boldsymbol{J}_2 \,\mathrm{d}v = \int_{l_2} \boldsymbol{E}_1 \cdot \mathrm{d}\boldsymbol{l} \iint_{A_2} \boldsymbol{J}_2 \cdot \mathrm{d}\boldsymbol{a} = -U_{21} I_2, \quad (2.37)$$

where l_2 is a path through the terminal region and A_2 is the corresponding cross section area. Integrating $\boldsymbol{E}_1$ along l_2 yields U_{21}, the open circuit voltage at antenna 2, measured when antenna 1 is radiating. I_2 is the terminal input current of antenna 2 when it is radiating. This is illustrated in Figure 2.3 a) and b). Thus, (2.37) provides a link between the field quantities $\boldsymbol{E}$ and $\boldsymbol{J}$ to the network quantities U and I. In terms of the reaction concept introduced by Rumsey [1954], this may as well be written as

$$\iiint_{T_2} \boldsymbol{E}_1 \cdot \boldsymbol{J}_2 \,\mathrm{d}v = -U_{21} I_2 = \langle 2, 1 \rangle\,, \quad (2.38)$$

that is the reaction at antenna 2 due to the sources of antenna 1. Employing the volume equivalence theorem, one may now introduce a new set of equivalent current densities $\boldsymbol{J}_{\mathrm{eq},2}$ radiating into free space that represent the radiation of antenna 2 as shown in Figure 2.3 c). The reaction principle still holds and one obtains [Richmond 1961]

$$\langle 2, 1 \rangle = -U_{21} I_2 = \iiint_{V_2} \boldsymbol{E}_1 \cdot \boldsymbol{J}_{\mathrm{eq},2} \,\mathrm{d}v, \quad (2.39)$$

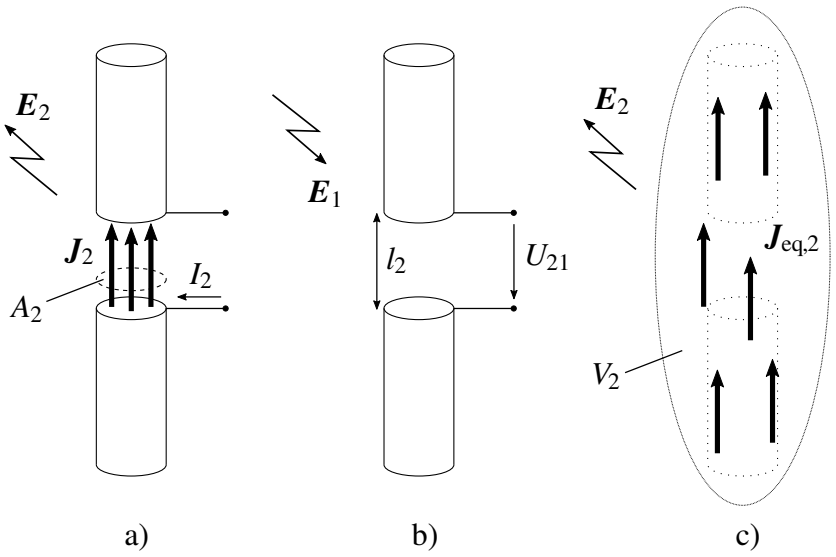

Figure 2.3: Illustration of the relation between field quantities $\boldsymbol{E}_2$ and $\boldsymbol{J}_2$ and network quantities U_{21} and I_2 at antenna 2: a) Transmit case, b) Receive case, c) Transmit case with equivalent current densities $\boldsymbol{J}_{\mathrm{eq},2}$

where V_2 is the volume of antenna 2, supporting the equivalent current densities $\boldsymbol{J}_{\mathrm{eq},2}$. $\boldsymbol{E}_1$ is now the electric field due to the sources of antenna 1 radiating into free space.

It may be noted that a similar relation can also be established using the magnetic field and magnetic current densities by considering current loops [Volakis and Sertel 2012, p. 21]. However, due to the equivalence principle it is fully sufficient to work with electric currents and fields only. Consequently, (2.39) will serve as the basis for the transmission equations derived in later chapters.

2.4 Propagating Plane-Wave Expansion

Equation (2.39) gives the open circuit voltage at a receiving antenna due to an electric field. Expressing the electric field in terms of the generating equivalent surface sources according to (2.29) one obtains the double integral representation

$$U_2 = \iiint\limits_{V_2} -\frac{\boldsymbol{J}_2(\boldsymbol{r})}{I_2} \cdot \iint\limits_{A} \left[\overline{\mathbf{G}}_J^E(\boldsymbol{r},\boldsymbol{r}') \cdot \boldsymbol{J}_A(\boldsymbol{r}') + \overline{\mathbf{G}}_M^E(\boldsymbol{r},\boldsymbol{r}') \cdot \boldsymbol{M}_A(\boldsymbol{r}') \right] \mathrm{d}a' \, \mathrm{d}v, \tag{2.40}$$

in the spatial domain, where $\boldsymbol{r}$ and $\boldsymbol{r}'$ have been interchanged and the surface A does not necessarily need to be closed. From this expression it becomes already apparent that evaluating many of these spatial integrals numerically will be computationally too expensive in most cases and some kind of fast algorithm will be required. Throughout this thesis an expansion of the scalar Green's function in propagating plane waves is used to arrive at a diagonalized transmission equation with the ability of employing hierarchical schemes to reduce the memory consumption. The complete transmission equations for the cases of antenna and scattering

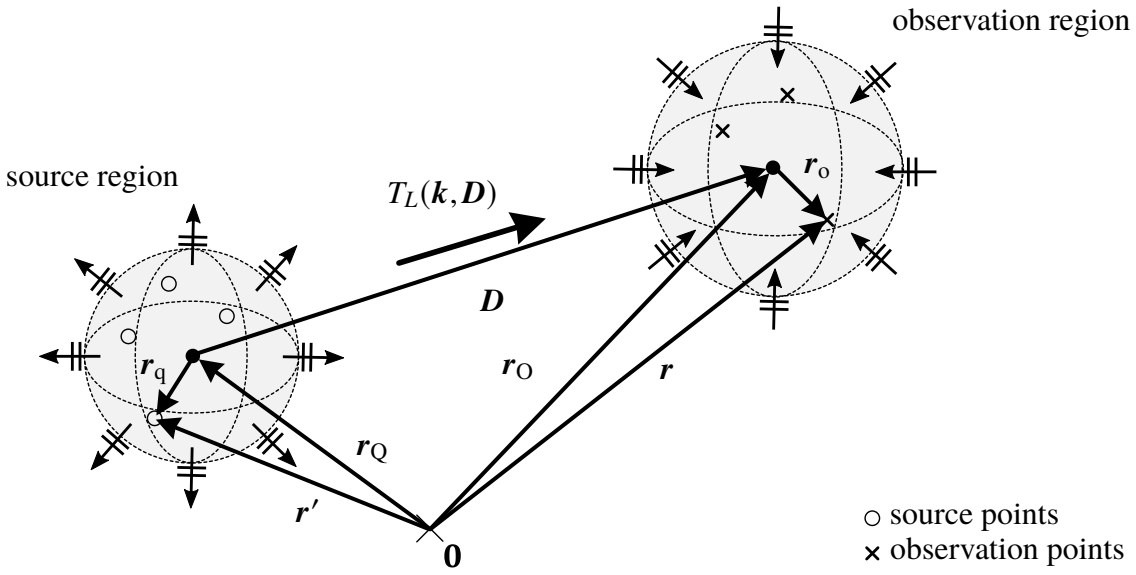

Figure 2.4: Field computation using the FMM. The source and observation points are grouped and well separated, such that $|\boldsymbol{D}| > |\boldsymbol{d}| = \left|\boldsymbol{r}_\mathrm{o} - \boldsymbol{r}_\mathrm{q}\right|$. The translation operator T_L converts the spectrum of outgoing plane waves at $\boldsymbol{r}_\mathrm{Q}$ into a spectrum of incident plane waves at the observation region with center at $\boldsymbol{r}_\mathrm{O}$.

measurements will be considered in detail later in the corresponding chapters. In the following, the expansion of the scalar Green's function and of the radiated electric field due to some source currents in free space will be introduced.

2.4.1 Expansion of the Scalar Green's Function

The expansion is closely related to the fast multipole method (FMM) introduced by Greengard and Rokhlin [1987] and is based on the addition theorem for spherical waves [Stratton 1941, p. 414]

$$\frac{\mathrm{e}^{-\mathrm{j}k|\boldsymbol{r}-\boldsymbol{r}'|}}{|\boldsymbol{r}-\boldsymbol{r}'|} = -\mathrm{j}k \sum_{l=0}^{\infty} (-1)^l (2l+1)\, \mathrm{j}_l(kd)\, \mathrm{h}_l^{(2)}(kD)\, \mathrm{P}_l\left(\hat{d}\cdot\hat{D}\right), \tag{2.41}$$

as well as the propagating plane-wave expansion [Stratton 1941, p. 410]

$$\mathrm{j}_l(kd)\, \mathrm{P}_l\left(\hat{d}\cdot\hat{D}\right) = \frac{-\mathrm{j}^l}{4\pi} \oiint \mathrm{P}_l\left(\hat{k}\cdot\hat{D}\right) \mathrm{e}^{-\mathrm{j}\,\boldsymbol{k}\cdot\boldsymbol{d}}\, \mathrm{d}^2\hat{k}. \tag{2.42}$$

Here, j_l is the spherical Bessel function of the first kind, $\mathrm{h}_l^{(2)}$ is the second kind spherical Hankel function, P_l is the Legendre polynomial (all of order l) and the source and observation vectors, following the notation in [Coifman et al. 1993], are related by $\boldsymbol{D} = \boldsymbol{r}_\mathrm{O} - \boldsymbol{r}_\mathrm{Q}$ and $\boldsymbol{d} = \boldsymbol{r}_\mathrm{o} - \boldsymbol{r}_\mathrm{q}$ as shown in Figure 2.4. For (2.41) to hold it is required that $|\boldsymbol{D}| = D > d = |\boldsymbol{d}|$. The integration in (2.42) is carried out over the unit sphere for all angular directions of the normalized wave vectors and is thus said to be in k-space. Plugging (2.42) into (2.41) and noting that in any

practical implementation l must be finite, the order of summation and integration may be interchanged. This results in

$$\frac{\mathrm{e}^{-\mathrm{j}k|\boldsymbol{r}-\boldsymbol{r}'|}}{|\boldsymbol{r}-\boldsymbol{r}'|} \approx \iint \mathrm{e}^{-\mathrm{j}\,\boldsymbol{k}\cdot\boldsymbol{d}} T_L\left(kD, \hat{k}\cdot\hat{D}\right)\,\mathrm{d}^2\hat{k}, \tag{2.43}$$

where

$$T_L\left(kD, \hat{k}\cdot\hat{D}\right) = \frac{-\mathrm{j}k}{4\pi}\sum_{l=0}^{L}(-\mathrm{j})^l\,(2l+1)\,\mathrm{h}_l^{(2)}(kD)\,\mathrm{P}_l\left(\hat{k}\cdot\hat{D}\right) \tag{2.44}$$

is the propagating plane-wave translation operator of order L. With respect to the spherical waves in (2.41), L is called the (spherical) multipole number. The value of L is chosen according to the spatial extent of the source and receive region described by $kd_{\max}$, which determines the maximum spatial frequency components to be considered [Bucci and Franceschetti 1987]. An empirically determined formula for L to give very good results was found by Song and Chew [2001] to be

$$L = kd_{\max} + 1.8d_0^{2/3}\,(kd_{\max})^{1/3} \tag{2.45}$$

where d_0 is the number of decimal digits of accuracy. While L must be chosen large enough for the sum in (2.41) to converge to the desired accuracy, it should not be chosen to be much larger than kD, the argument of the spherical Hankel function, as the higher order terms of the Hankel function grow exponentially and swamp the lower order terms, causing numerical inaccuracies [Bogaert et al. 2008; Koc et al. 1999]. At the same time (but generally less severe), the Bessel functions j_l on the left-hand side of (2.42) decrease exponentially, which becomes difficult to represent in terms of the oscillatory integral on the right-hand side [Bogaert et al. 2008]. Both problems also correspond to the low-frequency breakdown of the MLFMM as $k \to 0$ [Bogaert et al. 2008; Wallén and Sarvas 2005; Xia et al. 2018]. However, in the area of antenna and RCS measurements one is typically interested in finding solutions in the mid-frequency range and for well separated source and observation points. The mentioned numerical instabilities are thus less problematic and will not be further discussed here. Depending on the application, typical values for d_0 in (2.45) are 4 to 5, resulting in an accuracy of around $-80\,\mathrm{dB}$ to $-100\,\mathrm{dB}$ for the plane-wave expansion, which is usually sufficient if real (and consequently noisy) measurement data is processed. The spherical Hankel functions and Legendre polynomials up to the required order L can be efficiently computed by the recurrence relations (A.3) and (A.5) given in Appendix A.1. The exponential in (2.43) is quasi-bandlimited and can be approximated by a periodic polynomial of order L in ϑ and φ [Sarvas 2003]. As will be discussed in the context of discretization of the given equations, the quadrature rule for evaluating the integral in (2.43) numerically has to be chosen accordingly.

2.4.2 Expansion of the Radiated Electric Field

Inserting the expansion of the scalar Green's function (2.43) into the dyadic expressions in (2.22) and (2.23) yields

$$\overline{\mathbf{G}}_J^E(\boldsymbol{r},\boldsymbol{r}') \approx -\mathrm{j}\frac{kZ_\mathrm{F}}{4\pi}\iint \left(\bar{\mathbf{I}} - \hat{k}\hat{k}\right)\mathrm{e}^{-\mathrm{j}\,\boldsymbol{k}\cdot\boldsymbol{d}} T_L\left(kD, \hat{k}\cdot\hat{D}\right)\,\mathrm{d}^2\hat{k} \tag{2.46}$$

and

$$\overline{\mathbf{G}}_M^E(\boldsymbol{r},\boldsymbol{r}') \approx \mathrm{j}\frac{k}{4\pi} \oiint \left(\hat{k}\times\bar{\mathbf{I}}\right) \mathrm{e}^{-\mathrm{j}\,\boldsymbol{k}\cdot\boldsymbol{d}} T_L\left(kD, \hat{k}\cdot\hat{D}\right)\, \mathrm{d}^2\hat{k}. \tag{2.47}$$

With these expressions and the general relation (2.21) the electric field at a point in the observation region due to some (equivalent) electric and magnetic current densities may be written as[2]

$$\begin{aligned}\boldsymbol{E}(\boldsymbol{r}) = \iiint_V \Bigg[&-\mathrm{j}\frac{kZ_\mathrm{F}}{4\pi} \oiint \left(\bar{\mathbf{I}} - \hat{k}\hat{k}\right) \mathrm{e}^{-\mathrm{j}\,\boldsymbol{k}\cdot\boldsymbol{d}} T_L\left(kD, \hat{k}\cdot\hat{D}\right)\, \mathrm{d}^2\hat{k}\cdot\boldsymbol{J}(\boldsymbol{r}') \\ &+\mathrm{j}\frac{k}{4\pi} \oiint \left(\hat{k}\times\bar{\mathbf{I}}\right) \mathrm{e}^{-\mathrm{j}\,\boldsymbol{k}\cdot\boldsymbol{d}} T_L\left(kD, \hat{k}\cdot\hat{D}\right)\, \mathrm{d}^2\hat{k}\cdot\boldsymbol{M}(\boldsymbol{r}')\Bigg]\, \mathrm{d}v' \end{aligned} \tag{2.48}$$

$$\begin{aligned}= \oiint &\mathrm{e}^{-\mathrm{j}\boldsymbol{k}\cdot\boldsymbol{r}_o} T_L\left(kD, \hat{k}\cdot\hat{D}\right) \\ &\left[-\mathrm{j}\frac{kZ_\mathrm{F}}{4\pi}\left(\bar{\mathbf{I}} - \hat{k}\hat{k}\right) \iiint_V \boldsymbol{J}(\boldsymbol{r}')\,\mathrm{e}^{\mathrm{j}\boldsymbol{k}\cdot\boldsymbol{r}_\mathrm{q}}\,\mathrm{d}v' + \mathrm{j}\frac{1}{4\pi}\boldsymbol{k}\times\iiint_V \boldsymbol{M}(\boldsymbol{r}')\,\mathrm{e}^{\mathrm{j}\boldsymbol{k}\cdot\boldsymbol{r}_\mathrm{q}}\,\mathrm{d}v'\right] \mathrm{d}^2\hat{k}, \end{aligned} \tag{2.49}$$

where $\boldsymbol{d} = \boldsymbol{r}_\mathrm{o} - \boldsymbol{r}_\mathrm{q}$ and $\boldsymbol{r}' = \boldsymbol{r}_\mathrm{Q} + \boldsymbol{r}_\mathrm{q}$ as defined before. The terms in the square brackets involving the spatial volume integrals give the plane-wave spectra of $\boldsymbol{J}$ and $\boldsymbol{M}$,

$$\tilde{\boldsymbol{J}}(\boldsymbol{k})\,\mathrm{e}^{-\mathrm{j}\boldsymbol{k}\cdot\boldsymbol{r}_\mathrm{Q}} = -\mathrm{j}\frac{kZ_\mathrm{F}}{4\pi}\left(\bar{\mathbf{I}} - \hat{k}\hat{k}\right) \iiint_V \boldsymbol{J}(\boldsymbol{r}')\,\mathrm{e}^{\mathrm{j}\boldsymbol{k}\cdot(\boldsymbol{r}'-\boldsymbol{r}_\mathrm{Q})}\,\mathrm{d}v' \tag{2.50}$$

and

$$\tilde{\boldsymbol{M}}(\boldsymbol{k})\,\mathrm{e}^{-\mathrm{j}\boldsymbol{k}\cdot\boldsymbol{r}_\mathrm{Q}} = \mathrm{j}\frac{1}{4\pi}\boldsymbol{k}\times\iiint_V \boldsymbol{M}(\boldsymbol{r}')\,\mathrm{e}^{\mathrm{j}\boldsymbol{k}\cdot(\boldsymbol{r}'-\boldsymbol{r}_\mathrm{Q})}\,\mathrm{d}v', \tag{2.51}$$

respectively, which correspond to the far-field radiation patterns in (2.27). They are defined with respect to the origin of the coordinate system and shifted here to the source region center $\boldsymbol{r}_\mathrm{Q}$. In general, the plane-wave spectra are obtained from the spatial Fourier transforms as

$$\tilde{\boldsymbol{J}}(\boldsymbol{k}) = -\mathrm{j}\frac{kZ_\mathrm{F}}{4\pi}\left(\bar{\mathbf{I}} - \hat{k}\hat{k}\right) \iiint_V \boldsymbol{J}(\boldsymbol{r}')\,\mathrm{e}^{\mathrm{j}\boldsymbol{k}\cdot\boldsymbol{r}'}\,\mathrm{d}v' = -\mathrm{j}\frac{kZ_\mathrm{F}}{4\pi}\left(\bar{\mathbf{I}} - \hat{k}\hat{k}\right) \mathcal{F}\left\{\boldsymbol{J}(\boldsymbol{r}')\right\} \tag{2.52}$$

and

$$\tilde{\boldsymbol{M}}(\boldsymbol{k}) = \mathrm{j}\frac{1}{4\pi}\boldsymbol{k}\times\iiint_V \boldsymbol{M}(\boldsymbol{r}')\,\mathrm{e}^{\mathrm{j}\boldsymbol{k}\cdot\boldsymbol{r}'}\,\mathrm{d}v' = \mathrm{j}\frac{1}{4\pi}\boldsymbol{k}\times\mathcal{F}\left\{\boldsymbol{M}(\boldsymbol{r}')\right\}, \tag{2.53}$$

where for the single frequency case the far-field radiation pattern is evaluated on the sphere with $\boldsymbol{k} = k\hat{r}$, which is sometimes considered to be a special case of the Ewald sphere, originally

[2] In the following it is assumed that (2.43) is sufficiently well fulfilled to write '=' instead of '≈'.

defined for scattering problems [Devaney 2012, p. 23]. Consequently, one gets the linear and factorized integral representation of the electric field in k-space,

$$\boldsymbol{E}(\boldsymbol{r}) = \oiint \mathrm{e}^{-\mathrm{j}\boldsymbol{k}\cdot\boldsymbol{r}_\mathrm{o}} T_L\left(kD, \hat{k}\cdot\hat{D}\right)\left[\tilde{\boldsymbol{J}}(\boldsymbol{k}) + \tilde{\boldsymbol{M}}(\boldsymbol{k})\right] \mathrm{e}^{-\mathrm{j}\boldsymbol{k}\cdot\boldsymbol{r}_\mathrm{Q}}\,\mathrm{d}^2\hat{k}, \tag{2.54}$$

where the translation operator T_L is said to be diagonal as it converts each outgoing plane wave of the source spectra into one incident plane wave at the reference location of the observation region r_O. This is illustrated in Figure 2.4. Integrating over the spectrum of incident plane waves at the observation location yields the electric field at that point, where the exponential $\mathrm{e}^{-\mathrm{j}\boldsymbol{k}\cdot\boldsymbol{r}_\mathrm{o}}$ can be thought of being the propagating plane-wave spectrum of an ideal receive probe, shifted by $\boldsymbol{r}_\mathrm{o}$ from the reference location of the observation region.

2.4.3 Spherical Wave Expansion of the Plane-Wave Spectra

The definition of the plane-wave spectra in (2.52) and (2.53) provides the connection between the k-space and spatial representation of the sources, generating the electric field $\boldsymbol{E}(\boldsymbol{r})$ in (2.54). An alternative spectral representation may be obtained by expanding the plane-wave spectra in spherical wave functions on the unit sphere, i.e., using the limiting far-field form of the spherical wave functions [J. E. Hansen 1988, p. 312]. As will be discussed in connection with the actual implementation of the transformation algorithm, this representation has the advantage that after discretization (and depending on the chosen sampling grid) the spherical waves lead to a system of equations with less unknowns and an orthonormal basis, thus improving its conditioning [T. B. Hansen et al. 2019]. Moreover, they can also be used to represent the k-space spectra of the spatial basis function when working with localized (surface current) sources, leading to a significant reduction in the required computer memory [Eibert 2005].

The notation employed here follows the one in [J. E. Hansen 1988] and is based on an expansion in vector spherical harmonics. The outgoing electric field in spherical coordinates may then be written as

$$\boldsymbol{E}(\boldsymbol{r}) = \lim_{N\to\infty} k\sqrt{Z_\mathrm{F}} \sum_{s=1}^{2}\sum_{n=1}^{N}\sum_{m=-n}^{n} q_{smn}\boldsymbol{F}_{smn}(r,\vartheta,\varphi), \tag{2.55}$$

where $\boldsymbol{F}_{1mn}$ and $\boldsymbol{F}_{2mn}$ are the spherical waves for the outgoing field given by (A.12) and (A.13) in Appendix A.2 and q_{smn} are the corresponding expansion coefficients. N is the maximum order of multipoles used for the expansion. As noted before in the context of the propagating plane-wave expansion, its value must be chosen according to the degrees of freedom of the electric field [Bucci; Gennarelli, et al. 1998]. With respect to the multipole order L defined in (2.45), an appropriate choice is $N = \lfloor L/2 \rfloor$, where $\lfloor x \rfloor$ represents the next lower integer value to x. With the far-field representation of (2.55)

$$\boldsymbol{K}_{smn}(\vartheta,\varphi) = \lim_{kr\to\infty}\left\{\frac{kr}{\mathrm{e}^{-\mathrm{j}kr}}\boldsymbol{F}_{smn}(r,\vartheta,\varphi)\right\} \tag{2.56}$$

the combined plane-wave spectrum

$$\tilde{\boldsymbol{V}}(\boldsymbol{k}) = \tilde{\boldsymbol{J}}(\boldsymbol{k}) + \tilde{\boldsymbol{M}}(\boldsymbol{k}) \tag{2.57}$$

may be expressed as

$$\tilde{\boldsymbol{V}}(\boldsymbol{k}) = \sqrt{Z_\mathrm{F}} \sum_{s=1}^{2} \sum_{n=1}^{N} \sum_{m=-n}^{n} \tilde{q}_{smn} \boldsymbol{K}_{smn}(\vartheta, \varphi) \tag{2.58}$$

where the far-field spherical wave functions are given in (A.14) and (A.15). An important consequence of this representation is that the plane-wave spectrum $\tilde{\boldsymbol{V}}(\boldsymbol{k})$ is now exactly band-limited according to the maximum multipole order $N \sim L/2$. With the definition given in Appendix A the spherical wave functions $\boldsymbol{F}_{smn}$ and $\boldsymbol{K}_{smn}$ are power-normalized, such that the total radiated power of the outgoing field is

$$P_\mathrm{rad} = \frac{1}{2} \sum_{smn} |\tilde{q}_{smn}|^2 \tag{2.59}$$

where the summation is carried out over all expansion coefficients.

2.4.4 Far-Field Translations and the Gaussian Beam Approach

As can be seen from (2.44), the translation operator is rotationally symmetric around its maximum along the direction of propagation $\hat{D}$, depending only on the absolute value kD and the angle $\cos\theta = \hat{k} \cdot \hat{D}$. In the limiting far-field case for $kD \to \infty$, the scalar Green's function may be approximated by evaluating a single plane-wave contribution in (2.43) [Chew et al. 2002]. With the large argument approximation of the spherical Hankel function [Olver et al. 2010, p. 265]

$$\lim_{x\to\infty} \mathrm{h}_l^{(2)}(x) = \mathrm{j}^{l+1} \frac{\mathrm{e}^{-\mathrm{j}x}}{x}, \tag{2.60}$$

one may write the translation operator in the form of a Dirac delta in k-space as [Eibert et al. 2015]

$$\lim_{kD\to\infty} T_L\left(kD, \hat{k} \cdot \hat{D}\right) \approx \frac{\mathrm{e}^{-\mathrm{j}kD}}{D} \delta\left(\hat{k} - \hat{D}\right). \tag{2.61}$$

Consequently, one obtains the electric field under far-field conditions from (2.54) as

$$\boldsymbol{E}_\mathrm{FF}(\boldsymbol{r}) \approx \mathrm{e}^{-\mathrm{j}\boldsymbol{k}_D \cdot \boldsymbol{r}_\mathrm{o}} \left[\tilde{\boldsymbol{J}}(\boldsymbol{k}_D) + \tilde{\boldsymbol{M}}(\boldsymbol{k}_D)\right] \frac{\mathrm{e}^{-\mathrm{j}\boldsymbol{k}_D \cdot \boldsymbol{D}}}{D}, \tag{2.62}$$

where $\boldsymbol{k}_D$ is the wave vector corresponding to the direction of $\hat{D}$.

In near-field measurement scenarios the requirement to assume far-field translations are usually not fulfilled, as a large significant part of the plane-wave source spectrum would be discarded. However, for moderately large separations between the FMM transmit and receive groups it may be sufficient to consider only a limited angular range of the spectrum around the direction of propagation, thus reducing the overall computational effort. In order to avoid truncation effects when evaluating the standard translation operator (2.44), a directive translation operator based on the concept of Gaussian beams has been introduced by T. B. Hansen [2013]. In this case the translation operator is written as

$$T_L^\mathrm{GB}\left(kD, \hat{k} \cdot \hat{D}\right) = \frac{-\mathrm{j}k}{4\pi} \mathrm{e}^{k\Delta\left(\hat{k}\cdot\hat{D}\right)} \sum_{l=0}^{L} (-\mathrm{j})^l (2l+1)\, \mathrm{h}_l^{(2)}(kD - \mathrm{j}k\Delta)\, \mathrm{P}_l\left(\hat{k} \cdot \hat{D}\right), \tag{2.63}$$

where $j\Delta$ is an imaginary shift in the complex plane of the translation distance. The larger Δ, the more directive is the translation operator, i.e., the narrower is the spectral filtering of the corresponding plane-wave spectrum. Δ may be selected dependent on the size of the source region and the translation distance to achieve a desired accuracy. For $\Delta = 0$, (2.63) reduces to the standard form of T_L in (2.44). For very large size near-field measurements problems, the Gaussian beam approach may help to reduce the computation time and memory requirements as demonstrated in [Eibert et al. 2016].

2.5 The Inverse Source Problem

Computing the electric field due to some radiating or scattering sources in (2.54) (or similarly using the spatial relation in (2.21)) is called the *forward* or *direct problem*. In order to determine the far-field pattern of an antenna or the RCS of an object under test from the known (radiated or scattered) electric field $\boldsymbol{E}(\boldsymbol{r})$, one has to solve (2.54) for the unknown sources, which is called the *inverse problem*. In a scattering scenario this may correspond to solving for the unknown equivalent sources according to (2.34) that generally depend on the total field itself. In both cases one obtains a linear integral equation, which, after discretization, may be expressed in terms of a linear operator $\mathbf{A}$ working on the unknown sources $\boldsymbol{q}$ resulting in the measured vector $\boldsymbol{b}$, that is

$$\mathbf{A}(\boldsymbol{q}) = \boldsymbol{b}, \tag{2.64}$$

where in this form $\mathbf{A}$ is called the forward operator. The inverse problem corresponds to determining $\boldsymbol{q}$ from knowledge of $\boldsymbol{b}$ and $\mathbf{A}$.

2.5.1 Ill-posedness of the Inverse Problem

The inverse problem in (2.64) is ill-posed in the sense of Hadamard as at least one of the following three conditions is not fulfilled: 1) existence of a solution, 2) uniqueness of the solution and 3) stability with respect to small changes of the input data [Colton and Kress 2013, p. 95]. The non-existence of a solution appears in almost any real measurement where the right-hand side $\boldsymbol{b}$ is inevitably noisy and thus no exact solution exists. The non-uniqueness can have several reasons. Beside the possibility of having infinitely many solutions as consequence of the volume equivalence theorem or the surface equivalence theorem (when working with electric and magnetic surface currents without additional side constraints for example), also "essentially" non-radiating sources can be present [Bleistein and Cohen 1977][Devaney 2012, p. 27]. While truly non-radiating sources correspond to the null space of the forward operator, essentially non-radiating sources are those whose fields decay so quickly that they cannot be detected at the measurement position due to sensitivity limitations or noise [Devaney 2012, p. 33]. With respect to the spherical wave expansion introduced in (2.55) this corresponds to the spherical multipoles whose order $l > N$, creating evanescent waves. Moreover, when working with localized sources (e.g., surface current densities) the number of unknowns in the resulting system of equations is usually larger than the number of measurement samples and the degrees of freedom of radiated or scattered field. This results in an under-determined system with possibly infinitely many solutions.

The instability is a property of the right-hand side $\boldsymbol{b}$ (the quality of the measurement) as well as of the operator $\mathbf{A}$ and thus strongly depends on the underlying model. If (2.64) is used to setup a linear system of equations

$$\mathbf{Aq} = \mathbf{b}, \tag{2.65}$$

where $\mathbf{A} \in \mathbb{C}^{M \times N}$ is the system matrix, $\mathbf{q} \in \mathbb{C}^{M}$ contains the unknown source coefficients and $\mathbf{b} \in \mathbb{C}^{M}$ the measurement samples, than the instability is due to the fact that $\mathbf{A}$ is ill-conditioned, with a high (or even infinite) condition number [P. C. Hansen 2010, p. 54]. Even small defects in the measurement data $\mathbf{b}$ thus lead to arbitrarily large errors in the solution. Physically, this can be interpreted as a strong amplification of high frequency components (higher order modes) present in the measured data by the inverse operator, which attenuates higher order components in the forward direction. Consequently, even if $\mathbf{A}$ is invertible, solving the inverse problem directly will generally not yield the correct solution. For this reason, some sort of regularization will be required to solve the inverse problems.

2.5.2 Approximate Solution and Regularization

To overcome the problem of non-existence of a solution in (2.65) and as $\mathbf{A}$ is not necessarily square, it is common to solve a least squares problem of the form

$$\min_{\mathbf{q}} \|\mathbf{Aq} - \mathbf{b}\|_2 . \tag{2.66}$$

Since this equation may still have an infinite number of solutions, one may also introduce some constraint on the solution $\mathbf{q}$. Most commonly one seeks the minimum energy solution in form of the ℓ^2-norm, which appears to be a natural choice regarding the underlying physics. Consequently, the constrained least squares problem to be solved is

$$\min_{\mathbf{q}} \|\mathbf{q}\|_2 \qquad \text{such that} \qquad \|\mathbf{Aq} - \mathbf{b}\|_2 = \min, \tag{2.67}$$

where it has been taken into account that $\mathbf{b}$ might be noisy and, thus, the residual error at the right should only be minimized to approximate the noise-free solution. One possibility for doing so is by means of a truncated singular value decomposition (SVD), which has the advantage that the right selection of the truncation leads to a regularized solution in that high frequency components stemming from the noise are filtered out [P. C. Hansen 2010, p. 55]. However, a drawback for most problems is that the SVD requires an explicit generation of the matrix $\mathbf{A}$, which may be infeasible in terms of computation time and memory, even for moderately sized problems.

An alternative is to work with iterative solvers that only require the repeated evaluation of matrix-vector products [Saad 2003]. As many solvers require square matrices, a common approach is to setup the normal equation [Saad 2003, p. 229]

$$\mathbf{A}^{\mathrm{H}}\mathbf{Aq} = \mathbf{A}^{\mathrm{H}}\mathbf{b}, \tag{2.68}$$

where $\mathbf{A}^{\mathrm{H}}$ is the conjugate transpose of $\mathbf{A}$, which solves the least-squares problem

$$\min_{\mathbf{q}} \|\mathbf{b} - \mathbf{Aq}\|_2 . \tag{2.69}$$

Alternatively, one can set $\mathbf{q} = \mathbf{A}^{\mathrm{H}}\mathbf{u}$ and solve

$$\mathbf{A}\mathbf{A}^{\mathrm{H}}\mathbf{u} = \mathbf{b}, \tag{2.70}$$

which corresponds to the least-squares problems

$$\min_{\mathbf{u}} \left\| \mathbf{q} - \mathbf{A}^{\mathrm{H}}\mathbf{u} \right\|_2 . \tag{2.71}$$

By solving one of the normal equations, the problem is no longer ill-posed. However, it may still be very ill-conditioned (in general even worse-conditioned as before) as the condition number of $\mathbf{A}^{\mathrm{H}}\mathbf{A}$ or $\mathbf{A}\mathbf{A}^{\mathrm{H}}$ is the square of the condition number of $\mathbf{A}$ [Saad 2003, p. 231].

In an iterative solver, the residual error after step i in (2.68), $\mathbf{r}_i = \mathbf{A}^{\mathrm{H}}\mathbf{b} - \mathbf{A}^{\mathrm{H}}\mathbf{A}\mathbf{q}_i$, will be in the function space of the unknowns $\mathbf{q}$ and (2.68) is usually called the normal residual (NR) equation. On the other hand, in (2.70) the residual error $\mathbf{r}_i = \mathbf{b} - \mathbf{A}\mathbf{A}^{\mathrm{H}}\mathbf{u}_i$ is in the space of the measurement vector and (2.70) is thus called the normal error (NE) equation [Saad 2003, p. 230]. A popular iterative method for solving both types of equations is the generalized minimal residual (GMRES) method introduced by Saad and Schultz [1986]. It belongs to the Krylov subspace methods and was shown to be very robust with respect to noisy input data if the iterations are stopped as soon as the norm of the residual error is on the order of the perturbations ϵ [Eldén and Simoncini 2012], that is

$$\|\mathbf{r}_i\|_2 \leq \epsilon. \tag{2.72}$$

In this respect the NE equation is beneficial as it establishes a direct relation between the residual error and the (noisy) measurement data. The process of stopping the iterative solver early enough can be interpreted as a regularization method according to finding the optimal point along the L-curve [P. C. Hansen 1992], as in the GMRES method not only the residual error is monotonically decreasing, but at the same time the ℓ^2-norm of the solution vector is monotonically increasing. Thus, by stopping at a certain residual error norm $\|\mathbf{r}_i\|_2$ one inherently finds the corresponding minimum norm solution $\|\mathbf{q}_i\|_2$. Stopping too early corresponds to an over-smoothing of the solution as higher frequency components are neglected. Iterating too long includes more noise contributions into the solution vector [P. C. Hansen 1992]. If a good estimate for the stopping residual is not available, it is also possible to consider the relative convergence rate. It was shown in [Kornprobst et al. 2019] that the residual error of the NE equation reliably stagnates at the noise level, thus providing a good indication when to stop the iterations. Throughout this thesis a GMRES solver working on the NE or NR system of equations is used to solve the different inverse problems that are encountered.

2.5.3 Other Solution Approaches

Beside the least-squares minimization approaches for solving the inverse source problem, a variety of other formulations exists [Colton and Kress 2013]. Covering them all would certainly be beyond the scope of this thesis. However, for the sake of completeness it appears worthwhile to mention at least two classes of formulations, where in the field of antenna measurements, inverse scattering and electromagnetic imaging a lot of effort has been put into.

The first one is finding solutions with magnitude-only measurement data, that is solving linear systems of equations of the form

$$|\mathbf{Aq}| = |\mathbf{b}|\,, \tag{2.73}$$

often denoted as a phase-less or phase-retrieval problem [Fienup 1982]. Generally, when solving these kinds of problems one faces the difficulty of having local minima, which requires some kind of additional information about the problem (other than the phase of the measurement data) in order to reliably find an appropriate solution [Paulus et al. 2017]. Thus, the overall measurement effort will be increased but one can avoid the difficulties of accurately measuring the phase of the radiated fields.

The second formulation is a minimization of the ℓ^0-norm of the solution vector in the least squares problem in (2.67), which is pursued in the framework of compressed sensing (also known as compressive sensing or sparse recovery) in order to reduce the required number of measurement samples to solve the inverse problem. In particular the minimization problem

$$\min_{\mathbf{q}} \|\mathbf{q}\|_p \qquad \text{such that} \qquad \|\mathbf{Aq} - \mathbf{b}\|_2 \leq \epsilon, \tag{2.74}$$

where $p \leq 1$ and ϵ is an error bound corresponding to the noise in the measurement data, has been considered to reconstruct a sparse set of solution coefficients (that is a set with only few essentially non-zero coefficients) in the area of electromagnetic scattering and imaging [Oliveri et al. 2017] as well as antenna measurements [Migliore 2014]. More recently, the minimum required number of measurement samples in the context of compressed sensing for spherical antenna near-field measurements has been investigated [Hofmann et al. 2019]. It could be shown that a significant reduction of measurement samples can only be achieved if the assumption of a sparse solution vector is actually justified, which, unfortunately, appears to be generally not the case. Thus, in most cases it will be difficult to reliably find a fitting solution to the inverse source problem.

3 The Inverse Source Problem in Antenna Near-Field Measurements

One of the main tasks in antenna measurements is to determine the far field (FF) radiation pattern of an antenna, preferably including the gain and the polarization [Parini et al. 2014, p. 63]. As was shown in Section 2.4.2, the radiation pattern is nothing else but the spectrum of plane waves defined by (2.52) for electric sources and (2.53) for magnetic sources. The general relation between the plane-wave spectra and the electric field is given by (2.54), which forms the basis for the inverse source problem to be solved. To account for the vector nature of the electric field and in order to correctly determine the polarization, it is common to measure two (preferably orthogonal) field components. However, in any real life measurement setup it is not possible to acquire the electric field values directly, but only a corresponding signal from the measurement probe. Accounting for the influence of the probe antenna is known as "probe correction" and forms an important part of accurate near-field antenna (as well as RCS) measurements [Parini et al. 2014, p. 182].

In contrast to the directivity, which gives the beam focusing properties of an antenna, the gain also accounts for the losses in the antenna structure and can thus not be directly computed from the radiation pattern alone [Balanis 2016, p. 61]. Under far-field conditions and with the known gain of the probe antenna, it is common to directly measure input and receive powers at the antenna terminals and relate them by the Friis transmission equation [Friis 1946]. This is known as the direct method. Alternatively, if the gain of the probe antenna is unknown, one can also replace the AUT by another reference antenna, whose gain has been accurately determined before, and perform a second comparison measurement under the same conditions as for the first measurement with the AUT. By comparing the power levels of the measurements (AUT and reference antenna), the gain of the AUT can be determined, which is thus called the comparison (or substitution) method [Parini et al. 2014, p. 658]. Both methods can also be applied in the near field (NF), where, however, the direct method is often preferred as it avoids performing a second (laborious) measurement. In either case a near-field transmission equation is required that correctly relates the measured values to the probe and antenna gain, taking polarization effects into account.

In this chapter, based on the plane-wave expansion and the reciprocity theorem introduced before, a fully factorized and diagonal near-field transmission equation is derived to determine the radiation pattern and possibly the gain of an AUT from transmission factor measurements in the near field of the two antennas. This process is commonly called near-field to far-field transformation (NFFFT). It will be shown that with an appropriate discretization, this form of the transmission equation is well suited for the integration into hierarchical schemes as employed by the MLFMM. Consequently, even for large scale problems and for a large number of arbitrarily distributed measurement samples one can evaluate the matrix-vector products efficiently, as required by the iterative GMRES solver introduced before. Using both synthetic (i.e., simulated or analytically computed) and measured test data, the correctness and accuracy

of the presented formulation is validated before the same algorithmic principles are carried over to the case of scattering measurements in the next chapter.

3.1 Near-Field Transmission Equation in k-space

Starting from the general reciprocity relation it was shown in Section 2.3 that the open circuit voltage U_2 at the terminals of a receiving antenna 2 (the measurement probe) due to the electric field $\boldsymbol{E}(\boldsymbol{r})$ generated by antenna 1 (the AUT) may be written as

$$U_2 = \iiint\limits_{V_2} -\frac{\boldsymbol{J}_2(\boldsymbol{r})}{I_2} \cdot \boldsymbol{E}(\boldsymbol{r}) \, \mathrm{d}v, \tag{3.1}$$

where the current density $\boldsymbol{J}_2$ is a free-space equivalent source representation of the probe antenna confined to the volume V_2 and I_2 is the current at the input terminal when it operates in transmit mode. With the propagating plane-wave expansion of the electric field

$$\boldsymbol{E}(\boldsymbol{r}) = \oiint \mathrm{e}^{-\mathrm{j}\boldsymbol{k}\cdot\boldsymbol{r}_\mathrm{o}} T_L\left(kD, \hat{k}\cdot\hat{D}\right) \tilde{\boldsymbol{V}}(\boldsymbol{k}) \, \mathrm{e}^{-\mathrm{j}\boldsymbol{k}\cdot\boldsymbol{r}_\mathrm{Q}} \, \mathrm{d}^2\hat{k}, \tag{3.2}$$

one obtains

$$U_2(\boldsymbol{r}_m) = \iiint\limits_{V_2} -\frac{\boldsymbol{J}_2(\boldsymbol{r}-\boldsymbol{r}_m)}{I_2} \cdot \left[\oiint \mathrm{e}^{-\mathrm{j}\boldsymbol{k}\cdot\boldsymbol{r}_\mathrm{o}} T_L\left(kD, \hat{k}\cdot\hat{D}\right) \tilde{\boldsymbol{V}}_\mathrm{T}(\boldsymbol{k}) \, \mathrm{e}^{-\mathrm{j}\boldsymbol{k}\cdot\boldsymbol{r}_\mathrm{Q}} \, \mathrm{d}^2\hat{k} \right] \mathrm{d}v, \tag{3.3}$$

where $\boldsymbol{r}_m$ is the location of the probe antenna reference location when acquiring the m-th measurement sample. As noted before $\boldsymbol{r}_m$ is required to lie somewhere in the observation region according to Figure 2.4 in order for the expansion in (3.2) to be valid. $\tilde{\boldsymbol{V}}_\mathrm{T}$ is the plane-wave spectrum of the transmitting AUT. Moreover, with respect to Figure 2.4 it may be noted that

$$\boldsymbol{r}_\mathrm{o} = \boldsymbol{r} - \boldsymbol{r}_\mathrm{O} = (\boldsymbol{r} - \boldsymbol{r}_m) + (\boldsymbol{r}_m - \boldsymbol{r}_\mathrm{O}) \tag{3.4}$$

and consequently, after interchanging the order of the integrals,

$$\begin{aligned} U_2(\boldsymbol{r}_m) = {} & \oiint \left[\iiint\limits_{V_2} -\frac{\boldsymbol{J}_2(\boldsymbol{r}-\boldsymbol{r}_m)}{I_2} \mathrm{e}^{-\mathrm{j}\boldsymbol{k}\cdot(\boldsymbol{r}-\boldsymbol{r}_m)} \, \mathrm{d}v \right] \mathrm{e}^{-\mathrm{j}\boldsymbol{k}\cdot(\boldsymbol{r}_m-\boldsymbol{r}_\mathrm{O})} \\ & \cdot T_L\left(kD, \hat{k}\cdot\hat{D}\right) \tilde{\boldsymbol{V}}_\mathrm{T}(\boldsymbol{k}) \, \mathrm{e}^{-\mathrm{j}\boldsymbol{k}\cdot\boldsymbol{r}_\mathrm{Q}} \, \mathrm{d}^2\hat{k} \\ = {} & \oiint \frac{4\pi}{\mathrm{j}kZ_\mathrm{F}} \frac{1}{I_2} \tilde{\boldsymbol{V}}_\mathrm{R}(-\boldsymbol{k}) \, \mathrm{e}^{-\mathrm{j}\boldsymbol{k}\cdot(\boldsymbol{r}_m-\boldsymbol{r}_\mathrm{O})} \cdot T_L\left(kD, \hat{k}\cdot\hat{D}\right) \tilde{\boldsymbol{V}}_\mathrm{T}(\boldsymbol{k}) \, \mathrm{e}^{-\mathrm{j}\boldsymbol{k}\cdot\boldsymbol{r}_\mathrm{Q}} \, \mathrm{d}^2\hat{k}, \end{aligned} \tag{3.5}$$

where $\tilde{\boldsymbol{V}}_\mathrm{R}(-\boldsymbol{k})$ is the plane-wave spectrum of the receiving probe antenna for incident plane waves and defined with respect to its reference location. The factor $\mathrm{e}^{-\mathrm{j}\boldsymbol{k}\cdot(\boldsymbol{r}_m-\boldsymbol{r}_\mathrm{O})}$ accounts for the phase shift between the center of the observation region $\boldsymbol{r}_\mathrm{O}$ and the measurement position $\boldsymbol{r}_m$.

In practice, it is difficult to measure voltages at high frequencies and it is thus common to work with power waves and scattering parameters instead [Pozar 2012, p. 178]. Moreover, if one is interested in determining not only the radiation pattern but also the antenna gain, it is beneficial to have a transmission equation that directly establishes a connection between power or gain-normalized representations of the AUT and the probe antenna.

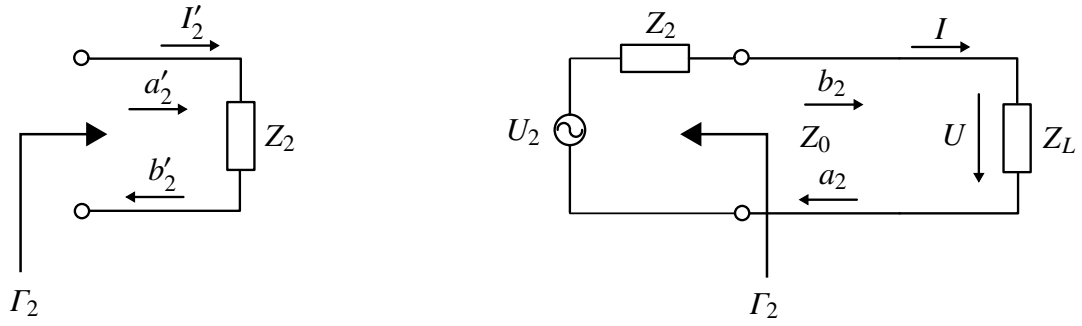

a) b)

Figure 3.1: Equivalent networks for antenna 2 (probe): a) Transmitting case, b) Receiving case

3.1.1 Gain-Normalized Transmission Equation

Consider the case of a receiving antenna 2 (probe) with no load impedance connected. In that case the open circuit receive voltage is given by (3.5), that is

$$U_2(\boldsymbol{r}_m) = \oiint \frac{4\pi}{\mathrm{j}kZ_\mathrm{F}} \frac{1}{I_2'} \tilde{\boldsymbol{V}}_\mathrm{R}(-\boldsymbol{k}) \cdot T_L\left(kD, \hat{k} \cdot \hat{D}\right) \tilde{\boldsymbol{V}}_\mathrm{T}(\boldsymbol{k}) \, \mathrm{d}^2\hat{k}, \tag{3.6}$$

where I_2' is the terminal current of the probe antenna 2 in transmit mode and for the convenience of a shorter notation it is assumed that $\boldsymbol{r}_m = \boldsymbol{r}_O$ as well as $\boldsymbol{r}_Q = 0$. With respect to the equivalent probe antenna network in Figure 3.1 a) and with the real reference impedance Z_0

$$I_2' = \frac{1}{\sqrt{Z_0}}\left(a_2' - b_2'\right) = \frac{1}{\sqrt{Z_0}} a_2'\left(1 - \Gamma_2\right) \tag{3.7}$$

holds, where

$$\Gamma_2 = \frac{Z_2 - Z_0}{Z_2 + Z_0} \tag{3.8}$$

is the input reflection coefficient of the probe antenna in the transmit case and Z_2 the corresponding input impedance. In the receive case as shown in Figure 3.1 b), the received power wave at the load Z_L is

$$b_2 = \frac{U + Z_0 I}{2\sqrt{Z_0}} = \frac{U_2}{2\sqrt{Z_0}} \frac{Z_L + Z_0}{Z_L + Z_2} \tag{3.9}$$

and for a matched load with $Z_L = Z_0$ one obtains

$$b_2 = \frac{U_2}{2\sqrt{Z_0}} \frac{2Z_0}{Z_0 + Z_2} = \frac{U_2}{2\sqrt{Z_0}}\left(1 - \Gamma_2\right). \tag{3.10}$$

With the input power wave at the (transmitting) AUT (antenna 1) a_1, the transmission equation can then be written as

$$\frac{b_2}{a_1} = S_{21} = \frac{1}{2} \oiint \frac{4\pi}{\mathrm{j}kZ_\mathrm{F}} \frac{\tilde{\boldsymbol{V}}_\mathrm{R}(-\boldsymbol{k})}{a_2'} \cdot T_L\left(kD, \hat{k} \cdot \hat{D}\right) \frac{\tilde{\boldsymbol{V}}_\mathrm{T}(\boldsymbol{k})}{a_1'} \, \mathrm{d}^2\hat{k}, \tag{3.11}$$

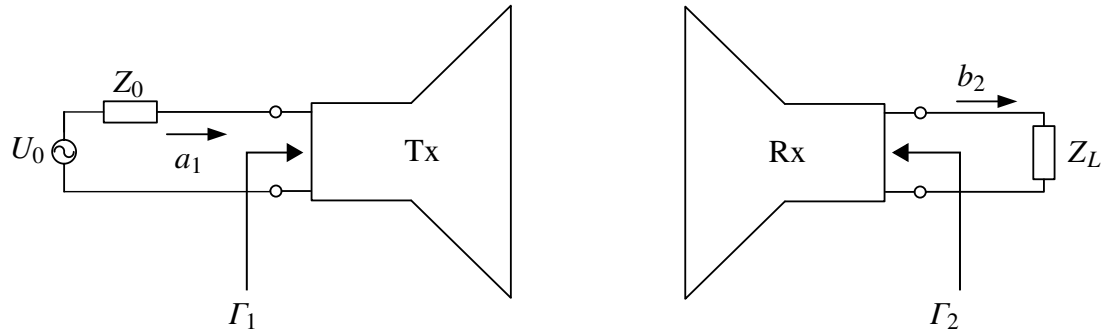

Figure 3.2: Signal flow between transmitting (Tx) antenna 1 and receiving (Rx) antenna 2 with a connected load Z_L.

where S_{21} is usually the measured quantity and it is assumed that also the generator is matched to the reference impedance Z_0. Additional mismatch correction factors can be considered if this is not the case and the gain has to be determined with very high accuracy (better than 0.5 dB) as described in, e.g., [Newell et al. 1988]. The signal flow between the transmitting and receiving antenna is shown in Figure 3.2.

Noting that the realized antenna gain is defined as

$$G(\boldsymbol{k}) = \lim_{r\to\infty} 4\pi r \frac{S(\boldsymbol{k})}{P_0} = 4\pi \frac{1}{2} \frac{\left|\tilde{V}(\boldsymbol{k})\right|^2}{Z_\mathrm{F}} \frac{2}{|a|^2}, \tag{3.12}$$

where

$$P_0 = \frac{1}{2}|a|^2 \tag{3.13}$$

is the offered input power, it makes sense to define the gain-normalized plane-wave spectrum as

$$\boldsymbol{W}(\boldsymbol{k}) = \sqrt{\frac{4\pi}{Z_\mathrm{F}}} \frac{\tilde{\boldsymbol{V}}(\boldsymbol{k})}{a}, \tag{3.14}$$

such that

$$|W(\boldsymbol{k})|^2 = G(\boldsymbol{k}). \tag{3.15}$$

As the realized gain is considered here, a possible mismatch due to the input reflection coefficient Γ is included in this definition. To determine the gain as defined in [IEEE 2014] (i.e., not including mismatch losses) a correction factor $\left(1 - |\Gamma|^2\right)$ can be taken into account. With the definition of the gain-normalized plane-wave spectrum, the transmission equation is written as

$$S_{21} = \oiint \frac{1}{\mathrm{j}2k} \boldsymbol{W}_\mathrm{R}(-\boldsymbol{k}) \cdot T_L\left(kD, \hat{k}\cdot\hat{D}\right) \boldsymbol{W}_\mathrm{T}(\boldsymbol{k})\, \mathrm{d}^2\hat{k}. \tag{3.16}$$

By using (3.16) to determine the gain-normalized radiation pattern $\boldsymbol{W}_\mathrm{T}(\boldsymbol{k})$ of the AUT, the influence of the probe antenna is correctly taken into account. However, evaluating the equation also requires knowledge about the (gain-normalized) probe pattern $\boldsymbol{W}_\mathrm{R}(\boldsymbol{k})$, which is typically acquired in a separate measurement or approximately known from simulation. As the probe pattern is usually not given in the same coordinate system as the AUT but in its own

local coordinate system, the rotation matrix $\overline{\mathbf{R}}$ is used for the transformation of the incident plane waves (propagating in direction $-\boldsymbol{k}$) from the AUT coordinate system into the (primed) probe coordinate system by

$$\boldsymbol{k}' = \overline{\mathbf{R}} \cdot \boldsymbol{k}. \tag{3.17}$$

To transform the probe pattern into the AUT coordinate system the inverse (i.e., the transposed) rotation matrix is used as

$$\boldsymbol{W}_{\mathrm{R}} = \overline{\mathbf{R}}^{\mathrm{T}} \cdot \boldsymbol{W}'_{\mathrm{R}}. \tag{3.18}$$

Consequently, the general transmission equation for a matched load (and arbitrary values of $\boldsymbol{r}_m$, $\boldsymbol{r}_O$ and $\boldsymbol{r}_Q$) becomes

$$S_{21} = \frac{1}{\mathrm{j}2k} \oiint \overline{\mathbf{R}}^{\mathrm{T}} \cdot \boldsymbol{W}'_{\mathrm{R}} \left(-\overline{\mathbf{R}} \cdot \boldsymbol{k}\right) \mathrm{e}^{-\mathrm{j}\boldsymbol{k}\cdot(\boldsymbol{r}_m - \boldsymbol{r}_{\mathrm{O}})} \cdot T_L \left(kD, \hat{k} \cdot \hat{D}\right) \boldsymbol{W}_{\mathrm{T}}(\boldsymbol{k}) \, \mathrm{e}^{-\mathrm{j}\boldsymbol{k}\cdot\boldsymbol{r}_{\mathrm{Q}}} \, \mathrm{d}^2\hat{k}. \tag{3.19}$$

As the probe antenna may be differently oriented at every measurement sample location, also the probe rotation matrix will generally be different for every sample location. Knowing the individual locations and rotation angles as well as the probe pattern, the gain-normalized radiation pattern of the AUT can be determined by measuring the transmission factor S_{21} with respect to the input terminals of the AUT and the probe antenna.

3.1.2 The Limiting Far-Field Case - Friis Equation

In the far-field limit as $kD \to \infty$ the translation operator T_L was shown in Section 2.4.4 to reduce to a single plane wave in the direction of $\boldsymbol{D}$, which may be conveniently expressed in terms of a Dirac delta with respect to $\hat{k}$. For this case, and by setting $\boldsymbol{r}_m = \boldsymbol{r}_{\mathrm{O}}$ as well as $\boldsymbol{r}_{\mathrm{Q}} = 0$ (i.e., the origin of the coordinate system is placed at the reference position of the AUT), the transmission equation (3.16) reduces to

$$S_{21} = \frac{1}{\mathrm{j}2k} \boldsymbol{W}_{\mathrm{R}}(-\boldsymbol{k}_D) \cdot \boldsymbol{W}_{\mathrm{T}}(\boldsymbol{k}_D) \frac{\mathrm{e}^{-\mathrm{j}kD}}{D}. \tag{3.20}$$

Recalling the definition of $\boldsymbol{W}$, i.e., $|W|^2 = G$ the antenna gain, and assuming two perfectly aligned antennas with matching polarization, this can be written in terms of the received power P_{R} and the input power P_0 as

$$\frac{P_{\mathrm{R}}}{P_0} = |S_{21}|^2 = |W_{\mathrm{R}}|^2 |W_{\mathrm{T}}|^2 \left(\frac{1}{2kD}\right)^2 = G_{\mathrm{R}} G_{\mathrm{T}} \left(\frac{\lambda}{4\pi D}\right)^2 = A_R A_T \frac{1}{\lambda^2 D^2}, \tag{3.21}$$

which is the well-known Friis transmission equation [Friis 1946] with $A_{R/T}$ the effective area of the receiving/transmitting antenna. In this regard, the transmission equations (3.16) can be seen as generalization of the Friis equation for a all propagating plane waves with wave vector $\boldsymbol{k}$ in all angular directions (the plane-wave spectrum), which is thus also valid in the near field.

3.2 Solving the Inverse Source Problem

In order to solve the inverse source problem for determining the far-field radiation pattern, a linear system of equations shall be set up to solve the problem numerically. As already discussed

in Section 2.5, by setting up a normal equation and solving the corresponding least-squares problem, the ill-posedness of the inverse source problem can be overcome. Choosing an iterative solver such as the GMRES helps to solve the (possibly ill-conditioned) matrix equation by employing its regularization properties. To this end, the near-field transmission equation (3.19) needs to be discretized and the k-space integral has to be solved numerically.

3.2.1 Discretization of the Plane-Wave Spectra

The plane-wave spectra as introduced before and given by (2.52) and (2.53) are the k-space representation of compactly supported sources in the spatial domain. Assuming that all source contributions are confined to a sphere with radius a, it was shown by Bucci and Franceschetti [1987] that the spatial frequency bandwidth N of their radiated (or similarly their scattered) fields is slightly larger than $N \approx ka$ and that this value corresponds to the degrees of freedom of the radiated field [Bucci and Franceschetti 1989]. The same result can also be obtained by considering the modal spectrum of the plane-wave spectrum according to (2.58) by noting that the spherical wave functions of order n decrease exponentially for $n > ka$ [J. E. Hansen 1988, p. 17]. The empirical formula for the order L of the FMM translation operator is a consequence of this. As a result, one can conclude that the spatial frequency bandwidth of the plane-wave spectra in (3.19) is about $L/2$ whereas the translation operator is of order L. Consequently, to represent the plane-wave spectra on a sphere and employing equiangular spherical coordinates, about $N_\varphi = L$ samples on the interval $\varphi = [0, 2\pi)$ and $N_\vartheta = \lceil L/2 \rceil$ samples[1] on the interval $\vartheta = (0, \pi)$ are needed. This corresponds to a maximum sampling distance of about $\lambda/2$ on the minimum sphere with radius $r = a$. However, it must be noted that due to the spherical coordinate system the number of samples at the pole region is much larger and the field is essentially oversampled in that region. This drawback is usually accepted, as an efficient numerical evaluation of the transmission equation (in particular of the k-space integral) is much easier to achieve for the standard spherical coordinates compared to any non-redundant grid on the sphere.

3.2.2 Numerical Evaluation of the k-space Integral

In the following it is again assumed that $\boldsymbol{r}_\mathrm{Q} = 0$ and $\boldsymbol{r}_m = \boldsymbol{r}_\mathrm{O}$ in order to use the sampling criteria for the plane-wave spectra stated in the previous section. The transmission equation (3.16) may then be written in a standard spherical coordinate system as

$$S_{21} = \frac{1}{\mathrm{j}2k} \int_0^{2\pi} \int_0^{\pi} \boldsymbol{W}_\mathrm{R}(-\boldsymbol{k}) \cdot \boldsymbol{T}_L(\boldsymbol{k}, \boldsymbol{D})\, \boldsymbol{W}_\mathrm{T}(\boldsymbol{k}) \sin\vartheta \,\mathrm{d}\vartheta \,\mathrm{d}\varphi, \tag{3.22}$$

where $\boldsymbol{k} = k\left(\sin\vartheta\cos\varphi\boldsymbol{e}_x + \sin\vartheta\sin\varphi\boldsymbol{e}_y + \cos\vartheta\boldsymbol{e}_z\right)$. The number of samples for the numerical integration must be chosen according to the total spatial frequency bandwidth of the integrand, where one has to keep in mind that, due to the discretization, the spectra are repeated

[1] $\lceil x \rceil$ denotes the next larger integer value to x.

periodically with the sampling frequency. The latter must be chosen such that no aliasing effects occur within the bandwidth of the source and probe spectra ($L/2$).

Trapezoidal rule in φ

The integrand in φ is periodic and approximately band-limited to $2L$, thus the integration can be efficiently performed by a trapezoidal rule with $N_\varphi \geq 2L + 1$ equidistant samples [J. E. Hansen 1988, p. 372]. The nodes and weights in φ are

$$\varphi_i = \frac{2\pi}{N_\varphi}(i-1) \quad \text{and} \quad w_{\varphi,i} = \frac{2\pi}{N_\varphi} \quad \text{where} \quad i = 1, 2, \ldots, N_\varphi \tag{3.23}$$

and consequently

$$\int_0^{2\pi} \boldsymbol{W}_\mathrm{R}(-\boldsymbol{k}) \cdot T_L(\boldsymbol{k}, \boldsymbol{D})\, \boldsymbol{W}_\mathrm{T}(\boldsymbol{k})\, \mathrm{d}\varphi = \sum_{i=1}^{N_\varphi} \boldsymbol{W}_\mathrm{R}(-\boldsymbol{k}_i) \cdot T_L(\boldsymbol{k}_i, \boldsymbol{D})\, \boldsymbol{W}_\mathrm{T}(\boldsymbol{k}_i)\, w_{\varphi,i}. \tag{3.24}$$

Gauss-Legendre quadrature in ϑ

For the integration in ϑ it is common to use the substitution $u = \cos\vartheta$ and an L-point Gauss-Legendre quadrature rule for solving

$$\int_0^{\pi} \boldsymbol{W}_\mathrm{R}(-\boldsymbol{k}) \cdot T_L(\boldsymbol{k}, \boldsymbol{D})\, \boldsymbol{W}_\mathrm{T}(\boldsymbol{k}) \sin\vartheta\, \mathrm{d}\vartheta = \int_{-1}^{1} \boldsymbol{W}_\mathrm{R}(-\boldsymbol{k}) \cdot T_L(\boldsymbol{k}_i, \boldsymbol{D})\, \boldsymbol{W}_\mathrm{T}(\boldsymbol{k})\, \mathrm{d}u, \tag{3.25}$$

which, again, has a band-limited integrand with $2L$. In this case the $N_\vartheta = L + 1$ nodes ϑ_i are the i-th root of the (monic) Legendre polynomial $P_L(u)$ and the weights are given by [Abramowitz and Stegun 1972, p. 887]

$$w_{\vartheta_i} = \frac{2}{(1 - x_i^2)[P_n'(u)]^2}. \tag{3.26}$$

Efficient routines for computing the nodes and weights can be found in [Press et al. 2007, p. 182-184]. The integral in ϑ is then evaluated as

$$\int_0^{\pi} \boldsymbol{W}_\mathrm{R}(-\boldsymbol{k}) \cdot T_L(\boldsymbol{k}, \boldsymbol{D})\, \boldsymbol{W}_\mathrm{T}(\boldsymbol{k}) \sin\vartheta\, \mathrm{d}\vartheta = \sum_{i=1}^{N_\vartheta} \boldsymbol{W}_\mathrm{R}(-\boldsymbol{k}_i) \cdot T_L(\boldsymbol{k}_i, \boldsymbol{D})\, \boldsymbol{W}_\mathrm{T}(\boldsymbol{k}_i)\, w_{\vartheta,i}. \tag{3.27}$$

Trapezoidal rule in ϑ

As it may be advantageous to also have equidistant (equiangular) samples along ϑ, for example to perform global interpolations along that dimension by means of the FFT, one can also work with a trapezoidal rule in ϑ by evaluating the periodic integral

$$\frac{1}{2}\int_{-\pi}^{\pi} \boldsymbol{W}_\mathrm{R}(-\boldsymbol{k}) \cdot T_L(\boldsymbol{k}, \boldsymbol{D})\, \boldsymbol{W}_\mathrm{T}(\boldsymbol{k}) \,|\sin\vartheta|\, \mathrm{d}\vartheta = \int_0^{\pi} \boldsymbol{W}_\mathrm{R}(-\boldsymbol{k}) \cdot T_L(\boldsymbol{k}, \boldsymbol{D})\, \boldsymbol{W}_\mathrm{T}(\boldsymbol{k}) \sin\vartheta\, \mathrm{d}\vartheta. \tag{3.28}$$

As pointed out by Sarvas [2003], the problem is now that $|\sin\vartheta|$ is not band-limited. However, if one is only interested in the result of the integration up to the spatial frequency bandwidth $L/2$ (the bandwidth of the receive spectrum), one may use a truncated Fourier series

$$|\sin\vartheta|_{2L} = \sum_{m=-2L}^{2L} a_m \mathrm{e}^{-\mathrm{j}m\vartheta} \qquad \text{where} \qquad a_m = \begin{cases} \frac{2}{\pi}\frac{1}{1-m^2} & m \text{ even} \\ 0 & m \text{ odd} \end{cases} \tag{3.29}$$

to compute the integral. The nodes and weights are then given by

$$\vartheta_i = \frac{\pi}{N_\vartheta + 1} i \quad \text{and} \quad w_{\vartheta,i} = |\sin\vartheta|_{2L}^{(i)} \frac{\pi}{N_\vartheta} \quad \text{where} \quad i = 1, 2, \ldots, N_\vartheta, \tag{3.30}$$

where this choice of the sampling points ensures that there are no redundant samples at the poles while the interval is still periodic over 2π. The sampling rate of the terms in the integral must be increased compared to the Gauss-Legendre case in (3.25), as the spectral content of the integrand in (3.28) is increased due to the truncated $|\sin\vartheta|$ term of order $2L$, and aliasing effects have to be avoided for the relevant spectral components of the probe spectrum, i.e., up to $L/2$ [Sarvas 2003]. To achieve this, the procedure is as follows (with the superscript sampling rates corresponding to the 2π-periodic case):

1. Compute $T_L^{(4L)}$ up to order L but with sampling rate $4L$.
2. Interpolate $\boldsymbol{W}_\mathrm{T}^{(4L)}$ (bandwidth $L/2$) to have $4L$ sampling rate.
3. Multiply $T_L^{(4L)}$ and $\boldsymbol{W}_\mathrm{T}^{(4L)}$ to obtain the receive spectrum with bandwidth $3L/2$.
4. Multiply the receive spectrum with the band-limited $|\sin\vartheta|_{2L}^{(4L)}$ term, which results in a bandwidth of $7L/4$. Due to the chosen sampling rate of $4L$, aliasing errors occur, but only for spatial frequencies larger than $L/2$.
5. Filter and down-sample the result to the bandwidth of $L/2$ to obtain
$$\{T_L^{(4L)}(\boldsymbol{k}_i, \boldsymbol{D})\, \boldsymbol{W}_\mathrm{T}^{(4L)}(\boldsymbol{k}_i)\, |\sin\vartheta|_{2L}^{(4L)}\}_{L/2}^{(L)}.$$
6. Multiply the filtered term with the probe receive spectrum and perform the integration.

By taking the samples in φ on the interval $[0, 2\pi)$, it is sufficient to store the samples in ϑ on the interval $(0, \pi)$ and one obtains the integral in ϑ as

$$\int_0^\pi \boldsymbol{W}_\mathrm{R}(-\boldsymbol{k}) \cdot T_L(\boldsymbol{k}, \boldsymbol{D})\, \boldsymbol{W}_\mathrm{T}(\boldsymbol{k}) \sin\vartheta \,\mathrm{d}\vartheta = \sum_{i=1}^{N_\vartheta} \boldsymbol{W}_\mathrm{R}(-\boldsymbol{k}_i) \cdot \left\{ T_L^{(2L)}(\boldsymbol{k}_i, \boldsymbol{D})\, \boldsymbol{W}_\mathrm{T}^{(2L)}(\boldsymbol{k}_i)\, w_{\vartheta_i}^{(2L)} \right\}_{L/2}^{(N_\vartheta)} \tag{3.31}$$

where $\{\ldots\}_{L/2}^{(N_\vartheta)}$ denotes the down-sampling and filtering to bandwidth $L/2$, the superscript sampling rates are with respect to the interval $(0, \pi)$ and $N_\vartheta = \lceil L/2 \rceil$.

Trapezoidal rule in ϑ and φ with filtering

Employing the filter and down-sample procedure for the trapezoidal rule in ϑ also for the integration in φ, the evaluation procedure for the 2D integral in (3.22) becomes

$$\begin{aligned}\int_0^{2\pi}\int_0^{\pi} \boldsymbol{W}_{\mathrm{R}}(-\boldsymbol{k}) \cdot T_L(\boldsymbol{k},\boldsymbol{D})\, \boldsymbol{W}_{\mathrm{T}}(\boldsymbol{k}) \sin\vartheta \,\mathrm{d}\vartheta \,\mathrm{d}\varphi \qquad (3.32)\\ = \sum_{i=1}^{N_\vartheta}\sum_{j=1}^{N_\varphi} \boldsymbol{W}_{\mathrm{R}}(-\boldsymbol{k}_{ij}) \cdot \left\{ T_L^{(2L,2L)}(\boldsymbol{k}_{ij},\boldsymbol{D})\, \boldsymbol{W}_{\mathrm{T}}^{(2L,2L)}(\boldsymbol{k}_{ij})\, w_{\vartheta_i}^{(2L)} w_{\varphi_j}^{(2L)} \right\}_{L/2,L}^{(N_\vartheta,N_\varphi)},\end{aligned}$$

where the sampling rates are given by the superscripts (N_ϑ, N_φ) and $\{\ldots\}_{L/2,L}^{(N_\vartheta,N_\varphi)}$ denotes the down-sampling and filtering to the bandwidth $L/2$ and L in ϑ and φ, respectively. The number of samples are $N_\vartheta = \lceil L/2 \rceil$ on the interval $(0,\pi)$ and $N_\varphi = 2L$ on the interval $[0,2\pi)$.

3.2.3 Choice of Basis Functions

The unknown quantity considered so far is the plane-wave spectrum $\boldsymbol{W}_{\mathrm{T}}(\boldsymbol{k})$ of the AUT, where for each angular direction of $\boldsymbol{k}$ the outgoing plane wave is commonly described in spherical components by its ϑ and φ component, i.e.,

$$\boldsymbol{W}_{\mathrm{T}}(\boldsymbol{k}_i) = W_{\mathrm{T}}^{\vartheta}(\boldsymbol{k}_i)\, \boldsymbol{e}_\vartheta + W_{\mathrm{T}}^{\varphi}(\boldsymbol{k}_i)\, \boldsymbol{e}_\varphi. \qquad (3.33)$$

If one is interested in determining the far-field radiation pattern, it appears to be a natural choice to solve directly for the corresponding plane-wave coefficients of the discretized spectrum as no additional computation is required. Using propagating plane-wave spectra in the field of NFFFTs was introduced and extensively studied in [Schmidt and Eibert 2009; Schmidt et al. 2008]. With respect to the scattering problems considered in the next chapter, it can already be noted that it is possible to extend the plane-wave spectrum to the description of the scattering matrix with its four components S_{VV}, S_{HV}, S_{HH} and S_{VH}. However, due to the chosen spherical sampling grid of the plane-wave spectrum, the pole regions are densely oversampled and the total number of unknown coefficients is relatively large. The redundancy introduced in this way typically leads to a larger condition number of the system matrix compared to a solution based on spherical wave functions [T. B. Hansen et al. 2019]. Due to the orthogonality of the underlying spherical multipoles, choosing the spherical-wave functions as given by $\boldsymbol{K}_{smn}(\vartheta,\varphi)$ in Appendix A.2 and discretizing the plane-wave spectra as

$$\boldsymbol{W}_{\mathrm{T}}(\boldsymbol{k}_i) = \frac{\sqrt{4\pi}}{a} \sum_{s=1}^{2}\sum_{n=1}^{N}\sum_{m=-n}^{n} \tilde{q}_{smn} \boldsymbol{K}_{smn}(\vartheta_i,\varphi_i) \qquad (3.34)$$

usually leads to less unknown coefficients and a better conditioned matrix, provided the maximum multipole order N is chosen appropriately according to the size of the source region. As mentioned before, a good choice for a spherical source region with diameter d is given by $N = L/2$, where L is determined according to (2.45). If the available computer memory is not

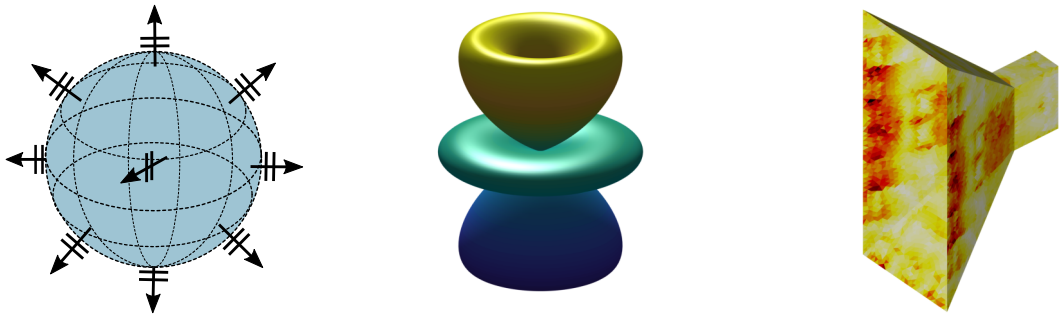

a) b) c)

Figure 3.3: Examples of different source representations: a) Plane-wave spectrum, b) Spherical Multipoles, c) Equivalent surface current densities, defined with RWG basis functions on a triangular grid

a limiting constraint, one will typically precompute the required spherical-wave functions in a preprocessing step to allow for a rapid evaluation of the transmission equation.

Beside these spectrally defined basis functions as depicted in Figure 3.3 a) and b), it is as well possible to work with spatially localized sources, most prominently with equivalent electric and magnetic surface current densities as defined in (2.29). In the area of NFFFTs this was first introduced by Petre and Sarkar [1992], employing planar reconstruction surfaces in front of the AUT and magnetic current densities only. More elaborated schemes work with triangular surface meshes that are conformal to the antenna structure (see Figure 3.3) in order to benefit from the localization of the sources [Eibert and Schmidt 2009]. Using localized surface current densities reduces the effect of truncation errors for measurement surfaces that cover only a limited angular range around the AUT, inherently performs a spatial filtering of parasitic reflections (coming from the mounting structure for example) and enables advanced diagnostic capabilities. Most commonly, the low-order divergence-conforming Rao-Wilton-Glisson (RWG) basis functions $\boldsymbol{\beta}(\boldsymbol{r})$ defined on the triangular patches of the surface mesh are used [Rao et al. 1982]. Their definition is given in Appendix A.3. The electric and magnetic surface current densities on a triangular patch are discretized as

$$\boldsymbol{J}_A(\boldsymbol{r}) = \sum_p J_p \boldsymbol{\beta}_p(\boldsymbol{r}') \quad \text{and} \quad \boldsymbol{M}_A(\boldsymbol{r}) = \sum_q M_q \boldsymbol{\beta}_q(\boldsymbol{r}'), \tag{3.35}$$

where p, q are the corresponding edges. The expansion into the plane-wave spectra is then given by

$$\tilde{\boldsymbol{J}}_{\mathrm{T}}(\boldsymbol{k}_i) = -\mathrm{j}\frac{kZ_{\mathrm{F}}}{4\pi}\left(\bar{\mathbf{I}} - \hat{k}\hat{k}\right) \cdot \sum_p J_p \iint_A \boldsymbol{\beta}_p(\boldsymbol{r}')\, \mathrm{e}^{\mathrm{j}\boldsymbol{k}_i\cdot\boldsymbol{r}'}\, da' \tag{3.36}$$

and

$$\tilde{\boldsymbol{M}}_{\mathrm{T}}(\boldsymbol{k}_i) = \mathrm{j}\frac{1}{4\pi}\boldsymbol{k}_i \times \sum_q M_q \iint_A \boldsymbol{\beta}_q(\boldsymbol{r}')\, \mathrm{e}^{\mathrm{j}\boldsymbol{k}_i\cdot\boldsymbol{r}'}\, da', \tag{3.37}$$

where A is the surface of the triangular patch. With the Fourier transform of the RWG basis functions

$$\tilde{\boldsymbol{\beta}}(\boldsymbol{k}_i) = \iint_A \boldsymbol{\beta}(\boldsymbol{r}')\, \mathrm{e}^{\mathrm{j}\boldsymbol{k}_i \cdot \boldsymbol{r}'} da' \tag{3.38}$$

this results in

$$\boldsymbol{W}_{\mathrm{T}}(\boldsymbol{k}_i) = \mathrm{j}k\sqrt{\frac{Z_{\mathrm{F}}}{4\pi}} \left[\sum_q M'_q \hat{k} \times \tilde{\boldsymbol{\beta}}_q(\boldsymbol{k}_i) - \left(\bar{\mathbf{I}} - \hat{k}\hat{k}\right) \sum_p J_p \tilde{\boldsymbol{\beta}}_p(\boldsymbol{k}_i) \right] \tag{3.39}$$

where the magnetic currents have been scaled by $1/Z_{\mathrm{F}}$ (that is, $M'_q = M_q/Z_{\mathrm{F}}$) to be on the same order of magnitude as the electric currents. The integration over the surface A of the triangular patch can be achieved by numerical quadrature (see, e.g., [Pinder 1999, p. 109]), where a common choice is to work with a 7-point rule and the edge length of the triangle is typically required to be less than $\lambda/10$ with λ being the free-space wavelength [Volakis and Sertel 2012, p. 269]. A memory efficient way to store the plane-wave spectra of the basis functions is achieved by expanding them again in spherical multipoles [Eibert 2005].

As a consequence of the surface equivalence theorem an infinite number of solutions for equivalent surface current densities defined on the mesh that encloses the AUT is possible. In particular, it is possible to work with electric or magnetic current densities only, with electric and magnetic current densities or with directive current elements such as the Huygens radiator (a combination of electric and magnetic currents) or currents with complex source locations [Eibert et al. 2016; Quijano and Vecchi 2010]. By enforcing a zero-field condition inside a closed mesh, it is possible to obtain the Love currents that carry a direct relation to the tangential field components, thus providing more information for diagnostic purposes, but do not seem to be beneficial for the solution of the inverse source problem [Kornprobst et al. 2019]. In most cases, working with electric and magnetic surface current densities is a robust choice and is thus the only (spatial) basis considered in this thesis.

In either case, by using equivalent surface current densities the number of unknowns in the linear system of equations will be greatly increased compared to using propagating plane waves or spherical-wave functions. Consequently, the problem may become under-determined. Due to this fact and depending on the "physical" choice of unknowns (i.e., electric or magnetic currents only, electric and magnetic currents, Love currents, etc.) the system matrix of the resulting linear system of equations will usually be worse conditioned [T. B. Hansen et al. 2019].

3.2.4 Hierarchical Schemes for the Solution of Large Problems

As mentioned before, it is desirable to solve the discretized inverse source problem iteratively in order to avoid an explicit matrix generation. Instead only matrix-vector products have to be evaluated repeatedly in every solver iteration. With the factorized and diagonal transmission equation in k-space derived in Section 3.1 the computational effort is already reduced compared to a direct evaluation of the corresponding spatial equation as given by (3.1). This is achieved by grouping all sources and computing the common plane-wave spectrum, followed by a multiplication with the diagonal translation operator and finally testing the incident plane-wave

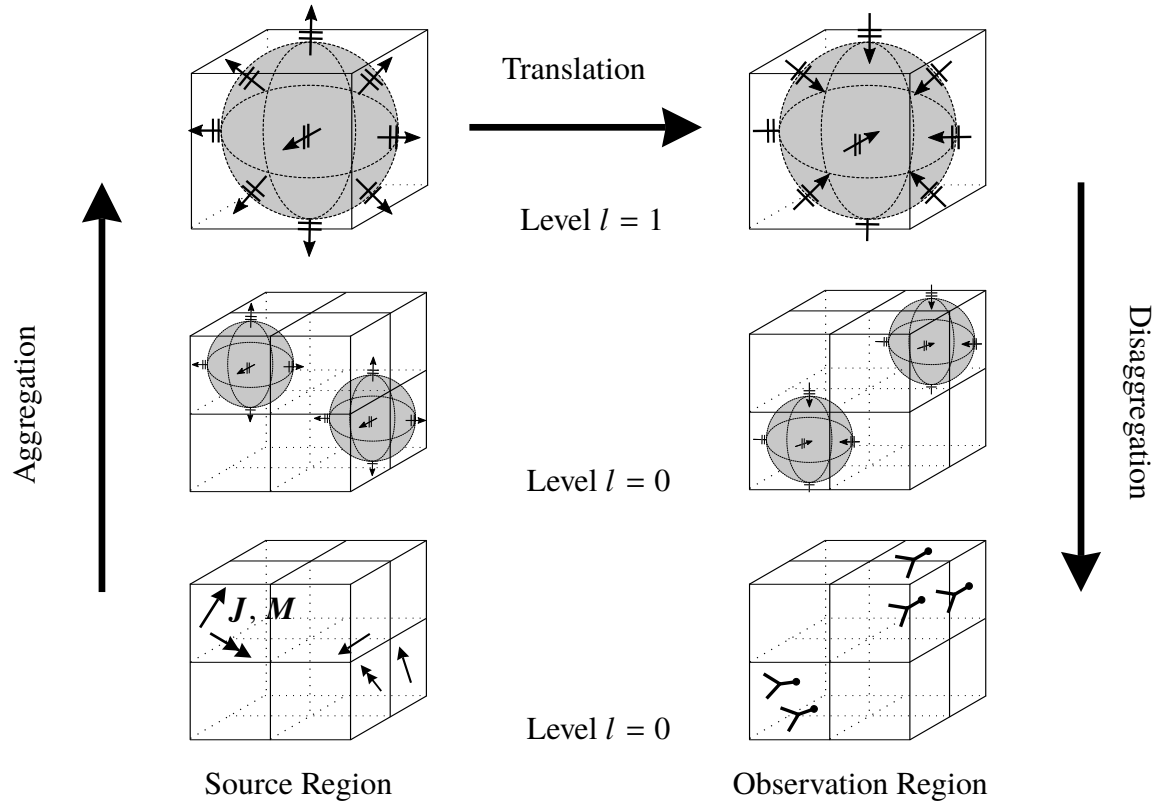

Figure 3.4: MLFMM principle: The source and observation regions are subdivided hierarchically and the source and probe spectra are evaluated with respect to small boxes. Aggregation means interpolation and summation of the child box spectra. Disaggregation is the reversed operation.

spectrum at the receiver location with the probe pattern. In this respect, the rows of the system matrix are not explicitly formed but computed on the fly. However, assuming the number of unknowns N corresponds directly to the degrees of freedom of the radiated field and the number of measurement samples has been chosen accordingly, the computation and memory complexity of this approach with respect to the number of unknowns N is still $O\left(N^2\right)$ [Schmidt et al. 2008]. In terms of the size of the source region with radius a, it was noted before that the number of coefficients in the plane-wave spectrum is $N \propto (ka)^2$. Consequently, the complexity is $O\left((ka)^4\right)$. Using the principles of the MLFMM it is possible to reduce the complexity to $O\left(N \log N\right)$ by employing a hierarchical scheme with interpolations and anterpolations[2] [Schmidt and Eibert 2009]. The idea is depicted in Figure 3.4. The source and observation regions are hierarchically subdivided into boxes using an octree structure. On the finest source level $l = 0$ (having the smallest boxes), the plane-wave spectra are computed with respect to the source contributions in that particular (sub-)box. When working with a surface mesh of an AUT, only the boxes intersecting the antenna structure are needed as they include all source contributions. In general, if one is interested in the outward propagating waves, only the outer sub-boxes of the octree are needed. On average, the number of boxes will thus increase by a

[2]The adjoint operation to interpolation.

factor of 4 when going from level $l+1$ to the next finer level l. At the same time, as the source region of a box on level l has a radius a_l that is only one half compared to the next higher level $l+1$, i.e., $a_l = a_{l+1}/2$, the number of plane-wave samples to represent the spectrum on level l is $N_l = N_{l+1}/4$. In an aggregation step, all plane-wave spectra $\boldsymbol{V}_p^l(\boldsymbol{k})$ of the boxes on level l are interpolated to the sampling rate of level $l+1$, shifted to the center of the common parent box $\boldsymbol{r}_q^{l+1}$ on level $l+1$ and summed up, that is

$$\boldsymbol{V}_q^{l+1}(\boldsymbol{k}) = \sum_p \tilde{\boldsymbol{V}}_p^l\left(\boldsymbol{k}^{(l+1)}\right) \mathrm{e}^{-\mathrm{j}\boldsymbol{k}\cdot\left(\boldsymbol{r}_q^{l+1}-\boldsymbol{r}_p^l\right)} \tag{3.40}$$

where $\boldsymbol{r}_p^l$ is the center position of box p on level l and $\tilde{\boldsymbol{V}}_p^l\left(\boldsymbol{k}^{(l+1)}\right)$ is the interpolated spectrum corresponding to that box. The disaggregation steps involve the reversed operations, i.e., shifting to the sub-box center and interpolation to a coarser grid (that is low-pass filtering), called anterpolation [Chew et al. 2001, p. 59].

For performing the inter- and anterpolations it is common to work with a fixed-point local interpolation which has $O(N)$ complexity but generally requires some oversampling of the plane-wave spectra for sufficient accuracy. Frequently, Lagrange interpolation polynomials of degree K are used, which fulfill the given function exactly in K sample points [Olver et al. 2010, p. 75]. As there is no specific requirement on the location of the sample points, this interpolation scheme can work directly on a Gauss-Legendre grid employed for the quadrature in ϑ. If an equidistant sampling in combination with a trapezoidal integration rule is used in ϑ and φ (see Section 3.2.2), it is as well possible to work with a Fourier transform based global interpolation, which is theoretically exact for band-limited functions [Sarvas 2003]. To this end, the Fourier transform of the plane-wave spectra is zero padded to achieve the desired higher sampling rate after performing the inverse Fourier transform. Computing the forward and inverse Fourier transform can be done very efficiently in terms of the FFT using the FFTW implementation [Frigo and Johnson 2005]. The required operations for a one-dimensional (1D) interpolation are given in Appendix A.4. Using this global interpolation, the complexity is $O(N \log N)$ but the overall computation time may still be faster than the corresponding local interpolation with oversampling. If not stated otherwise, the global interpolation is used for all the computations presented in this thesis.

As a consequence of the increased number of boxes on a finer level, where all corresponding plane-wave spectra have a reduced sampling rate, the complexity of each aggregation and disaggregation step stays constant for each level. The total number of levels depends on the size of the source (or observation) region and will approximately increase by one if the size is doubled, leading to $\log N$ levels. Thus, for a fixed point local interpolation the overall complexity is about $O(N \log N)$ and for the global FFT accelerated interpolation it is about $O\left(N \log^2 N\right)$. However, it must be noted that these are merely idealized values for well distributed source and observation points and the overall computation time will strongly depend on the particular problem configuration. Moreover, the translations as indicated in Figure 3.4 are not necessarily always on the highest (coarsest) level. As it is required by the FMM that source and observation region are well separated, it may be necessary to create translations on finer levels. While this increases the overall complexity it still allows one to efficiently process measurement samples that are located very close to the antenna. In fact, for the case of widely

distributed near-field samples it may be beneficial to perform translations on very different levels in order to reduce the computational effort of (dis-)aggregating from or to a common top level.

For solving one of the normal equations introduced in Section 2.5.2 not only the discretized forward operator (i.e., the matrix $\mathbf{A}$) has to be evaluated, but also the adjoint operator $\mathbf{A}^{\mathrm{H}}$. This is efficiently done by traversing the MLFMM trees in the reversed direction and taking complex conjugate quantities. The complex conjugate probe patterns are weighted by the measurement values and aggregated up to the translation level in the octree. The adjoint translation operator corresponds to the complex conjugate of the forward case. If sufficient computer memory is available one will usually try to precompute one of the two and take the complex conjugate when needed. In the source tree, the plane-wave spectra are finally disaggregated to the level on which the equivalent sources have been defined.

3.2.5 Measurement sample acquisition

To set up a linear system of equations that determines the radiation pattern completely (i.e., in all angular directions), the number of non-redundant measurement samples in the right-hand side vector has to be larger or equal to the degrees of freedom in the radiated field. As already discussed in Section 3.2.1, this leads to the requirement of a $\lambda/2$ sampling on the minimum sphere enclosing the radiating structure. Since the actual measurement surface will be separated from the AUT by at least a few wavelengths (to ensure no multiple interactions), the sampling distance can be chosen somewhat larger, of course depending on the actual measurement distance. In general, the required (non-redundant) sampling distance can thus be found by projecting the $\lambda/2$ sampling from the minimum sphere onto the measurement surface as, for example, demonstrated by Qureshi et al. [2013]. However, it must be noted that the distribution of measurement samples does not have to be regular (that is equidistant) in any dimension and the samples do not have to lie on a smooth surface. In fact, as a consequence of the plane-wave expansion and MLFMM principles, completely irregularly distributed samples can still be handled very efficiently. Nonetheless, for a full 3D solution of the AUT pattern, the radiated field has to be sampled completely around the antenna.

If measurement samples are only obtained for a limited angular range with respect to the minimum sphere of the AUT, it is still possible to obtain a correct solution for the radiation pattern. However, this solution will also be limited to a certain angular range as one enforces the solution to yield the measured values only in the measurement region. Outside this valid angular range, the far-field solution can assume more or less arbitrary values. The exact valid angular range for such non-closed measurement surfaces is hard to predict as it depends on the particular AUT, the measurement distance, the probe antenna and the type of equivalent sources that are employed (i.e., plane waves, spherical multipoles, surface current densities, ...). In most cases, one tries to capture all relevant field contributions by enlarging the measurement surface (e.g., in planar measurements) until the magnitude of the field has dropped by about $-40\,\mathrm{dB}$ to $-50\,\mathrm{dB}$.

While the location of the measurement samples does not have to follow a specified grid, their location with respect to the AUT as well as the orientation of the probe antenna have to be known accurately in order to setup the correct forward operator. An extensive study on the influence of probe position and orientation errors can be found in [Qureshi 2013]. In

general, and as long as randomly distributed errors are concerned, it can be assumed that all uncertainties of the probe position and orientation contribute to the overall noise level of the measurement. Other noise contributions in the measured (near-) field data are mainly due to parasitic echo contributions, undesired multiple interactions between the AUT and the probe, as well as thermal phase drifts and (to some extent) random noise introduced by the measurement equipment.

3.3 Test and Application Examples

The algorithm described in the previous section to determine the radiation pattern and gain of an antenna under test has been successfully implemented in the fast irregular antenna field transformation algorithm (FIAFTA), developed at the Technical University of Munich (TUM) and continuously improved over the past years (see, e.g., [Eibert et al. 2015; Neitz and Eibert 2017; Schmidt and Eibert 2009]). The following application examples are given to demonstrate its accuracy and show some of the key features that will also be used for the scattering problems in the upcoming chapters. The employed synthetic test data was obtained by either using numerical field computations based on a set of independent elementary dipole radiators [Schmidt et al. 2011], or by method of moments (MoM)-based simulations using the FEKO simulation software [Altair Engineering, Inc. 2019]. If not stated differently, the far-field error is defined to give the relative magnitude error with respect to the maximum of the reference and is commonly given in dB, that is

$$\Delta E_{\vartheta,\varphi}(\vartheta,\varphi) = 20\log_{10}\left(\frac{|E_{\vartheta,\varphi}(\vartheta,\varphi) - E^{\mathrm{ref}}_{\vartheta,\varphi}(\vartheta,\varphi)|}{\max_{\vartheta,\varphi}\left\{E^{\mathrm{ref}}_{\mathrm{abs}}(\vartheta,\varphi)\right\}}\right), \tag{3.41}$$

where $E_{\vartheta,\varphi}$ and $E^{\mathrm{ref}}_{\vartheta,\varphi}$ are the magnitudes of one polarization (usually the ϑ- or φ-component) of the computed electric field and the reference data, respectively, and

$$E^{\mathrm{ref}}_{\mathrm{abs}}(\vartheta,\varphi) = \sqrt{E^2_{\vartheta}(\vartheta,\varphi) + E^2_{\varphi}(\vartheta,\varphi)}. \tag{3.42}$$

The solutions to all examples have been computed by using the previously introduced iterative GMRES solver to minimize the residual error of the NE or NR normal equation (see Section 2.5.2). To obtain a regularized solution, the solver is usually stopped if the relative residual error is below a predefined threshold or the convergence rate (i.e., the relative decrease of the residual error) of the last n iterations has been below a certain threshold. In case of the NE type of normal equation, after the n-th iteration, the relative residual error is

$$r_n = \frac{\left\|\mathbf{b} - \mathbf{A}\mathbf{A}^{\mathrm{H}}\mathbf{u}_n\right\|_2}{\|\mathbf{b}\|_2}, \tag{3.43}$$

where $\mathbf{q_n} = \mathbf{A}^{\mathrm{H}}\mathbf{u}_n$ is the corresponding solution vector, $\mathbf{b}$ contains the measurement samples and $\mathbf{A}$ is the system matrix. As already mentioned in Section 2.5.2, the residual error in (3.43) is in the space of the measurement vector and thus corresponds directly to the relative observation error

$$\Delta b = \frac{\|\mathbf{b} - \mathbf{A}\mathbf{q}_n\|_2}{\|\mathbf{b}\|_2}. \tag{3.44}$$

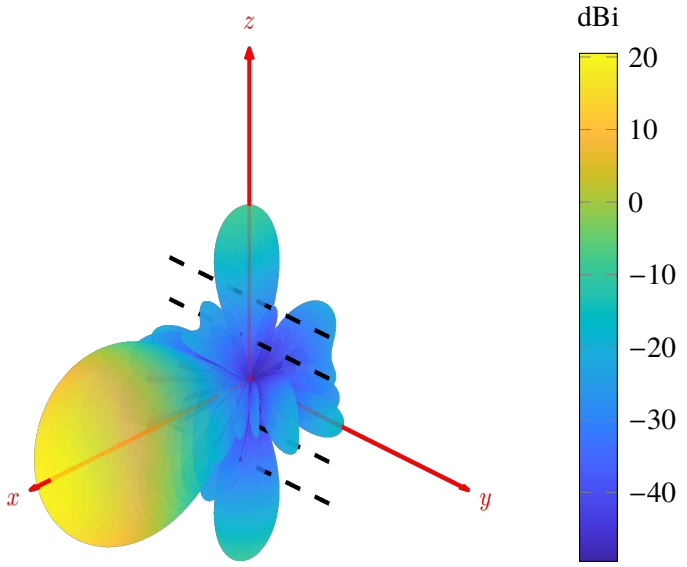

Figure 3.5: 5×6 array of elementary Huygens radiators with the magnitude of the corresponding directivity pattern D_{abs}.

In contrast, the relative residual error of the NR type of normal equation is

$$r_n = \frac{\left\| \mathbf{A}^{\mathrm{H}}\mathbf{b} - \mathbf{A}^{\mathrm{H}}\mathbf{A}\mathbf{x}_n \right\|_2}{\left\| \mathbf{A}^{\mathrm{H}}\mathbf{b} \right\|_2} \tag{3.45}$$

is in the space of the unknowns and thus a problem specific quantity. With respect to noisy measurement data it must be noted that, although called observation *error*, the difference in (3.44) does not necessarily have to be small for a "good" solution. In terms of regularization, one usually seeks a solution where the noise contribution is filtered out and consequently the observation error will be on the order of the noise (or the numerical perturbations).

3.3.1 Synthetic Dipole Array

To investigate the fundamental accuracy of the algorithm when solving an inverse source problem, an array of elementary dipoles is considered. The array consists of 5×6 y-oriented Huygens radiators in the yz-plane with a square diameter of about 0.46 m, radiating into the positive x-direction. The arrangement is shown in Figure 3.5 together with the resulting directivity pattern at 3 GHz. Both the radiated far field as well as the near field were computed for the E_ϑ and E_φ component. For the near field a standard, equiangular spherical sampling grid of radius $r = 1$ m with $N_\vartheta = 32$ and $N_\varphi = 64$ was used, resulting in 2048 measurement samples per polarization. The inverse problem is then solved for a spherical-wave function representation according to (2.58) with a maximum degree of $N = 30$, which leads to a total number of 1920 unknown spherical-wave coefficients. As for this kind of synthetic data the electric field at the sample locations is directly available, no probe correction is needed and the

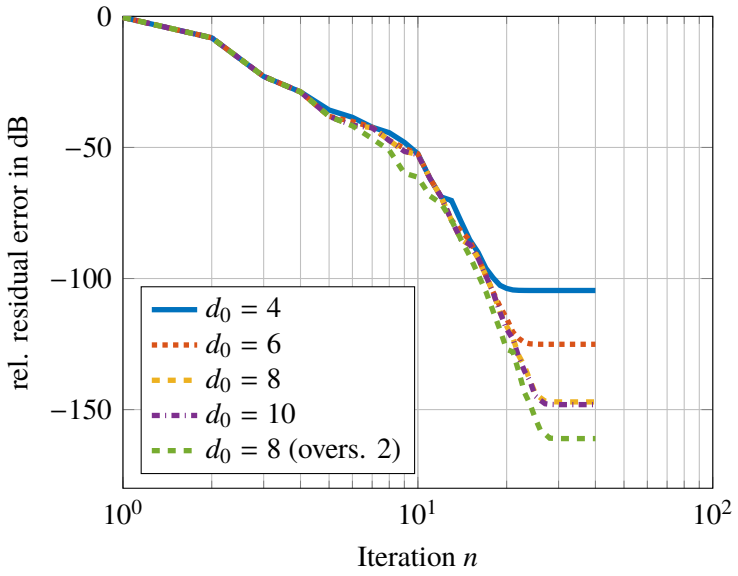

Figure 3.6: Convergence behavior for the dipole model. Relative residual error of NE normal equation with different values of d_0 in (2.45) after n iterations.

problem is solved using Hertzian dipole probes. This corresponds to solving (3.2) instead of the full transmission equation.

Due to the small size of the source region, no hierarchical octree structure was needed here, resulting in a small number of unknowns and a rather well conditioned system matrix. In order to test the numerical accuracy, the parameter d_0 in equation (2.45) that determines the maximum multipole order of the translation operator (and the sampling rate of the plane-wave spectra) is varied from 4 to 10. The NE type normal equation (2.70) is solved by means of the GMRES method. Figure 3.6 shows the resulting relative residual error, depending on the number of iterations n. It may be observed that up to the fourth iteration the solution is independent from the actual choice of d_0. This is due to the fact that the GMRES method determines the lower order modes, that carry most of the energy, first. Obviously, these modes are well determined in all cases. In the further course of iterations also the higher modes are considered, where the maximum order depends on the choice of d_0, which then determines the accuracy of the converged solution. For $d_0 \geq 8$ no significant further improvement is noted. In fact, as already discussed in Section 2.4.1, the accuracy of the far-field pattern solution may even decrease as the multipole order L of the translation operator becomes too large, that is $L >> kD$, since the numerical integration will fail for the oscillatory terms of the spherical Hankel function. To some extent this problem can be overcome by oversampling all plane-wave spectra and the translation operator. Doing so with a factor of 2 along ϑ and φ for $d_0 = 8$ leads to a residual error of about $-160\,\mathrm{dB}$. This corresponds to the numerical precision of the implementation, where some frequently used coefficients are precomputed and conveniently stored in memory with single floating point precision, and thus constitutes the absolute accuracy limit for otherwise undisturbed data[3]. The dominant φ component of the

[3]The data itself was computed with double floating point precision.

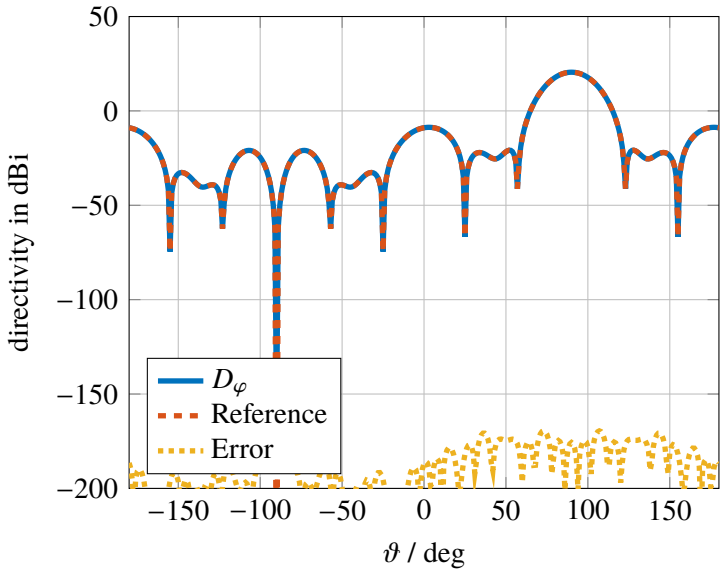

Figure 3.7: Directivity pattern of the 5×6 dipole array at $\varphi = 0°$, obtained from a solution with $d_0 = 8$ and $2\times$ oversampling along ϑ and φ.

corresponding directivity pattern is shown in Figure 3.7 for a cut angle at $\varphi = 0°$. Obviously, the far-field error is on the same order as the observation error with a maximum of about $-170\,\text{dB}$. Using an implementation of the algorithm that solely employs double floating point precision variables further reduces the residual error to $-174\,\text{dB}$ for this configuration. The maximum relative far-field error is around $-190\,\text{dB}$ in that case. As in any realistic measurement scenario one will never be able to reach these accuracy levels, the single floating point precision implementation will be used for all other test examples presented in this thesis.

In this example, for better comparison the solver was stopped after a fixed number of 40 iterations as it was noted before that at this point no further improvement occurred for any parameter choice. In more realistic scenarios, in particular when the measurement data is perturbed by noise, one usually seeks a regularized solution, where the noise contributions are filtered out. As can be seen from the curves of the relative residual error of the NE type normal equation in Figure 3.6, the error stagnates at the achievable accuracy limit. This in contrast to the NR type of normal equation as shown Figure 3.8. Here, the relative residual error decreases much further until it stagnates at some more or less arbitrary (problem specific) value. The corresponding observation error is almost identical to the NE type solution, however its explicit computation requires an additional evaluation of the forward operator in each solver iteration and is, thus, usually avoided. Consequently, choosing a stopping criterion according to a certain improvement rate of the residual error appears reasonable for the NE type of normal equation and will be further discussed in the context of the next application example.

3.3.2 Simulated Horn Antenna Using FEKO

Compared to an elementary dipole based model as used for the previous example, a MoM-based simulation model provides more realistic test data with respect to the radiation mechanisms

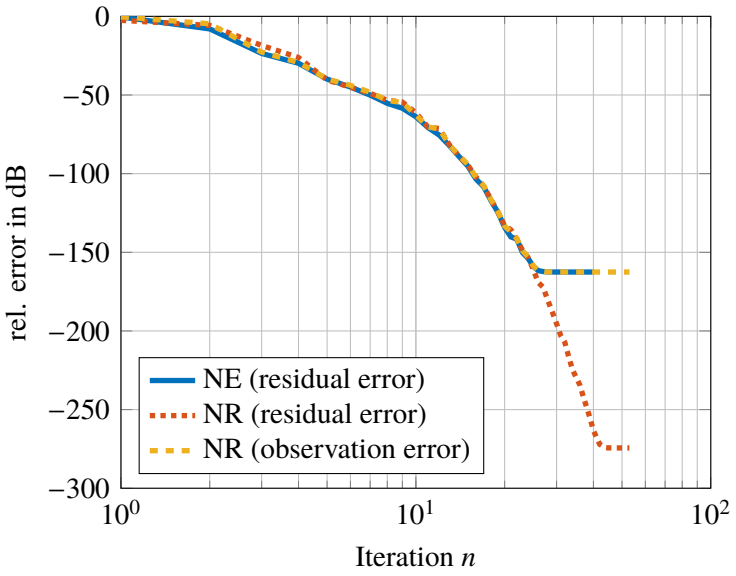

Figure 3.8: Convergence behavior for the dipole model. Relative residual/observation error of NR and NE normal equations for $d_0 = 8$ and 2× oversampling along ϑ and φ.

of a real antenna. Using the FEKO simulation software, the electric near field and far field of a pyramidal horn antenna at a frequency $f = 11\,\text{GHz}$ was computed. The horn antenna is confined to a minimum enclosing sphere with radius $r_{\text{min}} = 0.077\,\text{m}$ (about 2.8λ) and was discretized with a triangular surface mesh with a targeted edge length of about $\lambda/16$ to achieve a good agreement between the computed near- and far-field data. Figure 3.9 shows the simulation model with the triangular mesh and the exciting (single mode) hollow waveguide port at the back. The near field was sampled on a sphere with radius $r_{\text{meas}} = 0.3\,\text{m}$, using an equidistant spherical grid with $N_\vartheta = 30$ and $N_\varphi = 60$ samples, excluding any samples at the poles. Using again Hertzian dipole probes, the NFFFT is performed for different kinds of basis functions, namely electric and magnetic surface current densities (JM) defined with RWG basis functions on the simulation mesh, a spherical-wave expansion (SWE) and using plane-wave spectrum (PWS) coefficients. Initially, this is done for a single-level FMM mode, leading to 1566 unknowns in the SWE case, 3248 unknowns in the PWS case and 23 374 unknowns when using the surface current densities. Figure 3.10 shows the corresponding convergence behavior in terms of the relative residual error of the NE type normal equation. Using the SWE or PWS only few iterations are needed as the system matrix is well-conditioned, whereas the (JM) basis converges significantly slower. In all cases the minimum error is around −120 dB, which can be estimated to be the numerical accuracy of the simulation data for the chosen mesh size, that is the agreement of the computed near-field and far-field data. Using a multi-level mode for the FMM the number of unknowns is increased in the SWE and PWS case to 11 592 and 26 496 , respectively. Consequently, they also exhibit a slower convergence behavior as can be seen from Figure 3.11.

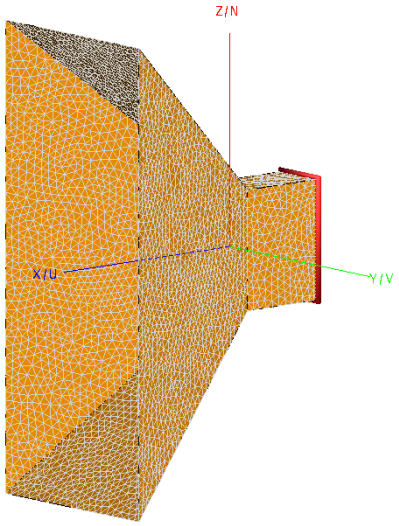

Figure 3.9: FEKO simulation model and triangular mesh of a pyramidal horn antenna. The model is excited by a single mode hollow waveguide port at the back.

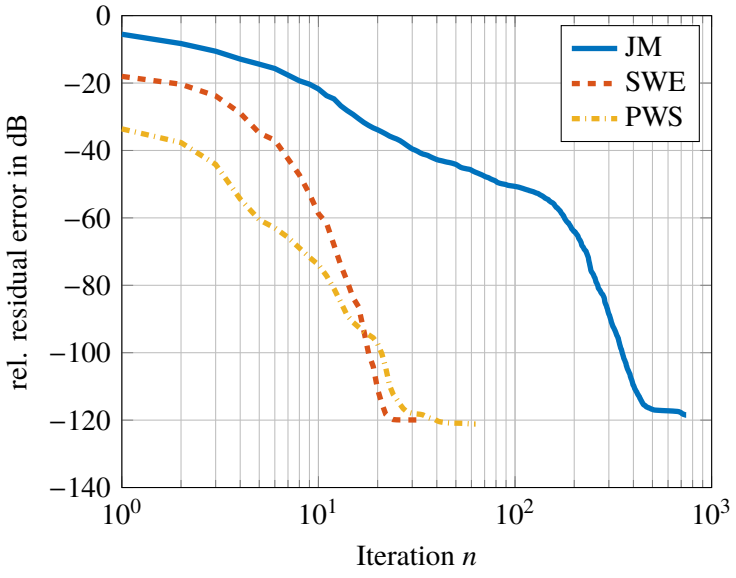

Figure 3.10: Convergence behavior for the FEKO horn antenna example with different basis functions. Relative residual error of the single-level FMM.

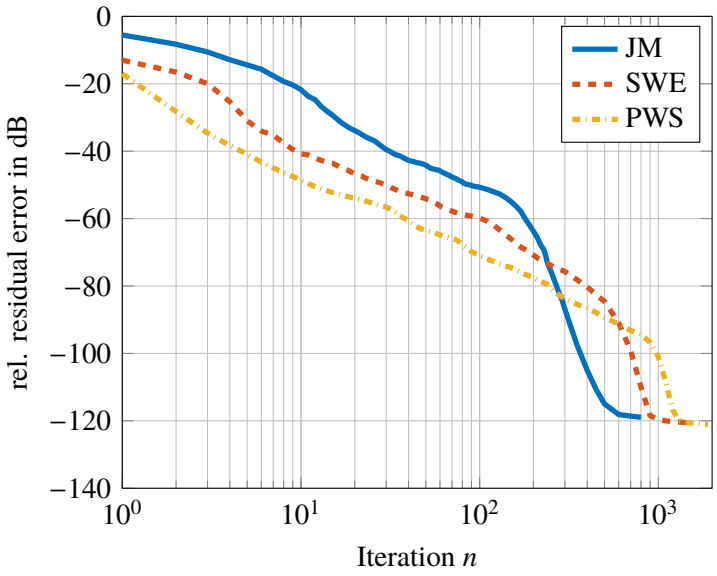

Figure 3.11: Convergence behavior for the FEKO horn antenna example with different basis functions. Relative residual error of the MLFMM mode.

In terms of the far-field error, all choices of basis functions yield very accurate results on the order of the numerical accuracy of the input data. This can be seen in Figure 3.12 for a cut of the dominant D_φ-component of the directivity pattern at $\varphi = 0°$. Due to the excellent convergence behavior in case of the single-level mode and the (always) reduced number of unknowns, the spherical-multipole based method (SWE) will be the preferred choice for the following application examples. However, it must be noted that in many application scenarios it may be advantageous to use a surface current density representation in order to benefit from the localization of the sources and diagnostic capabilities [Eibert et al. 2015].

As shown for the previous example, using a relative stopping criterion with respect to the observation error appears to be a good choice for the NE type of normal equation. This shall now be confirmed in the presence of noise on the measurement data and compared to the NR equation type. To this end, white Gaussian noise is added to the simulated measurement data of the horn antenna used before. With a single-level SWE approach, solutions to the NFFFT are sought for signal-to-noise ratios (SNRs) of 20 dB to 60 dB. The iterative solver is stopped for the NE and NR equation if the relative improvement is smaller than 0.1% for two consecutive iterations. Figure 3.13 shows the resulting convergence behavior in terms of the relative residual error for the NE equation (which converges to the same relative observation error as the NR equation). The relative residual error for the NR equation is depicted in Figure 3.14. Obviously, in case of the NR equation the solver iterates significantly longer until convergence of the residual error is achieved. At the same time, the solution in terms of the relative observation error is not improved from the moment on where the NE error stagnates. In this respect, the NE type of normal equation is clearly beneficial to minimize the number of solver iterations. Alternatively, if reliable a priori knowledge about the noise level is available, one could also set up a stopping criterion according to the discrepancy principle. That is to stop the solver if the relative residual error is below the magnitude of the noise. In case of the

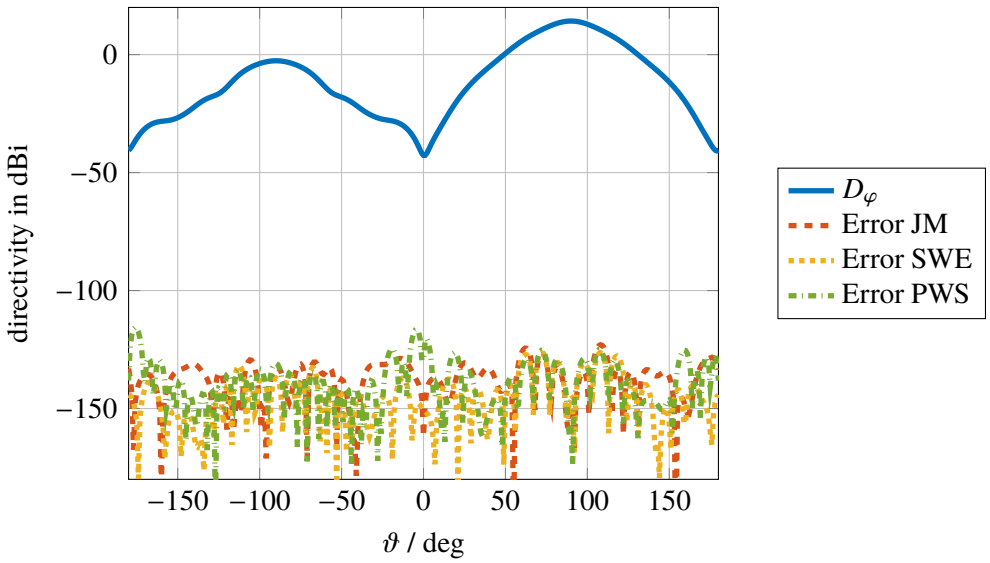

Figure 3.12: Directivity pattern of the FEKO horn antenna at $\varphi = 0°$ with error curves of different basis functions for the single-level mode.

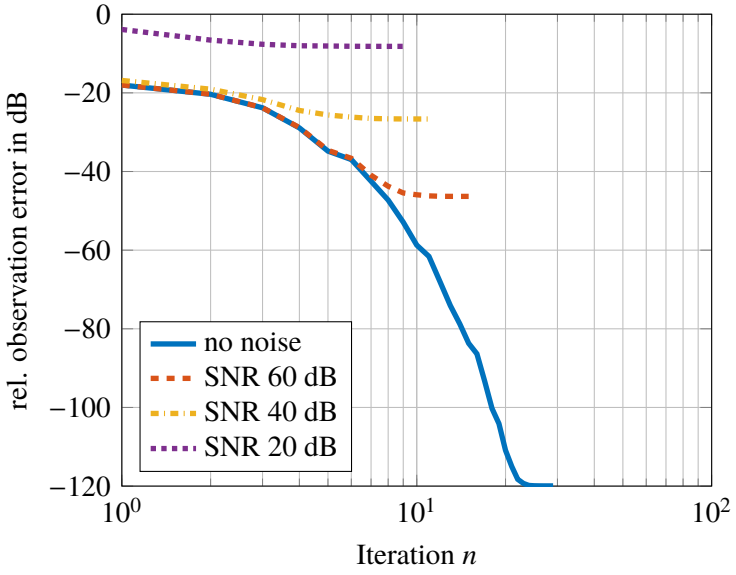

Figure 3.13: Convergence behavior for the FEKO horn antenna example with different levels of SNR. Relative residual/observation error of the NE type equation.

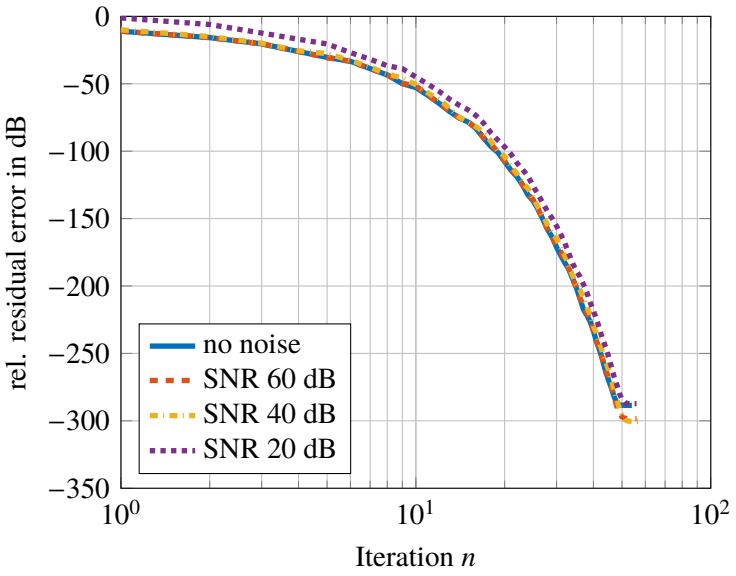

Figure 3.14: Convergence behavior for the FEKO horn antenna example with different levels of SNR. Relative residual error of the NR type equation.

NR equation, this would lead to about the same break points as the relative criterion for the NE case. Due to the reliability in finding a good break point for the solver, the NE type will be used throughout this thesis if not stated otherwise.

3.3.3 Measurement of a Double-Ridged Horn Antenna DRH400

In order to test the accuracy of the derived near-field transmission equation, in particular when determining the gain of an antenna, test measurements were conducted in the anechoic chamber of the TUM. The antenna under test is a double ridged horn antenna DRH400 [RFspin s.r.o. 2019]. Figure 3.15 shows the antenna mounted on a spherical positioner in the anechoic chamber. Spherical measurements on a radius $r_{\text{meas}} = 2.73\,\text{m}$ are performed for a frequency of $f = 1\,\text{GHz}$ to $6\,\text{GHz}$. Another double ridged horn antenna DRH18 with known values of the gain is used as the probe antenna. The DRH400 antenna can be enclosed by a minimum sphere with a radius of about 0.4 m. However, with respect to the spherical scan center the antenna is mounted with some offset, leading to a maximum radial extent of 0.8 m. The latter value is used for the spherical-multipole expansion based algorithm of NSI [NSI-MI Technologies, LLC 2019] that serves as a reference. The typical far-field distance $r_{\text{FF}} = 2d_{\text{max}}^2/\lambda$ for this antenna corresponds to about 2.4 m at a frequency of 1 GHz and 14.4 m at 6 GHz. Although not necessarily applicable for all frequencies in this case, for comparison also the Friis transmission equation is utilized to obtain the antenna gain. To this end, the phase center distances between the AUT and the probe are determined for all frequencies using the method described by Betjes [2007]. In order to obtain the gain from the near-field measurements, the system losses are determined by measuring the transmission factor when the cables at the antenna ports are directly through connected using another (known) cable. The magnitude corrected values of the transmission factor can then be used directly to compute

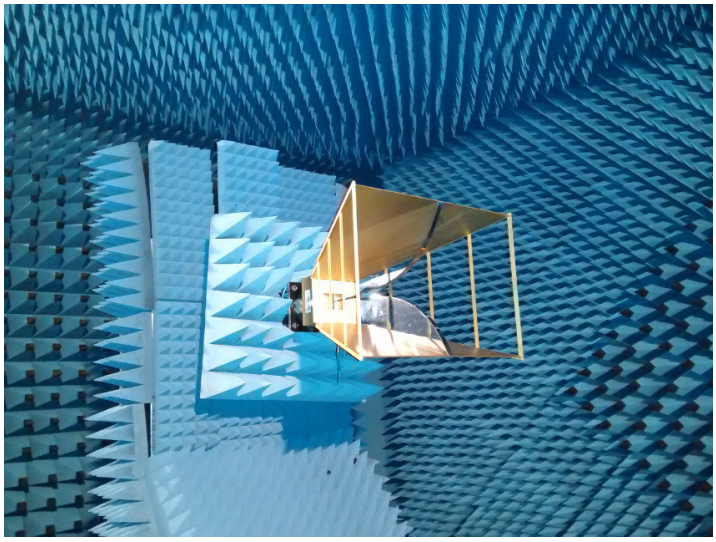

Figure 3.15: Double ridged horn antenna DRH400 in the anechoic chamber of the TUM. © 2019 IEEE

the gain-normalized pattern of the AUT by evaluating the transmission equation (3.19) or, equivalently, by evaluating the spherical-multipole transmission equation employed by the NSI software. The results for the realized gain in boresight direction ($\vartheta = 0°$) are shown in Figure 3.16 for the considered frequency range. Obviously, evaluating the Friis transmission equation provides only an inaccurate approximation of the gain, whereas very good agreement between the two NFFFT methods can be observed for all frequencies. There is a remaining difference of up to 0.15 dB, most likely due to the influence of parasitic reflections, noise and positioning errors during the near-field scan. These may contribute differently to the result for the two algorithms, in particular due to the differences in the probe correction. Typical pattern agreements (in terms of the error definition in (3.41)) for this measurement chamber are found to be on the order of −35 dB to −40 dB in the considered frequency range. Consequently, a remaining uncertainty of about ±0.15 dB can be expected for a maximum gain of 13 dBi. The gain-normalized far-field pattern in a cut plane at $\varphi = 0°$ and for $f = 4\,\mathrm{GHz}$ as obtained by FIAFTA and NSI is depicted in Figure 3.17 and 3.18 for the cross- and co-polarized field components, respectively. Here, the relative magnitude deviation between the two methods is around −40 dB over the complete gain-normalized far-field pattern.

It may be noted that a correct determination of the boresight (or maximum) gain from near-field measurements does not necessarily require a full spherical scan. As shown in [Neitz and Eibert 2017] the angular range around the near-field main lobe can be significantly decreased without compromising the accuracy of the gain in boresight direction. Due to the localization of the equivalent sources the NFFFT is generally quite robust against truncation errors as long as enough significant field contributions are captured. Of course the size of the scan aperture dictates the angular range for which the correct pattern result will be available, as it is well known from planar or cylindrical near-field measurements [Qureshi et al. 2013]. This case is shown in Figure 3.19, where the angular range of the spherical near-field data has been limited to $\vartheta_{\max} = \pm 19.5°$ and the result after performing the NFFFT is compared to the full scan solution. Within the valid angular range the relative error is on the order of the measurement accuracy. The absolute gain error at $\vartheta = 0°$ is less than 0.1 dBi.

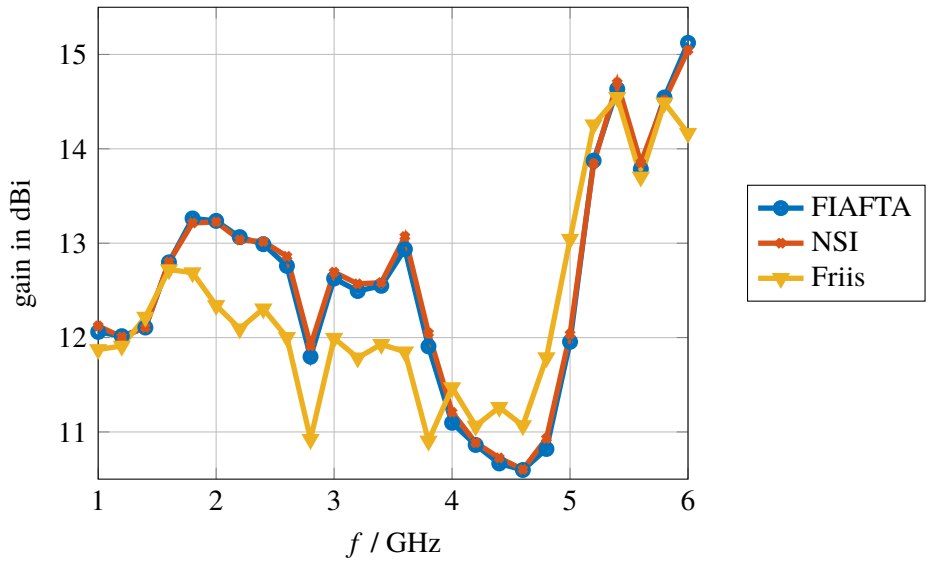

Figure 3.16: Realized gain in boresight direction determined by FIAFTA, the spherical-multipole based NSI software and by evaluating Friis equation. © 2019 IEEE

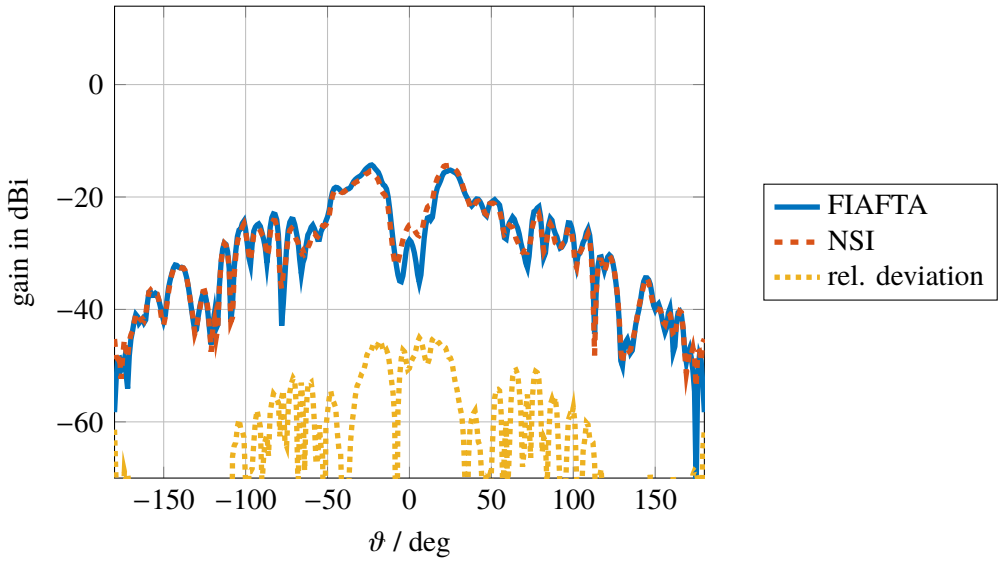

Figure 3.17: Cross-polarized field component of the gain-normalized FF pattern of the DRH400 antenna at $\varphi = 0°$ and $f = 4\,\text{GHz}$. Comparison between FIAFTA and NSI solution.

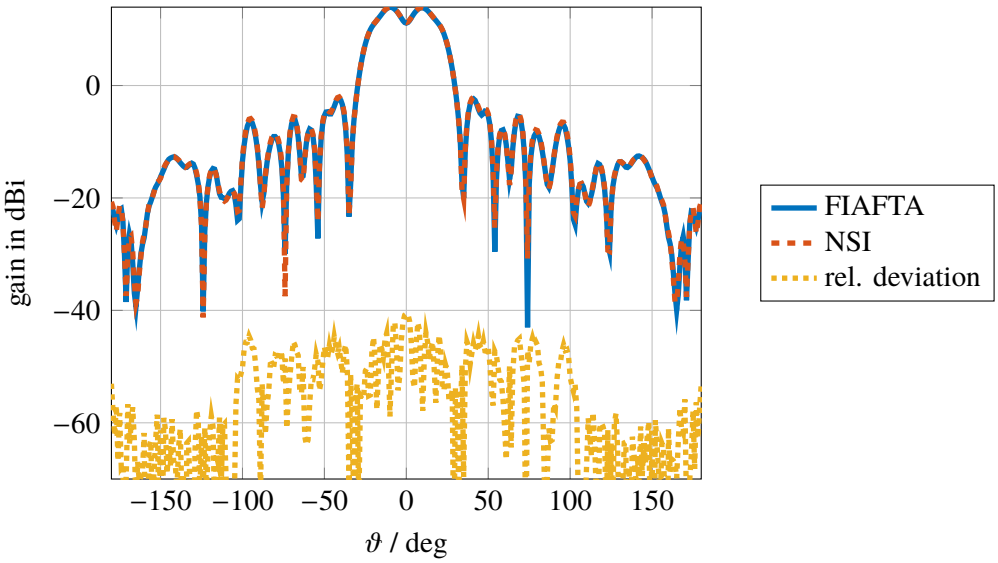

Figure 3.18: Co-polarized field component of the gain-normalized FF pattern of the DRH400 antenna at $\varphi = 0°$ and $f = 4\,\mathrm{GHz}$. Comparison between FIAFTA and NSI solution.

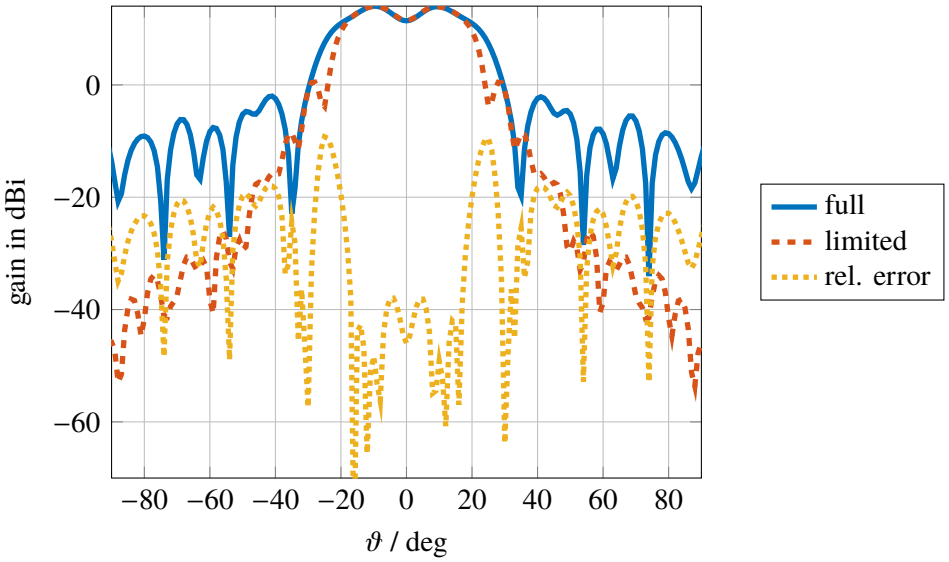

Figure 3.19: Co-polarized field component of the gain-normalized FF pattern of the DRH400 antenna at $\varphi = 0°$ and $f = 4\,\mathrm{GHz}$. Comparison between the FIAFTA solutions using a full spherical scan and a limited angular range of $\vartheta_{\max} = \pm 19.5°$.

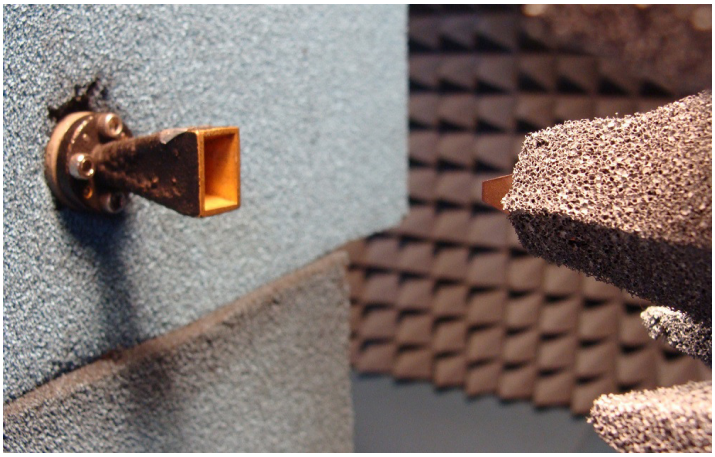

Figure 3.20: Standard gain horn antenna SGH27240 in the millimeter-wave near-field scanner of the TUM. © 2019 IEEE

3.3.4 Measurement of a Standard Gain Horn in W-band

To test the algorithm in case of higher frequencies, planar near-field measurements of a standard gain horn antenna SGH27240 [Flann Microwave Ltd. 2019] in the W-band were conducted with the millimeter-wave near-field scanner of TUM (see Fig. 3.20). While the measurement results presented here have been first reported in [Neitz et al. 2017], the volumetric near-field scanner is described and validated in [Hamberger et al. 2018]. For the considered planar scans, two different measurement distances of 20 mm and 40 mm from the AUT aperture to the open ended waveguide (OEWG) probe (WR10) were chosen, compared to far-field distances of about 120 mm (at 77 GHz) and 170 mm (at 110 GHz), respectively. While the normalized radiation characteristic of the probe antenna was determined by simulation, the maximum gain was identified by performing a separate measurement using two identical OEWG antennas. To account for the system losses of the near-field scanner, the results of a direct through connection measurement were subtracted from the near-field samples in each case. For this scenario, the transformation needs around 30 solver iterations to reach a relative residual error of 10^{-4}. The relative near-field error is about 2%. Figure 3.21 shows the computed realized gain of the standard gain horn in main-beam direction for the two measurement distances as well as for an irregular measurement, where randomly chosen samples from the two measurement planes were combined. Again, the results using the Friis transmission equation are given as an additional curve together with the data sheet values of the standard gain horn, which are provided with an accuracy of ±0.3 dB. It can be seen that the Friis equation approximates the true gain values at higher frequencies only for the larger measurement distance, whereas all solutions obtained from FIAFTA agree well to each other and with the reference. Since planar measurements were performed in this case, only a limited part of the complete plane-wave spectrum was captured. The maximum extents in the xy-measurement-plane from the boresight axis of the AUT are $x_{\mathrm{max}} = \pm 250\,\mathrm{mm}$ and $y_{\mathrm{max}} = \pm 130\,\mathrm{mm}$. For the measurement plane at $z = 20\,\mathrm{mm}$, this corresponds to maximum angular ranges in the E- and H-plane of $\vartheta_{\mathrm{max,E}} = 85°$ and $\vartheta_{\mathrm{max,H}} = 81°$, respectively. The

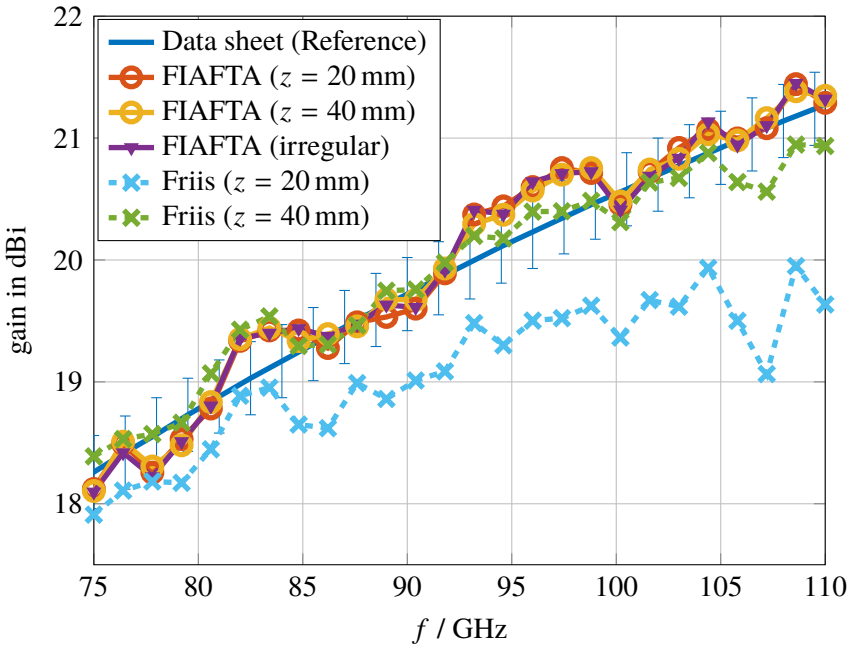

Figure 3.21: Comparison of gain values of the SGH27240 antenna in W-band. © 2019 IEEE

far-field pattern is only guaranteed to be reconstructed accurately within this angular range. However, the maximum gain may be determined with even fewer samples, as long as the AUT main beam is captured. This is shown in Figure 3.22, where for the SGH27240 scenario at $f = 75\,\text{GHz}$ the size of the near-field measurement plane at $z = 20\,\text{mm}$ as well as for the irregular case is continuously decreased in x and y direction and the absolute error of the maximum gain ΔG with respect to the full-measurement-plane solution is calculated. One can limit the measurement plane down to $\pm 15\,\text{mm}$ without introducing an error $\Delta G > 0.03\,\text{dB}$. The procedure is further illustrated in Figure 3.23, showing the magnitudes of the irregular near-field samples of the first polarization of the horn antenna in the full measurement plane. For all planar measurements, a non-redundant measurement scheme as described in [Qureshi et al. 2013] was employed. The dashed black line indicates a limitation of $\pm 15\,\text{mm}$ in the x- and y-direction, where the NF magnitude has dropped by less than $-15\,\text{dB}$ with respect to the main lobe.

3.3.5 Portable Antenna Measurement System (PAMS)

A great advantage of the employed propagating plane-wave based formulation is the ability to integrate it into an MLFMM-based hierarchical scheme. In this way, a large number of even irregularly distributed measurement samples can still be processed efficiently, which is in contrast to methods that, for example, rely on the FFT for an accelerated solution. The portable antenna measurement system (PAMS) developed by Airbus Defence and Space is a system that makes use of this fact and employs the FIAFTA [Geise et al. 2019]. It uses a gondola, carrying the radio frequency (RF) equipment and the measurement probe, that is moved by an overhead crane in a large (anechoic) chamber to perform validation measurements of large satellites.

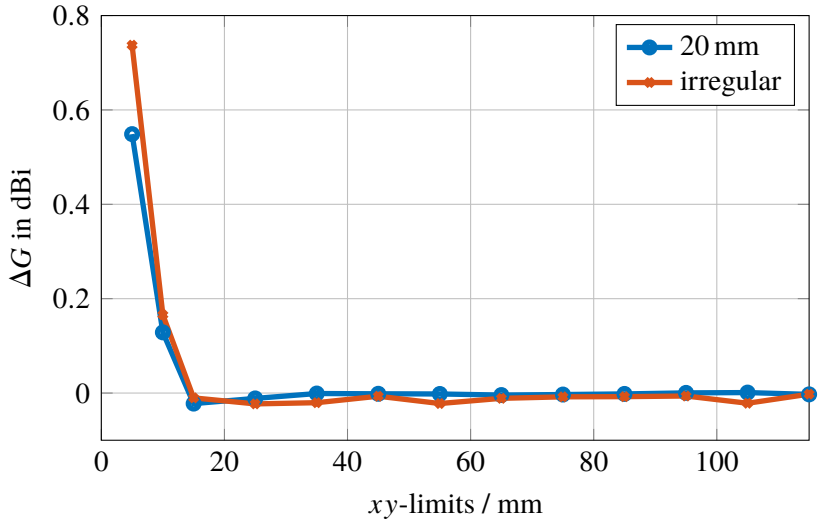

Figure 3.22: Maximum gain error of the SGH27240 antenna for a reduced measurement plane. © 2019 IEEE

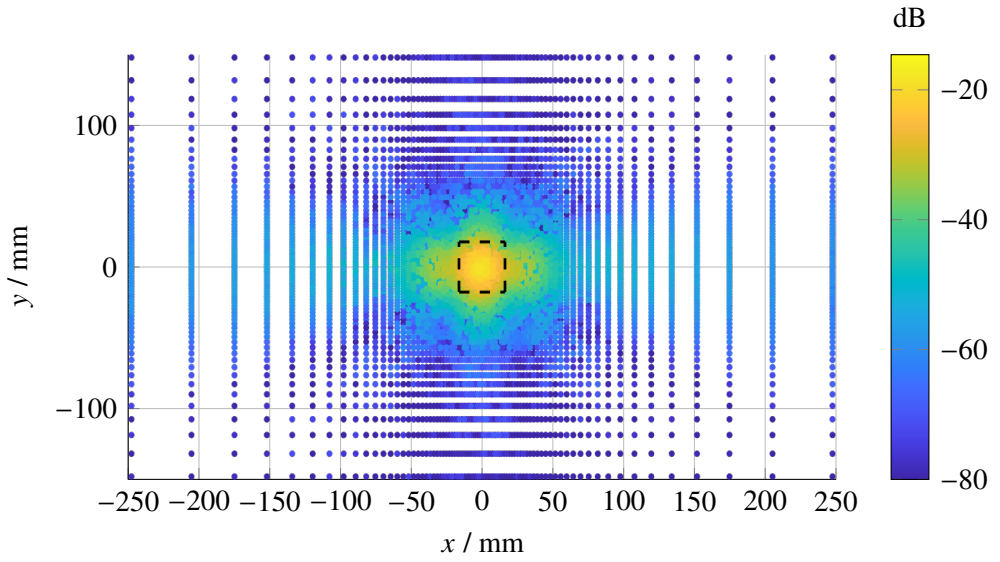

Figure 3.23: Magnitudes of near-field samples from non-redundant planar measurement of the SGH27240 antenna. Dashed line: Limitation to ±15 mm in x- and y-direction. © 2019 IEEE

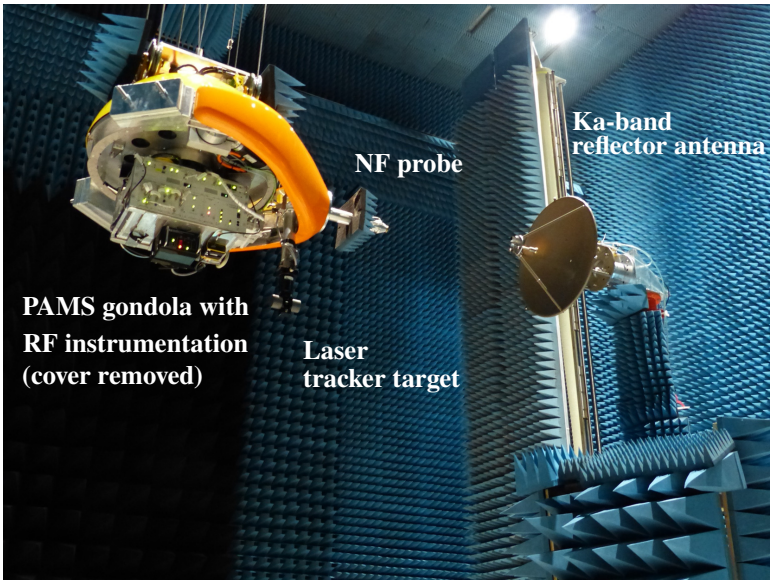

Figure 3.24: Test measurement of a Ka-band parabolic reflector antenna with the PAMS gondola. © 2019 IEEE

Due to the crane-based movement of the gondola, the resulting scan path may exhibit strong irregularities compared to a smooth surface. A 6D laser tracking device is attached to the measurement gondola and used to determine the exact position and orientation of the probe antenna along the scan path.

Figure 3.24 shows the setup of a test measurement using PAMS, where the AUT is a parabolic reflector antenna for the Ka-band. The probe antenna at the gondola is a dual linearly polarized corrugated horn antenna. An area of about 2 m × 2 m was scanned at a distance of 0.7 m in front of the reflector feed. The gondola moved continuously in the horizontal direction and stepped vertically. Measurement samples were acquired periodically along the path. The total acquisition time for the resulting more than 1.4 million near-field samples (two polarizations) was about 2.5 h. Figure 3.25 shows the magnitude of one of the acquired polarizations along the scan path. The swinging of the gondola is clearly visible with variations of up to 15 mm (1.7λ) in the direction towards the AUT. The scan speed was chosen such that the sample distance is smaller or equal to 0.4λ at 33.35 GHz for most parts of the scan surface, which results in this large number of measurement samples. After performing the NFFFT, which took 205 s with 4 threads on an Intel i7-4820K CPU and required 19.1 GB of RAM, the resulting far-field patterns are compared to the measurement results from the compensated compact range (CCR) of Airbus Defence and Space in Munich. As can be seen from the far-field cuts[4] of the normalized magnitudes at $\varphi = 0°$ in Figure 3.26 and 3.27, the maximum relative magnitude deviation is below −35 dB and −38 dB for the vertical and horizontal component, respectively.

The large number of measurement samples results in a dense oversampling of the radiated near field. As shown in [Geise et al. 2019], it is possible to reduce the total number of

[4]Only the angular range up to $\vartheta_{\max} = \pm 10°$ for which reference data from the CCR are available is shown here.

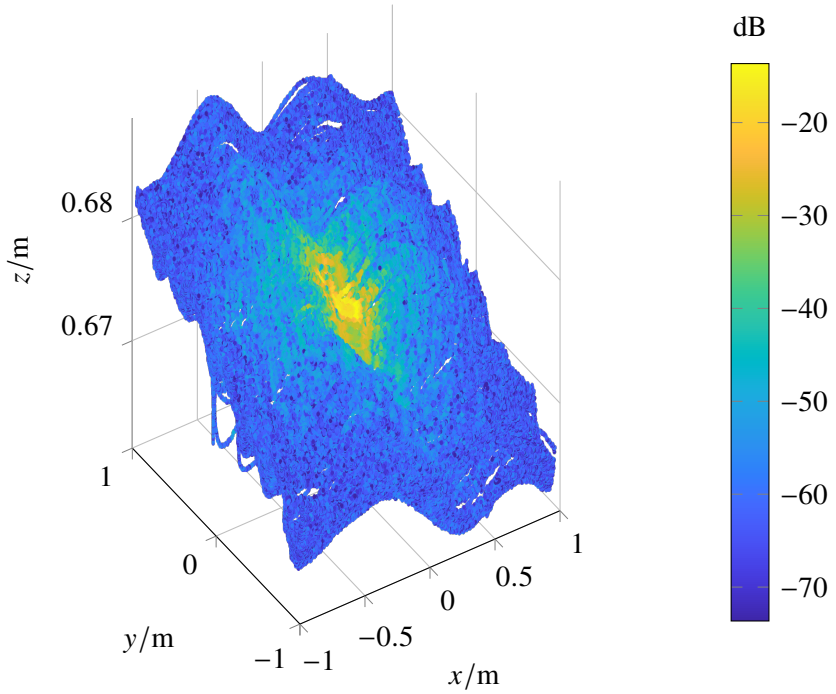

Figure 3.25: One polarization of the measured NF during the test measurement of the Ka-band parabolic reflector antenna. © 2019 IEEE

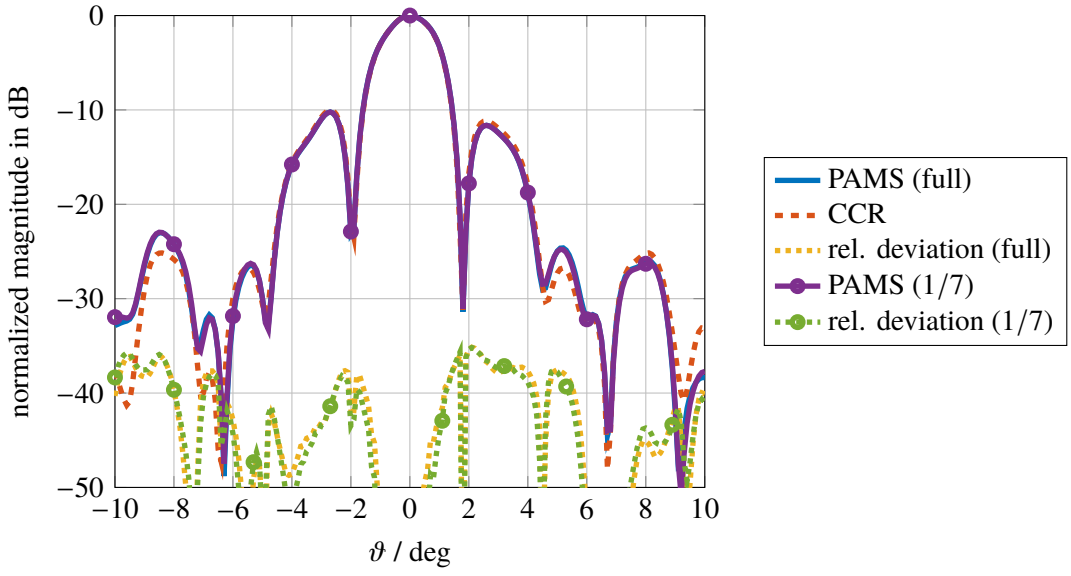

Figure 3.26: Vertically polarized FF cut of the Ka-band parabolic reflector antenna for $\varphi = 0°$ in comparison to CCR measurements. Shown are results with all measurement samples and with $1/7$ of the measurement samples. © 2019 IEEE

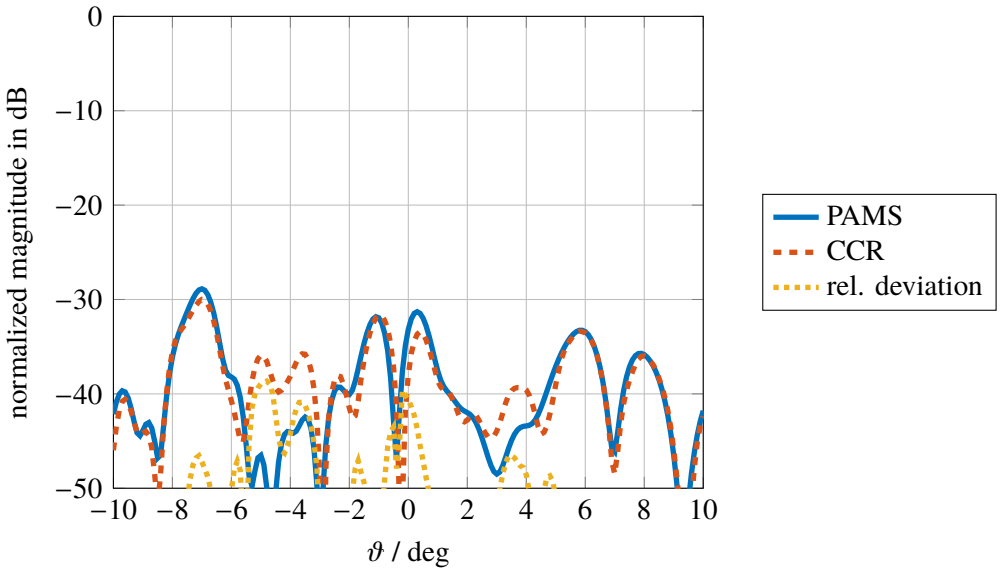

Figure 3.27: Horizontally polarized FF cut of the Ka-band parabolic reflector antenna for $\varphi = 0°$ in comparison to CCR measurements. © 2019 IEEE

measurement samples in this case down to $1/7$ of the total number without significantly decreasing the accuracy. This is also illustrated for the vertical far-field component in Figure 3.26. It may be noted, however, that due to the MLFMM structure of the transformation algorithm, reducing the number of measurement samples more or less uniformly over the complete scan surface, does not reduce the computation time by the same amount but generally much less. The agreement of the antenna gain for this example was found to be within ±0.34 dB compared to the CCR reference of 33.44 dBi.

4 The Inverse Source Problem in Near-Field RCS Measurements

In the previous chapter it has been shown how the concept of propagating plane-wave spectra over the Ewald sphere can be employed to generalize the far-field quantity antenna gain (i.e., the effective area of an antenna as used in the Friis transmission equation) to the near field. One obtains a diagonalized transmission equation that allows for a very efficient implementation by means of the MLFMM. In the context of scattering problems, the question arises if this is equally possible for the effective cross section (i.e., the RCS) of a scattering object. As already mentioned in Section 2.2.2, it is possible to describe any scattering problem in terms of some equivalent sources radiating into free space. However, unlike the actual radiation problem in the area of antenna measurements, these sources are now dependent on the incident field or (in general) even the total field that results from the interaction with the scattering object. As will be shown later on, this fundamental difference leads to a non-linear equation of the material properties of the scatterer and makes the task of finding a solution to the inverse scattering problem generally more complicated than the one of finding a solution to the inverse radiation problem.

Deriving an algorithm that determines the RCS of an object under test from scattering measurements in the near field, that is for non-plane waves, will be the main topic of this chapter. To this end the conceptual basics of RCS measurements are introduced first. It is then investigated how the defining far-field quantities are related to the general (near-field) scattering problem, revealing the problem of neither measuring scattered plane waves nor having a plane-wave incidence. Two approaches to cope with this issue will be presented. The first one is based on a linearization of the scattering problem by means of the Born approximation [Devaney 2012, p. 491]. As a result, in the monostatic case, where incident and scattered wave are traveling along opposite angular directions, the scattering mechanisms can be approximately described by a collection of independent point scatterers. The concept of radiating reflectors [Cafforio et al. 1991] allows one to consider the scattering centers as the actual sources of radiation and, thus, one arrives at a (linear) inverse source problem again [Schnattinger et al. 2014]. The spatial distribution of these point scatterers (often called the reflectivity distribution) is related to the spectral scattering matrix by a spatial Fourier transform. For this reason almost all methods employing this linearization are said to be "image-based", even if they work exclusively in the spectral domain and no spatial image is computed explicitly [LaHaie 2003]. Nonetheless, it is quite common in the field of RCS measurements to compute a point scatterer image for diagnostic purposes and, generally, the Fourier relation between scattering matrix and scattering coefficient distribution forms the basis for most (inverse) SAR imaging principles. This will be further discussed in the context of the linearized RCS transformation approaches, where also some methods for the efficient computation of a spatial image from spectral data will be evaluated.

The problem of the linearized approach is that multiple interactions at the object are

neglected and it will be shown that in the case of complex shaped targets, the achievable accuracy of this method is inevitably limited. To overcome this issue, an algorithmic procedure will be presented that is based on a larger set of bistatic measurement data and employs a field synthesis approach to virtually create an incident plane wave [Neitz et al. 2019]. This method is able to accurately determine the RCS of an arbitrary scattering object, however, at the price of a higher measurement effort.

Extensive experimental studies have been performed to validate and compare the different transformation approaches by means of simulated and measured test data. Some examples to evaluate the key features of the presented algorithms will be given in Chapter 5.

4.1 Radar Cross Section Fundamentals

Historically, the RCS σ was defined as the effective echo area in the radar equation [Fink 1945] that relates the total scattered power P_{sca} from an object to the power density of the incident field S_{inc}, that is

$$\sigma = P_{\mathrm{sca}} / S_{\mathrm{inc}}. \tag{4.1}$$

Although not explicitly required by the radar equation itself, the RCS is (similar to the antenna gain) usually considered to be a far-field quantity, relating incident and scattered plane waves [Knott 2006, p. 17]. Leaving polarization effects aside, this leads to the common formal definition

$$\sigma = \lim_{r \to \infty} 4\pi r^2 \frac{|E_{\mathrm{sca}}|^2}{|E_{\mathrm{inc}}|^2}, \tag{4.2}$$

where E_{sca} and E_{inc} are the magnitudes of the scattered and incident electric field, respectively. In the simple radar range equation, σ is implicitly evaluated for a specific orientation of the transmitting and receiving radar antenna(s) and by taking into account their polarization. More generally, one considers the scattering matrix[1] $\bar{\mathbf{S}}$ that relates two orthogonal vector components of $\boldsymbol{E}_{\mathrm{inc}}$ and $\boldsymbol{E}_{\mathrm{sca}}$, including information about the phase relations and for arbitrary angular directions of the incident and scattered plane waves [Ruck et al. 1970, p. 17]. With the common choice of vertical (V) and horizontal (H) components with respect to the coordinate system of the scatterer, the scattering matrix may then be defined as

$$\begin{bmatrix} E_{\mathrm{V}}^{\mathrm{sca}}(\vartheta,\varphi) \\ E_{\mathrm{H}}^{\mathrm{sca}}(\vartheta,\varphi) \end{bmatrix} = \begin{bmatrix} S_{\mathrm{VV}}(\vartheta,\varphi,\vartheta',\varphi') & S_{\mathrm{VH}}(\vartheta,\varphi,\vartheta',\varphi') \\ S_{\mathrm{HV}}(\vartheta,\varphi,\vartheta',\varphi') & S_{\mathrm{HH}}(\vartheta,\varphi,\vartheta',\varphi') \end{bmatrix} \begin{bmatrix} E_{\mathrm{V}}^{\mathrm{inc}}(\vartheta',\varphi') \\ E_{\mathrm{H}}^{\mathrm{inc}}(\vartheta',\varphi') \end{bmatrix}, \tag{4.3}$$

which accounts for the general bistatic case with the primed coordinates corresponding to the direction of the incident plane wave. In terms of the wave vectors of the incident and scattered plane waves, (4.3) may as well be written as

$$\boldsymbol{E}_{\mathrm{sca}}(\boldsymbol{k}) = \bar{\mathbf{S}}(\boldsymbol{k}, -\boldsymbol{k}') \cdot \boldsymbol{E}_{\mathrm{inc}}(-\boldsymbol{k}'), \tag{4.4}$$

where $-\boldsymbol{k}'$ denotes the wave vector of an incident plane wave with respect to the coordinate system of the scattering object. For many radar applications, however, the monostatic scenario

[1] It is common to refer to the dyad $\bar{\mathbf{S}}$ as the scattering "matrix".

with $\vartheta = \vartheta'$ and $\varphi = \varphi'$ is the most interesting one in which case one has $\boldsymbol{k} = -\boldsymbol{k}'$. Considering the polarization effects described by $\bar{\mathbf{S}}$, the RCS may be defined as

$$\sigma(\boldsymbol{k}, -\boldsymbol{k}') = \lim_{r\to\infty} 4\pi r^2 \|\bar{\mathbf{S}}(\boldsymbol{k}, -\boldsymbol{k}') \cdot \hat{u}^{(i)}\|^2, \tag{4.5}$$

where $\hat{u}^{(i)}$ is the unit vector of the incident field for a specific polarization i, or in a dyadic form as

$$\overline{\boldsymbol{\sigma}}(\boldsymbol{k}, -\boldsymbol{k}') = \lim_{r\to\infty} 4\pi r^2 \begin{bmatrix} |S_{\mathrm{VV}}(\boldsymbol{k}, -\boldsymbol{k}')|^2 & |S_{\mathrm{VH}}(\boldsymbol{k}, -\boldsymbol{k}')|^2 \\ |S_{\mathrm{HV}}(\boldsymbol{k}, -\boldsymbol{k}')|^2 & |S_{\mathrm{HH}}(\boldsymbol{k}, -\boldsymbol{k}')|^2 \end{bmatrix}. \tag{4.6}$$

It must be emphasized that the given relations are only valid in the far field, where both the incident and the scattered field may be described by a single plane wave. Similar to the case of determining the radiation pattern in antenna measurements, direct methods for measuring the RCS are thus usually based on far-field (outdoor) ranges or compact range facilities [Knott 2006]. Nonetheless, a variety of near-field approaches has been developed over the past decades, almost all of them relying on a linearization of the scattering problem [LaHaie 2003] as mentioned before.

4.2 Integral Representation of the Scattered Field

To derive the necessary transmission equations of scattering experiments in the near field of an object under test, the general scattering problem is considered as already introduced for the volume equivalence theorem in Section 2.2.2. The scatterer is described by its (possibly lossy) material properties $\mu(\boldsymbol{r})$ and $\varepsilon(\boldsymbol{r})$ in the volume V that is embedded in a homogeneous background medium. For the sake of simplicity this medium is assumed to be free space with $\mu_\mathrm{b} = \mu_0$ and $\varepsilon_\mathrm{b} = \varepsilon_0$. If a transmitting antenna radiates the incident electric field $\boldsymbol{E}_\mathrm{inc}$ into free space, the scattered field due to the presence of the scattering object is

$$\boldsymbol{E}_\mathrm{sca}(\boldsymbol{r}) = \boldsymbol{E}(\boldsymbol{r}) - \boldsymbol{E}_\mathrm{inc}(\boldsymbol{r}), \tag{4.7}$$

where $\boldsymbol{E}$ is the total electric field. In terms of the volume equivalence the scattered field may be thought to be due to the equivalent volume current densities

$$\boldsymbol{J}_\mathrm{eq}(\boldsymbol{r}) = \mathrm{j}\omega\left(\bar{\boldsymbol{\varepsilon}}(\boldsymbol{r}) - \varepsilon_0\bar{\mathbf{I}}\right) \cdot \boldsymbol{E}(\boldsymbol{r}) \tag{4.8}$$

and

$$\boldsymbol{M}_\mathrm{eq}(\boldsymbol{r}) = \mathrm{j}\omega\left(\bar{\boldsymbol{\mu}}(\boldsymbol{r}) - \mu_0\bar{\mathbf{I}}\right) \cdot \boldsymbol{H}(\boldsymbol{r}), \tag{4.9}$$

where the permittivity and permeability may generally be anisotropic. This leads to the integral representation of the scattered field

$$\boldsymbol{E}_\mathrm{sca}(\boldsymbol{r}) = \iiint_V \left[\overline{\mathbf{G}}_J^E(\boldsymbol{r}, \boldsymbol{r}') \cdot \boldsymbol{J}_\mathrm{eq}(\boldsymbol{r}') + \overline{\mathbf{G}}_M^E(\boldsymbol{r}, \boldsymbol{r}') \cdot \boldsymbol{M}_\mathrm{eq}(\boldsymbol{r}')\right] \mathrm{d}v'. \tag{4.10}$$

Obviously, the equivalent sources (and consequently also the scattered electric field) depend on the total electric field itself. Thus, the sources will change depending on the type, location and

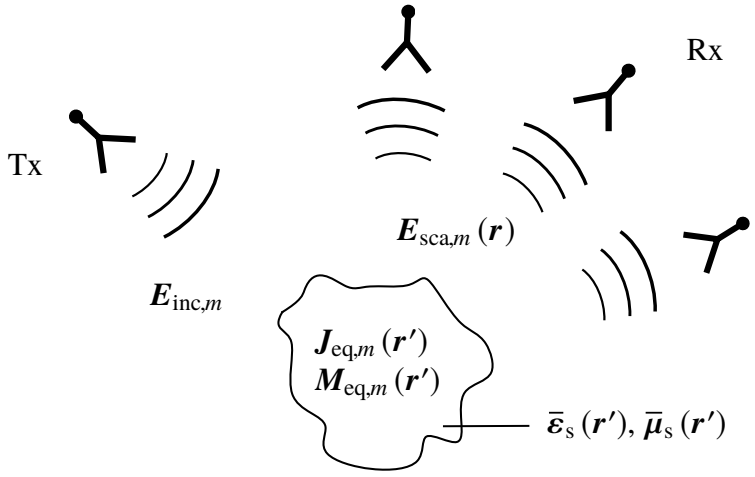

Figure 4.1: Inverse scattering problem with a single transmitting antenna m, illuminating an arbitrary object with $\bar{\boldsymbol{\varepsilon}}_{\mathrm{s}}(\boldsymbol{r}')$ and $\bar{\boldsymbol{\mu}}_{\mathrm{s}}(\boldsymbol{r}')$. The scattered field $\boldsymbol{E}_{\mathrm{sca},m}(\boldsymbol{r})$ may be expressed in terms of the equivalent current densities $\boldsymbol{J}_{\mathrm{eq},m}(\boldsymbol{r}')$ and $\boldsymbol{J}_{\mathrm{eq},m}(\boldsymbol{r}')$. © 2019 IEEE

rotation of the transmitting antenna(s) illuminating the object. The scattering scenario for a single transmitting antenna m is depicted in Figure 4.1, where the permittivity and permeability of the scatterer are denoted as $\bar{\boldsymbol{\varepsilon}}_{\mathrm{s}}(\boldsymbol{r}')$ and $\bar{\boldsymbol{\mu}}_{\mathrm{s}}(\boldsymbol{r}')$, respectively. With the excitation dependent equivalent current densities $\boldsymbol{J}_{\mathrm{eq},m}(\boldsymbol{r})$ and $\boldsymbol{M}_{\mathrm{eq},m}(\boldsymbol{r})$, the scattered electric field for this setup is

$$\boldsymbol{E}_{\mathrm{sca},m}(\boldsymbol{r}) = \iiint\limits_{V} \left[\overline{\mathbf{G}}_J^E(\boldsymbol{r},\boldsymbol{r}') \cdot \boldsymbol{J}_{\mathrm{eq},m}(\boldsymbol{r}') + \overline{\mathbf{G}}_M^E(\boldsymbol{r},\boldsymbol{r}') \cdot \boldsymbol{M}_{\mathrm{eq},m}(\boldsymbol{r}') \right] \mathrm{d}v'. \tag{4.11}$$

4.3 Scattered Plane-Wave Spectra and RCS

Similar to the case of antenna near-field measurements a diagonalized transmission equation for scattering experiments may be derived by employing an expansion of the scattered field in propagating plane waves on the Ewald sphere. To this end one may repeat the steps described in Section 2.4.2 for the scattered electric field in (4.11), which results in

$$\boldsymbol{E}_{\mathrm{sca},m}(\boldsymbol{r}) = \oiint \tilde{\boldsymbol{Q}}_m(\boldsymbol{k})\, T_L\left(\hat{k}\cdot\hat{D}, kD\right) \mathrm{d}^2\hat{k}, \tag{4.12}$$

where $\tilde{\boldsymbol{Q}}_m(\boldsymbol{k})$ is the excitation dependent scattered plane-wave spectrum of the corresponding equivalent current densities and the definition of the location vectors $\boldsymbol{r}$ and $\boldsymbol{D}$ is according to Figure 2.4. For simplicity $\boldsymbol{r}_o = \boldsymbol{r}_Q = 0$ is chosen here, nonetheless the more general case may also be considered as it was done for the radiated field of an antenna in Section 3.1.

To determine the RCS one is interested in the ratio of incident and scattered plane waves according to (4.2). For the case of an incident plane wave with wave vector $\boldsymbol{k}_n$ and polarization (i), the excitation dependent scattered plane-wave spectrum may as well be written as

$\tilde{\boldsymbol{Q}}^{(i)}(\boldsymbol{k}, -\boldsymbol{k}_n)$. In terms of spherical vector components and by choosing two (orthogonal) polarizations $i = 1, 2$ two scattered plane-wave spectra

$$\tilde{\boldsymbol{Q}}^{(1,2)}(\boldsymbol{k}, \boldsymbol{k}_n) = \tilde{Q}_{\vartheta}^{(1,2)}(\boldsymbol{k}, \boldsymbol{k}_n)\,\hat{\vartheta} + \tilde{Q}_{\varphi}^{(1,2)}(\boldsymbol{k}, \boldsymbol{k}_n)\,\hat{\varphi} \tag{4.13}$$

are thus obtained for every incident direction of $\boldsymbol{k}_n$. The dyadic scattering spectrum $\overline{\mathbf{Q}}$ can then be constructed by using the unit vectors $\hat{u}_n^{(i)}$ to describe the polarization of the incident plane wave, that is

$$\begin{aligned}
\overline{\mathbf{Q}}(\boldsymbol{k}, -\boldsymbol{k}_n) &= \tilde{\boldsymbol{Q}}^{(1)}(\boldsymbol{k}, -\boldsymbol{k}_n)\,\hat{u}_n^{(1)} + \tilde{\boldsymbol{Q}}^{(2)}(\boldsymbol{k}, -\boldsymbol{k}_n)\,\hat{u}_n^{(2)} \\
&= \tilde{\boldsymbol{Q}}_n^{(1)}(\boldsymbol{k}, -\boldsymbol{k})\left(\hat{\vartheta}_n^{(1)} + \hat{\varphi}_n^{(1)}\right) + \tilde{\boldsymbol{Q}}^{(2)}(\boldsymbol{k}, -\boldsymbol{k}_n)\left(\hat{\vartheta}_n^{(2)} + \hat{\varphi}_n^{(2)}\right) \\
&= \begin{bmatrix} \tilde{Q}_{\vartheta\vartheta}(\boldsymbol{k}, -\boldsymbol{k}_n) & \tilde{Q}_{\vartheta\varphi}(\boldsymbol{k}, -\boldsymbol{k}_n) \\ \tilde{Q}_{\varphi\vartheta}(\boldsymbol{k}, -\boldsymbol{k}_n) & \tilde{Q}_{\varphi\varphi}(\boldsymbol{k}, -\boldsymbol{k}_n) \end{bmatrix},
\end{aligned} \tag{4.14}$$

where the spherical components ϑ and φ of the global coordinate system were employed here. Using the far-field approximation for the FMM translation operator according to (2.61) in (4.12), the scattered electric field of a single plane wave in direction of $\boldsymbol{k}$ (and still due to an incident plane wave $\boldsymbol{k}_n$) may be expressed as

$$\boldsymbol{E}_{\mathrm{sca}}(\boldsymbol{k}, -\boldsymbol{k}_n) = \lim_{kr\to\infty} \boldsymbol{E}_{\mathrm{sca}}(\boldsymbol{r}, \boldsymbol{k}_n) = \tilde{\boldsymbol{Q}}(\boldsymbol{k}, -\boldsymbol{k}_n)\,\frac{\mathrm{e}^{-\mathrm{j}kr}}{r}. \tag{4.15}$$

Consequently, the general bistatic RCS $\sigma^{(i)}$ for an incident plane wave with polarization $\hat{u}_n^{(i)}$ is related to the dyadic scattering spectrum by

$$\begin{aligned}
\sigma^{(i)}(\boldsymbol{k}, \boldsymbol{k}_n) &= \lim_{r\to\infty} 4\pi r^2 \frac{\|\boldsymbol{E}_{\mathrm{sca}}^{(i)}(\boldsymbol{k}, -\boldsymbol{k}_n)\|^2}{\|\boldsymbol{E}_{\mathrm{inc}}^{(i)}(-\boldsymbol{k}_n)\|^2} \\
&= 4\pi \frac{\|\overline{\mathbf{Q}}(\boldsymbol{k}_n, \boldsymbol{k}_n) \cdot \hat{u}_n^{(i)}\|^2}{\|\boldsymbol{E}_{\mathrm{inc}}^{(i)}(-\boldsymbol{k}_n)\|^2},
\end{aligned} \tag{4.16}$$

where the magnitude of $\boldsymbol{E}_{\mathrm{inc}}(-\boldsymbol{k}_n)$ is usually known for a specific measurement setup. The problem of measuring the RCS thus corresponds to determining $\overline{\mathbf{Q}}$ for incident plane waves, which of course is generally not the case if the transmitting antenna is located in the near field.

4.4 Linearized Scattering Approaches

One way to overcome the problem of not having an incident plane wave in a near-field measurement is to derive an approximate linearized expression for the scattered field with an excitation independent description of the scatterer. This is commonly done in the area of inverse scattering problems where one is interested in determining the structure of the scatterer or its material parameters [Colton and Kress 2013, p. 370]. To this end it is assumed that the scatterer is non-magnetic ($\mu(\boldsymbol{r}) \approx \mu_0$) but the possibly lossy permittivity may be anisotropic, resulting in

$$\overline{\boldsymbol{\varepsilon}}(\boldsymbol{r}) = \varepsilon_0 \left(\overline{\boldsymbol{\varepsilon}}_{\mathrm{r}}(\boldsymbol{r}) - \mathrm{j}\frac{\overline{\boldsymbol{\kappa}}(\boldsymbol{r})}{\omega\varepsilon_0}\right), \tag{4.17}$$

where $\overline{\boldsymbol{\kappa}}(\boldsymbol{r})$ is the conductivity and $\overline{\boldsymbol{\varepsilon}}_{\mathrm{r}}(\boldsymbol{r})$ the real part of the relative permittivity. Consequently the equivalent magnetic current density in (4.10) vanishes and the scattered field becomes

$$\begin{aligned}\boldsymbol{E}_{\mathrm{sca}}(\boldsymbol{r}) &= \iiint_V \overline{\mathbf{G}}_J^E(\boldsymbol{r},\boldsymbol{r}') \cdot \boldsymbol{J}_{\mathrm{eq}}(\boldsymbol{r}')\,\mathrm{d}v' \\ &= \iiint_V \overline{\mathbf{G}}_e(\boldsymbol{r},\boldsymbol{r}') \cdot \omega^2\mu_0 \left(\overline{\boldsymbol{\varepsilon}}(\boldsymbol{r}') - \varepsilon_0\bar{\mathbf{I}}\right) \cdot \boldsymbol{E}(\boldsymbol{r}')\,\mathrm{d}v' \\ &= \iiint_V \overline{\mathbf{G}}_e(\boldsymbol{r},\boldsymbol{r}') \cdot \bar{\mathbf{s}}(\boldsymbol{r}') \cdot \boldsymbol{E}(\boldsymbol{r}')\,\mathrm{d}v', \end{aligned} \tag{4.18}$$

where $\overline{\mathbf{G}}_e$ is the dyadic Green's function of the electric field as defined in (2.18) and

$$\bar{\mathbf{s}}(\boldsymbol{r}') = \omega^2\mu_0\varepsilon_0 \left(\overline{\boldsymbol{\varepsilon}}_{\mathrm{r}}(\boldsymbol{r}') - \bar{\mathbf{I}}\right) = k^2 \left(\overline{\boldsymbol{\varepsilon}}'(\boldsymbol{r}') - \mathrm{j}\frac{\overline{\boldsymbol{\kappa}}(\boldsymbol{r}')}{\omega\varepsilon_0} - \bar{\mathbf{I}}\right) \tag{4.19}$$

is the spatial scattering center distribution of the object (also known as reflectivity or reflectance distribution). In the case of a low conductivity, i.e., $\kappa(\boldsymbol{r}') \ll \varepsilon'(\boldsymbol{r}')$, the spatial scattering center distribution may be approximated by

$$\bar{\mathbf{s}}(\boldsymbol{r}') \approx k^2 \left(\overline{\boldsymbol{\varepsilon}}'(\boldsymbol{r}') - \bar{\mathbf{I}}\right), \tag{4.20}$$

which is also known as the contrast function. After multiplication with $\boldsymbol{E}(\boldsymbol{r}')$ in (4.18) this term will correspond to the contributions of electric displacement current densities. On the other hand, for a high conductivity with $\kappa(\boldsymbol{r}') \gg \varepsilon'(\boldsymbol{r}')$ (the actually more relevant case in RCS measurements) one obtains

$$\bar{\mathbf{s}}(\boldsymbol{r}') \approx kZ_{\mathrm{F}} \left(-\mathrm{j}\overline{\boldsymbol{\kappa}}(\boldsymbol{r}') - \bar{\mathbf{I}}\right), \tag{4.21}$$

which leads to induced Ohmic current densities.

4.4.1 The Born Approximation

In order to remove the dependence of the total field in (4.18) it is common to employ the first order Born approximation[2] and replace the total field at the scatterer by the incident field [Devaney 2012, p. 256]. Thus, the scattered electric field may be expressed as

$$\boldsymbol{E}_{\mathrm{sca}}(\boldsymbol{r}) = \iiint_V \overline{\mathbf{G}}_e(\boldsymbol{r},\boldsymbol{r}') \cdot \bar{\mathbf{s}}(\boldsymbol{r}') \cdot \boldsymbol{E}_{\mathrm{inc}}(\boldsymbol{r}')\,\mathrm{d}v', \tag{4.22}$$

which is again a linear integral representation depending directly on the material parameters and the (usually known) incident field. As discussed in [Chew 1995, p. 485], the Born approximation is based on a single scatterer assumption, that is multiple interactions at the

[2] Named after Max Born for his work on quantum mechanics [Born 1926].

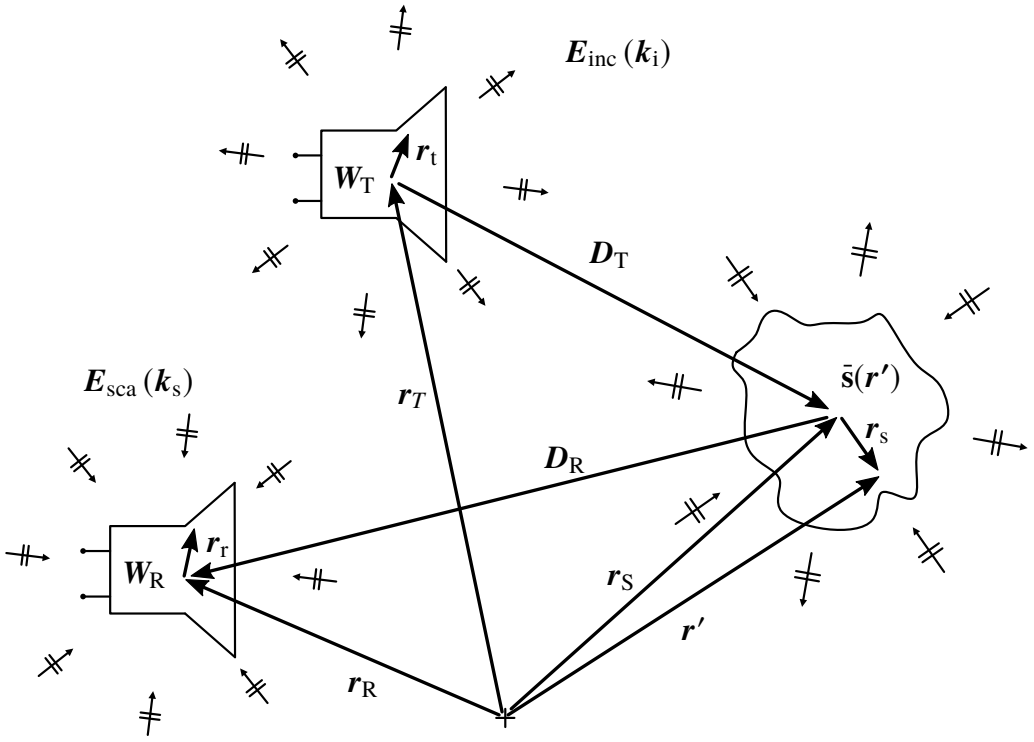

Figure 4.2: Linearized near-field scattering measurement scenario: The scattering object on the right is characterized by its spatial scattering center distribution $\bar{\mathbf{s}}(\boldsymbol{r}')$. Incident and scattered field are expanded in propagating plane-wave spectra.

object are neglected. Moreover, in a strict sense its validity is limited to weakly scattering targets with $\varepsilon_{\mathrm{r}}(\boldsymbol{r}') \approx 1$. Nonetheless, due to the simplicity of the resulting relation it is widely used in radar imaging, although its application may lead to imaging artifacts ("ghost targets") when multiple interactions occur at the target [Cheney and Borden 2009, p. 54]. As the RCS of many objects can be characterized quite well by only a few scattering centers (whose actual physical location is often not the primary concern), relatively accurate results in near-field RCS measurement are still possible within the scope of the Born approximation [LaHaie 2003].

4.4.2 Propagating Plane-Wave Expansion

The incident and scattered electric field in (4.22) may be expanded in propagating plane waves to obtain again an efficient (i.e., diagonalized) near-field transmission equation between the transmitting and receiving antenna in a scattering experiment or RCS measurement setup. To this end the near-field scattering measurement setup depicted in Figure 4.2 is considered. The transmitting (Tx) antenna with gain normalized far-field pattern $\boldsymbol{W}_{\mathrm{T}}$ creates the incident electric field $\boldsymbol{E}_{\mathrm{inc}}$ at the scatterer with spatial scattering center distribution $\bar{\mathbf{s}}$. The interaction of the incident field and the scattering dyad gives rise to the scattered field $\boldsymbol{E}_{\mathrm{sca}}$ at the receiving antenna with far-field pattern $\boldsymbol{W}_{\mathrm{R}}$. It is assumed here that any direct coupling between the two antennas, that is the incident field in (4.7), has been subtracted beforehand as it is customary in RCS measurements [Knott 2006, p. 377]. The wave vectors of the propagating plane waves

in the spectrum of the incident field are denoted as $\boldsymbol{k}_\mathrm{i}$ (they originate from the Tx antenna). Using the field expansions as in Section 2.4.2 the electric field due to the Tx antenna at $\boldsymbol{r}_\mathrm{T}$ that is incident at the scatterer may be written as

$$\boldsymbol{E}_\mathrm{inc}(\boldsymbol{r}') = \oiint \mathrm{e}^{-\mathrm{j}\boldsymbol{k}_\mathrm{i}\cdot\boldsymbol{r}_\mathrm{s}} T_L(\boldsymbol{k}_\mathrm{i}, \boldsymbol{D}_\mathrm{T})\, a\sqrt{\frac{Z_F}{4\pi}}\boldsymbol{W}_\mathrm{T}(\boldsymbol{k}_\mathrm{i})\, \mathrm{d}^2\hat{k}_\mathrm{i}, \tag{4.23}$$

where a is the input power wave at the Tx antenna, $\boldsymbol{D}_\mathrm{T} = \boldsymbol{r}_\mathrm{S} - \boldsymbol{r}_\mathrm{T}$ and T_L the FMM translation operator of order L. Within the first order Born approximation, the resulting scattered field at $\boldsymbol{r} = \boldsymbol{r}_\mathrm{R} + \boldsymbol{r}_\mathrm{r}$ can then be expressed as

$$\boldsymbol{E}_\mathrm{sca}(\boldsymbol{r}) = \iiint_V \overline{\mathbf{G}}_e(\boldsymbol{r}, \boldsymbol{r}') \cdot \bar{\mathbf{s}}(\boldsymbol{r}') \cdot \oiint \mathrm{e}^{-\mathrm{j}\boldsymbol{k}_\mathrm{i}\cdot\boldsymbol{r}_\mathrm{s}} T_L(\boldsymbol{k}_\mathrm{i}, \boldsymbol{D}_\mathrm{T})\, a\sqrt{\frac{Z_\mathrm{F}}{4\pi}}\boldsymbol{W}_\mathrm{T}(\boldsymbol{k}_\mathrm{i})\, \mathrm{d}^2\hat{k}_\mathrm{i}\, \mathrm{d}v'. \tag{4.24}$$

Expanding also the Green's function $\overline{\mathbf{G}}_e$ into outgoing (scattered) propagating plane waves $\boldsymbol{k}_\mathrm{s}$, i.e.,

$$\overline{\mathbf{G}}_e(\boldsymbol{r}_\mathrm{R} + \boldsymbol{r}_\mathrm{r}, \boldsymbol{r}') = \frac{1}{4\pi}\oiint \left(\bar{\mathbf{I}} - \hat{k}_\mathrm{s}\hat{k}_\mathrm{s}\right) \mathrm{e}^{-\mathrm{j}\boldsymbol{k}_\mathrm{s}\cdot\boldsymbol{d}} T_L(\boldsymbol{k}_\mathrm{s}, \boldsymbol{D}_\mathrm{R})\, \mathrm{d}^2\hat{k}_\mathrm{s}, \tag{4.25}$$

where $\boldsymbol{D}_\mathrm{R} = \boldsymbol{r}_\mathrm{R} - \boldsymbol{r}_\mathrm{S}$ and $\boldsymbol{d} = \boldsymbol{r}_\mathrm{r} - \boldsymbol{r}_\mathrm{s}$, the scattered field becomes after interchanging the order of the integrals

$$\begin{aligned}\boldsymbol{E}_\mathrm{sca}(\boldsymbol{r}) = {} & \oiint \left(\bar{\mathbf{I}} - \hat{k}_\mathrm{s}\hat{k}_\mathrm{s}\right) \mathrm{e}^{-\mathrm{j}\boldsymbol{k}_\mathrm{s}\cdot\boldsymbol{r}_\mathrm{r}} T_L(\boldsymbol{k}_\mathrm{s}, \boldsymbol{D}_\mathrm{R}) \\ & \cdot \oiint \iiint_V \bar{\mathbf{s}}(\boldsymbol{r}')\, \mathrm{e}^{\mathrm{j}(\boldsymbol{k}_\mathrm{s}-\boldsymbol{k}_\mathrm{i})\cdot\boldsymbol{r}_\mathrm{s}}\, \mathrm{d}v' \cdot T_L(\boldsymbol{k}_\mathrm{i}, \boldsymbol{D}_\mathrm{T})\, a\sqrt{\frac{Z_\mathrm{F}}{4\pi}}\boldsymbol{W}_\mathrm{T}(\boldsymbol{k}_\mathrm{i})\, \mathrm{d}^2\hat{k}_i\, \mathrm{d}^2\hat{k}_s \qquad (4.26) \\ = {} & \oiint \mathrm{e}^{-\mathrm{j}\boldsymbol{k}_s\cdot\boldsymbol{r}_r} T_L(\boldsymbol{k}_s, \boldsymbol{D}_R) \\ & \cdot \oiint \bar{\mathbf{S}}(\boldsymbol{k}_\mathrm{s}, -\boldsymbol{k}_\mathrm{i})\, \mathrm{e}^{-\mathrm{j}(\boldsymbol{k}_\mathrm{s}-\boldsymbol{k}_\mathrm{i})\cdot\boldsymbol{r}_\mathrm{S}} \cdot T_L(\boldsymbol{k}_\mathrm{i}, \boldsymbol{D}_\mathrm{T})\, a\sqrt{\frac{Z_\mathrm{F}}{4\pi}}\boldsymbol{W}_\mathrm{T}(\boldsymbol{k}_\mathrm{i})\, \mathrm{d}^2\hat{k}_\mathrm{i}\, \mathrm{d}^2\hat{k}_\mathrm{s}. \qquad (4.27)\end{aligned}$$

Here

$$\bar{\mathbf{S}}(\boldsymbol{k}_\mathrm{s}, -\boldsymbol{k}_\mathrm{i}) = \left(\bar{\mathbf{I}} - \hat{k}_s\hat{k}_s\right) \iiint_V \bar{\mathbf{s}}(\boldsymbol{r}')\, \mathrm{e}^{\mathrm{j}(\boldsymbol{k}_\mathrm{s}-\boldsymbol{k}_\mathrm{i})\cdot\boldsymbol{r}'}\, \mathrm{d}v' \tag{4.28}$$

is the bistatic (plane-wave) scattering matrix in k-space, shifted in (4.27) to the reference location $\boldsymbol{r}_\mathrm{S}$. It relates each incident plane wave with $-\boldsymbol{k}_\mathrm{i}$ at the scatterer to a scattered plane wave with $\boldsymbol{k}_\mathrm{s}$. The double k-space integral accounts for the fact that each plane wave in the spectrum of the incident field gives rise to a full spectrum of scattered plane waves.

The sphere that is described by the full angular spectrum of $\boldsymbol{k}_\mathrm{s}$ for each $\boldsymbol{k}_\mathrm{i}$ in (4.28) is called the Ewald sphere [Devaney 2012, p. 257], a 2D illustration is shown in Figure 4.3. The outer sphere defines the upper spatial frequency limit that is only reached by monostatic configurations ($\boldsymbol{k}_\mathrm{s} = -\boldsymbol{k}_\mathrm{i}$). For single-frequency setups, a full set of bistatic scattering data (i.e., an infinite number of Ewald spheres for all different $\boldsymbol{k}_\mathrm{i}$) is needed to span the full space up to $2k$. Using broadband monostatic configurations, the spanned space will be a spherical

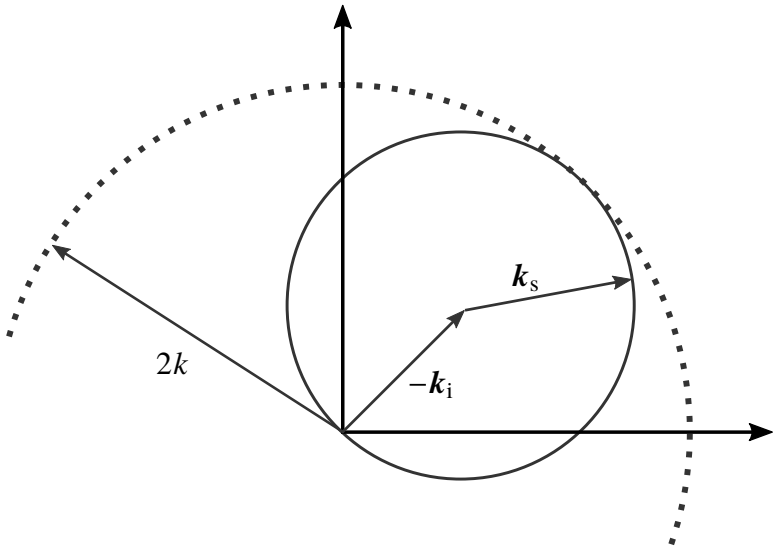

Figure 4.3: 2D illustration of the Ewald sphere (solid line) defined by the wave vectors $-\boldsymbol{k}_\mathrm{i}$ and $\boldsymbol{k}_\mathrm{s}$ of incident and scattered plane waves, respectively. The outer sphere (dotted line) defines the upper spatial frequency limit that is reached in a monostatic setup.

shell centered at the origin with inner radius k_min and outer radius k_max. In either case, if one wants to determine the spatial scattering center distribution $\bar{\mathbf{s}}(\boldsymbol{r})$ from the scattering matrix $\bar{\mathbf{S}}(\boldsymbol{k}_\mathrm{s}, -\boldsymbol{k}_\mathrm{i})$ the inverse Fourier integral of (4.28) has to be computed, that is

$$\tilde{\mathbf{s}}(\boldsymbol{r}) = \iiint\limits_{\boldsymbol{K}} \bar{\mathbf{S}}(\boldsymbol{k}_\mathrm{s}, -\boldsymbol{k}_\mathrm{i})\, \mathrm{e}^{-\mathrm{j}(\boldsymbol{k}_\mathrm{s}-\boldsymbol{k}_\mathrm{i})\cdot\boldsymbol{r}}\, \mathrm{d}^3\boldsymbol{k}, \tag{4.29}$$

where $\boldsymbol{K}$ denotes the available k-space area. Due to the upper frequency limit of k, (4.29) will always be a low-pass filtered representation of the true $\bar{\mathbf{s}}(\boldsymbol{r})$. In most practical measurement cases also the angular range of incident and scattered plane waves is limited. As will be discussed in the context of spatial imaging, these 3D filtering processes in k-space lead to the characteristic point spread function (PSF) of an imaging system that limits its spatial resolution [Mensa 1990, p. 143].

4.4.3 Near-field Transmission Equation in k-space

By employing the reciprocity relation (3.1) at the receiving (Rx) antenna as it was done for near-field antenna measurements in Section 3.1, one obtains from (4.27) the linearized k-space transmission equation for near-field scattering measurements

$$S_{21} = \frac{1}{\mathrm{j}2k} \oiint \boldsymbol{W}_\mathrm{R}(-\boldsymbol{k}_\mathrm{s})\, T_L(\boldsymbol{k}_\mathrm{s}, \boldsymbol{D}_\mathrm{R}) \cdot \oiint \bar{\mathbf{S}}(\boldsymbol{k}_\mathrm{s}, -\boldsymbol{k}_\mathrm{i}) \cdot T_L(\boldsymbol{k}_\mathrm{i}, \boldsymbol{D}_\mathrm{T})\, \boldsymbol{W}_\mathrm{T}(\boldsymbol{k}_\mathrm{i})\, \mathrm{d}^2\hat{k}_\mathrm{i}\, \mathrm{d}^2\hat{k}_\mathrm{s}, \tag{4.30}$$

where for convenience of notation it is assumed that $\boldsymbol{r}_\mathrm{S} = 0$, i.e., the scatterer resides at the origin of the coordinate system. Similar to the antenna measurement case, it is possible to express the gain normalized probe patterns $\boldsymbol{W}_\mathrm{R}$ and $\boldsymbol{W}_\mathrm{T}$ in their own local coordinate systems

and use rotation matrices to transform them into the coordinate system of the scatterer which serves as the reference. As the procedure is completely analogous to the one already described in Section 3.1 it is omitted here.

As noted before, the full bistatic scattering matrix $\bar{\mathbf{S}}(\boldsymbol{k}_\mathrm{s}, -\boldsymbol{k}_\mathrm{i})$ relates all plane waves of the incident field spectrum to all plane waves of the scattered field spectrum. In this respect it can be seen as an FMM propagating plane-wave version of the "reduced reflection integral" derived by Dinallo [1984], who employed plane waves defined over two reference planes between the scatterer and the Tx and Rx antenna. The problem is that, assuming the number of components in the incident and scattered plane-wave spectrum is $N_\vartheta \times N_\varphi$, the number of unknowns in $\bar{\mathbf{S}}$ will be $\left(N_\vartheta \times N_\varphi\right)^2$. Consequently, a full set of bistatic near-field measurements would be necessary to solve for $\bar{\mathbf{S}}$ exactly, which of course is difficult to realize in practice. However, as will be shown, it is possible to obtain an approximate solution of the monostatic scattering matrix by assuming the scatterer itself to be the source of radiation. In that case only monostatic measurements are required.

4.4.4 The Limiting Far-Field Case - Radar Range Equation

The bistatic transmission equation in (4.30) already simplifies significantly if the incident field is a single plane wave. Assuming the transmitting antenna is located sufficiently far away from the scatterer the far-field approximation of the translation operator as given by (2.61) can be employed. Consequently (4.30) reduces to

$$S_{21} = \frac{1}{\mathrm{j}2k} \oiint \boldsymbol{W}_\mathrm{R}(-\boldsymbol{k}_\mathrm{s})\, T_L(\boldsymbol{k}_\mathrm{s}, \boldsymbol{D}_\mathrm{R}) \cdot \bar{\mathbf{S}}\left(\boldsymbol{k}_\mathrm{s}, -\hat{D}_\mathrm{T}\right) \cdot \boldsymbol{W}_\mathrm{T}\left(\hat{D}_\mathrm{T}\right) \frac{\mathrm{e}^{-\mathrm{j}kD_\mathrm{T}}}{D_\mathrm{T}}\, \mathrm{d}^2\hat{k}_\mathrm{s}, \tag{4.31}$$

which is again an integral representation of the form encountered before in the context of near-field antenna measurements. If also the receiving antenna resides in the far field of the scatterer, employing the same approximation for the translation operator of the scattered field yields

$$S_{21} = \frac{1}{\mathrm{j}2k} \boldsymbol{W}_\mathrm{R}\left(-\hat{D}_\mathrm{R}\right) \frac{\mathrm{e}^{-\mathrm{j}kD_\mathrm{R}}}{D_\mathrm{R}} \cdot \bar{\mathbf{S}}\left(\hat{D}_\mathrm{R}, -\hat{D}_\mathrm{T}\right) \cdot \boldsymbol{W}_\mathrm{T}\left(\hat{D}_\mathrm{T}\right) \frac{\mathrm{e}^{-\mathrm{j}kD_\mathrm{T}}}{D_\mathrm{T}}. \tag{4.32}$$

In terms of powers this corresponds directly to the classical radar range equation, which can be seen by evaluating

$$|S_{21}|^2 = \frac{P_\mathrm{Rx}}{P_\mathrm{Tx}} = \left(\frac{\lambda}{4\pi}\right)^2 \|\boldsymbol{W}_\mathrm{R}\left(-\hat{D}_\mathrm{R}\right)\|^2 \frac{1}{D_\mathrm{R}^2} \|\bar{\mathbf{S}}\left(\hat{D}_\mathrm{R}, -\hat{D}_\mathrm{T}\right)\|^2 \|\boldsymbol{W}_\mathrm{T}\left(\hat{D}_\mathrm{T}\right)\|^2 \frac{1}{D_\mathrm{T}^2} \tag{4.33}$$

$$= A_\mathrm{R}\left(-\hat{D}_\mathrm{R}\right) \frac{1}{4\pi D_\mathrm{R}^2} \sigma\left(\hat{D}_\mathrm{R}, -\hat{D}_\mathrm{T}\right) G_\mathrm{T}\left(\hat{D}_\mathrm{T}\right) \frac{1}{4\pi D_\mathrm{T}^2}, \tag{4.34}$$

where

$$A_\mathrm{R}\left(-\hat{D}_\mathrm{R}\right) = \frac{\lambda^2}{4\pi} G_\mathrm{R}\left(-\hat{D}_\mathrm{R}\right) \tag{4.35}$$

is the effective area of the receiving antenna with respect to a plane wave that is incident from the angular direction of $\hat{D}_\mathrm{R}$. Similarly, $G_\mathrm{T}\left(\hat{D}_\mathrm{R}\right)$ is the gain of the transmitting antenna in the

direction of $\hat{D}_\mathrm{T}$ and

$$\sigma\left(\hat{D}_\mathrm{R}, -\hat{D}_\mathrm{T}\right) = 4\pi \left| \hat{u}_R \cdot \bar{\mathbf{S}}\left(\hat{D}_\mathrm{R}, -\hat{D}_\mathrm{T}\right) \cdot \hat{u}_T \right|^2 \tag{4.36}$$

is the corresponding bistatic RCS, where $\hat{u}_R$ and $\hat{u}_T$ are the polarization vectors of the receiving and transmitting probe antenna, respectively. As it was already noted for the Friis equation in Section 3.1.2, the expansion of the incident and scattered field in spectra of propagating plane waves as given by (4.27) can be thought of being a near-field generalization to the (single plane wave) far-field case of the classical radar range equation.

4.4.5 Monostatic Solution - The Radiating Reflectors Model

In most practical measurement scenarios it will be unfeasible to acquire a full set of bistatic scattering data to solve (4.30) for the complete bistatic scattering matrix $\bar{\mathbf{S}}$. Intuitively, since one is usually interested in determining the monostatic RCS, it would be desirable to solve this task by only acquiring monostatic scattering data in the near field. Restricting $\bar{\mathbf{S}}$ to only monostatic scattering, i.e., $\boldsymbol{k}_\mathrm{s} = -\boldsymbol{k}_\mathrm{i} = \boldsymbol{k}$, the sought solution is

$$\bar{\mathbf{S}}\left(\boldsymbol{k}_\mathrm{s}, -\boldsymbol{k}_\mathrm{i}\right) = \iiint\limits_V \bar{\mathbf{s}}\left(\boldsymbol{r}'\right) \mathrm{e}^{\mathrm{j}(\boldsymbol{k}_\mathrm{s}-\boldsymbol{k}_\mathrm{i})\cdot\boldsymbol{r}'}\, \mathrm{d}v' = \iiint\limits_V \bar{\mathbf{s}}\left(\boldsymbol{r}'\right) \mathrm{e}^{\mathrm{j}2\boldsymbol{k}\cdot\boldsymbol{r}'}\, \mathrm{d}v' = \bar{\mathbf{S}}\left(2\boldsymbol{k}\right), \tag{4.37}$$

which corresponds to the outer k-space sphere in Figure 4.3. By comparison with the antenna measurement case, where the plane-wave spectrum of some radiating current density was obtained by evaluating the far-field pattern on the sphere with radius k, one can think of (4.37) to be the result of the scattering center distribution to simultaneously radiate itself, however at only half the wave speed $c = c_0/2$ leading to the exponential $2\boldsymbol{k}$. This concept of the "radiating reflectors" originates from geophysics, where it was used in imaging algorithms for earth exploration [Claerbout 1985]. It was adapted for SAR and ISAR imaging by Cafforio et al. [1991] and Fortuny [1998], respectively. The spatial frequency formulation using propagating plane-wave spectra employed here was introduced by Schnattinger et al. [2014]. In a slightly modified form, using the gain normalized probe patterns and working with the transmission factor S_{21} as the measured quantity, one obtains

$$S_{21} = \frac{1}{\mathrm{j}2k} \oiint T_L\left(2\boldsymbol{k}, \boldsymbol{D}\right) \frac{1}{|\boldsymbol{D}|} \boldsymbol{W}_\mathrm{R}\left(-\boldsymbol{k}\right) \cdot \bar{\mathbf{S}}\left(2\boldsymbol{k}\right) \cdot \boldsymbol{W}_\mathrm{T}\left(\boldsymbol{k}\right)\, \mathrm{d}^2\hat{k} \tag{4.38}$$

where a monostatic measurement setup with $\boldsymbol{D}_\mathrm{R} = \boldsymbol{D}_\mathrm{T} = \boldsymbol{D}$ was assumed. The actual two-way propagation between the Tx/Rx antenna is modeled by the modified translation operator $T_L\left(2\boldsymbol{k}, \boldsymbol{D}\right)$. As this correctly accounts only for the phase, an additional magnitude correction factor $1/|\boldsymbol{D}|$ has been introduced to account for the $1/r^2$ dependency. To illustrate this, consider the multiplication of two scalar Green's functions as it will occur for such a scattering scenario, that is

$$G(\boldsymbol{r}, \boldsymbol{r}')G(\boldsymbol{r}, \boldsymbol{r}') = \frac{\mathrm{e}^{-\mathrm{j}2k|\boldsymbol{r}-\boldsymbol{r}'|}}{|\boldsymbol{r}-\boldsymbol{r}'|^2}. \tag{4.39}$$

Using the propagating plane-wave expansion according to (2.43), this is approximated by

$$\frac{\mathrm{e}^{-\mathrm{j}2k|\boldsymbol{r}-\boldsymbol{r}'|}}{|\boldsymbol{r}-\boldsymbol{r}'|^2} = \frac{\mathrm{e}^{-\mathrm{j}2k|\boldsymbol{D}+\boldsymbol{d}|}}{|\boldsymbol{D}+\boldsymbol{d}|^2} \approx \oiint \mathrm{e}^{-\mathrm{j}2\boldsymbol{k}\cdot\boldsymbol{d}} T_L\left(2kD, \hat{k}\cdot\hat{D}\right) \frac{1}{|\boldsymbol{D}|}\, \mathrm{d}^2\hat{k} \tag{4.40}$$

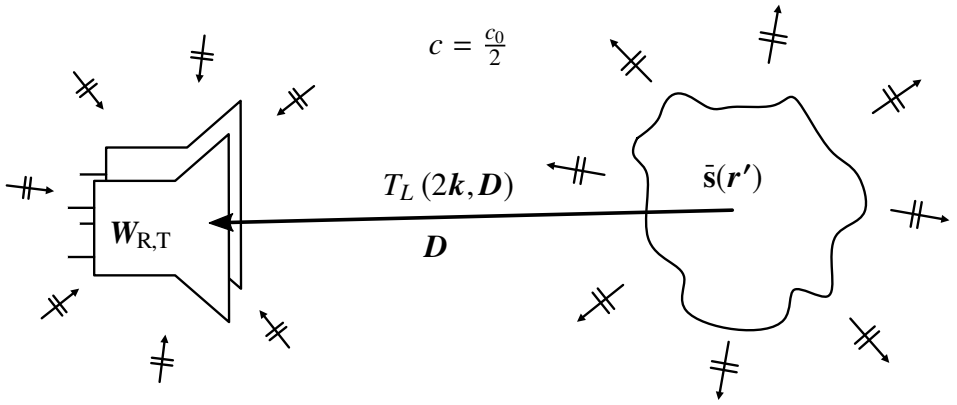

Figure 4.4: Monostatic near-field scattering setup under the assumption of "radiating reflectors". The scattering center distribution $\bar{\mathbf{s}}\,(\boldsymbol{r}')$ "radiates" the scattered field at one half of the original wave velocity c_0.

where the definition of $\boldsymbol{D}$ and $\boldsymbol{d}$ follows the general FMM scheme with respect to Figure 2.4. The additional $1/|\boldsymbol{D}|$ term can be interpreted as an excitation dependent weighting factor for the (radiating) equivalent sources.

For each k-space sample in (4.38), the multiplication of the Tx and Rx antenna patterns, typically given in terms of their spherical field components $W^{\mathrm{T}}_{\vartheta/\varphi}$ and $W^{\mathrm{R}}_{\vartheta/\varphi}$, respectively, with the scattering matrix $\bar{\mathbf{S}}$ has to be evaluated. By noting that

$$\boldsymbol{W}_{\mathrm{R}}\,(-\boldsymbol{k})\cdot\bar{\mathbf{S}}\,(2\boldsymbol{k})\cdot\boldsymbol{W}_{\mathrm{T}}\,(\boldsymbol{k}) = \begin{bmatrix} W^{\mathrm{R}}_{\vartheta}\,(-\boldsymbol{k}) \\ W^{\mathrm{R}}_{\varphi}\,(-\boldsymbol{k}) \end{bmatrix} \cdot \begin{bmatrix} S_{\mathrm{VV}}\,(2\boldsymbol{k}) & S_{\mathrm{VH}}\,(2\boldsymbol{k}) \\ S_{\mathrm{HV}}\,(2\boldsymbol{k}) & S_{\mathrm{HH}}\,(2\boldsymbol{k}) \end{bmatrix} \cdot \begin{bmatrix} W^{\mathrm{T}}_{\vartheta}\,(\boldsymbol{k}) \\ W^{\mathrm{T}}_{\varphi}\,(\boldsymbol{k}) \end{bmatrix} \tag{4.41}$$

where due to reciprocity for most scattering objects $S_{\mathrm{HV}} = S_{\mathrm{VH}}$, one may rewrite the above multiplication to obtain

$$\begin{aligned} \boldsymbol{W}_{\mathrm{R}}\,(-\boldsymbol{k})\cdot\bar{\mathbf{S}}\,(2\boldsymbol{k})\cdot\boldsymbol{W}_{\mathrm{T}}\,(\boldsymbol{k}) &= \begin{bmatrix} W^{\mathrm{R}}_{\vartheta}\,(-\boldsymbol{k})\,W^{\mathrm{T}}_{\vartheta}\,(\boldsymbol{k}) \\ W^{\mathrm{R}}_{\varphi}\,(-\boldsymbol{k})\,W^{\mathrm{T}}_{\varphi}\,(\boldsymbol{k}) \\ W^{\mathrm{R}}_{\varphi}\,(-\boldsymbol{k})\,W^{\mathrm{T}}_{\vartheta}\,(\boldsymbol{k}) + W^{\mathrm{R}}_{\vartheta}\,(-\boldsymbol{k})\,W^{\mathrm{T}}_{\varphi}\,(\boldsymbol{k}) \end{bmatrix} \cdot \begin{bmatrix} S_{\mathrm{VV}}\,(2\boldsymbol{k}) \\ S_{\mathrm{HH}}\,(2\boldsymbol{k}) \\ S_{\mathrm{HV}}\,(2\boldsymbol{k}) \end{bmatrix} \\ &= \check{\boldsymbol{W}}\,(\boldsymbol{k})\cdot\check{\mathbf{S}}\,(2\boldsymbol{k})\,. \end{aligned} \tag{4.42}$$

Consequently, the transmission equation for the near-field scattering problem employing the radiating reflectors model becomes

$$S_{21} = \frac{1}{\mathrm{j}2k}\oiint T_L\,(2\boldsymbol{k},\boldsymbol{D})\,\frac{1}{|\boldsymbol{D}|}\check{\boldsymbol{W}}\,(\boldsymbol{k})\cdot\check{\mathbf{S}}\,(2\boldsymbol{k})\;\mathrm{d}^2\hat{k}, \tag{4.43}$$

which has now again the form of the linear integral equation encountered in the case of antenna measurements, however, with the vectors $\check{\boldsymbol{W}}\,(\boldsymbol{k})$ and $\check{\mathbf{S}}\,(2\boldsymbol{k})$ having three field components now as defined above. Obviously, for a true monostatic setup with only a single antenna for transmission and reception one has $\boldsymbol{W}_{\mathrm{R}}\,(-\boldsymbol{k}) = \boldsymbol{W}_{\mathrm{T}}\,(\boldsymbol{k}) = \boldsymbol{W}\,(\boldsymbol{k})$ and the expression for $\check{\boldsymbol{W}}$

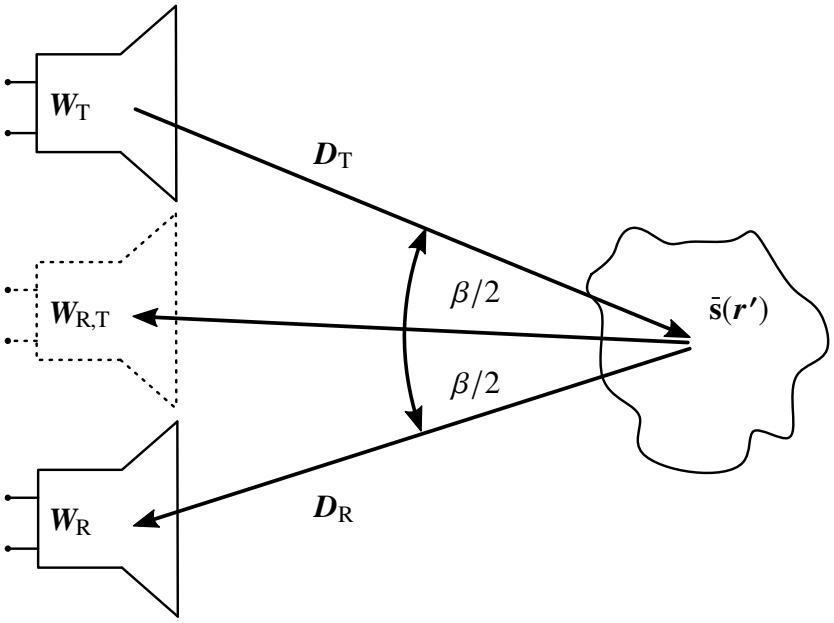

Figure 4.5: Linearized near-field scattering measurement scenario with quasi monostatic setup. The two separated Tx and Rx antennas are assumed to reside at the same position, defined by the bistatic angle β.

simplifies to

$$\breve{\boldsymbol{W}}\left(\boldsymbol{k}\right) = \begin{bmatrix} W_\vartheta^2\left(\boldsymbol{k}\right) \\ W_\varphi^2\left(\boldsymbol{k}\right) \\ 2W_\varphi\left(\boldsymbol{k}\right) W_\vartheta\left(\boldsymbol{k}\right) \end{bmatrix}. \tag{4.44}$$

Quasi-monostatic setups

In the realization of a monostatic scattering measurement setup it may be beneficial to work with separated Tx and Rx antennas to avoid the requirement of a splitting network and allow the operation in a continuous wave (CW) mode. In case the two antennas are located close to each other and separated by a fixed bistatic angle β, the combined probe pattern in (4.42) can be used to account explicitly for the probe patterns of both antennas while their common location is assumed to be at an angle $\beta/2$ in between them (see Figure 4.5). This is a consequence of the monostatic-bistatic equivalence principle established by Kell [1965]. As illustrated by the wave vectors in Figure 4.6, for a fixed bistatic angle β between incident and scattered plane wave, the equivalent monostatic plane-wave spectrum is given by a circle (a sphere in 3D) with radius $2k_\mathrm{mono} < 2k$, where the frequency is reduced by $f_\mathrm{mono} = f\cos(\beta/2)$. However, as the assumption is only valid for relatively small bistatic angles, the frequency shift may be considered negligible in many cases [Bradley et al. 2008].

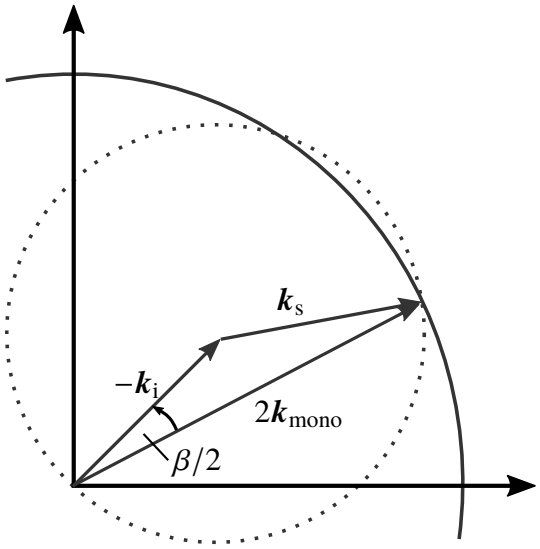

Figure 4.6: 2D illustration of the monostatic-bistatic equivalence principle. For a fixed bistatic angle between the wave vectors $-\boldsymbol{k}_\mathrm{i}$ and $\boldsymbol{k}_\mathrm{s}$, an equivalent quasi-monostatic setup can be defined with $2\boldsymbol{k}_\mathrm{mono}$.

Near-field Scattering Transformation Algorithm

In the form given by (4.43) the near-field scattering transmission equation can be used to setup a linear inverse source problem for the determination of the unknown monostatic scattering matrix $\bar{\mathbf{S}}$. The procedure then closely resembles the one employed for the antenna measurement case, whose implementation has been described in Section 3.2. Of course the near-field input measurement data is here the result of a monostatic scattering measurement. In particular, it is also possible to work with hierarchical MLFMM schemes, where the plane-wave spectra now consist of the three scattering matrix entries in $\check{\mathbf{S}}(2\boldsymbol{k})$. As a result of the "radiating reflectors" model where the wave velocity of the one way propagation is considered to be only one half of the true velocity, the spatial frequency is effectively doubled. Consequently, also the discretization of the plane-wave spectra must be chosen finer. In general twice the number of samples along ϑ and φ are needed. On the standard equiangular spherical grid this leads to

$$N_\varphi \geq \lceil 2ka \rceil \tag{4.45}$$

and

$$N_\vartheta \geq \lceil ka \rceil, \tag{4.46}$$

where a is the radius of the minimum sphere enclosing the scatterer. The same holds for the unknown scattering matrix entries that are also represented in terms of the coefficients of a plane-wave spectrum, and of course for the required number of measurement samples that has to be chosen accordingly. Consequently, compared to the antenna radiation case the total number of all coefficients is increased by a number of four.

In the MLFMM scheme implementation of the algorithm, translations of propagating plane-wave spectra may occur on different levels of the corresponding octree(s). As depicted in Figure 4.7, the translation distance between the source box q and the destination box p is

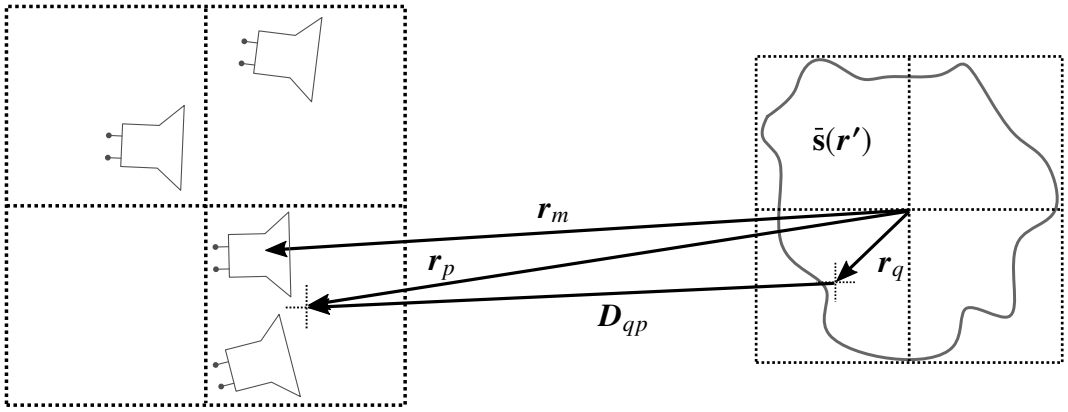

Figure 4.7: MLFMM implementation of the radiating reflectors based near-field scattering transformation algorithm.

$\boldsymbol{D}_{qp} = \boldsymbol{r}_q - \boldsymbol{r}_p$. In order to accurately account for the $1/r^2$ weighting when employing the radiating reflectors model, a magnitude correction of the translation operator is performed as described in [Schnattinger et al. 2014] by using

$$\frac{T_L\left(2\boldsymbol{k}, \boldsymbol{D}_{qp}\right)}{\left|\boldsymbol{D}_{qp}\right|} \frac{\left|\boldsymbol{r}_p\right|}{\left|\boldsymbol{r}_m\right|}. \tag{4.47}$$

Thus, for the case shown in Figure 4.7, the complete transmission equation to the measurement sample at $\boldsymbol{r}_m$ follows from summing all Q translated plane-wave spectra from the scatterer, that is

$$S_{21}\left(\boldsymbol{r}_m\right) = \frac{1}{\mathrm{j}2k} \oiint \check{\boldsymbol{W}}_m\left(\boldsymbol{k}\right) \mathrm{e}^{-\mathrm{j}\boldsymbol{k}\cdot\left(\boldsymbol{r}_m - \boldsymbol{r}_p\right)} \cdot \frac{\left|\boldsymbol{r}_p\right|}{\left|\boldsymbol{r}_m\right|} \sum_{q=1}^{Q} \frac{T_L\left(2\boldsymbol{k}, \boldsymbol{D}_{qp}\right)}{\left|\boldsymbol{D}_{qp}\right|} \check{\mathbf{S}}_q\left(2\boldsymbol{k}\right) \, \mathrm{d}^2\hat{k}, \tag{4.48}$$

where the exponential $\mathrm{e}^{-\mathrm{j}\boldsymbol{k}\cdot\left(\boldsymbol{r}_m - \boldsymbol{r}_p\right)}$ accounts for the phase shift between the actual measurement position $\boldsymbol{r}_m$ and the box center of the receiving group $\boldsymbol{r}_p$. It may be noted that this magnitude correction is not optimal since ideally one would correct the translation operator by a factor of $1/\left|\boldsymbol{r}_m - \boldsymbol{r}_q\right|$. However, to fully benefit from the hierarchical MLFMM structure it is not possible to separately correct all translated (incident) plane-wave spectra at the receiver side for all different measurement locations $\boldsymbol{r}_m$ within one group. The magnitude correction presented here provides a good compromise and allows one to correct the translation operator at different steps during the setup process of the algorithm. The correction with $1/\left|\boldsymbol{D}_{qp}\right|$ can be performed directly when computing the translation operator, the factor $\left|\boldsymbol{r}_p\right|$ is applied for every receiver group and, finally, the receive spectrum at every measurement location is divided by $1/|\boldsymbol{r}_m|$. The linear system of equations that results from sampling monostatically the scattered field is solved in a least squares sense by means of the GMRES method as already described in Section 2.5.2.

In summary, one can conclude that with the described algorithm it is possible to efficiently handle almost arbitrarily distributed, monostatic near-field scattering measurement samples. The accuracy of the solution will, however, be inevitably limited by the Born approximation

and the radiating reflector assumption. To overcome these limitations an alternative algorithm employing a set of bistatic scattering data for every transmitter position is described in Section 4.5.

4.4.6 Spatial Imaging

Within the linearizing Born approximation the spectral scattering matrix $\bar{\mathbf{S}}(\boldsymbol{k})$ and spatial scattering distribution $\bar{\mathbf{s}}(\boldsymbol{r})$ are related by the Fourier integral (4.28). By inversion of this integral, i.e., performing the inverse Fourier transform, the spatial distribution may be computed from the spectral representation according to (4.29), that is

$$\bar{\mathbf{s}}(\boldsymbol{r}) \approx \iiint_{\boldsymbol{K}} \bar{\mathbf{S}}(\boldsymbol{k})\, \mathrm{e}^{-\mathrm{j}\boldsymbol{k}\cdot\boldsymbol{r}}\, \mathrm{d}^3\boldsymbol{k}, \tag{4.49}$$

which forms the basis for all standard radar imaging procedures. As noted by Bleistein and Cohen [1977] this inversion is generally not unique due to the possible existence of non-radiating sources. However, as a result of the algorithm employed for the near-field to far-field transformation of the measured scattering data, $\bar{\mathbf{S}}(\boldsymbol{k})$ already corresponds to the least squares (minimum energy) solution, where non-radiating sources are effectively suppressed. Moreover, it may be noted that as long as no other known time dependency is taken into account, the radiating reflectors model assumes a simultaneous, pulse-like excitation of all scattering centers. This assumption corresponds to an equal weighting of all frequency components. Thus, at least theoretically an exact solution to (4.49) could be obtained. However, as mentioned before the k-space area $\boldsymbol{K}$ over which the plane-wave spectrum data is available will always be limited by the outer sphere that corresponds to the maximum measurement frequency $k_{\max}$ in a 3D version of the Ewald sphere representation in Figure 4.3. Consequently, in all practical cases it is only possible to reconstruct a low-pass filtered approximation of the true scattering center distribution by solving (4.49) [Devaney 2012, p. 258]. When working with the broadband monostatic scattering matrix $\bar{\mathbf{S}}(2\boldsymbol{k})$, the k-space area will correspond to a spherical shell with a minimum radius corresponding to $k_{\min}$ and outer radius $k_{\max}$. Depending on the measurement setup that was employed for determining the scattering matrix, the valid angular range of the spectral domain data may also be limited in φ and ϑ. Thus, the spatial image computation in the monostatic case becomes

$$\tilde{\mathbf{s}}(\boldsymbol{r}) = \int_{\vartheta_{\min}}^{\vartheta_{\max}} \int_{\varphi_{\min}}^{\varphi_{\max}} \int_{k_{\min}}^{k_{\max}} \bar{\mathbf{S}}(2\boldsymbol{k})\, \mathrm{e}^{-\mathrm{j}2\boldsymbol{k}\cdot\boldsymbol{r}}\, k^2 \sin\vartheta\, \mathrm{d}k\, \mathrm{d}\varphi\, \mathrm{d}\vartheta. \tag{4.50}$$

This situation corresponds to the typical ISAR imaging setup [Özdemir 2012, p. 121]. It can as well be interpreted as the Fourier transform of $\bar{\mathbf{S}}(2\boldsymbol{k})$ after multiplication with a window function

$$H(\boldsymbol{k}) = \begin{cases} 1 & \vartheta_{\min} \le \vartheta \le \vartheta_{\max},\ \varphi_{\min} \le \varphi \le \varphi_{\max},\ k_{\min} \le k \le k_{\max} \\ 0 & \text{else,} \end{cases} \tag{4.51}$$

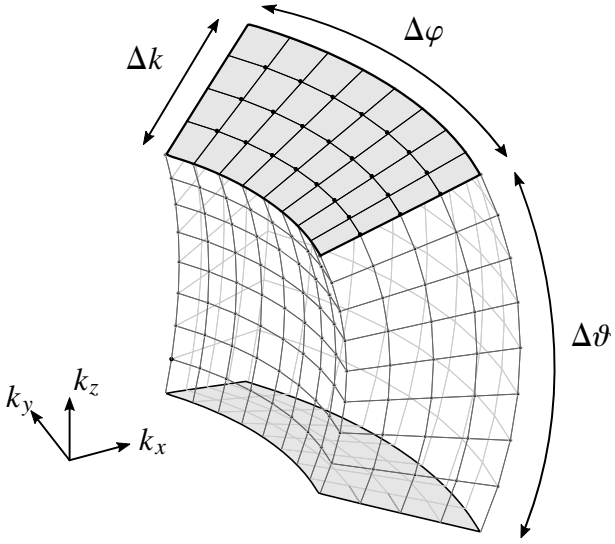

Figure 4.8: k-space area of a monostatic setup with limited angular and frequency range.

that is

$$\tilde{\mathbf{s}}(\boldsymbol{r}) = \bar{\mathbf{s}}(\boldsymbol{r}) * h(\boldsymbol{r}) = \iiint_{-\infty}^{\infty} \bar{\mathbf{S}}(2\boldsymbol{k})\, H(\boldsymbol{k})\, \mathrm{e}^{-\mathrm{j}2\boldsymbol{k}\cdot\boldsymbol{r}}\, \mathrm{d}^3\boldsymbol{k} = \mathcal{F}^{-1}\left\{\bar{\mathbf{S}}(2\boldsymbol{k})\, H(\boldsymbol{k})\right\} \tag{4.52}$$

where $h(\boldsymbol{r})$ is the point spread function (i.e., the impulse response) of the imaging setup and $*$ denotes a spatial convolution. Obviously, the window function given above corresponds to a 3D rectangular window, which results from simply taking all the available data. In general, any other window function can also be used for one, two or all three spectral dimensions in k-space, usually for lowering the side lobes. The size and shape of the resulting point spread function determine the achievable resolution of the image [Mensa 1990, p. 164]. For a k-space configuration as shown in Figure 4.8 with $\Delta k = k_{\max} - k_{\min}$, $\Delta\varphi = \varphi_{\max} - \varphi_{\min}$, $\Delta\vartheta = \vartheta_{\max} - \vartheta_{\min}$ and using a rectangular window, the spatial resolutions in the Cartesian image domain are approximately given by [Fortuny 1998]

$$\Delta x = \frac{c}{2\Delta f \sin\vartheta} = \frac{\pi}{\Delta k \sin\vartheta}, \tag{4.53}$$

$$\Delta y = \frac{\pi}{2k_c \sin(\Delta\varphi/2) \sin\vartheta}, \tag{4.54}$$

and

$$\Delta z = \frac{\pi}{k_c (\cos\vartheta_{\min} - \cos\vartheta_{\max})}, \tag{4.55}$$

where c is the propagation speed and k_c the wavenumber of the mid-frequency, i.e., $k_c = (k_{\max} - k_{\min})/2$. Δx is the *range* resolution, whereas Δy and Δz are the horizontal and vertical *cross range* resolution, respectively.

The numerical evaluation of (4.52) is usually performed by a suitable quadrature rule, which generally leads to

$$\tilde{\mathbf{s}}(\boldsymbol{r}) = \sum_{l=1}^{N_\vartheta} \sum_{m=1}^{N_\varphi} \sum_{n=1}^{N_k} \bar{\mathbf{S}}(\boldsymbol{k}_{lmn})\, M(\boldsymbol{k}_{lmn})\, \mathrm{e}^{-\mathrm{j}2\boldsymbol{k}_{lmn}\cdot\boldsymbol{r}} k_n^2 \sin\vartheta_l w_\vartheta(l) w_\varphi(m) w_k(n), \tag{4.56}$$

where $w_{\vartheta,\varphi,k}(l,m,n)$ are the corresponding quadrature weights. Computing this inverse discrete Fourier transform (DFT) is commonly referred to as *backpropagation* from far-field data [Esmersoy and Miller 1989]. Obviously, for large data sets and/or large image domains, the computational effort for computing an image by evaluating the triple summation in (4.56) may become very high. Denoting the total number of samples in the spectral domain by $N_K = N_\vartheta N_\varphi N_k$ and assuming that also the spatial image consists of N voxels (3D image cells), a direct evaluation of (4.56) has the complexity $O\left(N^2\right)$, where $N \propto (k_{\max} a)^3$. Thus, acceleration methods are required for an efficient and fast evaluation.

The inverse DFT can be computed separately for all dyadic components of the scattering matrix $\bar{\mathbf{S}}$. While the latter is commonly expressed in horizontal and vertical scattering components S_{HH}, S_{VV}, $S_{\mathrm{VH}} = S_{\mathrm{HV}}$, the spatial scattering center distribution is more intuitively described by its Cartesian components, that is

$$\tilde{\mathbf{s}}(\boldsymbol{r}) = \begin{pmatrix} \tilde{s}_{xx}(\boldsymbol{r}) & \tilde{s}_{xy}(\boldsymbol{r}) & \tilde{s}_{xz}(\boldsymbol{r}) \\ \tilde{s}_{yx}(\boldsymbol{r}) & \tilde{s}_{yy}(\boldsymbol{r}) & \tilde{s}_{yz}(\boldsymbol{r}) \\ \tilde{s}_{zx}(\boldsymbol{r}) & \tilde{s}_{zy}(\boldsymbol{r}) & \tilde{s}_{zz}(\boldsymbol{r}) \end{pmatrix} \tag{4.57}$$

where for a reciprocal target $\tilde{s}_{yx} = \tilde{s}_{xy}$, $\tilde{s}_{zx} = \tilde{s}_{xz}$ and $\tilde{s}_{zy} = \tilde{s}_{yz}$. The conversion of $\bar{\mathbf{S}}(\boldsymbol{k})$ to the Cartesian representation can be performed before the evaluation of (4.56) by the relations given in Appendix A.5.

FFT Accelerated Imaging with Polar Reformatting

The probably most common acceleration method for SAR/ISAR imaging is the polar (re-)format algorithm [Cheney and Borden 2009, p. 62]. If the spectral domain (far-field) data is given on a band-limited angular sector of the monostatic Ewald sphere as shown in Figure 4.8, it simply consists of an interpolation to a rectangular k-space grid followed by a 3D FFT of the spectral data to evaluate (4.56). Consequently, the complexity of this approach is $O(N \log N + pN)$ if a local interpolation scheme is used, which has a complexity of $O(pN)$. While the imaging step itself (i.e., the FFT evaluation) can be carried out very efficiently, the interpolation process may still be computational expensive and consequently p may be very large. For this reason, in many RCS imaging applications it is common to work with relatively simple nearest-neighbor schemes such as the 8-nearest-neighbor interpolation [Özdemir 2012, p. 196]. In this method every interpolated grid point results from the weighted sum of its eight (four in a 2D imaging setup) nearest neighboring points on the spherical grid, weighted by their inverse distance to the interpolated point. While computationally efficient, the nearest-neighbor interpolation tends to introduce image artifacts even for densely oversampled data as shown by Pan and Kak [1983]. Higher accuracy can be achieved by a 3D linear interpolation method as described by, e.g., Amidror [2002]. However, due to the non-equidistant distribution of the spherical samples the interpolation can easily become computationally expensive.

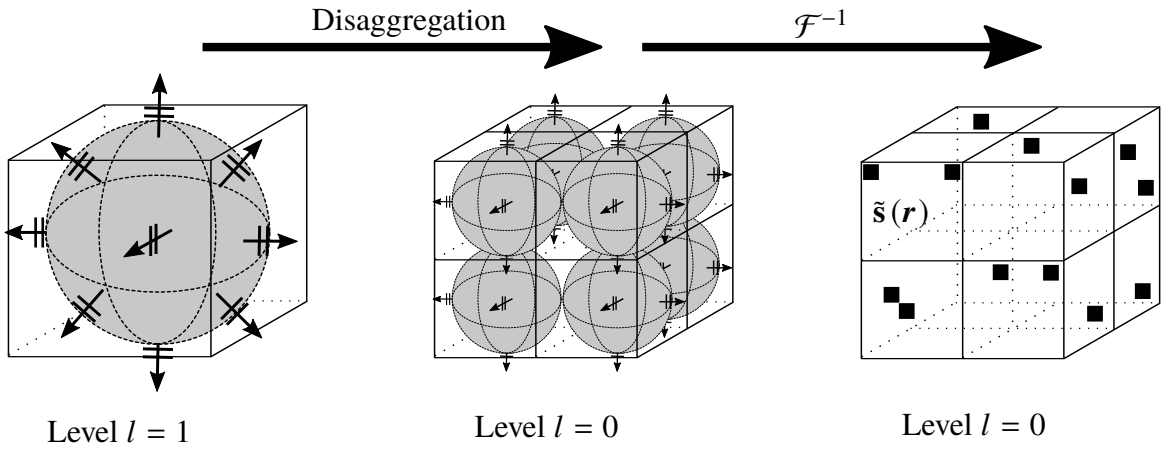

Figure 4.9: Hierarchical disaggregation of broadband scattering matrix (plane-wave spectra). The inverse Fourier transform for computing the spatial scattering center distribution is performed separately for each box on the lowest level.

Imaging by Hierarchical Disaggregation

An acceleration method that avoids the step of interpolation to a Cartesian k-space grid is the hierarchical disaggregation scheme proposed by Schnattinger et al. [2011]. As illustrated in Figure 4.9 the imaging domain is hierarchically subdivided using again an MLFMM octree structure. By disaggregating the monostatic scattering matrix that is defined on the highest level down to the lowest level, the complexity for evaluating (4.56) for each sub-box is reduced as fewer k-space samples are needed on lower levels as already discussed in Section 3.2.4. If the imaging domain is subdivided into L levels, the number of samples on each level l is about $N_l = N/8^{L-l}$, where the corresponding anterpolation is also performed in radial direction, i.e., with respect to k. On the lowest octree level the backpropagation according to (4.56) is evaluated separately for each sub-spectrum and only with respect to the voxels in the corresponding sub-box. In this way the complexity is reduced to about $O\left(N \log^2 N\right)$ if the global FFT-based anterpolation is used in ϑ and φ and $O\left(N \log N\right)$ for a local interpolation [Schnattinger 2014]. Compared to the simple polar reformat algorithm with 8-nearest-neighbor interpolation, the anterpolation on the sphere can be carried out with much higher accuracy, thus significantly improving the image quality. Moreover, it integrates nicely into the hierarchical MLFMM scheme already employed for the near-field scattering transformation, which makes it the preferred method in this thesis.

Other Approaches

Over the past decades a variety of different radar imaging algorithms has been developed, mostly to enable direct measurements in the near-field region of the object. However, as in the case considered here the spectral data is already given in the far field, only the image formation step is of interest. In [Fortuny 1998] this is done by performing 3D inverse fast Fourier transforms (IFFTs) over planar surfaces, in [Broquetas et al. 1998] and [Vaupel and Eibert 2006] a combination of 1D FFTs in φ and numerical quadrature in f is employed. The application

of tomographic backprojection algorithms for radar imaging as proposed by Munson et al. [1983] has been shown to deliver very accurate results, however at the cost of an increased complexity [Desai and Jenkins 1992]. The same holds true for the k-space decomposition method introduced by Boag [2001], which raises the complexity to about $O\left(N^{3/2}\right)$. More recently, the application of compressive sensing (CS) methods has gained wide attention in the area of radar imaging [Potter et al. 2010]. It appears to be attractive for the extraction of the dominant scattering centers and possibly allows to reduce the required number of k-space samples to do so. However, the actual requirements for a reliable application of CS, in particular with respect to some sort of sampling criterion and the question of how much a priori information about the sparsity is needed, are still open questions and subject to current research [Hofmann et al. 2019; Oliveri et al. 2017].

4.5 RCS Determination by Plane-Wave Field Synthesis

As shown in Section 4.3 the bistatic RCS of an object under test can be determined from near-field measurements by solving the corresponding integral equation (4.12) for the scattered plane-wave spectrum $\tilde{\boldsymbol{Q}}(\boldsymbol{k}, -\boldsymbol{k}_n)$, which is due to an incident plane wave with wave vector $\boldsymbol{k}_n$. Obviously, in a measurement setup, where both receiving and transmitting antennas reside in the near-field region of the scatterer, a plane-wave incidence is generally not the case. Still, the complete bistatic scattering dyad may be determined (at least theoretically) if a full set of bistatic scattering measurement data was acquired [Dinallo 1984]. However, beside the practical constraints in realizing such a measurement setup, the procedure would result in a quadratically increased number of data samples which in most cases makes this approach unfeasible. To overcome this problem and relax the requirements on the total number of measurements, an algorithm is presented here that employs a field synthesis approach to determine the monostatic RCS from relatively few bistatic scattered field samples around the location of the transmitting antenna [Neitz et al. 2019]. The basic idea is to weight the solutions $\tilde{\boldsymbol{Q}}_m(\boldsymbol{k})$ (that is the excitation dependent plane-wave spectra) of a series of near-field scattering experiments by the weighting factors that are needed to virtually synthesize a plane-wave field at the object by using the transmitting antenna at different near-field locations to illuminate the scatterer.

4.5.1 Bistatic Near-Field Scattering Measurements

With respect to the general bistatic scattering scenario depicted in Figure 4.1 the scattered field due to the transmitting antenna m with polarization (i) is

$$\boldsymbol{E}_{\mathrm{sca},m}(\boldsymbol{r}) = \oiint \tilde{\boldsymbol{Q}}_m^{(i)}(\boldsymbol{k})\, T_L\left(\hat{k}\cdot\hat{D}, kD\right)\, \mathrm{d}^2\hat{k}, \tag{4.58}$$

where the equivalent electric and magnetic current densities that "radiate" the scattered field have been expanded into the scattered plane-wave spectrum $\tilde{\boldsymbol{Q}}_m^{(i)}(\boldsymbol{k})$ and T_L is again the MLFMM translation operator of order L with the corresponding definitions of the vectors $\boldsymbol{d}$ and $\boldsymbol{D}$. To obtain an equation that relates the actually measured transmission factor $S_{21,m}^{(i)}(\boldsymbol{r})$

to the scattered plane-wave spectrum, the reciprocity relation is employed as done before (see Section 3.1). After subtracting the incident field from the measurement samples (that is performing a background subtraction [Knott 2006, p. 377]) the resulting near-field transmission equation becomes

$$S_{21,m}^{(i)}(\boldsymbol{r}) = \frac{1}{\mathrm{j}2k} \oiint \sqrt{\frac{4\pi}{Z_F}} \boldsymbol{W}_{\mathrm{R}}(\boldsymbol{k}) \cdot \frac{1}{a_m} \tilde{\boldsymbol{Q}}_m^{(i)}(\boldsymbol{k})\, T_L(\boldsymbol{k}, \boldsymbol{D})\, \mathrm{d}^2\hat{k}, \tag{4.59}$$

where $\boldsymbol{W}_{\mathrm{R}}(\boldsymbol{k})$ is the gain normalized far-field pattern of the receiving probe antenna and a_m is the input power wave of the transmitting antenna m. Obviously, this integral equation may be solved in an analogous manner to the antenna measurement case, including the flexibility and efficiency that results from the implementation of a hierarchical MLFMM structure. As it was observed before, the size of the scan aperture dictates the angular range of $\boldsymbol{k}$ for which the scattered plane-wave spectrum is correctly determined. This property will be employed in a later section for computing the monostatic RCS by sampling the scattered field only in the vicinity of the transmitting antenna.

It may be noted at this point that no linearization has been used in the description of the scattered field and, thus, all kinds of multiple interactions or shadowing effects at the scatterer are still preserved. By repeating each measurement with one specific Tx antenna configuration for two orthogonal polarizations (i), the complete (still excitation dependent) scattering matrix $\overline{\mathbf{Q}}_m(\boldsymbol{k})$ can be determined according to (4.13) and (4.14).

4.5.2 Plane-Wave Field Synthesis

In order to obtain the scattering matrix $\overline{\mathbf{Q}}$ of an incident plane wave, the excitation dependent solutions from the previous section have to be weighted and combined according to the location and orientation of their individual Tx antennas [Neitz et al. 2019]. The required weighting factors are those that virtually create the field of an incident plane wave within a specific target region if one combines the radiated field of all antennas with weighted input power. The algorithm employed here for determining these weighting factors was first presented by Mauermayer et al. [2015]. It is based on enforcing boundary conditions on the virtual surface of the target volume to set up a linear system of equation as described by Hill [1985]. Compared to other plane-wave field synthesis methods that are mostly based on optimizing the elements of planar antenna arrays (see, e.g., [Bucci et al. 2013]), the approach employed here offers great flexibility with respect to the location of the probe antennas. The basic principle is illustrated in Figure 4.10. The electric and magnetic fields of an incident plane wave with wave vector $\boldsymbol{k}_n$ and polarization (i), $\boldsymbol{E}_{\mathrm{syn}}^{(i)}(\boldsymbol{r}, \boldsymbol{k}_n)$ and $\boldsymbol{H}_{\mathrm{syn}}^{(i)}(\boldsymbol{r}, \boldsymbol{k}_n)$, respectively, are synthesized within a specific target region V by using the weighted sum of the fields of M transmitting antennas at different locations around or in front of the scatterer. The sought for weighting factors of the individual antenna fields are $\alpha_m^{(i)}(\boldsymbol{k}_n)$. If each antenna radiates the electric field $\boldsymbol{E}_m(\boldsymbol{r})$ and no mutual coupling occurs between the individual antenna elements (which is obviously the case if only a single antenna is moved around the scatterer) the synthesized electric field may be written as

$$\boldsymbol{E}_{\mathrm{syn}}^{(i)}(\boldsymbol{r}, \boldsymbol{k}_n) = \sum_{m=1}^{M} \alpha_m^{(i)} \boldsymbol{E}_m(\boldsymbol{r}) \tag{4.60}$$

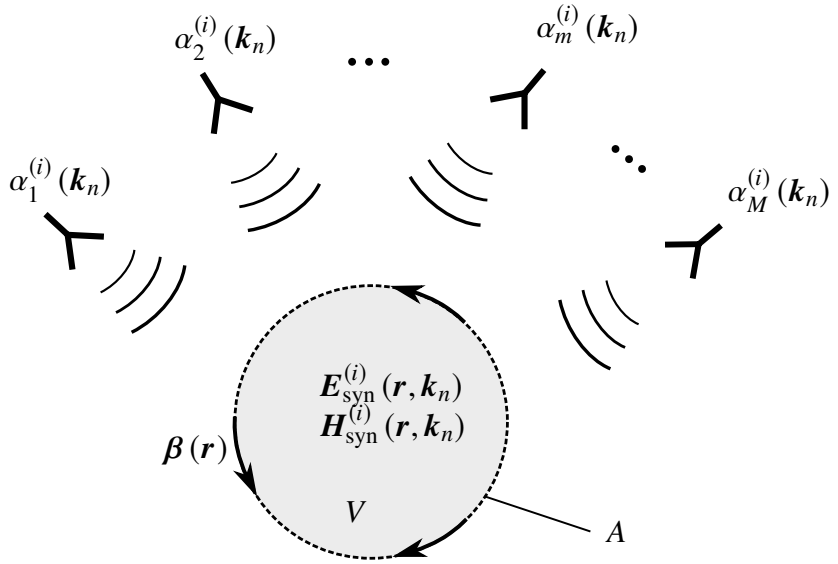

Figure 4.10: Synthesizing the field of a plane wave with wave vector $\boldsymbol{k}$ and polarization (i) within the volume V. The tangential fields are tested on the surface A by RWG basis functions $\boldsymbol{\beta}(\boldsymbol{r})$.

and similarly for the magnetic field. As a consequence of the uniqueness theorem the synthesized field inside the target volume V can be uniquely determined by the tangential fields on the bounding surface A [Jin 2015, p. 90]. For the case of a lossless background medium (free space) that is considered here, both the electric and magnetic tangential fields have to be considered as noted by [Hill 1985]. Consequently, by testing the synthesized field on the surface A by appropriate vector testing functions $\boldsymbol{\beta}_p(\boldsymbol{r})$ the following relation

$$\iint_A \boldsymbol{\beta}_p(\boldsymbol{r}) \cdot \boldsymbol{E}_{\text{syn}}^{(i)}(\boldsymbol{r},\boldsymbol{k}_n)\,\mathrm{d}a = \iint_A \boldsymbol{\beta}_p(\boldsymbol{r}) \cdot \sum_{m=1}^{M} \alpha_m^{(i)} \boldsymbol{E}_m(\boldsymbol{r})\,\mathrm{d}a \tag{4.61}$$

is obtained, where p denotes the index of one of the P vector testing functions. The surface A must be sufficiently smooth but otherwise may be arbitrarily shaped. It is discretized by using a triangular mesh. RWG basis functions defined on the corresponding triangles as described in Appendix A.3 are used as testing functions. Testing the electric and magnetic field according to (4.61) with all P RWG functions yields a linear $2P \times M$ system of equations $\mathbf{Ax} = \mathbf{b}$, where the elements of the right-hand side vector $\mathbf{b}$ correspond to the desired field values that have to be synthesized and the unknown solution vector $\mathbf{x}$ to the weighting factors α_m. In most cases, there will be more testing functions than unknown antenna coefficients and the resulting linear system of equations will be over-determined. As it was done before for finding the solution of inverse source problems, the regularized least-squares solution is determined by solving one of the normal equations employing a GMRES solver (see Section 2.5.2).

For the efficient solution of arbitrarily distributed probe antennas the radiated field of each antenna may again be expanded into propagating plane waves on the Ewald sphere, that is

$$\boldsymbol{E}_m(\boldsymbol{r},\boldsymbol{k}_n) = \oiint \tilde{\boldsymbol{W}}_m(\boldsymbol{k})\, T_L\left(\hat{k}\cdot\hat{D}_m, kD_m\right)\,\mathrm{d}^2\hat{k}, \tag{4.62}$$

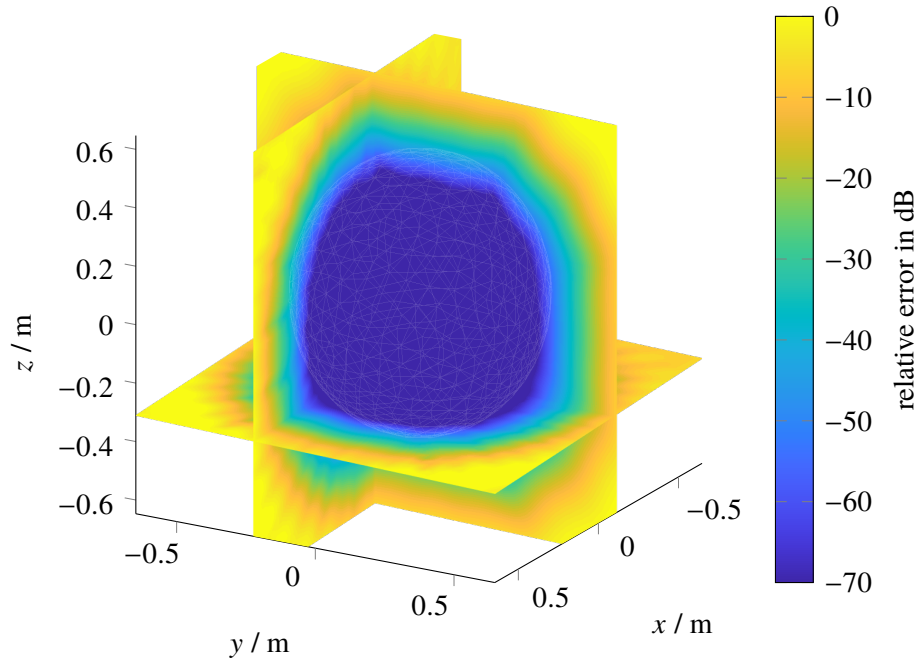

Figure 4.11: Relative error of the synthesized electric field of a plane wave, incident from $\vartheta = 90°$, $\varphi = 0°$, using transmitters on a full sphere with radius $r_{\text{meas}} = 1\,\text{m}$ and $\Delta\vartheta = \Delta\varphi = 10°$. The target volume was a sphere with radius $r_V = 0.4\,\text{m}$. © 2019 IEEE

and thus the synthesized electric field becomes

$$\boldsymbol{E}^{(i)}_{\text{syn}}(\boldsymbol{r}, \boldsymbol{k}_n) = \oiint \sum_{m=1}^{M} \alpha^{(i)}_m(\boldsymbol{k}_n)\, \tilde{\boldsymbol{W}}_m(\boldsymbol{k})\, T_L\left(\hat{k} \cdot \hat{D}_m, kD_m\right) \mathrm{d}^2\hat{k} \tag{4.63}$$

where $\tilde{\boldsymbol{W}}_m(\boldsymbol{k})$ is the plane-wave spectrum of the transmitting antenna m and T_L the FMM translation operator. While in general M different antennas could be employed for the field synthesis, the case of a single probe antenna is considered here. Consequently $\tilde{\boldsymbol{W}}_m$ is the correctly rotated version of the prototype antenna pattern at the corresponding probe location $\boldsymbol{r}_m$.

4.5.3 Numerical evaluation of the Plane-Wave Field Synthesis Approach

While the plane-wave synthesis approach itself has already been studied in detail in [Mauermayer et al. 2015], the geometry is adapted here to the needs of RCS measurements. The required angular range to achieve a desired accuracy of the synthesized field is investigated as presented in [Neitz et al. 2019]. As an example Figure 4.11 shows the result for a full spherical setup, synthesizing the field of a plane wave incident from $\vartheta_{\text{inc}} = 90°$ and $\varphi_{\text{inc}} = 0°$ at $f = 1.5\,\text{GHz}$. The target volume V is a sphere with radius $r_V = 0.4\,\text{m}$, the transmitting Hertzian dipole antennas are located on a spherical grid with angular spacing $\Delta\vartheta = \Delta\varphi = 10°$ and radius $r_{\text{meas}} = 1\,\text{m}$. At $\vartheta = 90°$ and with $r = r_V$, this angular spacing leads to a spatial sampling which is slightly denser than $\lambda/2$ and was found to be the maximum spacing to achieve an accurate

Table 4.1: Mean error $\overline{\Delta E}$ of the synthesized electric field and number of transmitter positions N, dependent on maximum angular range $\Delta\phi_{\max}^{\text{syn}}$ and grid type. © 2019 IEEE

	$\vartheta_{\text{inc}} = 0°$, $\varphi_{\text{inc}} = 0°$				$\vartheta_{\text{inc}} = 90°$, $\varphi_{\text{inc}} = 0°$			
	Uniform		Spherical		Uniform		Spherical	
$\Delta\phi_{\max}^{\text{syn}}$	N	$\overline{\Delta E}$	N	$\overline{\Delta E}$	N	$\overline{\Delta E}$	N	$\overline{\Delta E}$
full	2030	-66.6	2664	-70.8	2030	-66.9	2664	-74.0
±90°	1041	-69.7	1368	-69.2	1041	-69.9	1439	-70.4
±45°	293	-57.3	720	-55.6	293	-57.2	261	-57.3
±40°	245	-56.0	648	-53.7	245	-56.1	205	-57.1
±35°	197	-48.2	576	-47.1	197	-48.4	153	-49.1
±30°	157	-47.5	504	-42.0	157	-48.0	113	-47.4
±25°	109	-38.5	432	-37.5	109	-38.3	81	-39.3
±20°	81	-35.6	360	-28.2	81	-37.1	49	-28.8
±15°	49	-27.7	288	-26.5	49	-28.2	29	-27.4
±10°	25	-18.1	216	-18.6	25	-17.4	13	-18.6
±5°	9	-11.4	144	-10.7	9	-11.8	5	-10.6

solution. The boundary conditions are enforced on the triangular mesh of a sphere with a radius of $r_{\text{mesh}} = 0.4\,\text{m}$ and with a triangle edge length of $\lambda/4$ with λ being the free-space wave length. It was already shown in [Mauermayer et al. 2015] that this mesh size is sufficiently fine. As can be seen from Figure 4.11, the relative error of the synthesized electric field $\boldsymbol{E}_{\text{syn}}$ with respect to the electric field of an ideal plane wave $\boldsymbol{E}_{\text{pw}}$

$$\Delta E\left(\boldsymbol{r}\right) = \frac{\|\boldsymbol{E}_{\text{syn}}\left(\boldsymbol{r}\right) - \boldsymbol{E}_{\text{pw}}\left(\boldsymbol{r}\right)\|}{\max\|\boldsymbol{E}_{\text{pw}}\|} \tag{4.64}$$

is well below $-60\,\text{dB}$ for $r < 0.35\,\text{m}$ and slightly larger closer to the spherical mesh. Thus, it is beneficial to choose the mesh radius somewhat larger than the radius of the target volume. In general it can be concluded that with a full spherical setup of transmitting antennas the field inside the target volume may be synthesized with very high accuracy, theoretically only limited by the numerical accuracy of the employed MLFMM scheme, typically on the order of $-60\,\text{dB}$ to $-70\,\text{dB}$. In practice, the actually achieved accuracy will of course also depend on the hardware equipment, i.e., the positioning accuracy, power stability, etc. and how precisely the probe pattern have been determined before.

Choosing the sampling grid according to a standard spherical coordinate system leads to a non-uniform sampling point distribution with a higher sample density at the poles. If the angular range around the angle of incidence of the plane wave that has to be synthesized is limited, the number of samples will depend on the incident angle ϑ_{inc}. A more uniform

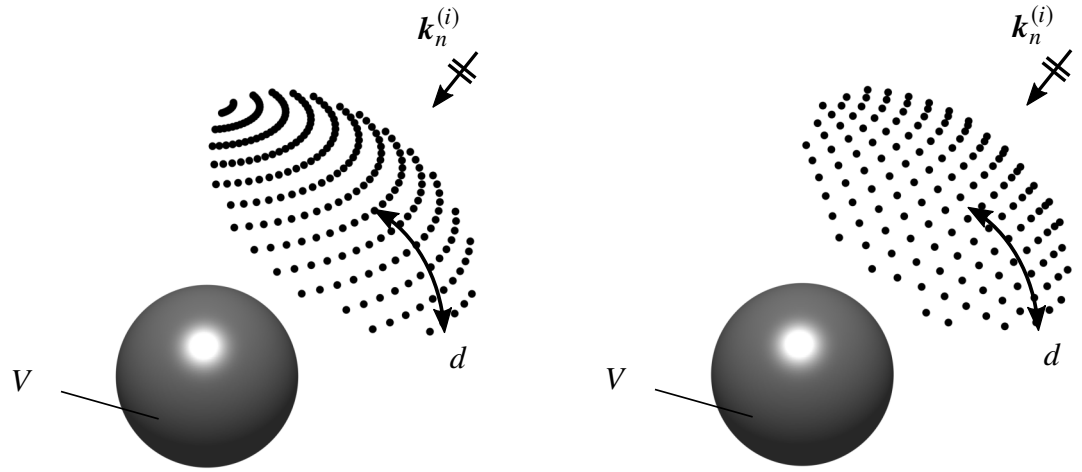

Figure 4.12: Spherical grid (left) and uniform Lebedev grid (right), limited to angular range $\Delta\phi_{\max}^{\text{syn}} \leq d$ around direction of incidence, used to synthesize the field of a plane wave with wave vector $\boldsymbol{k}_n^{(i)}$ in volume V. © 2019 IEEE

distribution which is mostly independent from the angle of incidence may be obtained by choosing the grid points according to, for example, a Lebedev sphere [Lebedev and Laikov 1999]. In Table 4.1 the mean relative error of the synthesized electric field $\overline{\Delta E}\,(\boldsymbol{r})$ and the number of sample locations N, both dependent on the limited angular range $\Delta\phi_{\max}^{\text{syn}}$, are listed for two angles of incidence $\vartheta_{\text{inc}} = 0°$ and $\vartheta_{\text{inc}} = 90°$. For the sampling grids, a Lebedev sphere of order 2030 and a standard spherical grid with $\Delta\vartheta = \Delta\varphi = 5°$ are chosen. In both cases, starting from the full grid, only those sample locations (ϑ_m, φ_m) are used for which the greater circle distance

$$d = \cos^{-1}\left[\sin\left(\pi/2 - \vartheta_{\text{inc}}\right)\sin\left(\pi/2 - \vartheta_m\right) + \cos\left(\pi/2 - \vartheta_{\text{inc}}\right)\cos\left(\pi/2 - \vartheta_m\right)\cos\left(\varphi_{\text{inc}} - \varphi_m\right)\right] \tag{4.65}$$

is less or equal than the maximum angular range, i.e., $d \leq \Delta\phi_{\max}^{\text{syn}}$ as illustrated in Fig. 4.12. Otherwise the scenario is the same as before. It may be observed that using the uniform (Lebedev) grid, the synthesized field error is indeed almost independent from the angle of incidence. The overall accuracy, however, mainly depends on the maximum angular range and not on the grid structure. Having a real positioning system in mind, where using a standard spherical grid may speed up the acquisition time significantly, it is chosen to continue with that kind of grid. Moreover, due to the symmetry of the spherical grid, it is sufficient to compute the field synthesis weights for one elevation cut only, that is, all values of ϑ_{inc} but only one value of φ_{inc}, even if only a limited angular range is used. Nevertheless, it may be noted that the algorithm is able to handle arbitrary sampling distributions.

Naturally, the required angular range depends on the distance of the transmitting antennas to the target volume. In the limiting case of $r_{\text{meas}} \to \infty$, that is, under far-field conditions, only a single transmitter position is required. Dependent on the ratio of the spherical target volume radius r_V to the measurement radius r_{meas}, the required angular range is assessed in Fig. 4.13. For large measurement radii and large angular ranges the accuracy is only limited by the employed translation operator in (4.63), resulting in a minimum error of around −70 dB.

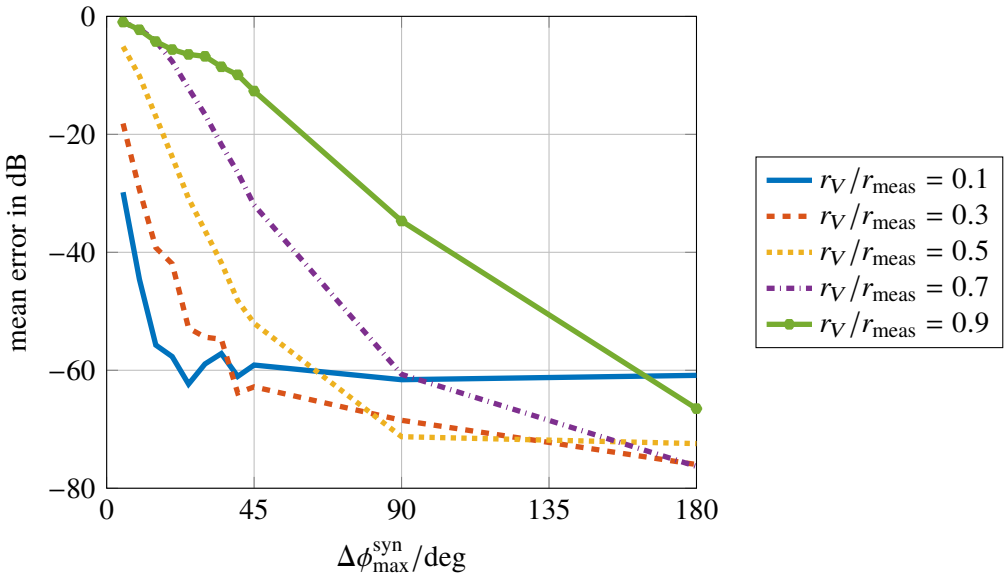

Figure 4.13: Mean error $\overline{\Delta E}$ of the synthesized electric field dependent on the maximum angular range $\Delta\phi^{\mathrm{syn}}_{\mathrm{max}}$ for different ratios of of the spherical target volume radius r_V to the measurement radius r_{meas}.

For typical ratios of $r_V/r_{\mathrm{meas}} = 0.3 - 0.5$ an angular range of ±20° to ±35° is sufficient to achieve a mean error of the synthesized field well below −40 dB.

4.5.4 Monostatic RCS Computation

As it was shown in [Neitz et al. 2019], using M different near-field setups with index m, the synthesized electric field of a plane wave with wave vector $\boldsymbol{k}_n$ and polarization (i) is given by (4.60) to be

$$\boldsymbol{E}^{(i)}_{\mathrm{syn}}(\boldsymbol{r}, \boldsymbol{k}_n) = \sum_{m=1}^{M} \alpha^{(i)}_m \boldsymbol{E}_m(\boldsymbol{r}) \,. \tag{4.66}$$

Due to linearity also the equivalent electric and magnetic current densities $\boldsymbol{J}^{(i)}_{\mathrm{eq}}(\boldsymbol{r}, \boldsymbol{k}_n)$ and $\boldsymbol{M}^{(i)}_{\mathrm{eq}}(\boldsymbol{r}, \boldsymbol{k}_n)$ that describe the scattering of an object when illuminated by that incident plane wave, can be expressed as a weighted sum of the equivalent current densities $\boldsymbol{J}_{\mathrm{eq},m}(\boldsymbol{r})$ and $\boldsymbol{M}_{\mathrm{eq},m}(\boldsymbol{r})$ that result from the individual near-field setups m. Thus, one obtains

$$\boldsymbol{J}^{(i)}_{\mathrm{eq}}(\boldsymbol{r}, \boldsymbol{k}_n) = \sum_{m=1}^{M} \alpha^{(i)}_m(\boldsymbol{k}_n)\, \boldsymbol{J}_{\mathrm{eq},m}(\boldsymbol{r}) \tag{4.67}$$

and

$$\boldsymbol{M}^{(i)}_{\mathrm{eq}}(\boldsymbol{r}, \boldsymbol{k}_n) = \sum_{m=1}^{M} \alpha^{(i)}_m(\boldsymbol{k}_n)\, \boldsymbol{M}_{\mathrm{eq},m}(\boldsymbol{r}) \,. \tag{4.68}$$

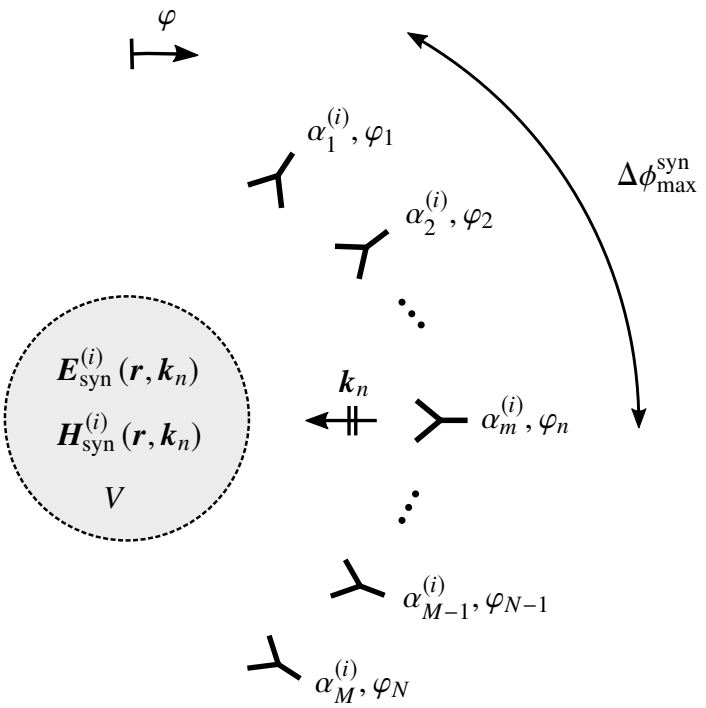

Figure 4.14: The electric field of a plane wave with wave vector $\boldsymbol{k}_n$ and polarization (i) within the volume V is synthesized by M transmitting antennas on a spherical grid. © 2019 IEEE

Consequently, the scattered plane-wave spectrum according to (4.12) for this plane-wave incidence becomes

$$\tilde{\boldsymbol{Q}}^{(i)}(\boldsymbol{k}, \boldsymbol{k}_n) \approx \sum_{m=1}^{M} \alpha_m^{(i)}(\boldsymbol{k}_n)\, \tilde{\boldsymbol{Q}}_m(\boldsymbol{k}), \tag{4.69}$$

and from this, the complete bistatic scattering spectrum is computed as

$$\overline{\mathbf{Q}}(\boldsymbol{k}, \boldsymbol{k}_n) \approx \sum_{i=1}^{2} \sum_{m=1}^{M} \alpha_m^{(i)}(\boldsymbol{k}_n)\, \tilde{\boldsymbol{Q}}_m^{(i)}(\boldsymbol{k})\, \hat{u}^{(i)}, \tag{4.70}$$

which includes all dyadic components of $\overline{\mathbf{Q}}$ (typically Q_{VV}, Q_{VH}, Q_{HV} and Q_{HH}) and where $\hat{u}^{(i)}$ denotes the unit vector of the linearly polarized incident plane wave with polarization (i). As the magnitude of the synthesized incident field may be freely chosen it can be set to $\|\boldsymbol{E}_{\text{inc}}^{(i)}(\boldsymbol{k}_n)\| = 1\,\text{V/m}$ and the RCS can be evaluated as

$$\sigma^{(i)}(\boldsymbol{k}_n, \boldsymbol{k}_n) = 4\pi \|\overline{\mathbf{Q}}(\boldsymbol{k}_n, \boldsymbol{k}_n) \cdot \hat{u}_n^{(i)}\|^2. \tag{4.71}$$

If one is interested in determining the *monostatic* scattering spectrum, i.e., $\overline{\mathbf{Q}}(\boldsymbol{k}_n, \boldsymbol{k}_n)$, then $\tilde{\boldsymbol{Q}}_m^{(i)}(\boldsymbol{k})$ in (4.70) only has to be evaluated at $\boldsymbol{k}_n$. Thus, the near-field sample locations in (4.59) can be chosen such that truncation errors may be tolerated as long as they do not affect the correct solution of $\tilde{\boldsymbol{Q}}_m^{(i)}(\boldsymbol{k}_n)$ for all m. This is further illustrated in Fig. 4.14. To synthesize the electric field of a plane wave incident at φ_n in V, M transmitting antennas are

required, spanning an angular range of $\pm\Delta\phi_{\max}^{\mathrm{syn}}$. For each transmitting antenna m the scattered plane-wave spectrum has to be evaluated at $\boldsymbol{k}_n$, i.e., φ_n. The locations of the receiving probes have to be chosen accordingly. One possibility would be to choose the same (spherical) grid as for the transmitting antennas, but in general any scan surface covering the required angular range to determine $\tilde{\boldsymbol{Q}}_m^{(i)}(\boldsymbol{k}_n)$ is possible. In this way, the actual measurement aperture size can be drastically reduced compared to a full bistatic setup. While the sampling locations $\boldsymbol{r}_n$ to capture the scattered field may be distributed irregularly and may vary for every position m of the transmitting antenna, the latter must not change during the acquisition in order to measure the (bistatic) scattered field for the exact same excitation at all sampling locations.

5 Near-Field Scattering and Imaging Examples

In the following a series of test and application examples is given to evaluate the presented methods for determining the monostatic RCS and for computing the corresponding spatial scattering center distributions. While the first part comprises scenarios where only monostatic near-field measurements were performed, in the second part the plane-wave field synthesis approach that is based on including additional bistatic measurement data is evaluated. The achievable accuracy in both cases is discussed, where it must be noted that in case of the linearized radiating reflectors approach no rule for estimating the accuracy for a specific object and measurement scenario is available. Instead the final far-field accuracy can only be determined empirically and will strongly depend on whether the object under test can be represented sufficiently well by the radiating reflectors model. In case of the plane-wave field synthesis approach, on the other hand, the achievable accuracy is mainly limited by the quality of the synthesized field. It can thus be estimated by the bistatic angular range that is spanned by the probe antennas.

As it was done for the evaluation of the near-field antenna measurement algorithm, simulated test data obtained by the Method-of-Moments solver of FEKO as well as measured near-field scattering data acquired in the anechoic chamber of the TUM are used for the validation of the two methods.

5.1 Imaging and RCS Computation by Monostatic Setups

5.1.1 Single-Frequency Plate Structure

The first simulated test object is a perfectly electrically conducting (PEC) plate as depicted in Figure 5.1. It has overall dimensions of 1.6 m by 1.25 m in height and width, respectively. To test the imaging resolution when computing the scattering center distribution, slots and holes of different size are cut out from the base plate. The width of the slots (having a length 0.3 m) varies from 0.01 m to 0.2 m and, similarly, the diameter of the holes varies from 0.04 m to 0.2 m. At a test frequency of 4 GHz the monostatically scattered near field from Hertzian dipole sources was computed using FEKO. The sampling locations are distributed irregularly within an angular range of $\varphi_{\max} = \pm 30°$ and $\vartheta_{\max} = 90° \pm 30°$ in front of the object, with a nominal angular step width of $\Delta\varphi = \Delta\vartheta = 1°$ and random variation of $\pm 0.5°$. The measurement radius[1] varies randomly between 1 m and 3 m. At each of the 3721 sampling locations the three scattered field components E_{VV}, E_{HV} (= E_{VH}) and E_{HH} are acquired. After setting up the MLFMM equation system, the object is subdivided into 13 056 boxes on the finest level and

[1] The nominal far-field distance for this object with diameter D would be $r_{\mathrm{FF}} = 4D^2/\lambda = 220\,\mathrm{m}$.

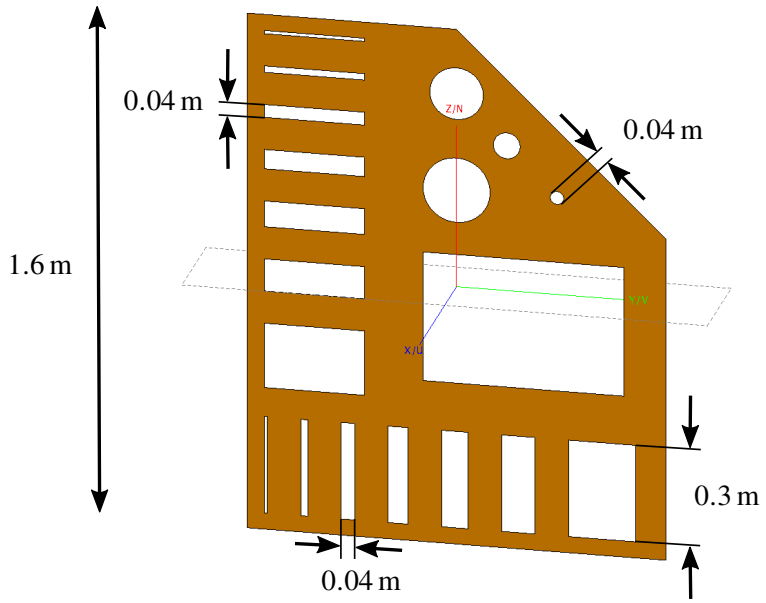

Figure 5.1: FEKO model of PEC plate structure with slots and holes of different size.

(4.48) is solved for the resulting 3.8 million unknown coefficients of the scattered plane-wave spectrum. The least squares solution is obtained by means of the NE normal equation and the GMRES method. Using 4 threads on an Intel i7-4820K CPU a solution with a relative observation error of about −35 dB is found after 174 s. Although no noise was added to the simulated near-field data (and in contrast to the simulated antenna radiation example in the previous chapter) a smaller observation error cannot necessarily be expected. This is due to the underlying radiating reflectors model employed now, which is only approximately able to represent the scattered field. Nonetheless, a good agreement between the obtained monostatic RCS and the FEKO reference data can be observed as shown for a vertical cut at $\varphi = 0°$ in Figures 5.2 – 5.4. The relative far-field error of the individual RCS components is on the order of −30 dB to −40 dB within the valid angular range in front of the object.

The same accuracy of the solution can also be observed in any other cut plane. Having determined the (monostatic) scattering matrix $\overline{\mathbf{S}}(2\boldsymbol{k})$ for a certain angular range, it is possible to compute a spatial image of the scattering centers by solving (4.50). This is done by performing a hierarchical disaggregation of the k-space spectrum prior to a direct evaluation of (4.56) as described in Section 4.4.6. For comparison, also a polar reformatting of the spherical k-space data using an 8-nearest-neighbor interpolation, followed by an FFT accelerated evaluation of the Fourier integral as described in Section 4.4.6 was performed. Obviously, for single frequency data one cannot expect any resolution of the spatial image in range direction and for this reason only images in the plane at $x = 0$ are computed. However, the resolution in cross-range direction (i.e., in y and z) for the given configuration can be estimated by (4.54) and (4.55) to $\Delta y = \Delta z = 0.038$ m. Figure 5.5 shows the resulting scattering center distribution images after computation with the two different methods. The left image is the result after hierarchical disaggregation, the right after polar reformatting with 8-nearest-neighbor interpolation and FFT processing. Depicted are the normalized magnitudes of the absolute value of $\tilde{\mathbf{s}}(\boldsymbol{r})$ at

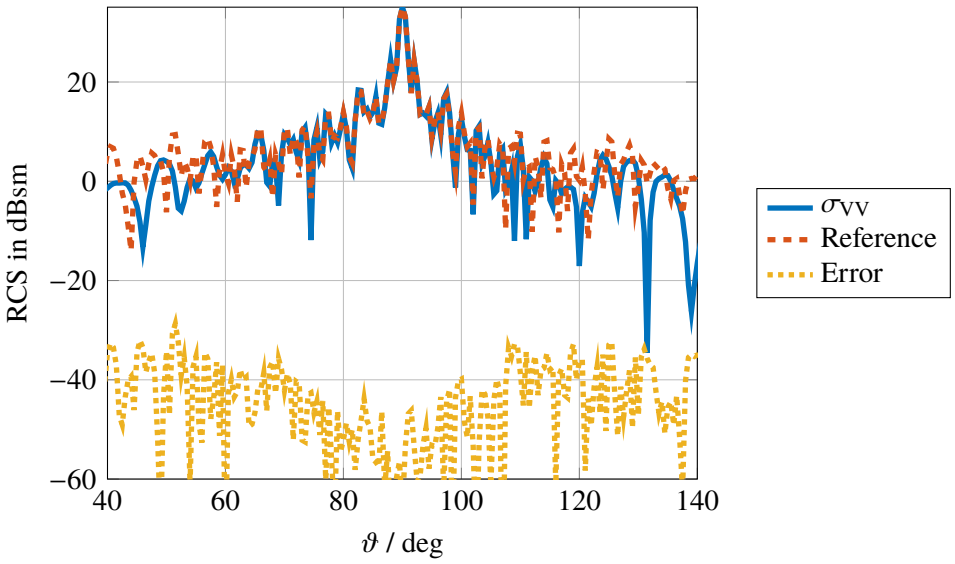

Figure 5.2: VV component of the computed monostatic RCS of the PEC plate structure compared to FEKO reference solution. Vertical cut at $\varphi = 0°$.

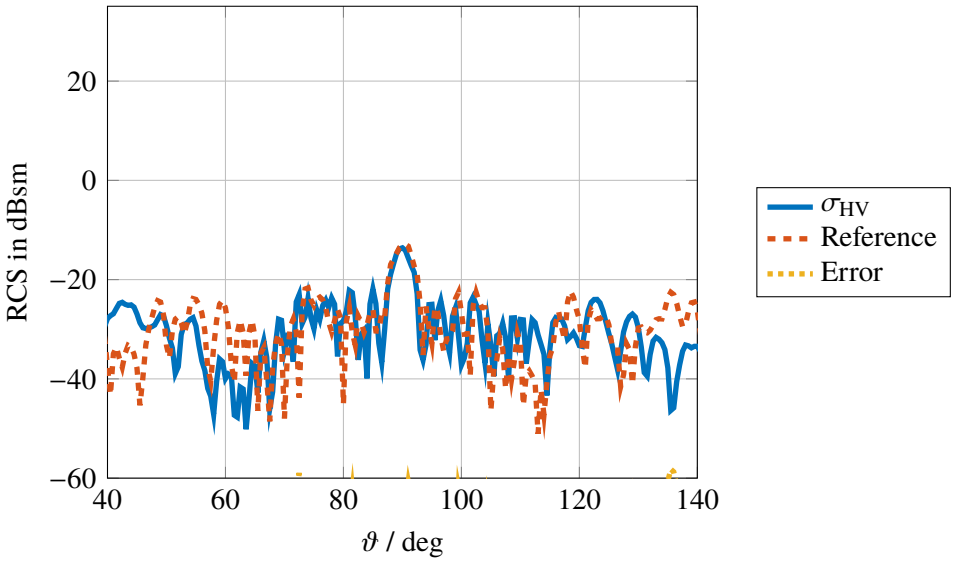

Figure 5.3: HV component of the computed monostatic RCS of the PEC plate structure compared to FEKO reference solution. Vertical cut at $\varphi = 0°$.

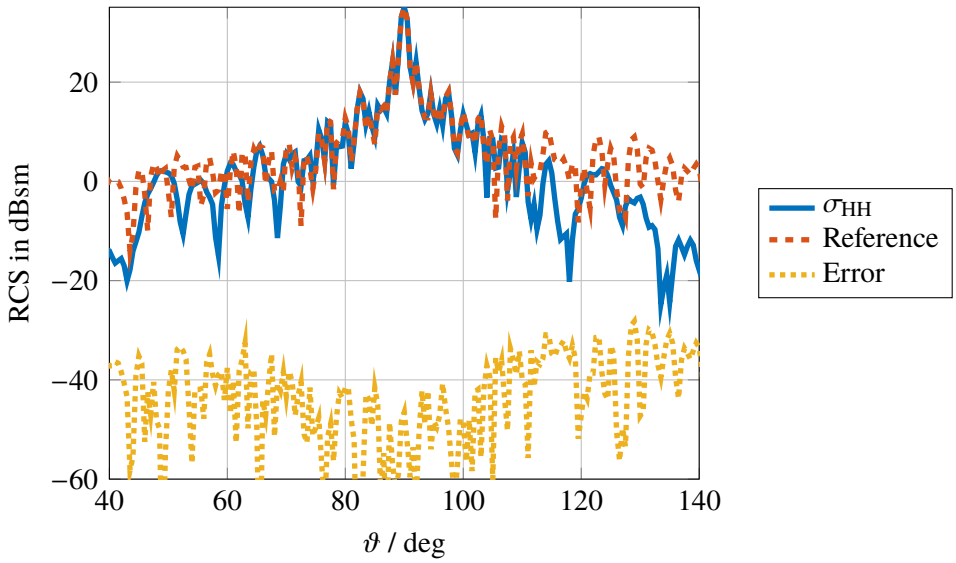

Figure 5.4: HH component of the computed monostatic RCS of the PEC plate structure compared to FEKO reference solution. Vertical cut at $\varphi = 0°$.

$x = 0$. In both cases a uniform spectral window with $\varphi_{\max} = \pm 30°$ and $\vartheta_{\max} = 90° \pm 30°$ was applied to the k-space data in order to extract the legitimate part of the scattered plane-wave spectrum. Obviously, both methods yield about the same resolution in the final image. The smallest resolvable slot width in both horizontal and vertical direction is 0.04 m as can be seen by comparison with Figure 5.1. This corresponds well to the estimation according to (4.53) – (4.55). For the FFT algorithm to produce sufficiently accurate results, the k-space data was interpolated by a factor of 8 in φ and ϑ prior to performing the polar reformatting. Still, the final image quality is slightly degraded towards the edges of the object, whereas the image after hierarchical disaggregation does not suffer from this degradation. On the other hand, performing the hierarchical disaggregation imaging took about 7 s using 4 threads on an Intel CPU, whereas the FFT imaging could be performed in about 1 s, including the spherical interpolation to a denser grid and the polar reformatting. In both cases the computation was performed for 256×256 pixels.

To further reduce the imaging artifacts at the expense of the resolution, other window functions can be applied to the k-space data. Figure 5.6 shows all dyadic components of the spatial scattering distribution that result from the hierarchical disaggregation imaging after applying a 2D Hamming window [Harris 1978] along φ and ϑ. The smoothing effect of the window function is apparent. While it is not surprising to see the dominance of the s_{yy}- and s_{zz}-component in the dyadic image, it may be noted that also the object edges leading to a "cross talk" between the scattered field components can be clearly identified.

This example shows that the radiating reflectors model is able to represent the scattering behavior of an object quite accurately, as long as the conditions to apply the underlying linearization are sufficiently well fulfilled. In particular this includes that no strong multiple interactions (i.e., multi-path reflections) at the object occur. In the next test example it will be demonstrated how a violation of this condition leads to a larger error in the predicted RCS.

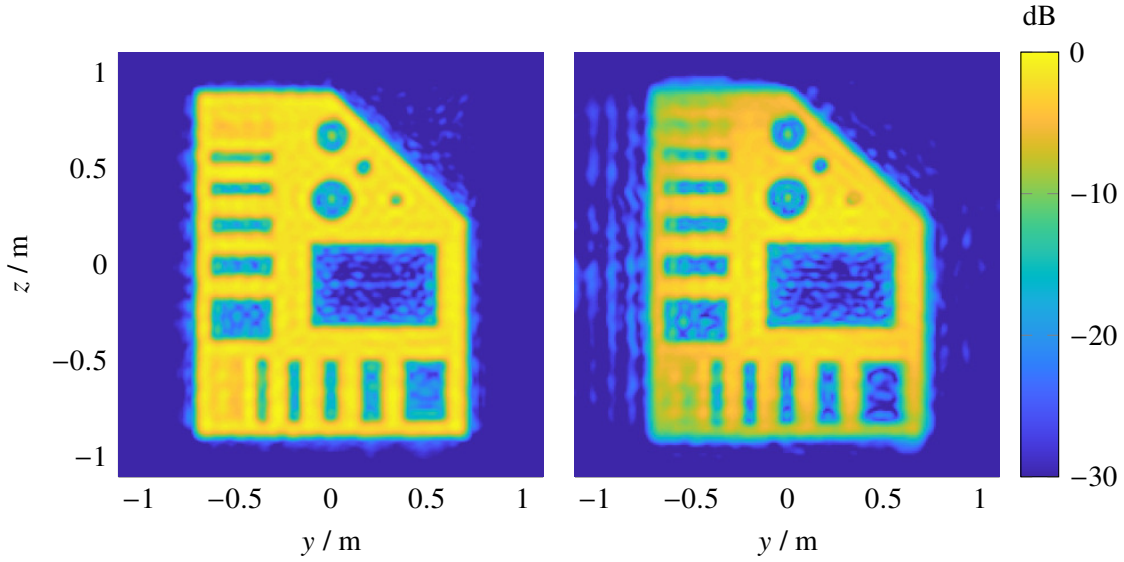

Figure 5.5: Spatial scattering center distribution images of the PEC plate structure after transforming the acquired NF data. Left: Result from hierarchical disaggregation imaging. Right: Result after polar reformatting with 8-nearest-neighbor interpolation and FFT processing. Depicted are the normalized magnitudes of $\|\tilde{\mathbf{s}}(\boldsymbol{r})\|$ at $x = 0$.

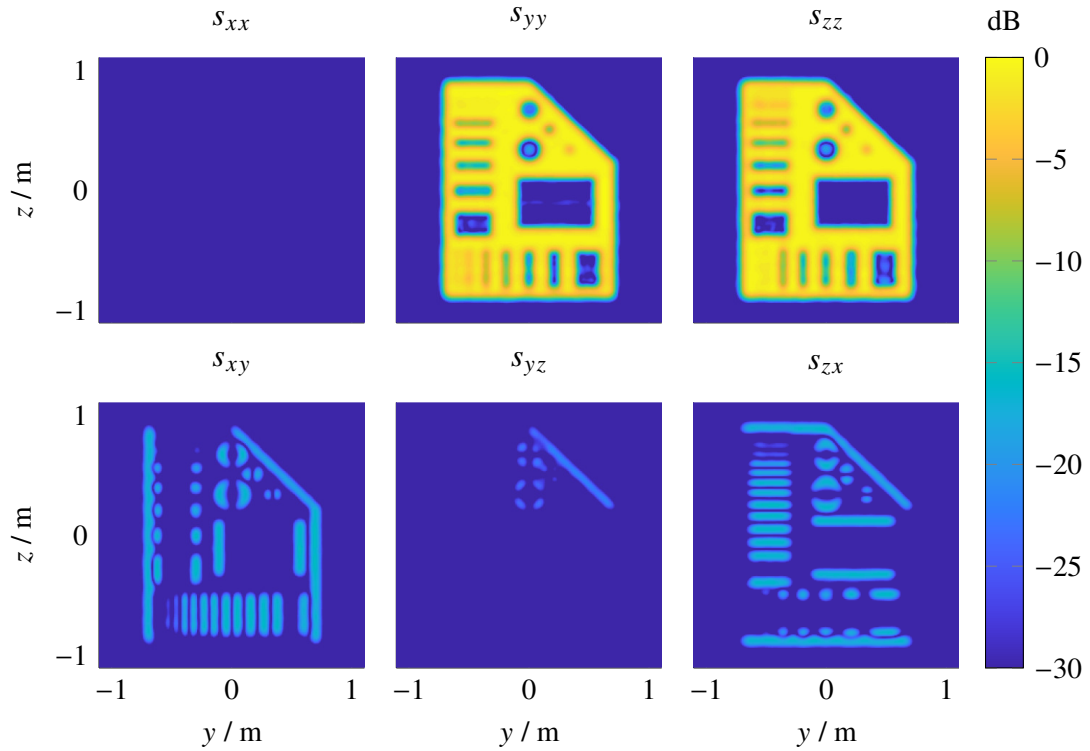

Figure 5.6: Spatial scattering center distribution images of the PEC plate structure obtained from hierarchical disaggregation with spectral windowing (Hamming window) after transforming the acquired NF data. Depicted are the normalized magnitudes of the dyadic of $\tilde{\mathbf{s}}(\boldsymbol{r})$ components at $x = 0$.

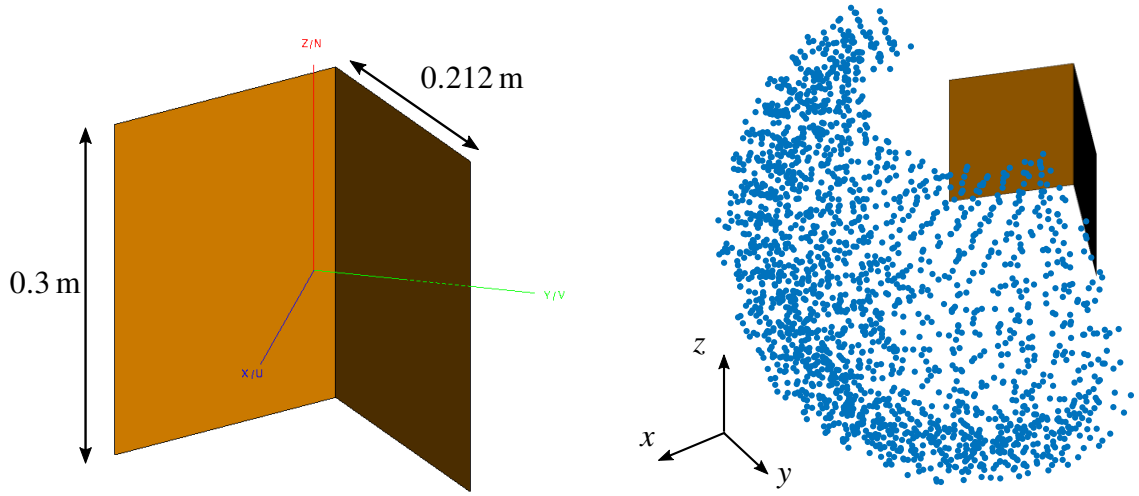

Figure 5.7: FEKO model of a PEC dihedral corner reflector. Left: Model with dimensions. Right: Irregular sample distribution in front of the corner reflector.

5.1.2 Dihedral Corner Reflector

Consider the case of a PEC dihedral corner reflector as shown in Figure 5.7. The scattered electric field due to Hertzian dipole sources in the vicinity of the object was computed using FEKO. Broadband test data was acquired for a frequency range of 4 GHz to 8 GHz with $\Delta f = 0.2\,\text{GHz}$. While the minimum sphere enclosing the corner reflector has a diameter of 0.9 m, the measurement samples are distributed irregularly on a spherical shell in front of the object with $\varphi_{\max} = \pm 90°$ and $\vartheta_{\max} = 90° \pm 60°$, where the random angular variation is again $\pm 0.5°$. The measurement radius varies randomly between 1.75 m and 2.25 m. In total, the three scattered field components E_{VV}, E_{HV} and E_{HH} are sampled at 21901 positions. The computed monostatic RCS after solving (4.48) at $f = 4\,\text{GHz}$ iteratively to a converging observation error of $-36\,\text{dB}$ is compared to the FEKO reference data in Figure 5.8 and 5.9 for the VV- and HH-component, respectively. Depicted are the horizontal cuts at $\vartheta = 90°$, where the largest far-field error is observed. In comparison to the previous example the maximum relative far-field error is now significantly higher, up to $-22\,\text{dB}$. This may be attributed to the inability of the radiating reflectors model to accurately represent the multiple interactions that occur when illuminating the opening of the dihedral corner reflector. Nevertheless the overall accuracy with respect to the reference data is still very good, which demonstrates that also in this case the monostatic scattering behavior is mainly determined by a discrete set of scattering centers.

Using the available broadband k-space data after transforming the near-field data separately for all frequencies, a 3D image of the scattering center distribution can be computed. This is again done by means of the hierarchical disaggregation algorithm. A Hamming window is applied in ϑ and φ with respect to the valid angular range of about $\varphi_{\max} = \pm 90°$ and $\vartheta_{\max} = 90° \pm 60°$ as well as in frequency direction. The result is shown in Figure 5.10, where the normalized maximum values of $\|\tilde{\mathbf{s}}(\boldsymbol{r})\|$ along each dimension are projected onto the faces of the cubic imaging domain with $128 \times 128 \times 128$ voxels. The white outline indicates the

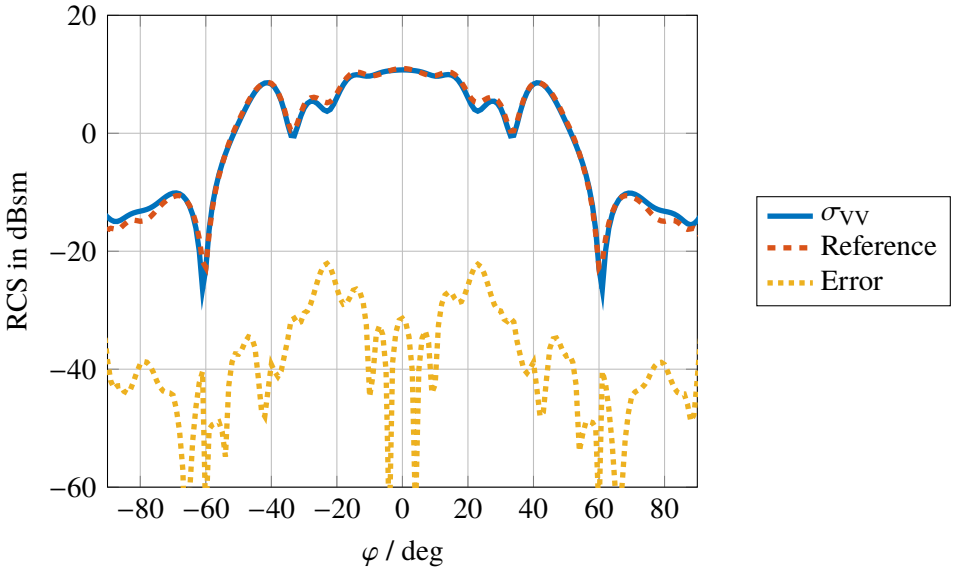

Figure 5.8: VV component of the computed monostatic RCS at 4 GHz of the PEC dihedral corner reflector compared to FEKO reference solution. Horizontal cut at $\vartheta = 90°$.

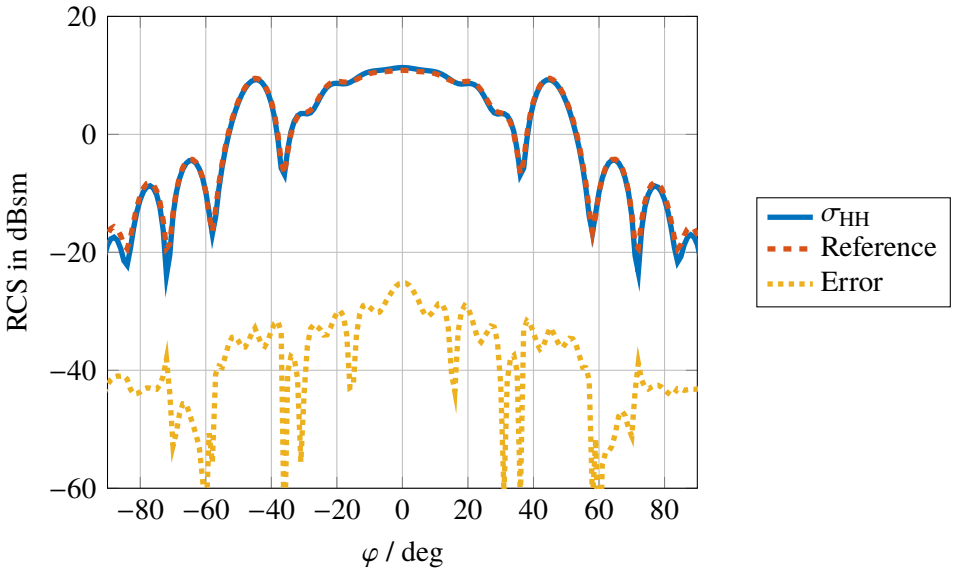

Figure 5.9: HH component of the computed monostatic RCS at 4 GHz of the PEC dihedral corner reflector compared to FEKO reference solution. Horizontal cut at $\vartheta = 90°$.

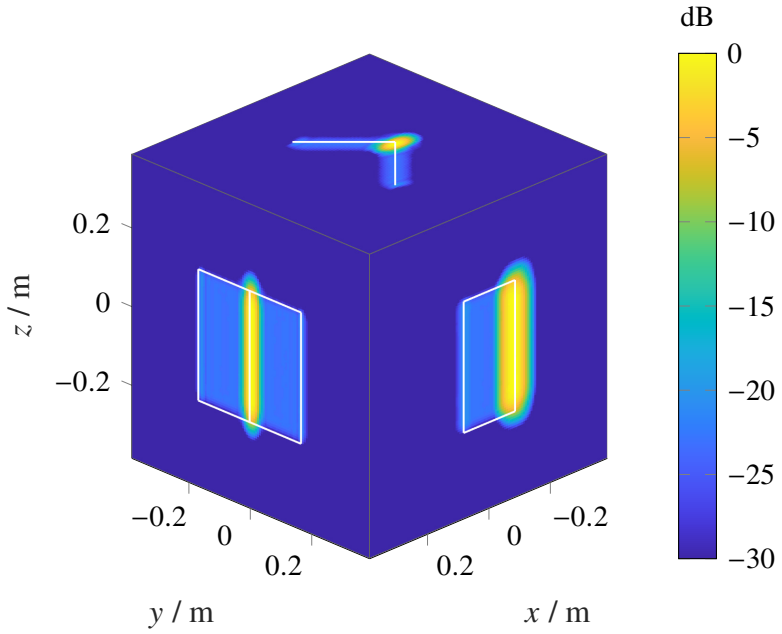

Figure 5.10: Spatial scattering center distribution image of the dihedral corner reflector after transforming the acquired NF data. Depicted are the normalized maximum values of $\|\tilde{\mathbf{s}}(\boldsymbol{r})\|$ along each dimension, projected onto the faces of the cubic imaging domain. The white outline indicates the dimensions of the original reflector structure.

dimensions of the original reflector structure. Due to the double reflection of a plane wave that hits the opening of the corner reflector, the scattering center distribution is dominated by a characteristic line (or dipole) shape (see, e.g., [Özdemir 2012, p. 142]).

In order to investigate the scattering behavior under a varying bistatic angle β between the transmitting and receiving probe antenna as introduced for the quasi-monostatic setups in Section 4.4.5 (see Figure 4.5), β is varied from 5° to 50°. Using the assumption of a quasi-monostatic setup, the RCS is again computed for each frequency sample. For a frequency of $f = 4\,\mathrm{GHz}$ the resulting maximum relative FF errors with respect to the monostatic FEKO reference data at 4 GHz and at the corresponding equivalent monostatic frequency $f_{\mathrm{mono}} = f\cos(\beta/2)$ are summarized in Table 5.1. Obviously, for this setup already a relatively small bistatic angle of $\beta = 5°$ leads to a higher maximum error. For larger angles the quasi-monostatic assumption clearly does no longer hold and in these cases correcting the frequency seems to be even detrimental to finding an accurate solution. Again the observed effect may be attributed to the strong multiple interactions at the object. These interactions change significantly for varying bistatic angles and so does the found solution. Moreover, the validity of the quasi-monostatic assumption will (of course) depend on the measurement radius. It can be expected that for larger measurement radii wider separations between the Tx and Rx probe can be tolerated.

While the varying bistatic angles do not help to determine the monostatic RCS in this case, their corresponding radar images can help to identify the different dominant scattering centers along the structure of the corner reflector. This is shown in Figure 5.11, where $\|\tilde{\mathbf{s}}(\boldsymbol{r})\|$ in a cut plane at $z = 0$ is depicted for the varying bistatic angles β. It can be clearly observed how the

Table 5.1: Maximum monostatic RCS error after transforming NF data with different bistatic angles β and assuming quasi-monostatic setups.

β	0°	5°	10°	20°	30°	50°
f_{mono} / GHz	4.0000	3.9962	3.9848	3.9392	3.8637	3.6252
max. error at 4 GHz	−22.0 dB	−15.3 dB	−5.3 dB	−1.7 dB	−0.9 dB	−0.3 dB
max. error at f_{mono}	-	−15.2 dB	−5.3 dB	−1.5 dB	−0.6 dB	−0.2 dB

dominant scattering centers are shifted from the back of the corner reflectors toward the front edges. At the same time, imaging artifacts in the form of "ghost images" due to incorrectly localized double reflections appear at different locations behind the reflector structure. By combining the individual images after normalization a more detailed image of the complete structure may be obtained as shown in Figure 5.12. Here, the normalized maximum values of $\|\tilde{\mathbf{s}}(\boldsymbol{r})\|$ along each dimension are again projected onto the faces of the cubic imaging domain.

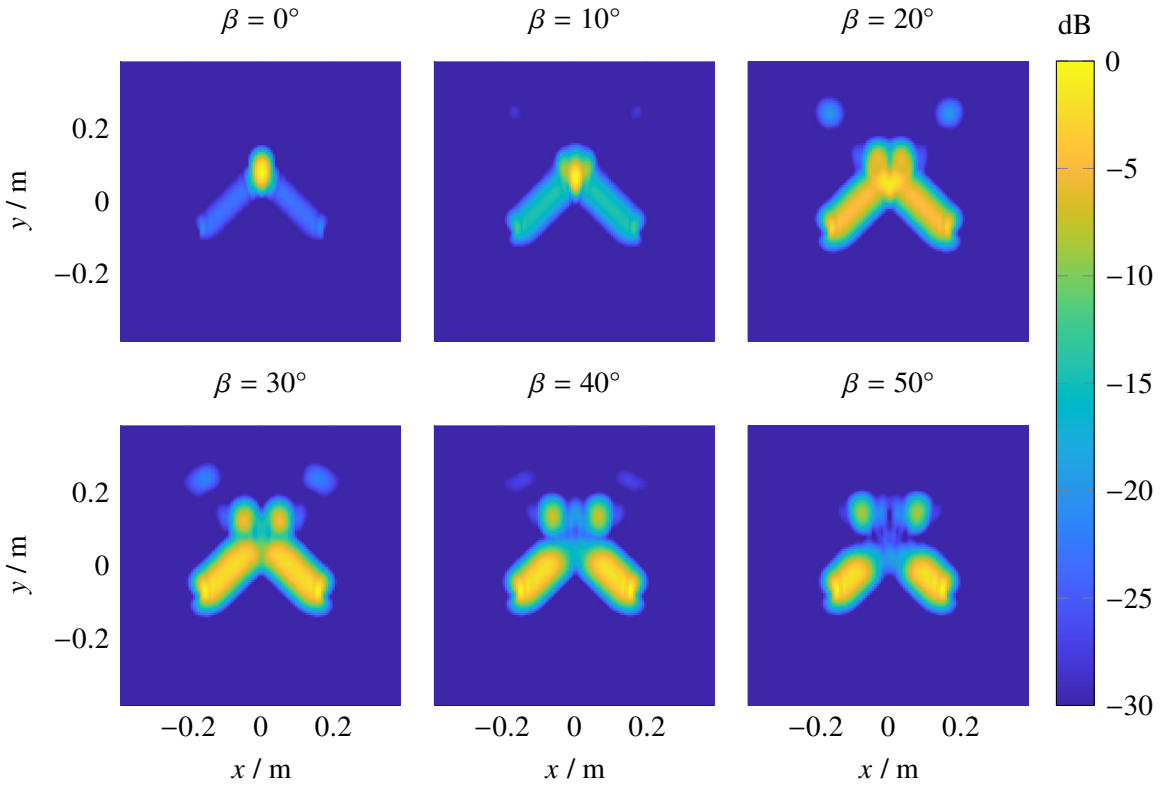

Figure 5.11: Spatial scattering center distribution image of the dihedral corner reflector after transforming the NF data that was acquired by using different bistatic angles β. Depicted are the normalized values of $\|\tilde{\mathbf{s}}(\boldsymbol{r})\|$ at $z = 0$.

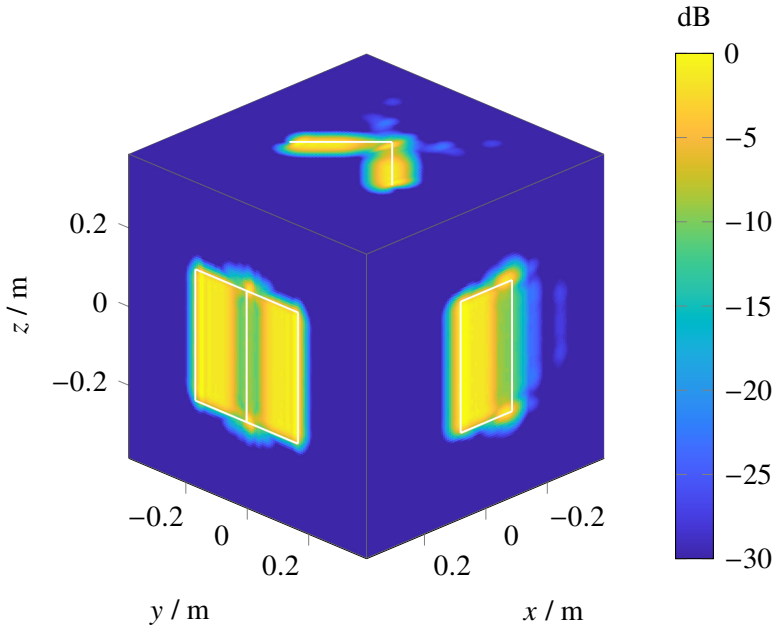

Figure 5.12: Spatial scattering center distribution image of the dihedral corner reflector after combining the images for different bistatic angles β. Depicted are the normalized maximum values of $\|\tilde{\mathbf{s}}(\boldsymbol{r})\|$ along each dimension, projected onto the faces of the cubic imaging domain. The white outline indicates the dimensions of the original reflector structure.

5.1.3 Metallic Plate Measurement

In order to validate the transformation algorithm experimentally, test measurements were performed in the anechoic chamber of the TUM. The first test object is a simple metallic (aluminum) plate as shown in Figure 5.13 on the left. The plate has a size of $0.52\,\mathrm{m} \times 0.8\,\mathrm{m}$ and is attached to a spherical positioner. To measure all co- and cross-polarized scattered field components a dual polarized horn antenna was used for reception and the transmitting double ridged horn antenna can be rotated by 90° along the polarization axis. The probe antennas are shown in Figure 5.13 on the right. The measurement radius of the spherical near-field scan setup is about 2.8 m with respect to the midpoint between the two probes that are separated by[2] 0.265 m. Thus, quasi-monostatic measurements are performed where the bistatic angle between the probe antennas is $\beta = 5.4°$.

To eliminate the contribution of the direct coupling between the probe antennas from the measured data, a background subtraction was performed. To this end, in addition to the test data of the object under test, scattering data of the empty chamber was acquired while the spherical positioner was rotated in azimuth for one full horizontal circle. This data was then subtracted from the measured scattering data of the object under test. In this way the scattered field from the plate was obtained for a frequency range of 4 to 12 GHz with $\Delta f = 50\,\mathrm{MHz}$ on a complete hemisphere with $\Delta\varphi = \Delta\vartheta = 0.6°$. This resulted in 90 751 samples per frequency and measured field component. The number of unknown plane-wave scattering coefficients on

[2]The picture in Figure 5.13 shows a setup with a slightly larger separation.

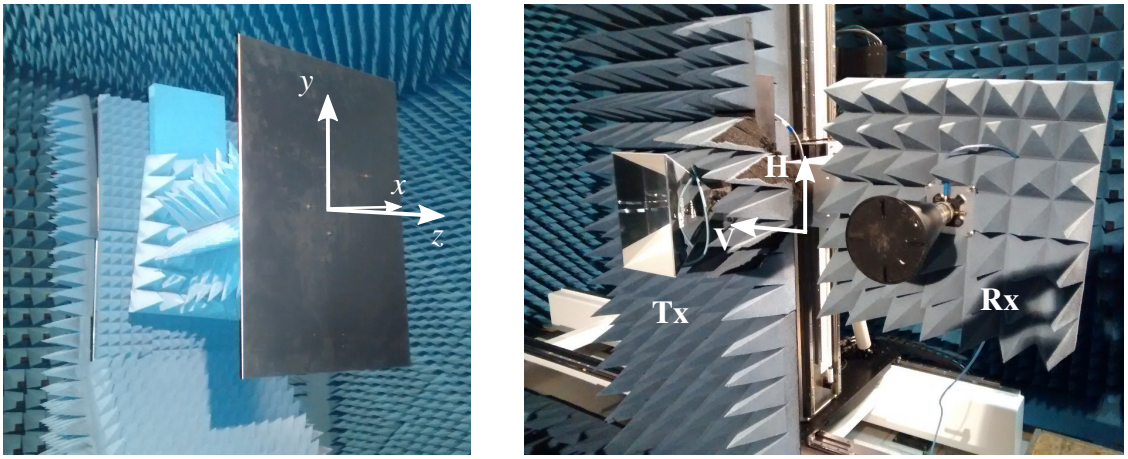

Figure 5.13: Quasi-monostatic NF scattering measurements in the anechoic chamber of TUM. Left: Metallic plate test object on spherical positioner. Right: Tx and Rx probe antennas.

the finest level of the MLFMM source tree varies with the frequency from about 2 millions up to 12 millions. Similarly, the time needed for transforming the measured near-field data increases from about 150 s to 1500 s using 4 threads on an Intel i7-4820K CPU. The relative observation error converges to values between −20 dB and −25 dB. The resulting RCS at $f = 4\,\mathrm{GHz}$ is shown in Figure 5.14 and 5.15 for the VV and HH component, respectively. Depicted are the normalized magnitudes in a cut plane at $\varphi = 0°$. The reference far-field data for this case was obtained by a FEKO simulation of a PEC plate having the same size. Relatively good agreement between the two data sets is found over a wide angular range with a relative deviation which is mostly on the order of −30 dB. Around $\vartheta = 1°$ the deviation of the HH component is slightly larger, up to −20 dB which is most likely due to a small misalignment of one of the probe antennas or the device under test (DUT). Also towards the end of the scan range ($\vartheta_{\max} = 90°$) the absolute agreement is reduced as for these observation angles the scattered field signal is significantly lower. Apparently, the dynamic range of the measurement setup is no longer sufficient in this case. The effect is more dominant for the VV component, where the coupling between the Tx and Rx probe is stronger due to their relative position to each other.

After processing all the available near-field data to obtain broadband k-space data, a 3D scattering center distribution image is computed employing the hierarchical disaggregation algorithm. The result is shown in Figure 5.16, where the normalized maximum values of all dyadic components of $\tilde{\mathbf{s}}(\boldsymbol{r})$ are projected onto the faces of the imaging domain. Again, the dominant s_{xx} and s_{yy} component can be clearly identified. Considering all dyadic components even relatively small details of the structure are revealed, such as the four mounting screws at the center of the plate. However, the image suffers from some ghost image artifacts, most likely due to multiple interactions of the plate with the spherical positioner and the mounting structure. Nonetheless the overall image quality is very satisfactory, in particular if one considers the simplicity of the measurement setup.

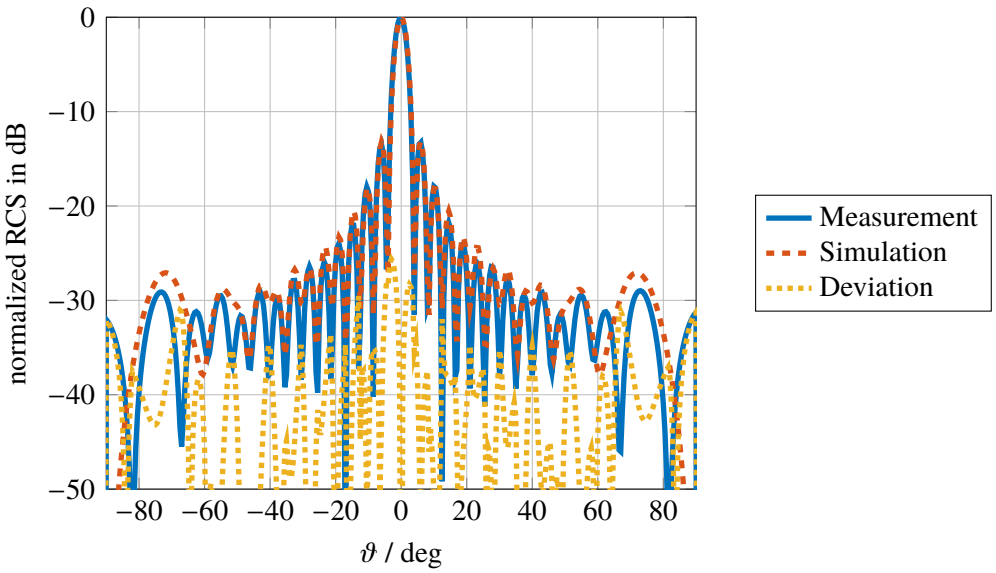

Figure 5.14: VV component of the computed normalized monostatic RCS at 4 GHz of the metallic plate compared to FEKO reference solution. Vertical cut at $\varphi = 0°$.

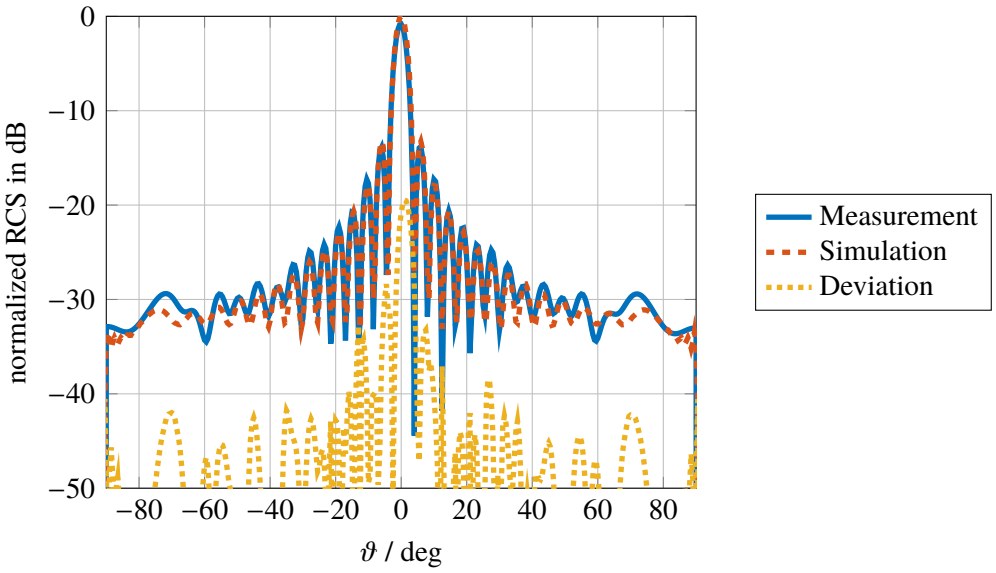

Figure 5.15: HH component of the computed normalized monostatic RCS at 4 GHz of the metallic plate compared to FEKO reference solution. Vertical cut at $\varphi = 0°$.

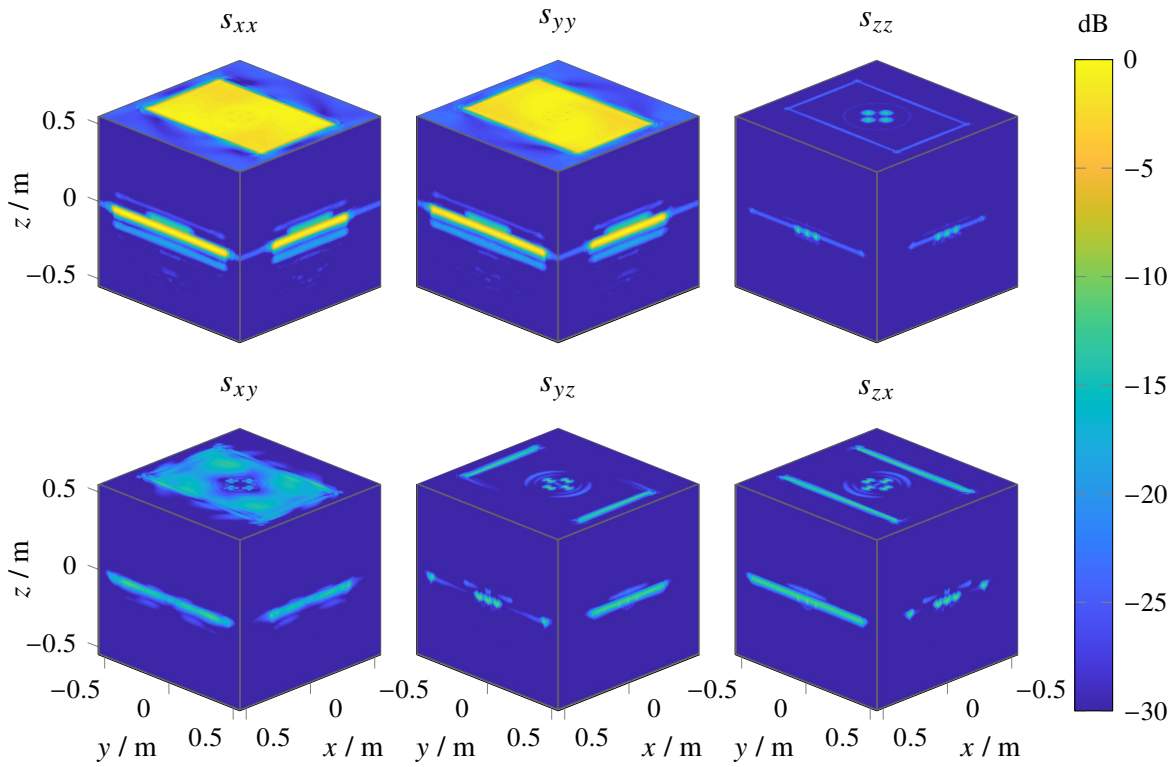

Figure 5.16: Spatial scattering center distribution image of the metallic plate obtained from hierarchical disaggregation after transforming the acquired broadband NF data. Depicted are the normalized maximum values of the dyadic components of $\tilde{\mathbf{s}}(\boldsymbol{r})$, projected onto the faces of the imaging domain.

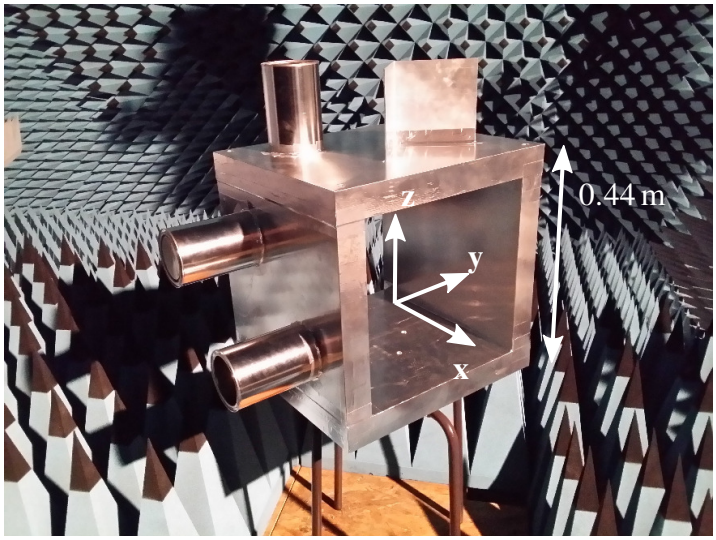

Figure 5.17: Metallic test object "Cuby". © 2019 IEEE

5.1.4 Monostatic Measurement of Test Object "Cuby"

To test the near-field RCS measurement approach experimentally in the case of a more complex shaped target, the metallic (aluminum) test object "Cuby" was designed. Figure 5.17 shows a photograph of the object in the anechoic chamber of the TUM. While the structure of the object is sufficiently complex to expect the occurrence of multiple interactions, it is still based on simple geometrical shapes such as a corner reflector and open and closed cylinders. Consequently, also for this object reference far-field data could be obtained by a FEKO simulation.

Leaving the measurement setup as before, all four orthogonal scattered near-field components were acquired (quasi-) monostatically. Again, the background subtraction method was used to eliminate the direct coupling between the probe antennas and to remove parasitic reflections from the walls as well as from the spherical positioner. The latter was used to rotate the test object for a complete spherical scan with respect to the local coordinate system of the object as shown in Figure 5.17. Measurement samples at 76 447 locations were acquired. The covered frequency range is 4 GHz to 8 GHz, which results in about 2 to 8 million unknown scattered plane-wave coefficients to represent the object that may be completely enclosed by a cube with edge lengths of 0.6 m. Compared to the previous example of the metallic plate, the iterative solver now reaches only a relative observation error between −15 dB and −22 dB, which already indicates the increased difficulties of accurately representing the scattering mechanisms with the linearized model. Using the results of the metallic plate measurements for an amplitude calibration of the processed near-field data, the monostatic RCS as shown in Figure 5.18 and 5.19 is obtained. Depicted are vertical cuts at $\varphi = 0°$ and at $f = 4\,\text{GHz}$ for the VV and HH component, respectively. Obviously the overall agreement is still good, although deviations of up to −16 dB occur, which was found to be the maximum deviation for all field components over the complete angular range.

Apparently, it is still possible to represent the far-field scattering behavior by a set of independently "radiating" point scatterers. A spatial image of the latter is obtained by

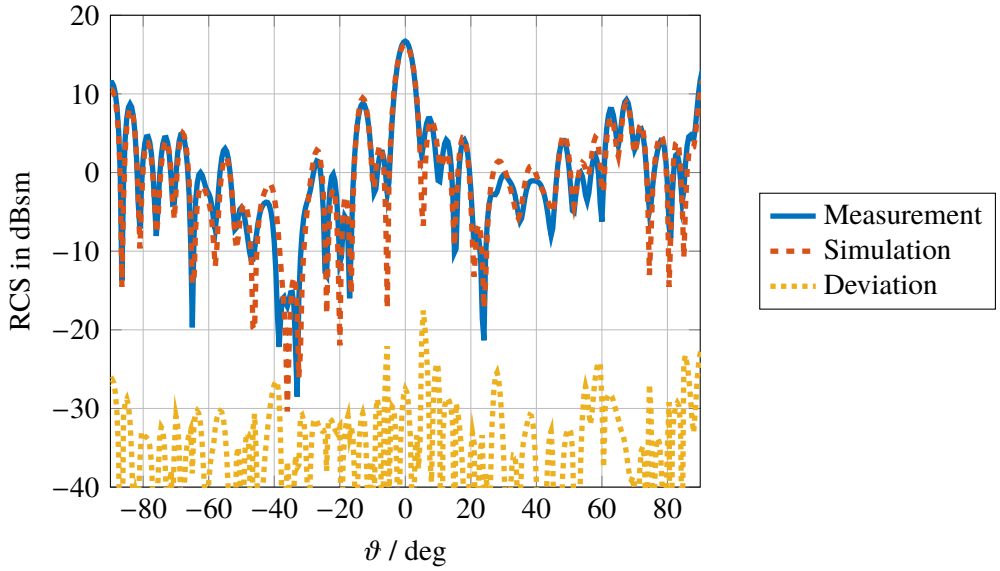

Figure 5.18: VV component of the computed monostatic RCS at 4 GHz of the metallic test object "Cuby" compared to FEKO reference solution. Vertical cut at $\varphi = 0°$.

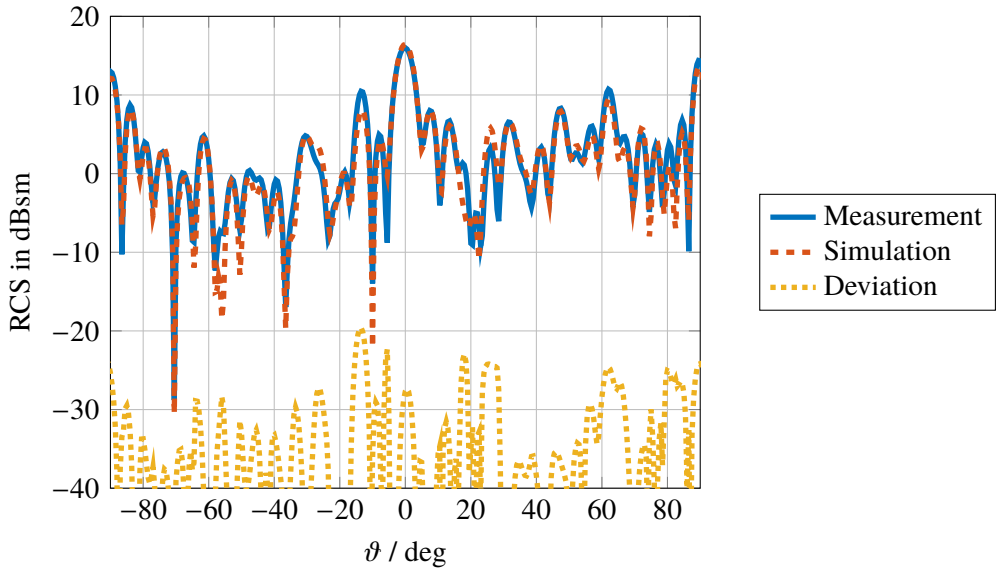

Figure 5.19: HH component of the computed monostatic RCS at 4 GHz of the metallic test object "Cuby" compared to FEKO reference solution. Vertical cut at $\varphi = 0°$.

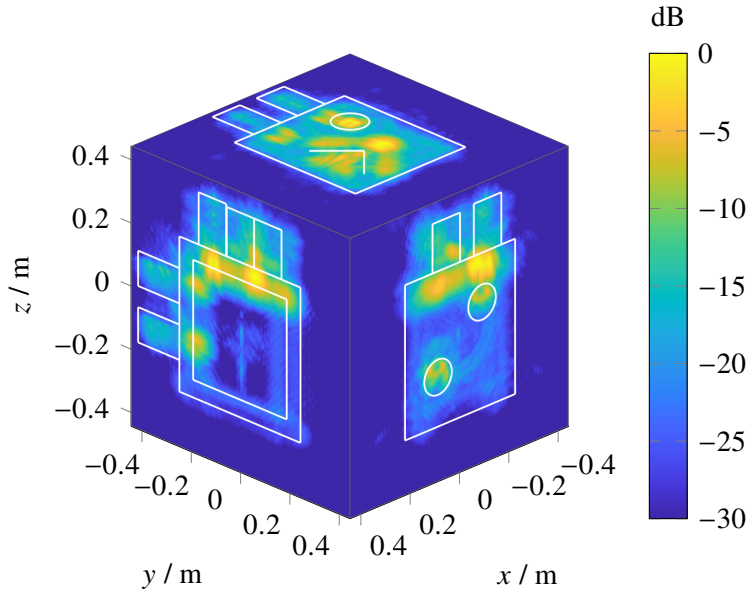

Figure 5.20: Spatial scattering center distribution image of the test object "Cuby" obtained by hierarchical disaggregation of the transformed broadband data. Depicted are the normalized maximum values of $\|\tilde{\mathbf{s}}(\boldsymbol{r})\|$ along each dimension, projected onto the faces of the cubic imaging domain. The white outline indicates the dimensions of the original structure.

processing the data for the complete frequency range as done before using the hierarchical disaggregation algorithm. Figure 5.20 shows the resulting normalized maximum values of $\|\tilde{\mathbf{s}}(\boldsymbol{r})\|$ along each dimension, projected onto the faces of the cubic imaging domain. The white outline indicates the dimensions of the original structure. The main scattering centers at the top of the structure are slightly displaced along the z-direction, presumably due to multiple reflections, for example at the corner reflector. The positions of the cylinders at the left side face can still be identified quite accurately. Nonetheless, the overall visual resemblance with the original structure is only approximately given in this case.

5.2 RCS Computation by Plane-Wave Field Synthesis

In the following some test examples are given to illustrate and validate the performance of the RCS computation algorithm that is based on the plane-wave field synthesis approach. In all cases multistatic near-field scattering data (i.e., bistatic scattering data for different bistatic angles) with different illumination directions are used. As discussed in Section 4.5.3, the size of the angular range that is spanned by the transmitting and receiving antenna(s) determines the achievable accuracy of the plane-wave field synthesis. If the scattered field data can be measured with sufficient precision (including the positioning of the probe antennas), it is only this angular range that limits the accuracy of the resulting monostatic RCS. Some of the results presented here have already been published in [Neitz et al. 2019].

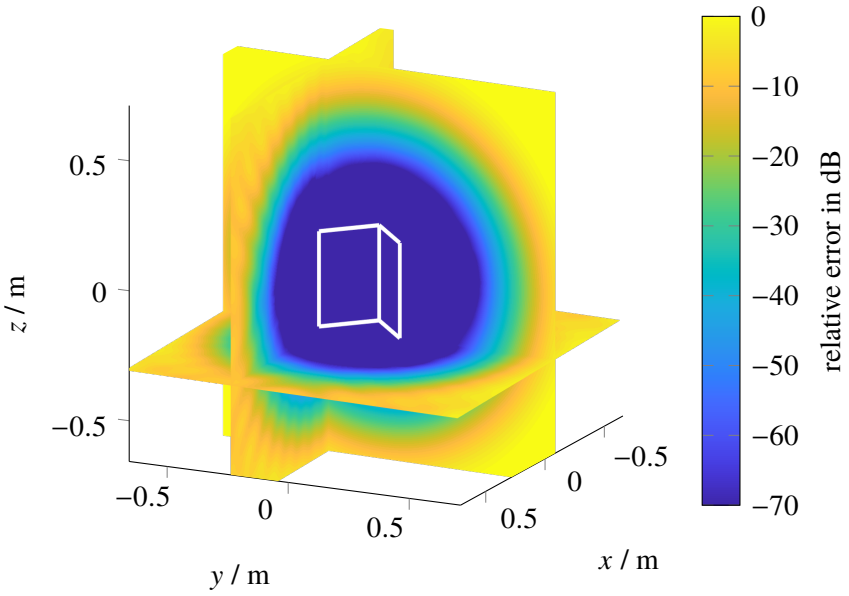

Figure 5.21: Relative error of the synthesized electric field of a plane wave, incident from $\vartheta = 90°$, $\varphi = 0°$, using transmitters on a full sphere with radius $r_{\text{meas}} = 1\,\text{m}$ and $\Delta\vartheta = \Delta\varphi = 5°$. The white outline indicates the dimensions of the dihedral corner reflector. © 2019 IEEE

5.2.1 Dihedral Corner Reflector

As a first example, the dihedral corner reflector already used in the previous section is considered, now at a frequency of 1.5 GHz. The dihedral reflector is located at the origin and may be enclosed by a minimum sphere of 0.25 m, the radius for the spherical field synthesis volume is chosen to be $r_V = 0.3\,\text{m}$. Near-field scattering data as well as far-field reference data is again obtained using the Method-of-Moments solver of FEKO. In a first step, full bistatic scattering data for transmitting and receiving Hertzian dipole antennas on a spherical grid with $r_{\text{meas}} = 1\,\text{m}$ and $\Delta\varphi = \Delta\vartheta = 5°$ is considered. As already discussed in Section 4.5.3, for this measurement setup the relative error of the synthesized plane-wave field within the target volume is as low as $-70\,\text{dB}$. This is demonstrated for a plane wave incident from $\vartheta = 90°$ and $\varphi = 0°$ in Figure 5.21. The white outline indicates the dimensions of the dihedral corner reflector.

For all transmitter positions the corresponding inverse source problem is solved as it was done in the case of the antenna near-field problems. Consequently, a separate solution is obtained for each polarization of the exciting (Tx) antenna. By weighting the plane-wave spectra with the computed plane-wave synthesis probe weights according to (4.70), the RCS of the dihedral reflector is determined. The relative magnitude error with respect to the simulated monostatic FEKO far-field reference data is below $-57\,\text{dB}$ over the whole spherical pattern and for all dyadic components of $\overline{\sigma}$. An error level of this order corresponds to the numerical accuracy that is typically observed for this kind of simulation data. In Fig. 5.22 the VV component of the computed RCS is shown for a horizontal cut at $\vartheta = 90°$ together with the solution using the linearized "radiating reflectors" approach which requires only monostatic near-field data. For the latter, the maximum relative error is about $-21\,\text{dB}$ due to multiple

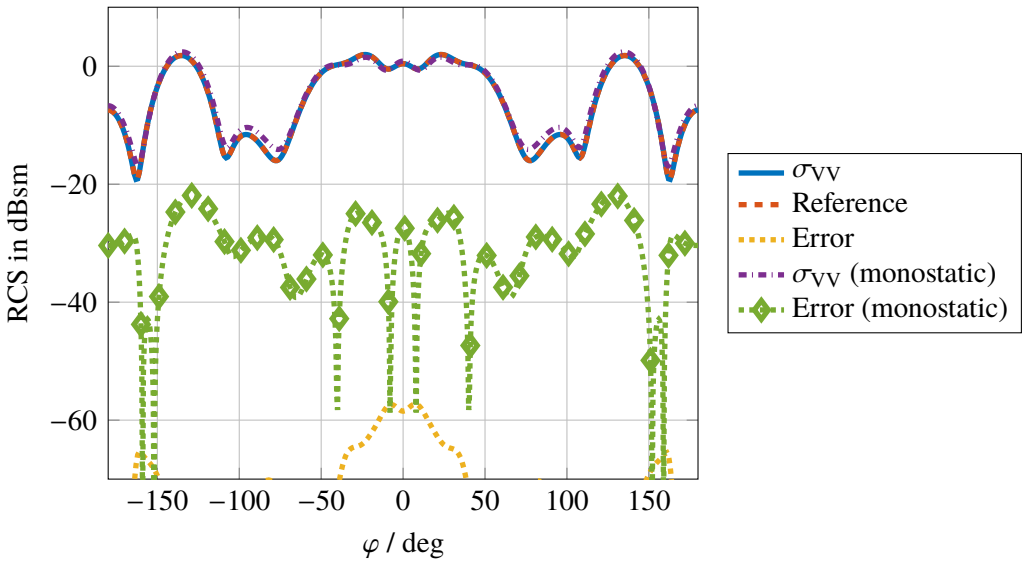

Figure 5.22: VV component of the computed monostatic RCS of the dihedral corner reflector obtained from a full set of bistatic NF data or using only monostatic NF data with the radiating reflectors model ("monostatic"). Depicted is a horizontal cut at $\vartheta = 90°$. © 2019 IEEE

interactions at the object.

In the next step the number of measurement samples is reduced. Starting from the full bistatic spherical setup that was used before, the maximum angular ranges for the field synthesis $\Delta\phi_{\max}^{\text{syn}}$ and the inverse source problem $\Delta\phi_{\max}^{\text{isp}}$ are limited according to a certain greater circle distance as given by (4.65) around the direction of incidence of the synthesized plane wave and the location of the transmitting antenna in the near field, respectively. For each combination the monostatic RCS of the dihedral corner reflector is determined and the maximum relative magnitude error of the complete FF pattern with respect to the FEKO reference solution is computed. The results for $\Delta\phi_{\max}^{\text{syn}} = 25°, 35°, 45°$ and $\Delta\phi_{\max}^{\text{isp}} = 15°$ to $90°$ are shown in Figure 5.23. It was shown in Section 4.5.3 that for a ratio $r_V/r_{\text{meas}} = 0.3$ of this setup a plane-wave field synthesis accuracy better than −45 dB can be achieved with all three angular ranges for the field synthesis that are considered here. However, depending on the truncation of the receiver scan area, this accuracy cannot always be achieved for the monostatic RCS. For small scan areas, the overall accuracy is limited by the truncation errors of the inverse source problems, as the correct solution of the scattered plane-wave spectrum is no longer found for the complete angular range (in k-space) that is considered for the field synthesis. Obviously, this effect is even more severe for larger angular ranges of the field synthesis. On the other hand, if the scan area is sufficiently large, the accuracy is only limited by the quality of the synthesized plane-wave field. With respect to additional errors introduced during a realistic measurement, an RCS accuracy better than −40 dB is usually considered to be sufficient for most applications.

In a realistic NF measurement setup it might be difficult to position both the transmitting and the receiving antennas on a spherical grid. Instead one may envision a setup where a static transmitting (Tx) antenna is pointing towards the origin of a spherical scan setup, while the receiving (Rx) antenna is moved in a plane around the Tx antenna. By rotating the DUT or

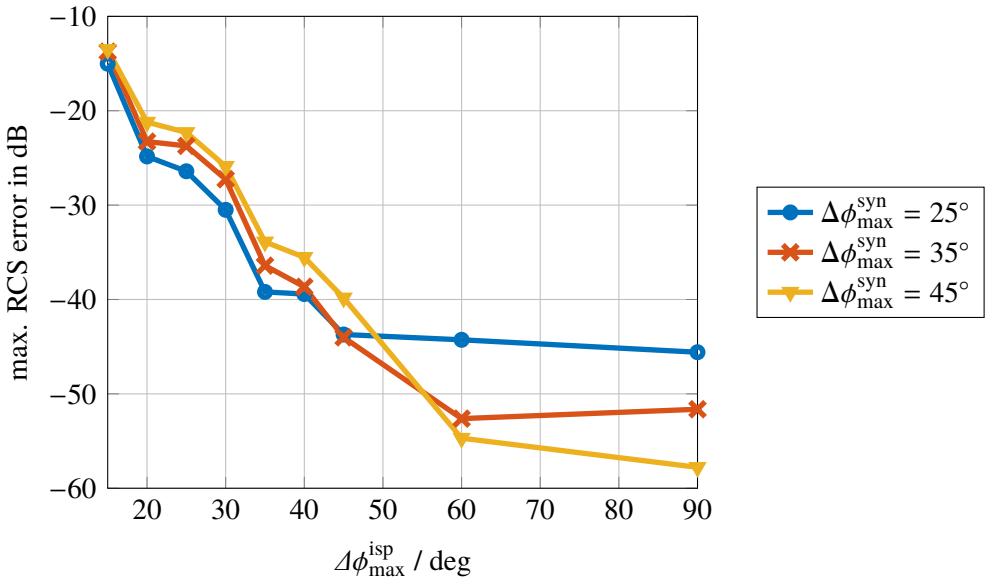

Figure 5.23: Maximum relative error of the computed monostatic RCS of the dihedral reflector using sets of bistatic NF scattering data with limited angular range. © 2019 IEEE

moving the complete Rx-Tx structure around it, a complete spherical scan is realized. This was demonstrated for the case of the dihedral corner reflector in [Neitz and Eibert 2018] and will also be illustrated by the next example.

5.2.2 Bike Model

The DUT is now the PEC model of a motor bike [Stratasys Solutions Ltd. 2018] as shown in Figure 5.24. It is assumed that for each transmitter position on a spherical grid, the Rx antenna is continuously rotating around the Tx antenna and moving radially outwards at the same time. Thus, a spiral measurement setup is realized. To reduce the simulation time, the measurement frequency was chosen to be 1 GHz and Hertzian dipole probes are used as transmitting and receiving antennas. The motor bike may be enclosed by a minimum sphere with radius $r_V = 1\,\mathrm{m}$, which is also chosen to be the target volume for the plane-wave field synthesis. The Tx antenna is moved on a spherical grid with $r_{\mathrm{meas}} = 2.5\,\mathrm{m}$ and $\Delta\varphi = \Delta\vartheta = 5°$. The maximum angular range for the field synthesis is limited to $\Delta\phi^{\mathrm{syn}}_{\mathrm{max}} = \pm 35°$ around the Tx antenna, realizing a plane-wave field synthesis accuracy better than −40 dB within the target volume. The spiral has a radius of $\rho_{\mathrm{spiral}} = 2\,\mathrm{m}$ and 11 turns, which results in 436 receiver samples per transmitter position, where it is assumed that two orthogonal field components are acquired at each position, both rotating along the spiral path. To determine the full 3D monostatic RCS, the Tx antenna is moved on a full spherical grid with 2664 transmitter positions in total. At each position the corresponding inverse source problem is iteratively solved as described before. The mean computation time is 14 s per problem using 4 threads on an Intel i7-4820K CPU. Although the overall computational effort may seem to be very large, one has to keep in mind that it will typically require less time to perform the computations than to conduct the actual measurements. Furthermore, all inverse source problems can be solved

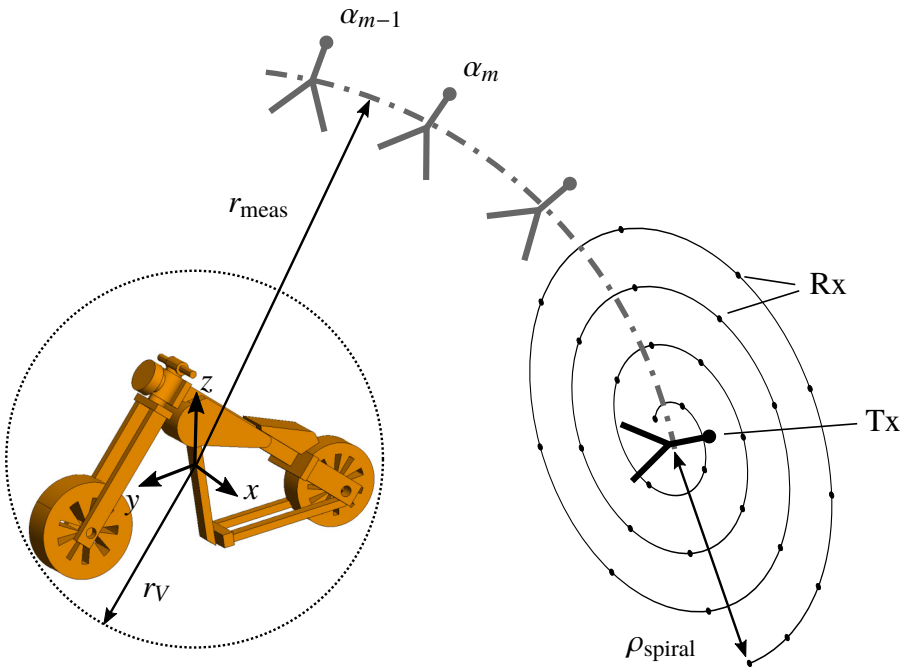

Figure 5.24: Basic scan setup to measure the RCS of a motorbike. The Rx antenna is moved on a planar spiral around the Tx antenna, which is moved on a spherical grid around the DUT. © 2019 IEEE

independently from (or in parallel to) each other. In fact, one could even start the processing after only having completed the corresponding NF measurement. Figure 5.25 shows the VV component of the computed monostatic RCS compared to the FEKO reference data. The relative magnitude error is lower than −44 dB for all components and all angular directions, which is in good agreement with the estimated plane-wave synthesis accuracy.

5.2.3 Metallic Plate Measurement

To validate the presented algorithm experimentally, also multistatic scattering measurements were conducted in the anechoic measurement chamber of the TUM. The setup consists of a spherical positioner for rotating the DUT, a static dual polarized receiving probe (conical horn antenna) pointing towards the spherical rotation origin and a linearly polarized transmitting OEWG probe, moving on a planar scan surface around the Rx antenna. The probe setup is depicted in Fig. 5.26 where also the scan path of the Tx probe is indicated. In contrast to the quasi-monostatic measurements presented in the previous section, the use of the OEWG antenna allows one to move the two probe antennas closer to each other to have a sufficiently small sample spacing for the plane-wave field synthesis.

Due to the mast holding the receiving probe, the scan path is not completely continuous but exhibits a gap below the Rx probe. This does, however, not pose a problem for the transformation algorithm which is able to handle irregular probe locations as noted before. At each Rx-Tx position the uncalibrated transmission factor S_{21} between the two probes is measured for all four scattering components by rotating the OEWG antenna by 90° and employing the two channels of the receive horn. The measurement frequency was chosen

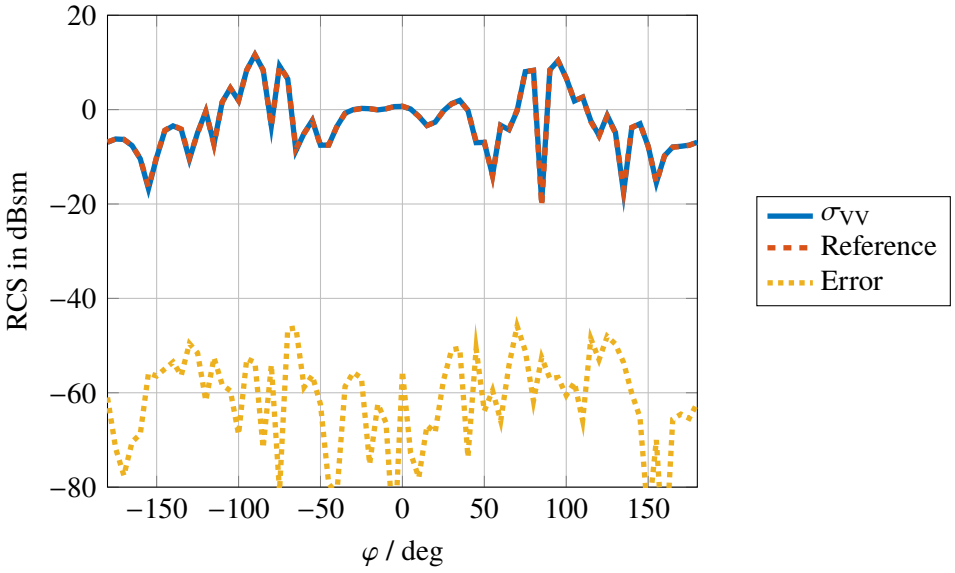

Figure 5.25: VV component of the computed monostatic RCS of the motor bike, determined from spiral scan NF data and compared to FEKO reference data. Depicted is a horizontal cut at $\vartheta = 90°$. © 2019 IEEE

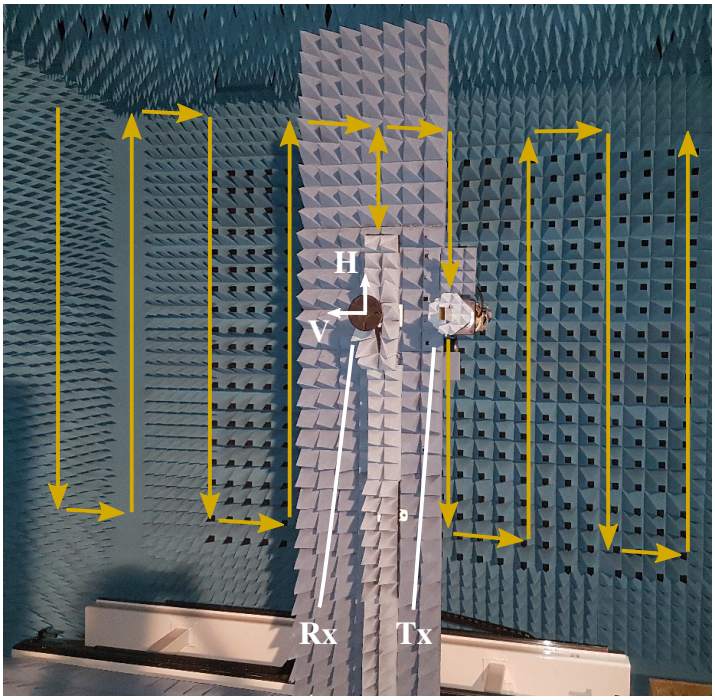

Figure 5.26: Bistatic scan setup in the anechoic chamber of TUM. The transmitting OEWG probe (Tx) is moved along the indicated planar path around the static receiving horn antenna (Tx). © 2019 IEEE

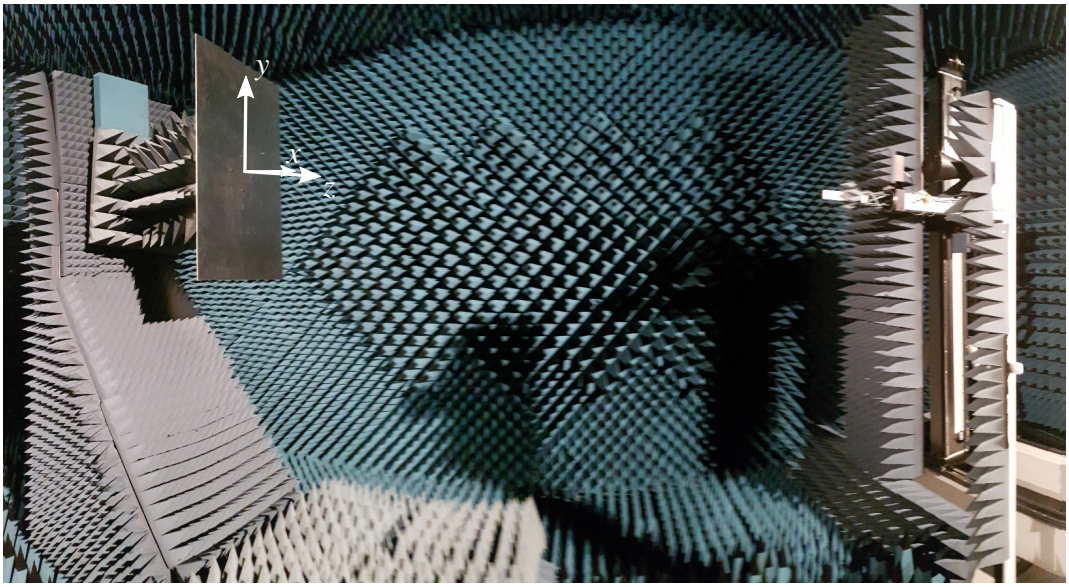

Figure 5.27: Multistatic scattering measurement of a metallic plate in the anechoic chamber of the TUM. The test object is mounted on a spherical positioner. The Tx probe antenna is moving in a plane around the static Rx probe. © 2019 IEEE

to be 4 GHz. As it was done for the monostatic data, an empty chamber measurement was performed beforehand and subtracted from the raw measurement data to remove the incident field (i.e., the direct coupling between the antennas) as well as parasitic reflections. This was done for each angular position of the planar scan grid (with respect to the spherical coordinate system of the target).

The first measurement test object is again the metallic plate that was already used before. It has a size of 0.8 m × 0.52 m and is rotated with an angular step width of $\Delta\varphi_{\mathrm{Rx}} = \Delta\vartheta_{\mathrm{Rx}} = 2°$ to cover the complete upper hemisphere[3]. The Rx probe is positioned in a radial distance of $r_{\mathrm{meas}} = 2.65\,\mathrm{m}$ with the Tx antenna scanning an area of $x = \pm 1.2\,\mathrm{m}$ and $y = \pm 0.8\,\mathrm{m}$ around it. To realize a $\lambda/2$ sampling on a minimum sphere with $r_V = 0.55\,\mathrm{m}$ enclosing the DUT, the planar step width was set to $\Delta x = \Delta y = 0.18\,\mathrm{m}$, resulting in 144 planar scan positions for each angular position and a total measurement time of about 80 h. Figure 5.27 shows the complete setup.

The size of the planar scan area allows for using an angular range of $\Delta\phi_{\mathrm{max}}^{\mathrm{syn}} = \pm 16°$ for the field synthesis, which theoretically leads to a mean error of the synthesized plane-wave field of −46 dB in the spherical target volume. In contrast to the simulation examples considered before, the field synthesis solution is now subject to small probe positioning errors, parasitic reflections, noise and imperfect knowledge of the radiation properties of the transmitter. Thus, the actual error of the synthesized field will be somewhat larger. The computed monostatic RCS is compared to the FEKO reference data as shown in Fig. 5.28 and 5.29 for the VV and HH component, respectively. Depicted is the normalized RCS in an elevation cut at $\varphi = 0°$. The relative deviation with respect to the simulated data is always lower than −30 dB for the

[3]The static Rx probe always points toward the origin of the spherical rotation center, hence the subscript notation

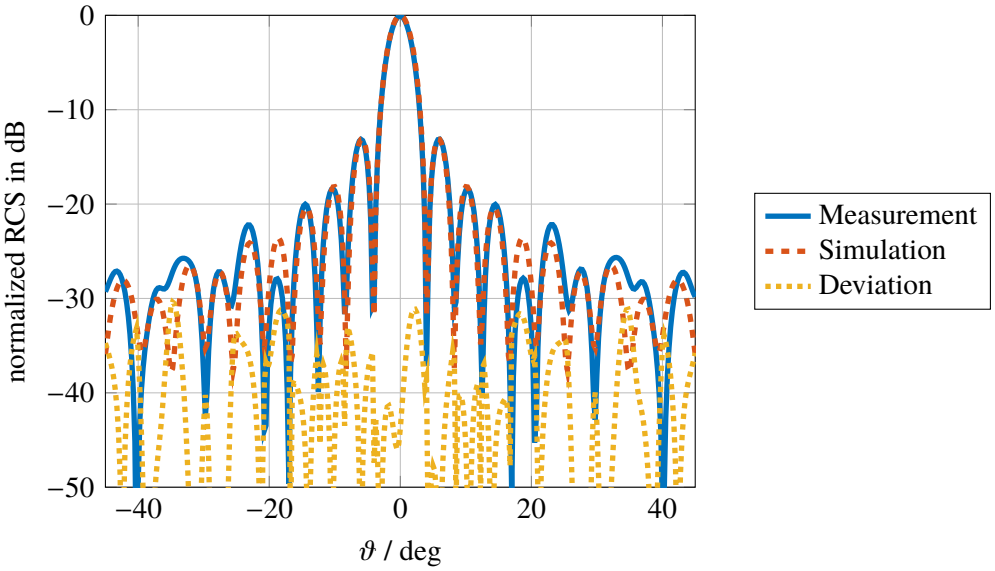

Figure 5.28: VV component of the computed normalized monostatic RCS from multistatic NF measurements at 4 GHz of the metallic plate compared to FEKO reference solution. Vertical cut at $\varphi = 0°$. © 2019 IEEE

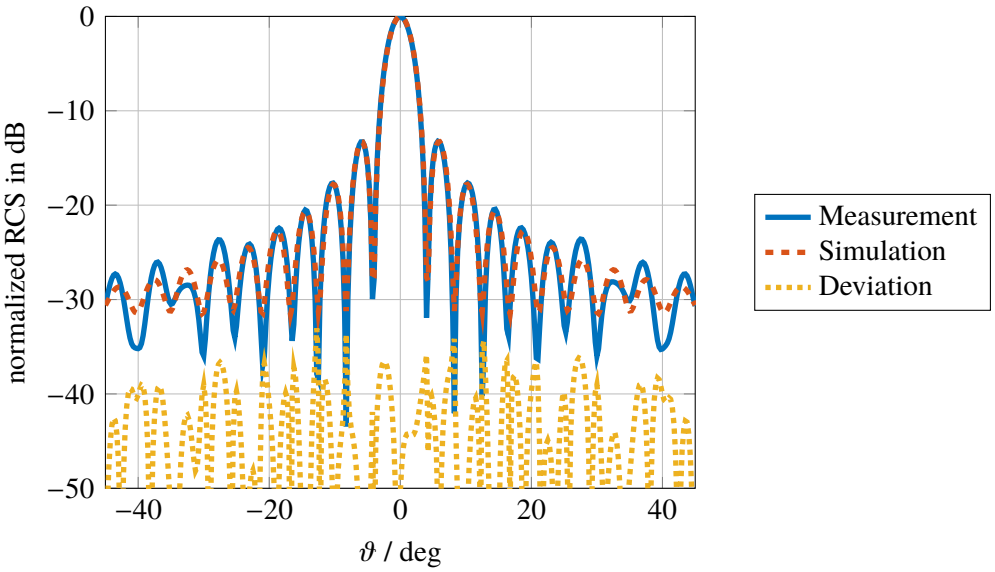

Figure 5.29: HH component of the computed normalized monostatic RCS from multistatic NF measurements at 4 GHz of the metallic plate compared to FEKO reference solution. Vertical cut at $\varphi = 0°$. © 2019 IEEE

VV component and even better for the HH component. Compared to the monostatic solution in the previous section the results are on a similar average deviation level, however the alignment is much better. On the other hand, as the two probes are for some planar positions now closer to each other and the OEWG probe has a less directive radiation pattern, the effect of a limited dynamic range due to the direct coupling appears to be worse. This limits the accuracy for smaller RCS values (at $|\vartheta| > 20°$), in particular for the VV component where the coupling is the strongest due to the configuration of the measurement setup. The mean time for solving the inverse problems with 144 planar measurement samples for one angular direction was about 1.5 s using 4 threads on an Intel i7-4820K CPU. The converging relative observation errors is around −30 dB for small angles ϑ_{Rx}, where the reflected signal is still strong within the planar scan area, and reaches −10 dB and more for $|\vartheta_{\mathrm{Rx}}| > 20°$, where most of the scattered field power is outside the scan area.

5.2.4 Measurement of Test Object "Cuby"

Finally, also the test object "Cuby" depicted in Figure 5.17 is used to validate the multistatic algorithm for the case of a more complex target. The employed measurement setup is the same as before with a spherical target volume for the plane-wave field synthesis with radius $r_V = 0.55$ m and a test frequency of 4 GHz. By comparing the obtained RCS results from the measurement of the metallic plate to the simulated FEKO data an amplitude calibration factor is obtained to determine the actual RCS in dBsm. The results in a vertical cut plane at $\varphi = 0°$ are shown in Figure 5.30 and 5.31 for the VV and HH component, respectively. The depicted deviation is with respect to the simulated far-field reference data obtained by FEKO. As an additional reference the results from the monostatic NF measurement presented in the previous section are given as well.

Compared to the metallic plate measurement, the relative observation error to which the solver converges is now lower for most of the individual inverse source problems. Although for small angles of ϑ_{Rx} it is only as low as −26 dB, the mean error is around −15 dB compared to −5 dB before with the monostatic setup. While in case of the metallic plate for most angles ϑ_{Rx} the scattered field power was mainly directed towards one particular direction (possibly outside the bistatic scan range), this is no longer the situation for this target. Consequently, for a wider angular range of ϑ_{Rx} significant field components can be captured, despite the limited dynamic range of the overall measurement setup.

Considering the monostatic results from the previous section it appears that the deviation from the FEKO reference data is now slightly larger for some angles ϑ. In particular for those parts of the RCS pattern where the magnitude is relatively low, the monostatic solution seems to resolve the pattern with higher accuracy. Again, this is most likely due to the limited dynamic range of the measurement setup. As in the case of the bistatic measurements stronger coupling between the probes could be observed (due to the wider radiation pattern of the OEWG probe), the Tx power of the utilized vector network analyzer was reduced. But still the strong coupling limits the ability to resolve weakly reflected signals. It can be expected that with a more dedicated hardware setup, where it is possible to use probe antennas having a higher directivity, more accurate results could be achieved. Nonetheless, the obtained results clearly demonstrate the applicability of the presented algorithm as well as its versatility with respect to possible near-field scan setups.

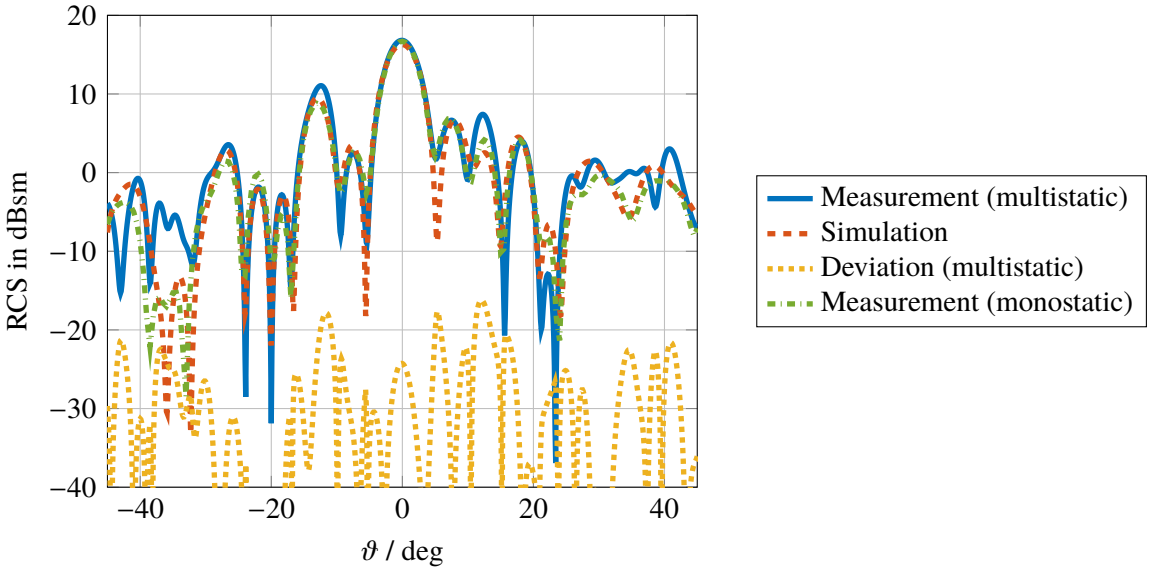

Figure 5.30: VV component of the computed monostatic RCS from multistatic NF measurements at 4 GHz of the metallic test object "Cuby" compared to FEKO reference solution. Vertical cut at $\varphi = 0°$. The result from the monostatic NF measurement is given as an additional reference.

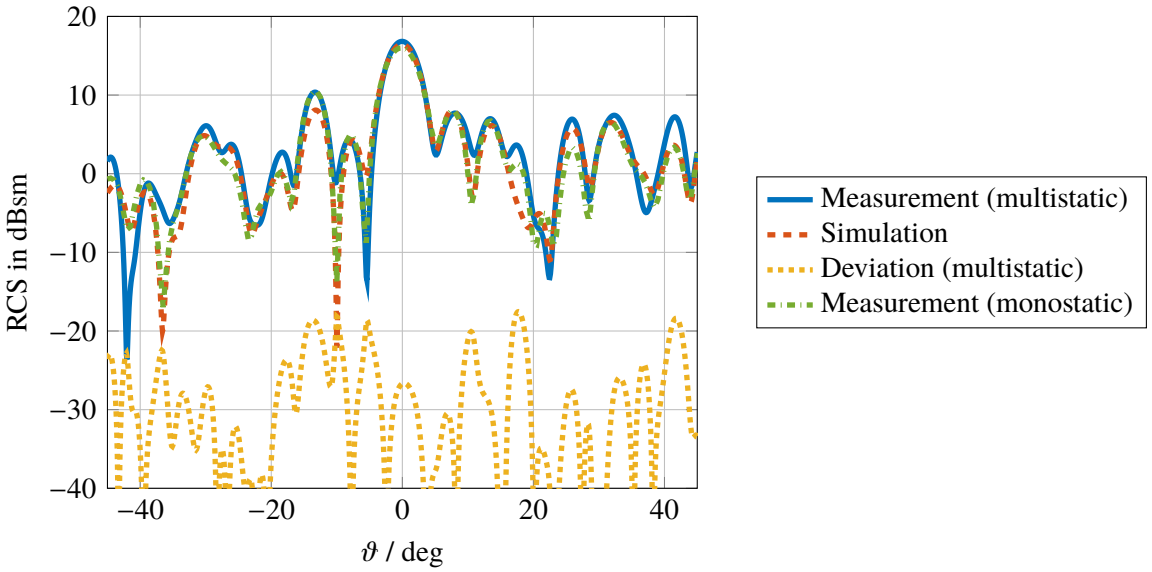

Figure 5.31: HH component of the computed monostatic RCS from multistatic NF measurements at 4 GHz of the metallic test object "Cuby" compared to FEKO reference solution. Vertical cut at $\varphi = 0°$. The result from the monostatic NF measurement is given as an additional reference.

6 Conclusion and Outlook

The test and application examples presented in this thesis demonstrate that expanding the electric field into a spectrum of propagating plane waves leads to very efficient and versatile transformation algorithms for both antenna and RCS measurements in the near field. This is mainly due to the hierarchical multi-level schemes that can be implemented in this way. For the examples shown here a global FFT-based interpolation was used for the involved aggregation and disaggregation steps. It was noted that, as long as a complete plane-wave spectrum is processed, this scheme is beneficial as it does not require additional oversampling of the spectra, it is exact to numerical precision and it can benefit from efficient implementations such as the FFTW. For the solution of the resulting linear systems of equations, an iterative GMRES method was chosen to find the regularized (minimum energy) solution of a normal equation in order to overcome the ill-posedness of the original problem. Employing synthetic and simulated test data the normal error (NE) equation was shown to provide a better stopping criterion compared to the normal residual (NR) equation. In this context also the choice of different basis functions was discussed. It was demonstrated that global basis functions such as spherical wave functions lead to a better conditioned system matrix of the linear system of equations, however, at the price of larger memory requirements and no diagnostic capabilities as available by using equivalent surface currents. The underlying propagating plane-wave based and gain-normalized transmission equation that was derived in this thesis was shown to converge to the well known Friis equation in the far-field limit. Thus, it has the instructive property of being a direct generalization of the far-field case by considering a full spectrum of plane waves. A similar relation was obtained for the scattering case. Here, the transmission equation between the probe antennas and including the scattering dyad was shown to be a generalization of the classical radar range equation.

With the presented algorithm even large antenna measurement problems with millions of unknowns and irregularly distributed sample locations are processed in a relatively short time as demonstrated by, for example, the crane-based measurement setups. Moreover, by utilizing localized equivalent sources the influence of truncation errors is also kept to a minimum. Thus it becomes possible to determine, e.g., the boresight antenna gain from a relatively small scan surface around the direction of maximum radiation. This aspect was demonstrated using planar measurements of a standard gain horn antenna in the W-band and was then also employed for the determination of the RCS of an object under test. As derived in this thesis, in a near-field scattering setup it is sufficient to measure the scattered field in a relatively small area around the transmitting antenna in order to accurately compute the monostatic RCS by additionally solving a field synthesis problem with respect to the transmitter positions. Using simulated test and reference data it was shown that the achievable accuracy of this approach is essentially only limited by the size of the angular range that was used for the field synthesis. This is in contrast to the radiating reflectors model based algorithm that was presented as well, where the actual accuracy is more or less unpredictable. Due to the underlying linearized model of the latter the accuracy will definitely be limited in the case of a complex target and the

resulting uncertainty is difficult to estimate in advance. It was also tried to demonstrate this difference between the two methods by near-field scattering measurements with a specifically designed test object. While the overall results are satisfactory in the sense that the applicability of both methods was validated, the limited sensitivity of the hardware setup (unfortunately) did not allow to reveal the true benefits of the field synthesis approach. Certainly, this would be possible with a more dedicated hardware setup, possibly utilizing arrays of more directive probe antennas. This could also help to significantly reduce the acquisition time.

The Fourier integral relation between the RCS and the spatial scattering center distribution allows for a relatively simple image formation once the RCS has been determined. In this regard the presented algorithms can also serve the purpose of near-field imaging. As demonstrated by comparison to a classical polar reformatting method, the multi-level plane-wave spectrum representation allows for an efficient evaluation of the Fourier integral without requiring the error-prone interpolation to a Cartesian grid.

It can be expected that, depending on the available computer hardware, even faster transformations will be possible by employing massive parallelization. To this end, it may be advantageous to perform (more) FMM translations on levels with smaller sub-boxes in order to avoid the repeated aggregation and disaggregations steps as they are typically less efficient with respect to parallel computing. In this context, as already demonstrated for antenna measurements by Eibert et al. [2016], using Gaussian beam translations could also help to further reduce the computation times and memory requirements for near-field scattering problems by not always considering the full angular plane-wave spectrum.

In general, a remaining challenge of the presented methods is to process broadband frequency data. So far, as the presented transformation algorithms are working on single frequency data only, a separate evaluation for each frequency is required. While this can of course be easily done in parallel, it still implies a tremendous computational effort, in particular for broadband imaging applications. An approach to overcome this issue might be to perform time domain transformations as already investigated for near-field antenna measurements by, e.g., T. B. Hansen [1997] and Bucci; D'Elia, et al. [1998].

For the image-based RCS transformations a different optimization with respect to the measurement time can possibly result from a compressive sampling strategy. In contrast to the antenna measurement cases considered in, e.g., [Hofmann et al. 2019], a 3D set of scattering centers actually is sparse with respect to the spatial domain in which they are defined. Consequently, it might be possible to employ an ℓ^1-minimization strategy to solve for these scattering centers with a reduced number of measurement samples.

From an application point of view near-field RCS measurements using UAVs might be of great interest in order to characterize large scale objects. As currently a lot of effort is put into UAV-based antenna measurements most of the necessary hardware should be readily available. Similarly, the portable crane-based solution presented by Geise et al. [2019] could be extended to scattering measurements. In both cases a straightforward approach would be to measure the monostatic response and employ the radiating reflectors model. However, one could also think of a bistatic approach with one (more or less) static probe antenna and a second one rotating around it. In this case, the remaining challenge would be to keep the transmitting antenna approximately at a fixed position with respect to the object under test, in order to measure the scattered field for an almost constant excitation.

Without a doubt even further advancements in the field of near-field measurements will be

made in the future, possibly enabling a variety of other applications. Due to their versatility the presented plane-wave spectrum algorithms appear to be an excellent starting point for any further research and development tasks.

A Appendix

A.1 Recurrence Relations

A.1.1 Spherical Bessel/Hankel Functions

Definition in terms of Bessel/Hankel function $\mathrm{H}_n^{(i)}(z)$:

$$\mathrm{h}_n^{(i)}(z) = \sqrt{\frac{\pi}{2z}}\mathrm{H}_{n+1/2}^{(i)}(z) \tag{A.1}$$

Recurrence relation:

$$\mathrm{h}_n^{(i)}(z) = \frac{2(n-1)}{z}\mathrm{h}_{n-1}^{(i)}(z) - \mathrm{h}_{n-2}^{(i)}(z) \tag{A.2}$$

Starting values for spherical Hankel function of 2nd kind:

$$\mathrm{h}_0^{(2)}(z) = -\frac{1}{\mathrm{j}z}\mathrm{e}^{-\mathrm{j}z} \qquad \mathrm{h}_1^{(2)}(z) = \left(-\frac{1}{\mathrm{j}z} - 1\right)\mathrm{e}^{-\mathrm{j}z} \tag{A.3}$$

A.1.2 Legendre Polynomials

Starting values:

$$\mathrm{P}_0(x) = 1 \qquad \mathrm{P}_1(x) = x \tag{A.4}$$

$$l\mathrm{P}_l(x) = (2l-1)x\mathrm{P}_{l-1}(x) - (l-1)\mathrm{P}_{l-2}(x) \tag{A.5}$$

A.1.3 Normalized Associated Legendre Polynomials

Definition in terms of associated Legendre polynomial $\mathrm{P}_l^m(x)$:

$$\bar{\mathrm{P}}_l^m(x) = \sqrt{\frac{2l+1}{2}\frac{(l-m)!}{(l+m)!}}\mathrm{P}_l^m(x) \tag{A.6}$$

Starting value:

$$\bar{\mathrm{P}}_0^0(x) = \frac{1}{\sqrt{2}} \tag{A.7}$$

Recurrence relations:

$$\bar{\mathrm{P}}_m^m(x) = -\sqrt{\frac{2m+1}{2m}}\sqrt{1-x^2}\bar{\mathrm{P}}_{m-1}^{m-1}(x) \tag{A.8}$$

$$\bar{\mathrm{P}}_{m+1}^m(x) = \sqrt{2m+3}x\bar{\mathrm{P}}_m^m(x) \tag{A.9}$$

$$\bar{\mathrm{P}}_l^m(x) = \sqrt{\frac{4l^2-1}{l^2-m^2}}\left[x\bar{\mathrm{P}}_{l-1}^m(x) - \sqrt{\frac{(l-1)^2-m^2}{4(l-1)^2-1}}\bar{\mathrm{P}}_{l-2}^m(x)\right] \tag{A.10}$$

$$(1-x^2)\frac{\mathrm{d}\bar{\mathrm{P}}_l^m(x)}{\mathrm{d}x} = -\sqrt{1-x^2}\bar{\mathrm{P}}_l^{m+1}(x)\sqrt{(l+m+1)(l-m)} - mx\bar{\mathrm{P}}_l^m(x) \tag{A.11}$$

A.2 Spherical Wave Functions for Outgoing Waves

General case:

$$\boldsymbol{F}_{1mn}(r,\vartheta,\varphi) = -\mathrm{j}\mathrm{h}_n^{(2)}(kr)T_2(\vartheta)\mathrm{e}^{-\mathrm{j}\varphi}\boldsymbol{e}_\vartheta - \mathrm{h}_n^{(2)}(kr)T_1(\vartheta)\mathrm{e}^{-\mathrm{j}\varphi}\boldsymbol{e}_\varphi \tag{A.12}$$

$$\begin{aligned}\boldsymbol{F}_{2mn}(r,\vartheta,\varphi) = {}& \sqrt{\frac{n(n+1)}{2\pi}}\frac{\mathrm{h}_n^{(2)}(kr)}{kr}\bar{\mathrm{P}}_n^{|m|}\cos\vartheta\mathrm{e}^{-\mathrm{j}\varphi}\boldsymbol{e}_r \\ & + \frac{1}{kr}\frac{\mathrm{dh}_n^{(2)}(kr)}{\mathrm{d}(kr)}T_1(\vartheta)\mathrm{e}^{-\mathrm{j}\varphi}\boldsymbol{e}_\vartheta - \mathrm{j}\frac{1}{kr}\frac{\mathrm{dh}_n^{(2)}(kr)}{\mathrm{d}(kr)}T_2(\vartheta)\mathrm{e}^{-\mathrm{j}\varphi}\boldsymbol{e}_\varphi\end{aligned} \tag{A.13}$$

Under far-field conditions:

$$\boldsymbol{K}_{1mn}(r,\vartheta,\varphi) = -\mathrm{j}\mathrm{h}_n^{(2)}(kr)T_2(\vartheta)\mathrm{e}^{-\mathrm{j}\varphi}\boldsymbol{e}_\vartheta - \mathrm{h}_n^{(2)}(kr)T_1(\vartheta)\mathrm{e}^{-\mathrm{j}\varphi}\boldsymbol{e}_\varphi \tag{A.14}$$

$$\boldsymbol{K}_{2mn}(r,\vartheta,\varphi) = \mathrm{h}_n^{(2)}(kr)T_1(\vartheta)\mathrm{e}^{-\mathrm{j}\varphi}\boldsymbol{e}_\vartheta - \mathrm{j}\mathrm{h}_n^{(2)}(kr)T_2(\vartheta)\mathrm{e}^{-\mathrm{j}\varphi}\boldsymbol{e}_\varphi \tag{A.15}$$

In both cases $\mathrm{h}_n^{(2)}$ is the spherical Hankel function of the second kind as defined in (A.1) and

$$T_1(\vartheta) = -\frac{1}{\sqrt{2\pi}}\frac{1}{\sqrt{n(n+1)}}\frac{\partial\bar{\mathrm{P}}_n^{|m|}\cos\vartheta}{\partial\vartheta} \tag{A.16}$$

$$T_2(\vartheta) = \frac{1}{\sqrt{2\pi}}\frac{1}{\sqrt{n(n+1)}}\frac{m\bar{\mathrm{P}}_n^{|m|}\cos\vartheta}{\sin\vartheta}. \tag{A.17}$$

with $\bar{\mathrm{P}}_n^m$ the normalized associated Legendre polynomial defined in (A.6), which ensures numerical stability in combination with the recurrence relations (A.8) - (A.11).

A.3 Rao-Wilton-Glisson (RWG) Basis Functions

Definition with respect to Figure A.1:

$$\boldsymbol{\beta}_{ij}(\boldsymbol{r}) = \begin{cases} \dfrac{l_{ij}}{2A_{ij}^{+}}(\boldsymbol{r} - \boldsymbol{r}_i), & \boldsymbol{r} \in T_{ij}^{+} \\ \dfrac{l_{ij}}{2A_{ij}^{-}}(\boldsymbol{r}_i - \boldsymbol{r}), & \boldsymbol{r} \in T_{ij}^{-} \\ 0 & \text{else} \end{cases} \tag{A.18}$$

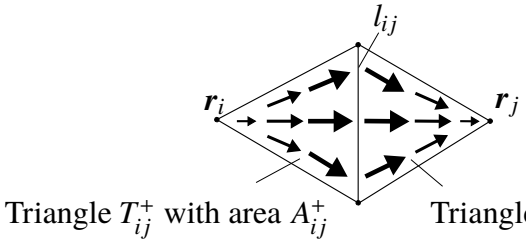

Figure A.1: Definition of RWG basis functions.

A.4 Global Interpolation Using the FFT

Consider a 2π periodic sample sequence y_N of length N. The Fourier transform using an N point FFT is

$$Y_N = \mathrm{FFT}_N\{y_N\}. \tag{A.19}$$

The zero padded spectral domain sequence $\tilde{Y}_{N+M}$ is constructed as

$$\tilde{Y}_{N+M} = \left[Y_N(1), \ldots, Y_N\left(\frac{N+1}{2}\right), 0_M, Y_N\left(\frac{N+3}{2}\right), \ldots, Y_N(N)\right] \tag{A.20}$$

if N is uneven, and as

$$\begin{aligned} \tilde{Y}_{N+M} = [&Y_N(1), \ldots, \\ &Y_N\left(\frac{N}{2}+1\right), 0.5Y_N\left(\frac{N}{2}+2\right), 0_{M-1}, 0.5Y_N\left(\frac{N}{2}+2\right), Y_N\left(\frac{N}{2}+3\right), \\ &\ldots, Y_N(N)] \end{aligned} \tag{A.21}$$

if N is even. 0_M is a series of zero entries of length M. Taking the $N+M$ point IFFT the interpolated sequence

$$\tilde{y}_{N+M} = \mathrm{IFFT}_{N+M}\left\{\tilde{Y}_{N+M}\right\} \tag{A.22}$$

is obtained.

A.5 Cartesian Representation of the Scattering Matrix

With the spherical unit vectors

$$\hat{u}_{\mathrm{H}}(\boldsymbol{k}) = \hat{\varphi}(\boldsymbol{k}) = -\sin\varphi_k \hat{x} + \cos\varphi_k \hat{y} \tag{A.23}$$

as well as

$$\hat{u}_{\mathrm{V}}(\boldsymbol{k}) = \hat{\vartheta}(\boldsymbol{k}) = \cos\varphi_k \cos\vartheta_k \hat{x} + \sin\varphi_k \cos\vartheta_k \hat{y} - \sin\vartheta_k \hat{z} \tag{A.24}$$

and assuming reciprocity one obtains

$$\begin{aligned}
S_{xx}(\boldsymbol{k}) &= \hat{x} \cdot \bar{\mathbf{S}}(\boldsymbol{k}) \cdot \hat{x} \\
&= \hat{x} \cdot S_{\vartheta\vartheta}(\boldsymbol{k}) \hat{\vartheta}(\boldsymbol{k}) \hat{\vartheta}(\boldsymbol{k}) \cdot \hat{x} + \hat{x} \cdot S_{\vartheta\varphi}(\boldsymbol{k}) \hat{\vartheta}(\boldsymbol{k}) \hat{\varphi}(\boldsymbol{k}) \cdot \hat{x} \\
&\quad + \hat{x} \cdot S_{\varphi\vartheta} \hat{\varphi}(\boldsymbol{k}) \hat{\vartheta}(\boldsymbol{k}) \cdot \hat{x} + \hat{x} \cdot S_{\varphi\varphi}(\boldsymbol{k}) \hat{\varphi}(\boldsymbol{k}) \hat{\varphi}(\boldsymbol{k}) \cdot \hat{x} \\
&= S_{\vartheta\vartheta}(\boldsymbol{k}) \left(\hat{x} \cdot \hat{\vartheta}(\boldsymbol{k}) \hat{\vartheta}(\boldsymbol{k}) \cdot \hat{x} \right) + 2 S_{\vartheta\varphi}(\boldsymbol{k}) \left(\hat{x} \cdot \hat{\vartheta}(\boldsymbol{k}) \hat{\varphi}(\boldsymbol{k}) \cdot \hat{x} \right) \\
&\quad + S_{\varphi\varphi}(\boldsymbol{k}) (\hat{x} \cdot \hat{\varphi}(\boldsymbol{k}) \hat{\varphi}(\boldsymbol{k}) \cdot \hat{x}) \\
&= S_{\vartheta\vartheta}(\boldsymbol{k}) \cos^2\varphi_k \cos^2\vartheta_k - 2 S_{\vartheta\varphi}(\boldsymbol{k}) \sin\varphi_k \cos\varphi_k \cos\vartheta_k + S_{\varphi\varphi}(\boldsymbol{k}) \sin^2\varphi_k .
\end{aligned} \tag{A.25}$$

Similarly, the other components may be expressed as

$$\begin{aligned}
S_{xy}(\boldsymbol{k}) &= S_{yx}(\boldsymbol{k}) = \hat{x} \cdot \bar{\mathbf{S}}(\boldsymbol{k}) \cdot \hat{y} \\
&= S_{\vartheta\vartheta}(\boldsymbol{k}) \sin\varphi_k \cos\varphi_k \cos^2\vartheta_k \\
&\quad + S_{\vartheta\varphi}(\boldsymbol{k}) \left(\cos^2\varphi_k - \sin^2\varphi_k \right) \cos\vartheta_k - S_{\varphi\varphi}(\boldsymbol{k}) \sin\varphi_k \cos\varphi_k
\end{aligned} \tag{A.26}$$

$$\begin{aligned}
S_{xz}(\boldsymbol{k}) &= S_{zx}(\boldsymbol{k}) = \hat{x} \cdot \bar{\mathbf{S}}(\boldsymbol{k}) \cdot \hat{z} \\
&= -S_{\vartheta\vartheta}(\boldsymbol{k}) \cos\varphi_k \sin\vartheta_k \cos\vartheta_k + S_{\vartheta\varphi}(\boldsymbol{k}) \sin\varphi_k \sin\vartheta_k
\end{aligned} \tag{A.27}$$

$$\begin{aligned}
S_{yy}(\boldsymbol{k}) &= \hat{y} \cdot \bar{\mathbf{S}}(\boldsymbol{k}) \cdot \hat{y} \\
&= S_{\vartheta\vartheta}(\boldsymbol{k}) \sin^2\varphi_k \cos^2\vartheta_k + 2 S_{\vartheta\varphi}(\boldsymbol{k}) \sin\varphi_k \cos\varphi_k \cos\vartheta_k + S_{\varphi\varphi}(\boldsymbol{k}) \cos^2\varphi_k
\end{aligned} \tag{A.28}$$

$$\begin{aligned}
S_{yz}(\boldsymbol{k}) &= S_{zy}(\boldsymbol{k}) = \hat{y} \cdot \bar{\mathbf{S}}(\boldsymbol{k}) \cdot \hat{z} \\
&= -S_{\vartheta\vartheta}(\boldsymbol{k}) \sin\varphi_k \sin\vartheta_k \cos\vartheta_k - S_{\vartheta\varphi}(\boldsymbol{k}) \cos\varphi_k \sin\vartheta_k
\end{aligned} \tag{A.29}$$

$$\begin{aligned}
S_{zz}(\boldsymbol{k}) &= \hat{z} \cdot \bar{\mathbf{S}}(\boldsymbol{k}) \cdot \hat{z} \\
&= S_{\vartheta\vartheta}(\boldsymbol{k}) \sin^2\vartheta_k .
\end{aligned} \tag{A.30}$$

References

Abramowitz, M. and Stegun, I. E., eds. (1972). *Handbook of Mathematical Functions*. 10th edition. Washington, DC: National Bureau of Standards Applied Mathematics Series - 55.

Ahmed, S. S.; Schiessl, A.; Gumbmann, F.; Tiebout, M.; Methfessel, S. and Schmidt, L. (2012). "Advanced microwave imaging". In: *IEEE Microwave Magazine* 13 (6), pp. 26–43.

Altair Engineering, Inc. (2019). *Altair Feko*. URL: `https://altairhyperworks.com/product/FEKO` (visited on 10/07/2019).

Alvarez, Y.; Las-Heras, F. and Pino, M. R. (2007). "Reconstruction of equivalent currents distribution over arbitrary three-dimensional surfaces based on integral equation algorithms". In: *IEEE Transactions on Antennas and Propagation* 55 (12), pp. 3460–3468.

Amidror, I. (2002). "Scattered data interpolation methods for electronic imaging systems: a survey". In: *Journal of Electronic Imaging* 11 (2), pp. 157 - 176 –20.

Balanis, C. A. (2012). *Advanced Engineering Electromagnetics*. 2nd edition. Hoboken, NJ: John Wiley & Sons.

Balanis, C. A. (2016). *Antenna Theory: Analysis and Design*. 4th edition. Hoboken, NJ: John Wiley & Sons.

Betjes, P. N. (2007). "An algorithm for automated phase center determination and its implementation". In: *Proc. 29th Annual Symposium of the Antenna Measurement Techniques Association*. St. Louis, MI, USA.

Bleistein, N. and Cohen, J. K. (1977). "Nonuniqueness in the inverse source problem in acoustics and electromagnetics". In: *Journal of Mathematical Physics* 18 (2), pp. 194–201.

Boag, A. (2001). "A fast multilevel domain decomposition algorithm for radar imaging". In: *IEEE Transactions on Antennas and Propagation* 49 (4), pp. 666–671.

Bogaert, I.; Peeters, J. and Olyslager, F. (2008). "A nondirective plane wave MLFMA stable at low frequencies". In: *IEEE Transactions on Antennas and Propagation* 56 (12), pp. 3752–3767.

Born, M. (1926). "Quantenmechanik der Stoßvorgänge". In: *Zeitschrift der Physik* 38, p. 803.

Bradley, C. J.; Collins, P. J.; Falconer, D. G.; Fortuny-Guasch, J. and Terzuoli Jr., A. J. (2008). "Evaluation of a near-field monostatic-to-bistatic equivalence theorem". In: *IEEE Transactions on Geoscience and Remote Sensing* 46 (2), pp. 449–457.

Broquetas, A.; Palau, J.; Jofre, L. and Cardama, A. (1998). "Spherical wave near-field imaging and radar cross-section measurement". In: *IEEE Transactions on Antennas and Propagation* 46 (5), pp. 730–735.

Bucci, O. M.; D'Elia, G. and Migliore, M. D. (1998). "Near-field far-field transformation in time domain from optimal plane-polar samples". In: *IEEE Transactions on Antennas and Propagation* 46 (7), pp. 1084–1088.

Bucci, O. M.; Gennarelli, C. and Savarese, C. (1998). "Representation of electromagnetic fields over arbitrary surfaces by a finite and nonredundant number of samples". In: *IEEE Transactions on Antennas and Propagation* 46, pp. 351–359.

Bucci, O. M. and Migliore, M. D. (2006). "Effective estimation of 2-D monostatic radar cross sections from near-field measurements". In: *IEEE Transactions on Antennas and Propagation* 54 (2), pp. 750–752.

Bucci, O. M.; Migliore, M. D.; Panariello, G. and Pinchera, D. (2013). "Plane-wave generators: design guidelines, achievable performances and effective synthesis". In: *IEEE Transactions on Antennas and Propagation* 61 (4), pp. 2005–2018.

Bucci, O. M. and Franceschetti, G. (1987). "On the spatial bandwidth of scattered fields". In: *IEEE Transactions on Antennas and Propagation* AP-35 (12), pp. 1445–1454.

Bucci, O. M. and Franceschetti, G. (1989). "On the degrees of freedom of scattered fields". In: *IEEE Transactions on Antennas and Propagation* 37 (7), pp. 918–926.

Cafforio, C.; Prati, C. and Rocca, F. (1991). "SAR data focusing using seismic migration techniques". In: *IEEE Transactions on Aerospace and Electronic Systems* 27 (2), pp. 194–207.

Cakoni, F.; Colton, D. and Monk, P. (2011). *The Linear Sampling Method in Inverse Electromagnetic Scattering*. Philadelphia, PA: Society for Industrial and Applied Mathematics.

Carson, J. R. (1929). "Reciprocal theorems in radio communication". In: *Proceedings of the IRE* 17 (6), pp. 952–956.

Chandra, R.; Zhou, H.; Balasingham, I. and Narayanan, R. M. (2015). "On the opportunities and challenges in microwave medical sensing and imaging". In: *IEEE Transactions on Biomedical Engineering* 62 (7), pp. 1667–1682.

Cheney, M. and Borden, B. (2009). *Fundamentals of Radar Imaging*. Philadelphia, PA: Society for Industrial and Applied Mathematics (SIAM).

Chew, W. C. (1995). *Waves and Fields in Inhomogenous Media*. Ed. by Dudley, D. G. IEEE Press Series on Electromagnetic Waves. Piscataway, NJ: Wiley-IEEE Press.

Chew, W. C.; Cui, T. J. and Song, J. M. (2002). "A FAFFA-MLFMA algorithm for electromagnetic scattering". In: *IEEE Transactions on Antennas and Propagation* 50 (11), pp. 1641–1649.

Chew, W. C.; Jin, J.-M.; Michielssen, E. and Song, J. (2001). *Fast and Efficient Algorithms in Computational Electromagnetics*. Norwood, MA: Artech House Publishers.

Claerbout, J. F. (1985). *Imaging the Earth's Interior*. Oxford: Blackwell Science Inc, p. 412.

Coifman, R.; Rokhlin, V. and Wandzura, S. (1993). “The fast multipole method for the wave equation: A pedestrian prescription”. In: *IEEE Antennas and Propagation Magazine* 35 (3), pp. 7–12.

Colton, D. and Kress, R. (2013). *Inverse Acoustic and Electromagnetic Scattering Theory*. 3rd edition. Applied Mathematical Sciences 93. New York, NY: Springer-Verlag.

Cown, B. J. and Ryan, C. E. (1989). “Near-field scattering measurements for determining complex target RCS”. In: *IEEE Transactions on Antennas and Propagation* 37 (5), pp. 576–585.

Desai, M. D. and Jenkins, W. K. (1992). “Convolution backprojection image reconstruction for spotlight mode synthetic aperture radar”. In: *IEEE Transactions on Image Processing* 4 (4), pp. 505–517.

Devaney, A. J. (2012). *Mathematical Foundations of Imaging, Tomography and Wavefield Inversion*. Cambridge: Cambridge University Press.

Dinallo, M. A. (1984). “Extension of plane-wave scattering-matrix theory of antenna - antenna interactions to three antennas: a near-field radar cross section concept”. In: *Proc. Antenna Applications Symposium*. Vol. 2. Urbana, IL, USA, pp. 665–686.

Eibert, T. F. (2005). “A diagonalized multilevel fast multipole method with spherical harmonics expansion of the k-space integrals”. In: *IEEE Transactions on Antennas and Propagation* 53 (2), pp. 814–817.

Eibert, T. F. and Schmidt, C. H. (2009). “Multilevel fast multipole accelerated inverse equivalent current method employing Rao–Wilton–Glisson discretization of electric and magnetic surface currents”. In: *IEEE Transactions on Antennas and Propagation* 57 (4), pp. 1178–1185.

Eibert, T. F.; Vojvodić, D. and Hansen, T. B. (2016). “Fast inverse equivalent source solutions with directive sources”. In: *IEEE Transactions on Antennas and Propagation* 64 (11), pp. 4713–4724.

Eibert, T. F.; Kılıç, E.; Lopez, C.; Mauermayer, R. A. M.; Neitz, O. and Schnattinger, G. (2015). “Electromagnetic field transformations for measurements and simulations (invited paper)”. In: *Progress in Electromagnetics Research, PIER* 151, pp. 127–150.

Eldén, L. and Simoncini, V. (2012). “Solving ill-posed linear systems with GMRES and a singular preconditioner”. In: *SIAM Journal on Matrix Analysis and Applications* 33 (4), pp. 1369–1394.

Esmersoy, C. and Miller, D. (1989). “Backprojection versus backpropagation in multidimensional linearized inversion”. In: *Geophysics* 54, pp. 921–926.

Falconer, D. G. (1988). “Extrapolation of near-field RCS measurements to the far zone”. In: *IEEE Transactions on Antennas and Propagation* 36 (6), pp. 822–829.

Farr, E.; B. Rogers, R.; R. Salo, G. and N. Truske, T. (1989). “Near-field bistatic RCS (radar cross-section) measurements”. In: *Rome Air Development Center, Technical Report* (RADC-TR-89-189).

Fienup, J. R. (1982). “Phase retrieval algorithms: A comparison”. In: *Applied Optics* 21 (15), pp. 2758–2769.

Fink, D. G. (1945). “The radar equation”. In: *Electronics* 18, pp. 92–94.

Flann Microwave Ltd. (2019). *Flann Microwave*. URL: `https://www.flann.com` (visited on 10/07/2019).

Fortuny-Guasch, J. and Lopez-Sanchez, J. M. (2001). “Extension of the 3-D range migration algorithm to cylindrical and spherical scanning geometries”. In: *IEEE Transactions on Antennas and Propagation* 49 (10), pp. 1434–1444.

Fortuny, J. (1998). “An efficient 3-D near-field ISAR algorithm”. In: *IEEE Transactions on Aerospace and Electronic Systems* 34 (4), pp. 1261–1270.

Frigo, M. and Johnson, S. G. (2005). “The design and implementation of FFTW3”. In: *Proceedings of the IEEE* 93 (2), pp. 216–231.

Friis, H. T. (1946). “A note on a simple transmission formula”. In: *Proceedings of the IRE* 34 (5), pp. 254–256.

Geise, A.; Neitz, O.; Migl, J.; Steiner, H.; Fritzel, T.; Hunscher, C. and Eibert, T. F. (2019). “A crane based portable antenna measurement system — system description and validation”. In: *IEEE Transactions on Antennas and Propagation* 67 (5), pp. 3346–3357.

Greengard, L. and Rokhlin, V. (1987). “A fast algorithm for particle simulations”. In: *Journal of Computational Physics* 73 (2), pp. 325–348.

Guay, R.; Drolet, G. and Bray, J. R. (2017). “Measurement and modelling of the dynamic radar cross-section of an unmanned aerial vehicle”. In: *IET Radar, Sonar Navigation* 11 (7), pp. 1155–1160.

Hamberger, G. F.; Koenen, C.; Neitz, O.; Mauermayer, R. A. M.; Eisner, C. J.; Siart, U. and Eibert, T. F. (2018). “Setup and characterization of a volumetric W-band near-field antenna measurement system”. In: *IEEE Transactions on Antennas and Propagation* 66 (10), pp. 5498–5510.

Hansen, J. E., ed. (1988). *Spherical Near-Field Antenna Measurements*. London: Peter Peregrinus.

Hansen, P. C. (1992). “Analysis of discrete ill-posed problems by means of the l-curve”. In: *SIAM Review* 34 (4), pp. 561–580.

Hansen, P. C. (2010). *Discrete Inverse Problems: Insight and Algorithms*. Fundamentals of Algorithms. Philadelphia, PA: Society for Industrial and Applied Mathematics (SIAM).

Hansen, T. B. (1997). “Formulation of spherical near-field scanning for electromagnetic fields in the time domain”. In: *IEEE Transactions on Antennas and Propagation* 45 (4), pp. 620–630.

Hansen, T. B. (2011). “Spherical near-field scanning with higher-order probes”. In: *IEEE Transactions on Antennas and Propagation* 59 (11), pp. 4049–4059.

Hansen, T. B.; Paulus, A. and Eibert, T. F. (2019). “On the condition number of a normal matrix in near-field to far-field transformations”. In: *IEEE Transactions on Antennas and Propagation* 67 (3), pp. 2028–2033.

Hansen, T. B. (2013). “Translation operator based on gaussian beams for the fast multipole method in three dimensions”. In: *Wave Motion* 50, pp. 940–954.

Harrington, R. F. (2001). *Time-Harmonic Electromagnetic Fields*. New York, NY: John Wiley & Sons.

Harris, F. J. (1978). “On the use of windows for harmonic analysis with the discrete fourier transform”. In: *Proceedings of the IEEE*, pp. 51–83.

Hill, D. A. (1985). “A numerical method for near-field array synthesis”. In: *IEEE Transactions on Electromagnetic Compatibility* EMC-27 (4), pp. 201–211.

Hofmann, B.; Neitz, O. and Eibert, T. F. (2019). “On the minimum number of samples for sparse recovery in spherical antenna near-field measurements”. In: *IEEE Transactions on Antennas and Propagation* 67 (12), pp. 7597–7610.

Huygens, C. (1690). *Traite de la Lumiere*. translated into english by S. P. Thompson, MacMillan and Co., London 1912.

IEEE (2007). *Recommended Practice for Radar Cross-Section Test Procedures*. IEEE Std. 1502-2007.

IEEE (2012). *Recommended Practice for Near-Field Antenna Measurements*. IEEE Std. 1720-2012.

IEEE (2014). *Standard for Definitions of Terms for Antennas*. IEEE Std. 145-2013.

Jenn, D. (2005). *Radar and Laser Cross Section Engineering*. 2nd edition. AIAA education series. Reston, VA: American Institute of Aeronautics and Astronautics.

Jin, J.-M. (2015). *Theory and Computation of Electromagnetic Fields*. Second Edition. Hoboken, NJ: John Wiley & Sons.

Kell, R. E. (1965). “On the derivation of bistatic RCS from monostatic measurements”. In: *Proceedings of the IEEE* 53 (8), pp. 983–988.

Kılıç, E. and Eibert, T. F. (2015). “Solution of 3D inverse scattering problems by combined inverse equivalent current and finite element methods”. In: *Journal of Computational Physics* 288, pp. 131–149.

Knott, E. (2006). *Radar Cross Section Measurements*. Raleigh, NC: SciTech Pub.

Koc, S.; Song, J. and Chew, W. (1999). “Error analysis for the numerical evaluation of the diagonal forms of the scalar spherical addition theorem”. In: *SIAM Journal on Numerical Analysis* 36 (3), pp. 906–921.

Kong, J. A. (1986). *Electromagnetic Wave Theory*. Hoboken, NJ: John Wiley & Sons.

Kornprobst, J.; Mauermayer, R. A. M.; Neitz, O.; Knapp, J. and Eibert, T. F. (2019). "On the solution of inverse equivalent surface-source problems". In: *Progress in Electromagnetics Research, PIER* 165, pp. 47–65.

LaHaie, I. J. (2003). "Overview of an image-based technique for predicting far-field radar cross section from near-field measurements". In: *IEEE Antennas and Propagation Magazine* 45 (6), pp. 159–169.

Lebedev, V. I. and Laikov, D. N. (1999). "A quadrature formula for the sphere of the 131st algebraic order of accuracy". In: *Doklady Mathematics* 59 (3), pp. 477–481.

Love, A. E. H. (1901). "The integration of the equations of propagation of electric waves". In: *Philosophical Transactions of the Royal Society of London* 197, pp. 1–45.

Marchetti, E.; Cassidy, S.; Norouzian, F.; Hoare, E. G.; Cherniakov, M. and Gashinova, M. (2019). "Automotive targets characterization in the low-thz band". In: *Proc. 20th International Radar Symposium (IRS)*, pp. 1–6.

Mauermayer, R. A. M.; Weitsch, Y. and Eibert, T. F. (2015). "Electromagnetic field synthesis by hierarchical plane wave-based field transformation". In: *IEEE Transactions on Antennas and Propagation* 63 (12), pp. 5561–5572.

Mehrholz, D.; Leushacke, L.; Flury, W.; Jehn, R.; Klinkrad, H. and Landgraf, M. (2002). "Detecting, tracking and imaging space debris". In: *ESA bulletin* 109, pp. 128–134.

Melin, J. O. (1987). "Measuring radar cross section at short distance". In: *IEEE Transactions on Antennas and Propagation* 35 (8), pp. 991–996.

Mensa, D. L. (1990). *High Resolution Radar Cross-Section Imaging*. Revised. Norwood, MA: Artech House Inc.

Migliore, M. D. (2014). "A simple introduction to compressed sensing/sparse recovery with applications in antenna measurements". In: *IEEE Antennas and Propagation Magazine* 56 (2), pp. 14–26.

Mott, H. (2007). *Remote Sensing with Polarimetric Radar*. 1st ed. Hoboken, NJ: Wiley-IEEE Press.

Munson, D. C.; O'Brien, J. D. and Jenkins, W. K. (1983). "A tomographic formulation of spotlight-mode synthetic aperture radar". In: *Proceedings of the IEEE* 71 (8), pp. 917–925.

Myint, S. J.; Schneider, C.; Röding, M.; Galdo, G. D. and Thomä, R. S. (2019). "Statistical analysis and modeling of vehicular radar cross section". In: *Proc. 13th European Conference on Antennas and Propagation (EuCAP)*, pp. 1–5.

Neitz, O.; Mauermayer, R. A. M. and Eibert, T. F. (2019). "3D monostatic RCS determination from multistatic near-field measurements by plane-wave field synthesis". In: *IEEE Transactions on Antennas and Propagation* 67 (5), pp. 3387–3396.

Neitz, O.; Mauermayer, R. A. M.; Weitsch, Y. and Eibert, T. F. (2017). "A propagating plane-wave-based near-field transmission equation for antenna gain determination from

irregular measurement samples". In: *IEEE Transactions on Antennas and Propagation* 65 (8), pp. 4230–4238.

Neitz, O. and Eibert, T. F. (2017). "Measurement sample reduction for efficient antenna gain determination in the near-field". In: *Proc. IEEE International Symposium on Antennas and Propagation USNC/URSI National Radio Science Meeting*. Boston, MA, USA, pp. 161–162.

Neitz, O. and Eibert, T. F. (2018). "A plane-wave synthesis approach for 3D monostatic RCS prediction from near-field measurements". In: *Proc. 15th European Radar Conference (EuRAD)*. Madrid, Spain, pp. 99–102.

Newell, A. C.; Ward, R. D. and McFarlane, E. J. (1988). "Gain and power parameter measurements using planar near-field techniques". In: *IEEE Transactions on Antennas and Propagation* 36 (6), pp. 792–803.

NSI-MI Technologies, LLC (2019). *NSI-MI*. URL: `http://www.nsi-mi.com` (visited on 10/07/2019).

Oliveri, G.; Salucci, M.; Anselmi, N. and Massa, A. (2017). "Compressive sensing as applied to inverse problems for imaging: theory, applications, current trends, and open challenges." In: *IEEE Antennas and Propagation Magazine* 59 (5), pp. 34–46.

Olver, F. W. J.; Lozier, D. W.; Boisvert, R. F. and Clark, C. W., eds. (2010). *NIST Handbook of Mathematical Functions*. New York, NY: Cambridge University Press.

Özdemir, C. (2012). *Inverse Synthetic Aperture Radar Imaging with MATLAB Algorithms*. Hoboken, NJ: John Wiley & Sons, Inc.

Pan, S. X. and Kak, A. C. (1983). "A computational study of reconstruction algorithms for diffraction tomography: interpolation versus filtered backpropagation". In: *IEEE Transactions on Acoustics, Speech, and Signal Processing* 31 (5), pp. 1262–1275.

Parini, C.; Gregson, S. F.; McCormick, J. and Rensburg, D. J. V. (2014). *Theory and Practice of Modern Antenna Range Measurements*. London: The Institution of Engineering and Technology.

Paulus, A.; Knapp, J. and Eibert, T. F. (2017). "Phaseless near-field far-field transformation utilizing combinations of probe signals". In: *IEEE Transactions on Antennas and Propagation* 65 (10), pp. 5492–5502.

Peters, L. P.; Daniels, J. J. and Young, J. D. (1994). "Ground penetrating radar as a subsurface environmental sensing tool". In: *Proceedings of the IEEE* 82 (12), pp. 1802–1822.

Petre, P. and Sarkar, T. K. (1992). "Planar near-field to far-field transformation using an equivalent magnetic current approach". In: *IEEE Transactions on Antennas and Propagation* 40 (11), pp. 1348–1356.

Pieraccini, M.; Miccinesi, L. and Rojhani, N. (2017). "Rcs measurements and isar images of small uavs". In: *IEEE Aerospace and Electronic Systems Magazine* 32 (9), pp. 28–32.

Pinder, L. L. G. F. (1999). *Numerical Solution of Partial Differential Equations in Science and Engineering*. Hoboken, NJ: John Wiley & Sons.

Potter, L. C.; Ertin, E.; Parker, J. T. and Cetin, M. (2010). “Sparsity and compressed sensing in radar imaging”. In: *Proceedings of the IEEE* 98 (6), pp. 1006–1020.

Pozar, D. M. (2012). *Microwave Engineering*. 4th edition. Hoboken, NJ: John Wiley & Sons.

Press, W. H.; Teukolsky, S. A.; Vetterling, W. T. and Flannery, B. P. (2007). *Numerical Recipes: The Art of Scientific Computing*. 3rd edition. Cambridge: Cambridge University Press.

Quijano, J. L. A. and Vecchi, G. (2010). “Field and source equivalence in source reconstruction on 3D surfaces”. In: *Progress in Electromagnetics Research, PIER* 103, pp. 67–100.

Qureshi, M. A.; Schmidt, C. H. and Eibert, T. F. (2013). “Efficient near-field far-field transformation for nonredundant sampling representation on arbitrary surfaces in near-field antenna measurements”. In: *IEEE Transactions on Antennas and Propagation* 61 (4), pp. 2025–2033.

Qureshi, M. A. (2013). “Near-Field Error Analysis and Efficient Sampling Techniques for the Fast Irregular Antenna Field Transformation Algorithm”. Dissertation. München: Technische Universität München.

Rao, S.; Wilton, D. and Glisson, A. (1982). “Electromagnetic scattering by surfaces of arbitrary shape”. In: *IEEE Transactions on Antennas and Propagation* 30 (3), pp. 409–418.

RFspin s.r.o. (2019). *RFspin*. URL: `http://www.rfspin.com` (visited on 10/07/2019).

Richmond, J. (1961). “A reaction theorem and its application to antenna impedance calculations”. In: *IRE Transactions on Antennas and Propagation* 9 (6), pp. 515–520.

Ruck, G. T.; Barrick, D. E.; Stuart, W. D. and Krichbaum, C. K. (1970). *Radar Cross Section Handbook*. Vol. vol. 1. New York, NY: Plenum Press.

Rumsey, V. H. (1954). “Reaction Concept in Electromagnetic Theory”. In: *Physical Review* 94, pp. 1483–1491.

Saad, Y. (2003). *Iterative Methods for Sparse Linear Systems*. 2nd edition. Philadelphia, PA: Society for Industrial and Applied Mathematics (SIAM).

Saad, Y. and Schultz, M. (1986). “GMRES: a generalized minimal residual algorithm for solving nonsymmetric linear systems”. In: *SIAM Journal on Scientific and Statistical Computing* 7 (3), pp. 856–869.

Sarvas, J. (2003). “Performing interpolation and anterpolation entirely by fast fourier transform in the 3-D multilevel fast multipole algorithm”. In: *SIAM Journal on Numerical Analysis* 41 (6), pp. 2180–2196.

Schelkunoff, S. A. (1936). “Some equivalence theorems of electromagnetics and their application to radiation problems”. In: *The Bell System Technical Journal* 15 (1), pp. 92–112.

Schmidt, C. H. and Eibert, T. F. (2009). “Multilevel plane wave based near-field far-field transformation for electrically large antennas in free-space or above material halfspace”. In: *IEEE Transactions on Antennas and Propagation* 57 (5), pp. 1382–1390.

Schmidt, C. H.; Leibfritz, M. M. and Eibert, T. F. (2008). “Fully probe-corrected near-field far-field transformation employing plane wave expansion and diagonal translation operators”. In: *IEEE Transactions on Antennas and Propagation* 56 (3), pp. 737–746.

Schmidt, C. H.; Schobert, D. T. and Eibert, T. F. (2011). “Electric dipole based synthetic data generation for probe-corrected near-field antenna measurements”. In: *Proc. 5th European Conference on Antennas and Propagation (EuCAP)*. Rome, Italy, pp. 3269–3273.

Schnattinger, G.; Mauermayer, R. A. M. and Eibert, T. F. (2014). “Monostatic radar cross section near-field far-field transformations by multilevel plane-wave decomposition”. In: *IEEE Transactions on Antennas and Propagation* 62 (8), pp. 4259–4268.

Schnattinger, G.; Schmidt, C. and Eibert, T. (2011). “3-D imaging by hierarchical disaggregation”. In: *German Microwave Conference (GeMiC)*, pp. 1–4.

Schnattinger, G. (2014). “Elektromagnetische Nahfeld- und Fernfeld-Bildgebungsverfahren basierend auf hierarchischen Felddarstellungen”. PhD thesis. Technical University of Munich.

Song, J. and Chew, W. C. (2001). “Error analysis for the truncation of multipole expansion of vector green’s functions”. In: *IEEE Microwave and Wireless Components Letters* 11 (7), pp. 311–313.

Stratasys Solutions Ltd. (2018). *GrabCAD*. URL: `https://grabcad.com` (visited on 10/07/2019).

Stratton, J. A. (1941). *Electromagnetic Theory*. New York, NY: McGraw-Hill Book Company.

Tai, C. (1994). *Dyadic Green Functions in Electromagnetic Theory*. Second Edition. Hoboken, NJ: IEEE Press.

Vaupel, T. and Eibert, T. F. (2006). “Comparison and application of near-field ISAR imaging techniques for far-field radar cross section determination”. In: *IEEE Transactions on Antennas and Propagation* 54 (1), pp. 144–151.

Volakis, J. L. and Sertel, K. (2012). *Integral Equation Methods for Electromagnetics*. Raleigh, NC: SciTech Publishing.

Wallén, H. and Sarvas, J. (2005). “Translation procedures for broadband MLFMA”. In: *Progress in Electromagnetics Research, PIER* 55, pp. 47–78.

Xia, T.; Meng, L. L.; Liu, Q. S.; Gan, H. H. and Chew, W. C. (2018). “A low-frequency stable broadband multilevel fast multipole algorithm using plane wave multipole hybridization”. In: *IEEE Transactions on Antennas and Propagation* 66 (11), pp. 6137–6145.

Yaghjian, A. D. (1986). “An overview of near-field antenna measurements”. In: *IEEE Transactions on Antennas and Propagation* 34 (1), pp. 30–45.

Publications of the Author

Azhar, A.; Neitz, O.; Knapp, J.; Baumgartner, R.; Mitic, G. and Eibert, T. F. (2019). "Near-field high-resolution imaging based on inverse equivalent source methods". In: *Proc. International Conference on Electromagnetics in Advanced Applications (ICEAA)*. Granada, Spain.

Eibert, T. F.; Kılıç, E.; Lopez, C.; Mauermayer, R. A. M.; Neitz, O. and Schnattinger, G. (2015a). "Electromagnetic field transformations for measurements and simulations (invited paper)". In: *Progress in Electromagnetics Research, PIER* 151, pp. 127–150.

Eibert, T. F.; Kılıç, E.; Lopez, C.; Mauermayer, R. A. M.; Neitz, O. and Schnattinger, G. (2015b). "Electromagnetic field transformations with spectral field representations on the Ewald sphere". In: *Proc. Progress in Electromagnetics Research Symposium (PIERS)*. Prague, Czech Republic, p. 118.

Geise, A.; Neitz, O.; Migl, J.; Steiner, H.; Fritzel, T.; Hunscher, C. and Eibert, T. F. (2019). "A crane based portable antenna measurement system — system description and validation". In: *IEEE Transactions on Antennas and Propagation* 67 (5), pp. 3346–3357.

Hamberger, G. F.; Koenen, C.; Neitz, O.; Mauermayer, R. A. M.; Eisner, C. J.; Siart, U. and Eibert, T. F. (2018). "Setup and characterization of a volumetric W-band near-field antenna measurement system". In: *IEEE Transactions on Antennas and Propagation* 66 (10), pp. 5498–5510.

Hofmann, B.; Neitz, O. and Eibert, T. F. (2019a). "Applying compressed sensing with predictable accuracy to spherical antenna near-field measurements". In: *Proc. Progress in Electromagnetics Research Symposium (PIERS)*. Rome, Italy.

Hofmann, B.; Neitz, O. and Eibert, T. F. (2019b). "On the minimum number of samples for sparse recovery in spherical antenna near-field measurements". In: *IEEE Transactions on Antennas and Propagation* 67 (12), pp. 7597–7610.

Hofmann, B.; Neitz, O.; Mauermayer, R. A. M. and Eibert, T. F. (2018). "Sparse recovery in spherical antenna near-field measurements". In: *Proc. Kleinheubacher Tagung*. Miltenberg, Germany.

Kılıç, E.; Neitz, O. and Eibert, T. F. (2015). "A finite element boundary element domain decomposition inverse scattering technique". In: *Proc. International Conference on Electromagnetics in Advanced Applications (ICEAA)*. Torino, Italy, pp. 985–988.

Kornprobst, J.; Knapp, J.; Neitz, O. and Eibert, T. F. (2019). "Measurement-error controlled iterative least-squares solution of inverse field transformation problems". In: *Proc. 41st Annual Symposium of the Antenna Measurement Techniques Association (AMTA)*. San Diego, CA, USA.

Kornprobst, J.; Mauermayer, R. A. M.; Neitz, O.; Knapp, J. and Eibert, T. F. (2019). "On the solution of inverse equivalent surface-source problems". In: *Progress in Electromagnetics Research, PIER* 165, pp. 47–65.

Kornprobst, J.; Neitz, O.; Knapp, J.; Mauermayer, R. A. and Eibert, T. F. (2019). "Solving inverse equivalent source problems by the normal error system of normal equations". In: *Proc. International Conference on Electromagnetics in Advanced Applications (ICEAA)*. Granada, Spain.

Neitz, O.; Mauermayer, R. A. M. and Eibert, T. F. (2019). "3D monostatic RCS determination from multistatic near-field measurements by plane-wave field synthesis". In: *IEEE Transactions on Antennas and Propagation* 67 (5), pp. 3387–3396.

Neitz, O.; Mauermayer, R. A. M.; Weitsch, Y. and Eibert, T. F. (2017). "A propagating plane-wave-based near-field transmission equation for antenna gain determination from irregular measurement samples". In: *IEEE Transactions on Antennas and Propagation* 65 (8), pp. 4230–4238.

Neitz, O. and Eibert, T. F. (2015). "Fourier based 3D ISAR near-field imaging and radar cross section transformation". In: *Proc. International Conference on Electromagnetics in Advanced Applications (ICEAA)*. Torino, Italy, pp. 1198–1201.

Neitz, O. and Eibert, T. F. (2016). "ISAR near-field imaging using monostatic-bistatic equivalence and plane-wave expansion". In: *Proc. IEEE International Symposium on Antennas and Propagation (APSURSI)*. Fajardo, PR, USA, pp. 171–172.

Neitz, O. and Eibert, T. F. (2017a). "Antenna gain determination in the near-field using propagating plane-wave expansions". In: *Proc. XXXIInd General Assembly and Scientific Symposium of the International Union of Radio Science (URSI GASS)*. Montreal, Canada, pp. 1–3.

Neitz, O. and Eibert, T. F. (2017b). "Measurement sample reduction for efficient antenna gain determination in the near-field". In: *Proc. IEEE International Symposium on Antennas and Propagation USNC/URSI National Radio Science Meeting*. Boston, MA, USA, pp. 161–162.

Neitz, O. and Eibert, T. F. (2018). "A plane-wave synthesis approach for 3D monostatic RCS prediction from near-field measurements". In: *Proc. 15th European Radar Conference (EuRAD)*. Madrid, Spain, pp. 99–102.

Neitz, O. and Eibert, T. F. (2019). "Monostatic RCS prediction from irregularly distributed near-field samples using plane-wave field synthesis". In: *Proc. 13th European Conference on Antennas and Propagation (EuCAP)*. Krakow, Poland, pp. 1–5.

Neitz, O.; Hofmann, B. and Eibert, T. F. (2019). "Plane-wave field synthesis for monostatic RCS prediction from multistatic near-field samples on irregular grids". In: *Proc. Progress in Electromagnetics Research Symposium (PIERS)*. Rome, Italy.

Neitz, O.; Mauermayer, R. A. M. and Eibert, T. F. (2016). "Antenna gain determination from irregular near-field samples using plane wave expansions". In: *Proc. Kleinheubacher Tagung*. Miltenberg, Germany.